

2-9-2011

# LARGE AREA 3D PHOTONIC CRYSTALS WITH EMBEDDED WAVEGUIDES

Alexander Raub

Follow this and additional works at: [https://digitalrepository.unm.edu/ece\\_etds](https://digitalrepository.unm.edu/ece_etds)

---

## Recommended Citation

Raub, Alexander. "LARGE AREA 3D PHOTONIC CRYSTALS WITH EMBEDDED WAVEGUIDES." (2011).  
[https://digitalrepository.unm.edu/ece\\_etds/216](https://digitalrepository.unm.edu/ece_etds/216)

This Dissertation is brought to you for free and open access by the Engineering ETDs at UNM Digital Repository. It has been accepted for inclusion in Electrical and Computer Engineering ETDs by an authorized administrator of UNM Digital Repository. For more information, please contact [disc@unm.edu](mailto:disc@unm.edu).

Alexander Kenneth Raub


*Candidate*

Electrical and Computer Engineering

*Department*

This dissertation is approved, and it is acceptable in quality and form for publication:

*Approved by the Dissertation Committee:*

 \_\_\_\_\_, Chairperson  
\_\_\_\_\_  
\_\_\_\_\_  
\_\_\_\_\_  
\_\_\_\_\_  
\_\_\_\_\_

\_\_\_\_\_  
\_\_\_\_\_  
\_\_\_\_\_  
\_\_\_\_\_

**LARGE AREA 3D PHOTONIC CRYSTALS  
WITH EMBEDDED WAVEGUIDES**

**BY**

**ALEXANDER KENNETH RAUB**

B.S., Microelectronic Engineering, Rochester Institute of Technology, 1995

M.S., Electrical Engineering, The University of New Mexico, 2002

DISSERTATION

Submitted in Partial Fulfillment of the  
Requirements for the Degree of

**Doctor of Philosophy  
Engineering**

The University of New Mexico  
Albuquerque, New Mexico

**December, 2010**

© 2010, Alexander Kenneth Raub

## ACKNOWLEDGMENTS

I like to acknowledge Dr. S. R. J. Brueck, my advisor and thesis chair, for his guidance and technical assistance. I worked many years with Dr. Brueck, as a student, and as a friend. His patients and dedications to my work are never lost on me. Through the years of our working relationship, his influence is forever lasting on me.

I also like to extend a special thanks to a good friend and colleague Dr. David Bruce Burckel. Without the assistance he gave me, I may not have been able to achieve all the work done in this dissertation. His moral support is greatly appreciated and very much needed at times.

I need to give acknowledgments to some of my other lab members, Svyatoslav “Slava” Smolev, Xiang He, and Alexander “Sasha” Neumann, for their support and suggestions in regards to my projects. It is with friends like these that make working in a laboratory an enjoyable place to be.

**LARGE AREA 3D PHOTONIC CRYSTALS  
WITH EMBEDDED WAVEGUIDES**

**BY**

**ALEXANDER KENNETH RAUB**

ABSTRACT OF DISSERTATION

Submitted in Partial Fulfillment of the  
Requirements for the Degree of

**Doctor of Philosophy  
Engineering**

The University of New Mexico  
Albuquerque, New Mexico

**December, 2010**

# **LARGE AREA 3D PHOTONIC CRYSTALS WITH EMBEDDED WAVEGUIDES**

by

**Alexander Kenneth Raub**

**B.S., Microelectronic Engineering, Rochester Institute of Technology, 1995**

**M.S., Electrical Engineering, University of New Mexico, 2002**

**Ph.D., Engineering, University of New Mexico, 2010**

## **ABSTRACT**

A crystal is a periodic and repeating arrangement of atoms or molecules. Photonic crystals are structures with periodic variations in the dielectric constants that manipulate and control the properties of light propagation. Photonic crystals are analogous to semiconductor crystals with periodic potentials that are responsible for the bandgaps for electrons and holes. For electrons and holes, the periodic potential effectively determines how the charged particles propagate through the crystal under applied fields. Similarly, for photons in a photonic crystal, the periodic dielectric function can give rise to photon bandgaps that control the motion of appropriate photons through the crystal.

The most complicated and possibly the most interesting photonic crystals are three-dimensional repeating structures. The main experimental work for this dissertation concerns the description of the fabrication of three-dimensional photonic crystals using a novel interferometric lithography technique. The work also describes the experimental hardware and the appropriate mathematical models for interferometric lithography.

Additional work concerns the generation of band diagrams for three-dimensional photonic crystals using simulation and modeling. Experimental results for the transmission and reflection properties of the photonic crystals fabricated by interferometric lithography are presented and the results are compared to the simulated band diagram models.

A new method for fabricating waveguides embedded in three-dimensional photonic crystals is also developed in this dissertation. This new approach to waveguide fabrication lends itself straightforwardly to mass manufacturing using standard semiconductor lithography equipment. This is in contrast to previously reported techniques that do not scale to high volume manufacturing.

Photonic crystals with integrated waveguides are of particular significance due to the possibilities of guiding or confining light propagation in the photonic crystal. This is comparable to the way dopants in a semiconductor crystal can impact electronic propagation. Waveguides with photonic crystals can demonstrate non-linear optical behavior if the crystal contains material that exhibits the optical Kerr effect or a nonlinear susceptibility  $\chi^{(2)}$ . These non-linear photonic crystals can be used for optical computing applications.

Using the novel approaches presented in this dissertation, in conjunction with additional extensions, it is possible to fabricate a wide variety of three-dimensional photonic crystals that exhibit a complete bandgap. These three-dimensional photonic crystals can contain embedded omnidirectional bandgap restricted waveguides.



# TABLE OF CONTENTS

LIST OF FIGURES .....	xi
LIST OF TABLES .....	xvi
CHAPTER 1 INTRODUCTION .....	1
Introduction to Photonic Crystals .....	1
One-Dimensional Photonic Crystals .....	2
Two-Dimensional Photonic Crystals .....	3
Three-Dimensional Photonic Crystals .....	5
Photonic Crystal Waveguides .....	5
Previous Work .....	6
Ion Milling (Yablonovite) .....	7
Multi-step (woodpile) .....	8
Artificial Opals .....	10
Overview .....	12
CHAPTER 2 APPROACHES TO INTERFEROMETRIC LITHOGRAPHY	
FABRICATION OF PHOTONIC CRYSTALS .....	14
Introduction to Interferometric Lithography .....	14
Modeling Interferometric Lithography Approach to Photonic Crystals .....	15
One-Dimensional Interferometric Lithography .....	15
Two-Dimensional Interferometric Lithography .....	25
Three-Dimensional Interferometric Lithography .....	37
Independent Control of $z$ -Direction Periodicity .....	43
CHAPTER 3 WAVEGUIDE FABRICATION .....	51
Two Wavelength Approach to Waveguide Fabrication .....	52
Fabrication Technique .....	52
Photoresist Requirements .....	54
Embedded Waveguides .....	57
Fabrication Technique .....	57
Photoresist Requirements .....	60
CHAPTER 4 EXPERIMENTAL FABRICATION OF 3D PHOTONIC CRYSTALS ...	62

Introduction to Experimental Fabrication of 3D Photonic Crystals .....	62
Experimental Approaches .....	63
Fresnel Mirror Interferometer .....	63
Phase Mask Interferometer .....	66
Michelson Interferometer.....	74
3D Photonic Crystal Photoresist Profile Models .....	87
Experimental 3D Photonic Crystal SEM Images .....	101
355 nm Exposure in Negative Photoresist .....	107
244 nm Exposure in Positive Photoresist.....	112
3D Photonic Crystal with Waveguides SEM Images .....	120
Waveguide at the Surface of 3D Photonic Crystal .....	121
Waveguide Embedded in the Center of 3D Photonic Crystal.....	125
<b>CHAPTER 5 3D PHOTONIC CRYSTAL OPTICAL PROPERTIES.....</b>	<b>130</b>
Introduction to 3D Photonic Crystal Optical Properties.....	130
Photonic Crystal Structural Classification and Unit Cell .....	130
Three-Exposure Photonic Crystal Unit Cell .....	136
Four-Exposure Photonic Crystal Unit Cell.....	145
Band Diagrams of the Photonic Crystals.....	154
Three-Exposures Photonic Crystal Band Diagram .....	156
Four-Exposures Photonic Crystal Band Diagram.....	157
3D Photonic Crystals FTIR Measurements .....	159
Three-Exposures Transmission & Reflection Plots .....	159
Four-Exposures Transmission & Reflection Plots.....	162
Comparison of Measurements to Models .....	165
Three Exposure Photonic Crystals.....	166
Four-Exposure Photonic Crystals .....	167
<b>CHAPTER 6 SUMMARY and FUTURE WORK.....</b>	<b>170</b>
3D Photonic Crystal Fabrication.....	170
Embedded Waveguide Fabrication.....	170
Prospects and Limitations .....	171

High Index Contrast .....	172
Scaling.....	174
Photonic Crystal with a Complete Bandgap .....	178
Future Studies .....	180
APPENDICES .....	182
APPENDIX A MATHCAD PROGRAM FOR BOTTOM ANTIREFLECTION	
COATING CALCULATIONS .....	183
APPENDIX B MatLAB PROGRAM FOR 3D PHOTORESIST PLOTS .....	191
APPENDIX C PROCESS FLOW SHEETS 3D PHOTONIC CRYSTALS. ....	194
Process Flow for 355 nm One Layer 3-Exposure 3D PhC .....	194
Process Flow for 355 nm One Layer 4-Exposure 3D PhC .....	196
Process Flow for 244 nm One Layer 3-Exposure 3D PhC .....	197
Process Flow for 244 nm One Layer 4-Exposure 3D PhC .....	198
Process Flow for 355 nm PhC with 244 nm Surface Waveguides .....	199
Process Flow for 244 nm PhC with 193 nm Surface Waveguides .....	201
Process Flow for 355 nm PhC with 244 nm Embedded Waveguides .....	202
APPENDIX D BARC COAT PROGRAM .....	205
APPENDIX E PHOTORESIST COAT PROGRAM.....	206
APPENDIX F PHOTORESIST DEVELOP PROGRAM.....	207
APPENDIX G NEWPORT ROTATION STAGE CONTROLLER LABVIEW	
PROGRAM.....	208
APPENDIX H COHERENT INFINITY LASER EXPOSURE CONTROL LABVIEW	
PROGRAM.....	212
APPENDIX I JEOL SEM JIMAGE CAPTURE LABVIEW PROGRAM.....	215
APPENDIX J MatLAB PROGRAM FOR PHOTONIC CRYSTAL UNIT CELL .....	220
APPENDIX K MPB CONTROL SCRIPT FILES .....	224
REFERENCES .....	226

## LIST OF FIGURES

Figure 1 – 1D photonic crystal.....	2
Figure 2 – 2D photonic crystal.....	3
Figure 3 – 2D photonic crystal of a) dielectric posts, b) dielectric holes. ....	4
Figure 4 – Examples of 2D Photonic Crystal Fibers. ....	4
Figure 5 – 3D photonic crystal.....	5
Figure 6 – Yablonovite Photonic Crystals Fabrication.....	7
Figure 7 – Yablonovite PMMA Photonic Crystals, fabricated with X-ray. ....	8
Figure 8 – Woodpile Photonic Crystals Fabrication.....	9
Figure 9 – Example of 3D Woodpile Photonic Crystals cross-section SEM & top-down SEM images. ....	10
Figure 10 – Examples of 3D opal Photonic Crystals.....	11
Figure 11 – linearly polarized plane wave at an arbitrary angle $\theta$ .....	17
Figure 12 – Two-beam interference intensity plot as a function of polarization angle $\vartheta_p$ with a $NA \equiv n \cdot \sin(\theta) = 0.7$ .....	21
Figure 13 – Two-beam interference during exposure & after photoresist development. .	24
Figure 14 – 1D interference lithography photoresist pattern. ....	25
Figure 15 – linearly polarized plane wave at an arbitrary angle $\theta$ and rotation $\phi$ . ....	27
Figure 16 – A 2D single exposure interferometric lithography photoresist patterns with $\theta=8^\circ$ .....	30
Figure 17 – A 2D single exposure interferometric lithography photoresist patterns with $\theta=32^\circ$ .....	31
Figure 18 – A 2D multiple-exposure interferometric lithography photoresist patterns....	35
Figure 19 – A 2D hexagonal multiple-exposure interferometric lithography photoresist patterns. ....	36
Figure 20 – 3D five beam single exposure interferometric lithography photoresist patterns. ....	39
Figure 21 – 3D multiple-exposures interferometric lithography photoresist pattern. ....	43
Figure 22 – Definitions of plane-wave beam angles in the air and in the photoresist.....	46

Figure 23 – Cross-section of a three-dimensional pattern and pitch definitions. ....	47
Figure 24 – Photonic crystal pitch parameter space. ....	49
Figure 25 – 3D multiple-exposure interferometric lithography photoresist pattern with tilted incident beams. ....	50
Figure 26 – Two-wavelength fabrication of waveguide in photonic crystal. ....	54
Figure 27 – 2D photonic crystal of posts, with various waveguide exposures. ....	55
Figure 28 – Waveguide in a photonic crystal of posts, with various amounts of photoresist absorption at the waveguide exposure wavelength. Waveguide thickness is proportional to photoresist absorption. ....	57
Figure 29 – Waveguide on the surface and embedded in the center of 3D photonic crystals, with various amounts of photoresist absorption at the waveguide exposure wavelength. ....	59
Figure 30 – Two embedded waveguides in a photonic crystal of posts, and in 3D photonic crystal. ....	60
Figure 31 – Fresnel corner cube mirror interferometer diagram. ....	64
Figure 32 – Fresnel mirror interferometer with offset incident beams diagram, used for making PhCs. ....	65
Figure 33 – Comparison of imaging through a conventional <u>binary</u> mask and an <u>alternating shifter</u> PSM. ....	67
Figure 34 – Phase-shift mask with phase shifting layer $d=\lambda/2(n-1)$ . ....	67
Figure 35 – Examples of various phase-shift masks. ....	68
Figure 36 – Phase mask interferometer, with zero-order and without zero-order. ....	70
Figure 37 – Phase mask interferometer with off-axis illumination diagram, used for making PhCs. ....	71
Figure 38 – Standard Michelson interferometric lithography setup. ....	75
Figure 39 – Michelson interferometric lithography setup with off-axis illumination, used for making PhCs. ....	76
Figure 40 – Michelson interferometric lithography setup with off-axis illumination, and beam intensity ratio compensator. This setup allows for matching the beam intensities in the photoresist. ....	79

Figure 41 – Reflectance and transmittance off a window surface with an index of refraction $n_w = 1.5$ .....	80
Figure 42 – Beam displacement from an optical flat window. ....	80
Figure 43 – Phase errors along the photonic crystal due to rotation misalignment. ....	82
Figure 44 – Michelson interferometric lithography setup with off-axis illumination, beam intensity ratio compensator and phase control interferometer. Complete setup necessary for making PhCs. ....	85
Figure 45 – Experimental PhC Michelson interferometric lithography setup. ....	87
Figure 46 – Models of 3D photonic crystal, made using 3-exposure interferometric lithography. ....	90
Figure 47 – Close up of 3D photonic crystal models, made using 3-exposure interferometric lithography. ....	91
Figure 48 – Models of 3D photonic crystal, made using 4-exposure interferometric lithography. ....	93
Figure 49 – Close up of 3D photonic crystal models, made using 4-exposure interferometric lithography. ....	94
Figure 50 – Models of 3D photonic crystal, made using 6-exposure interferometric lithography with a resist threshold of 62%. ....	96
Figure 51 – Close up of 3D photonic crystal models, made using 6-exposure interferometric lithography with resist threshold of 62%. ....	97
Figure 52 – Models of 3D photonic crystal, made using 6-exposure interferometric lithography with a resist threshold of 38%. ....	99
Figure 53 – Models of 3D photonic crystal close up, made using 6-exposure interferometric lithography with resist threshold of 38%. ....	100
Figure 54 – Wobble plate geometries, used for averaging out beam inhomogeneities. .	103
Figure 55 – Modeled effect wobble optics have on beam intensity and CD across a wafer. ....	104
Figure 56 – Michelson interferometric lithography setup used to produce 3D photonic crystals. ....	106

Figure 57 – 45° cross-section SEM images of defect free 3D photonic crystal over large areas, made using 3-exposure interferometric lithography at 355 nm. ....	109
Figure 58 – Top-down SEM images of defect free 3D photonic crystal over large areas, made using 3-exposure interferometric lithography at 355nm. ....	110
Figure 59 – 45° cross-section SEM images of defect free 3D photonic crystal over large areas, made using 4-exposure interferometric lithography at 355 nm. ....	111
Figure 60 – Top-down SEM images of defect free 3D photonic crystal over large areas, made using 4-exposure interferometric lithography at 355nm. ....	112
Figure 61 – 45° cross-section SEM images of 3D photonic crystal over large areas, made using 3-exposure interferometric lithography at 244 nm. ....	115
Figure 62 – Top-down SEM images of 3D photonic crystal over large areas, made using 3-exposure interferometric lithography at 244nm. ....	116
Figure 63 – Absorption Scan of Unexposed NR7 and KRF M167J photoresists. ....	116
Figure 64 – Simulation of 3D photonic crystal in photoresist of varying absorption. ....	118
Figure 65 – 45° cross-section SEM images of 3D photonic crystal over large areas, made using 4-exposure interferometric lithography at 244 nm. ....	119
Figure 66 – Top-down SEM images of 3D photonic crystal over large areas, made using 4-exposure interferometric lithography at 244nm. ....	119
Figure 67 – Waveguide contact mask lithography setup. ....	121
Figure 68 – Cross-section SEM images of 355 nm 3-exposure 3D photonic crystal, with 244 nm surface waveguides in negative photoresist. ....	123
Figure 69 – Cross-section SEM images of 244 nm 3-exposure 3D photonic crystal, with 193 nm surface waveguides in positive photoresist. ....	124
Figure 70 – Cross-section SEM images of 355 nm 3-exposure 3D photonic crystal, with 244 nm embedded waveguides in positive photoresist. ....	128
Figure 71 – Cross-section SEM images of 355 nm 3-exposure 3D PhC, with 244 nm embedded waveguides in positive photoresist, after a wet chemical etch-back of the PhC cleaved cross-section to reveal the embedded waveguide. ....	129
Figure 72 – A periodic 2D pattern consisting of a motif and lattice. ....	131

Figure 73 – Three-exposure 3D photonic crystal structures, used for identifying unit cell. .....	136
Figure 74 – 3-exposure 3D PhC nodes, with primary unit cell in highlighted in red, plus interpenetrating unit cells highlighted in blue and green. ....	139
Figure 75 – Diagram of a unit cell for a 3-exposure 3D photonic crystal. ....	140
Figure 76 – Brillouin zone for the hexagonal unit cell. ....	141
Figure 77 – Brillouin zone for the hexagonal unit cell with labeled $k$ -points.....	144
Figure 78 – Four-exposure 3D photonic crystal structures, used for identifying unit cell. .....	146
Figure 79 – 4-exposure 3D PhC nodes, with primary unit cell in highlighted in red, plus interpenetrating unit cell highlighted in blue. ....	148
Figure 80 – Diagram of a unit cell for a 4-exposure 3D photonic crystal. ....	149
Figure 81 – Brillouin zone for the tetragonal centered unit cell. ....	150
Figure 82 – Brillouin zone for the tetragonal centered unit cell with labeled $k$ -points. .	153
Figure 83 – Band gap diagram for 3-exposure photonic crystal.....	156
Figure 84 – Band gap diagram for 4-exposure photonic crystal.....	158
Figure 85 – 3-exposure photonic crystal FTIR scan reflection plots.....	160
Figure 86 – 3-exposure photonic crystal FTIR scan transmission plots.....	161
Figure 87 – 4-exposure photonic crystal FTIR scan reflection plots.....	163
Figure 88 – 4-exposure photonic crystal FTIR scan transmission plots.....	164
Figure 89 – Three-exposure Photonic Crystal Band Diagram and Reflection Plot, comparing bandgaps to reflection peaks. ....	167
Figure 90 – Four-exposure Photonic Crystal Band Diagram and Reflection Plot, comparing bandgaps to reflection peaks. ....	168
Figure 91 – Immersion Michelson interferometric lithography setup with off-axis illumination, beam intensity ratio compensator. Setup needed for making PhCs with symmetrical periodicity. $\Lambda_x = \Lambda_y = \Lambda_z$ .....	178
Figure 92 – Band diagram of a 4-exposure fully symmetric photonic crystal made of silicon and air. ....	179



## LIST OF TABLES

Table 1 – Modeling parameters for a 3-exposure 3D photonic crystal.....	89
Table 2 – Modeling parameters for a 4-exposure 3D photonic crystal.....	92
Table 3 – Modeling parameters for a 6-exposure 3D photonic crystal.....	95
Table 4 – The relation between 3D crystal families, crystal systems, and lattice systems. .....	133
Table 5 – The 14 3D Bravais Lattices .....	134
Table 6 – Critical points of the hexagonal Brillouin zone.....	144
Table 7 – Critical points of the tetragonal centered Brillouin zone.....	153
Table 8 – Process flow and parameters for 355 nm single layer 3-exposure 3D PhC....	196
Table 9 – Process flow and parameters for 355 nm single layer 4-exposure 3D PhC....	197
Table 10 – Process flow and parameters for 244 nm single layer 3-exposure 3D PhC..	198
Table 11 – Process flow and parameters for 244 nm single layer 4-exposure 3D PhC..	199
Table 12 – Process flow for 355 nm PhC with 244 nm surface waveguides in negative photoresist.....	201
Table 13 – Process flow for 244 nm PhC with 193 nm surface waveguides in positive photoresist.....	202
Table 14 – Process flow for 355 nm PhC with 244 nm embedded waveguides in negative photoresist.....	204
Table 15 – BARC coat spin program.....	205
Table 16 – Photoresist coat spin program.....	206
Table 17 – Photoresist develop program.....	207

# CHAPTER 1

## INTRODUCTION

### *Introduction to Photonic Crystals*

A crystal is a periodic and repeating arrangement of atoms or molecules. Photonic crystals (PhCs) are structures with periodic variations in dielectric constants that manipulate and control the properties of light propagation. Photonic crystals are analogous to semiconductor crystals with periodic potentials that are responsible for the bandgaps for electrons and holes. For electrons and holes, the periodic potential effectively determines how the charged particles propagate through the crystal under applied fields. Similarly, for photons in a photonic crystal, the periodic dielectric function can give rise to photon bandgaps that control the motion of appropriate photons through the crystal.

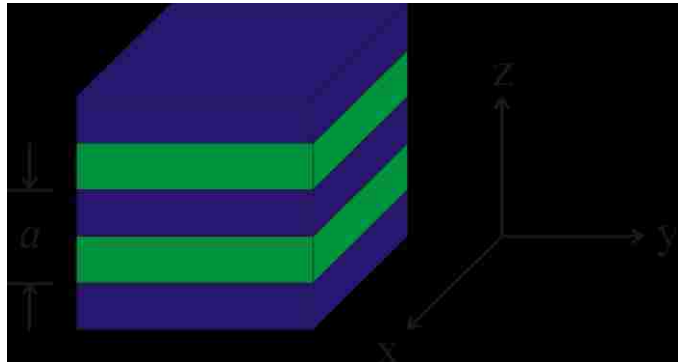
The period, fill factor, and structural arrangement of the crystal determine if the crystal periodic function allows or prohibits the propagation of waves with a given energy level and propagation direction. For electrons the energy structure of the crystal may give rise to a gap in the energy band that prevents electron waves from propagating in a given direction. If the crystal lattice potential is large enough, the gap extends to all possible propagation directions, resulting in a complete bandgap. A semiconductor has a complete bandgap between the conduction and valence energy bands. Similarly for photonic crystals that have a large difference in the periodic dielectric function made with low absorption loss material can have a complete photonic bandgap between the air and

dielectric bands, preventing light from propagating in any direction across a specific frequency ranges.

The following sections explain one-dimensional, two-dimensional, and three-dimensional photonic crystals. The sections will also give applications and examples of a photonic crystal.

## One-Dimensional Photonic Crystals

The simplest crystal is a one-dimensional crystal, which has a periodic dielectric function in only one direction; refer to Figure 1. The spatial period labeled as “ $a$ ” in Figure 1 of the stack is called the lattice constant, since it corresponds to the lattice constant of ordinary crystals composed of regular array of atoms. Such photonic crystals are commonly referred as multilayer dielectric films. They usually consist of alternating layers of material with different dielectric constants.



**Figure 1** – 1D photonic crystal.

One of the best-known and most common forms of a one-dimensional photonic crystal is the Bragg reflector. The photonic crystal has a forbidden bandgap for light with a frequency within a specified range propagating within a specified angular range perpendicular to the crystal surface; i.e. the photonic crystal acts as a band-pass mirror. In addition to the Bragg reflector, band-pass filters, polarizing

beam splitter, and antireflection coatings are all possible types of one-dimensional photonic crystals.<sup>1</sup>

## Two-Dimensional Photonic Crystals

A two-dimensional crystal has a periodic dielectric function in two directions; refer to Figure 2. Two-dimensional crystals are considered either photonic crystal slabs or photonic crystal fibers.

The photonic crystal slab is a photonic crystal with periodicity in two dimensions with the third dimension of finite height that resides on or between substrates. The wave propagation of a photonic crystal slab in-plane of the crystal is determined

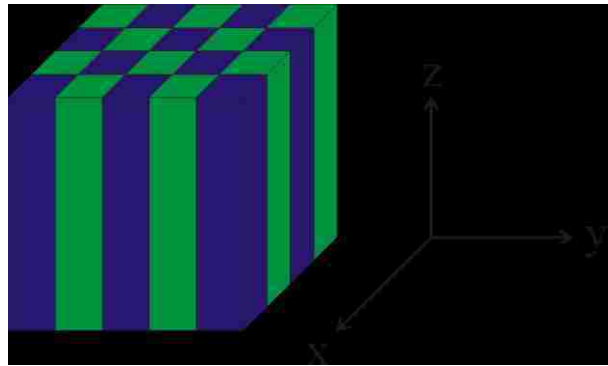
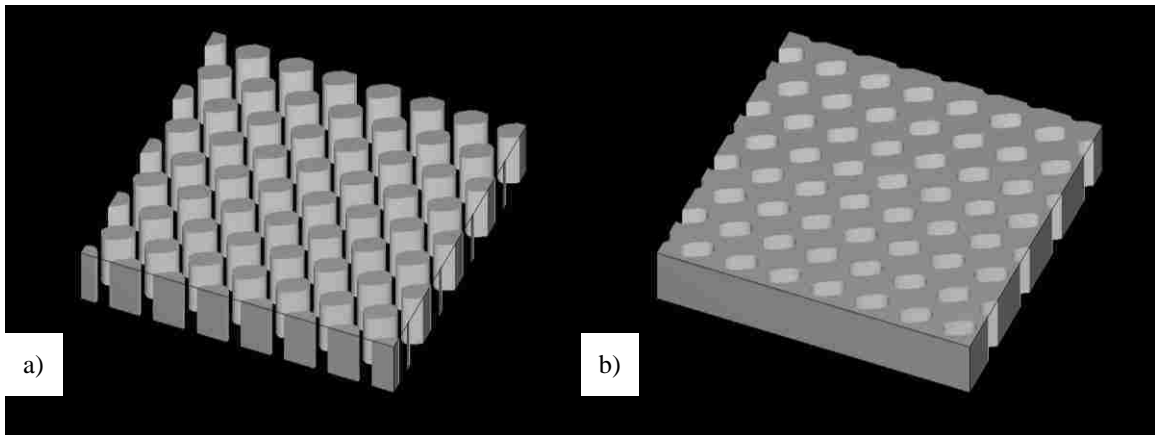


Figure 2 – 2D photonic crystal.

by the photonic crystal band structure, and the wave propagation perpendicular to the crystal is determined by index guiding. The photonic crystal fiber has periodicity in two transverse dimensions with the third dimension essentially being infinitely long.<sup>2</sup> Unlike the one-dimensional photonic crystal the propagation of waves in a two-dimensional photonic crystal can be restricted for all in-plane directions of propagation. Two-dimensional photonic crystals have a decisive influence on wave polarization propagation properties. The two-dimensional photonic crystal may possess a full-bandgap for one or both polarizations (TE and TM).

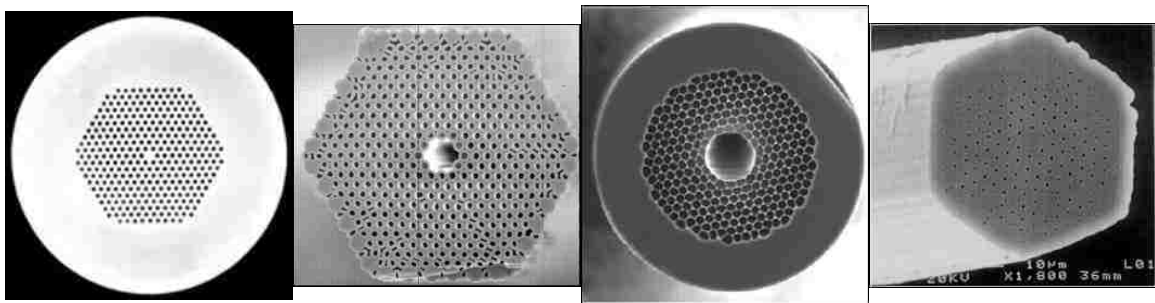
Photonic Crystal Slabs fall into two main categories: a periodic array of disconnected high dielectric cylinder posts in a low dielectric or air medium ( $n_2 > n_1$ ), and

the inverse periodic array of low dielectric or air holes in a high dielectric medium ( $n_1 > n_2$ ); refer to Figure 3.



**Figure 3** – 2D photonic crystal of a) dielectric posts, b) dielectric holes.

Some examples of application for 2D photonic crystal slabs are polarization beam splitters, super prisms, miniature monolithic reflective gratings, and output couplers. Photonic crystal fibers (PCF), also known as micro structured optical fiber (MOF) and holey fiber (HF), utilizes a photonic band gap effect to guide light rather than index guiding. Photonic crystal fibers have the advantage of having lower losses and smaller bending radii than their index guiding counterparts. Some examples of photonic crystal fibers are presented in Figure 4.<sup>3</sup>



**Figure 4** – Examples of 2D Photonic Crystal Fibers.

## Three-Dimensional Photonic Crystals

Similarly A three-dimensional crystal has a periodic dielectric function in all three directions; refer to Figure 5. Only three-dimensional photonic crystals allow for omnidirectional photonic bandgaps. The first experimental three-dimensional photonic crystal with a complete bandgap was demonstrated by Eli Yablonovitch in 1991.<sup>4</sup> Some applications of a bulk three-dimensional photonic crystal are: omnidirectional reflector, and band-edge lasers.

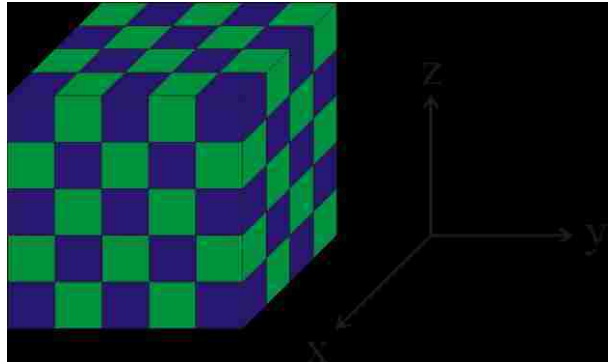


Figure 5 – 3D photonic crystal.

There are numerous ways to fabricate three-dimensional photonic crystals (PhCs), such as: ion-beam milling (Yablonovite),<sup>5</sup> a multi-step lithography and etching technique (layer-by-layer or woodpile approach),<sup>6</sup> artificial Opals, autocloning, 4 or 5-beam holography.<sup>7,8</sup> Most of these techniques are further examined at the end of this chapter and into the next chapter.

## ***Photonic Crystal Waveguides***

In a photonic crystal there exists a dielectric band (from the higher  $n_2$  media) and an air band (from the lower  $n_1$  media, typically  $n_1 = 1$  and thus the air band nomenclature), analogous to the valance and the conduction band, respectively, in a semiconductor crystal. Doping a semiconductor material can be achieved by either adding a donor or an acceptor atom. Both result in a change in the electrical properties of an atomic crystal. In a similar fashion, the optical properties of a photonic crystal can be

changed by introducing point defects, by either adding or removing dielectric material. Adding dielectric material to a photonic crystal unit cell is similar to a donor atom in an atomic crystal, creating states originating from the bottom of the air band. Likewise removing dielectric material from a photonic crystal unit cell is similar to an acceptor atom in an atomic crystal creating states originating from the top of the dielectric band.

If a line of point defects in an otherwise perfect photonic crystal lattice are introduced, an electromagnetic wave having a frequency within the bandgap of the photonic crystal structure can be guided through the crystal. In this case the line defect resembles a waveguide. A waveguide acts as an optical wire to guide an optical signal through the photonic crystal. Waveguides in photonic crystal can have low-loss bends that can be as sharp as  $90^\circ$ . Waveguide branching, beam splitting, and combining are all achievable in photonic crystals.<sup>9</sup> Waveguides placed within proximity of each other embedded in a photonic crystal can exhibit mode coupling between the waveguides.<sup>10</sup>

With the ability to controllably fabricate waveguides and point defects in photonic crystals, many useful photonic bandgap applications can be realized. For instance, high-Q microcavities, high-quality optical filters, channel drop filters, optical limiters, beam splitters, Bragg waveguide reflectors, optical spectrometers, optical switches, second harmonic generation structures, plus devices that control spontaneous emissions, are all possible, individually and in combination, using a photonic crystal.<sup>1</sup>

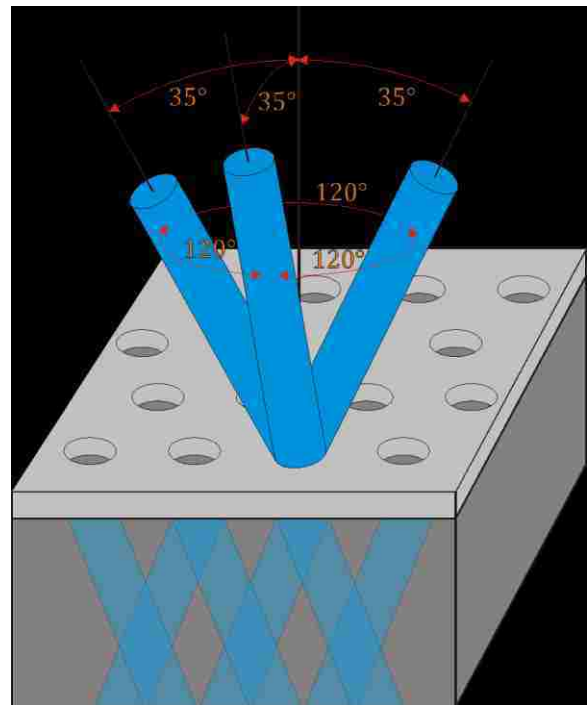
## ***Previous Work***

Three-dimensional photonic crystals are the focus of this work, and currently can be broken down into six major fabrication schemes: Yablonovite, woodpile, artificial

Opals, autocloning, two-photon absorption photolithography, and laser holography. This section will briefly look at some of the three-dimensional photonic crystal fabrication techniques that have been demonstrated to date. Because the three-dimensional photonic crystal fabrication technique used in this dissertation is a variation on the laser holography technique; greater focus will be given to prior work with this approach in the next chapter.

### **Ion Milling (Yablonovite)**

A three-dimensional photonic crystal via the use of ion milling was fabricated by Eli Yablonovitch and his group in 1991. It was the first crystal that demonstrated a complete photonic bandgap structure in the microwave region. The photonic crystal was fabricated by putting a metal mask on bulk GaAs, and etching holes at an angle into the substrate using chemically assisted ion beam etching (CAIBE). The metal mask was a two-dimensional array of holes arranged in a hexagonal orientation. Then ion milling of the substrate at an angle of  $35.26^\circ$  with respect to the normal to the surface was performed, creating an angled trench or hole in the substrate. The substrate was then rotated  $120^\circ$  and a second ion etch was performed, followed by a third and final substrate rotation of



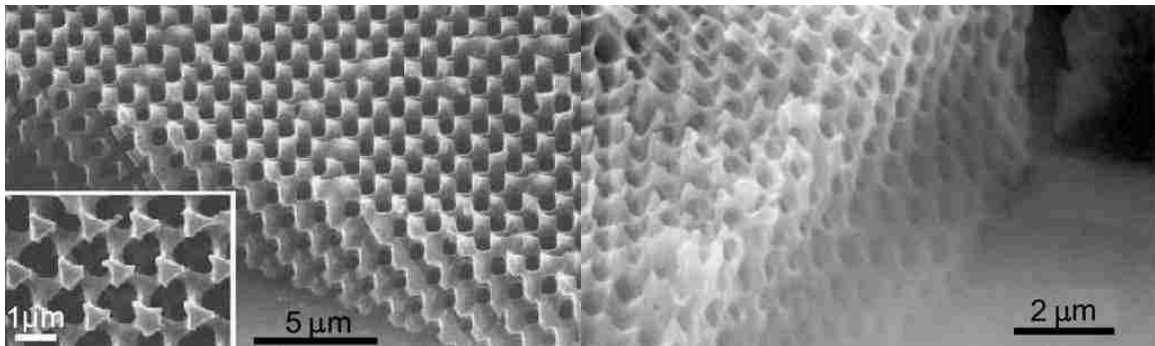
**Figure 6** – Yablonovite Photonic Crystals Fabrication.



120° and etch. The metal mask is chemically removed leaving behind a three-dimensional photonic crystal in the substrate material, see Figure 6. This photonic crystal is called a Yablonovite structure, after Eli Yablonovitch.<sup>11</sup>

One of the issues with this technique is the ability to etch deep holes and thus thick photonic crystals. The etch selectivity to the mask must be sufficient to allow a deep etch (many periods). Thickening the mask to increase etch times results in smaller etched holes due to the shadowing effects of a thick mask.

A similar technique uses X-rays to expose a PMMA substrate through the metal mask. Holes are then formed in the PMMA by using a solvent developer to remove the exposed PMMA. Finally the metal mask is chemically removed from the PMMA, leaving the photonic crystal. An example of a three-dimensional Yablonovite photonic crystal made out of PMMA exposed by X-ray lithography is shown in Figure 7.<sup>12</sup>

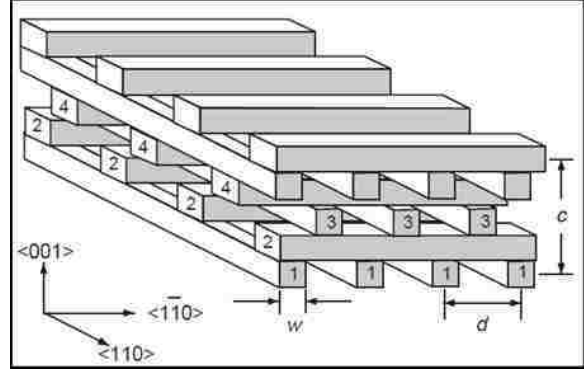


**Figure 7** – Yablonovite PMMA Photonic Crystals, fabricated with X-ray.

### **Multi-step (woodpile)**

Making three-dimensional photonic crystals utilizing modern micro-fabrication technologies of multiple thin-film process steps are referred to as woodpile type photonic crystals. These photonic crystals are built one layer-by-layer at time until the desired

thickness is obtained. A diagram of the layer structure is shown in Figure 8. It consists of layers of one-dimensional rods with a stacking sequence that repeats itself every four layers with a repeat distance of  $c$ . Within each layer, the axes of the rods



**Figure 8** – Woodpile Photonic Crystals Fabrication.

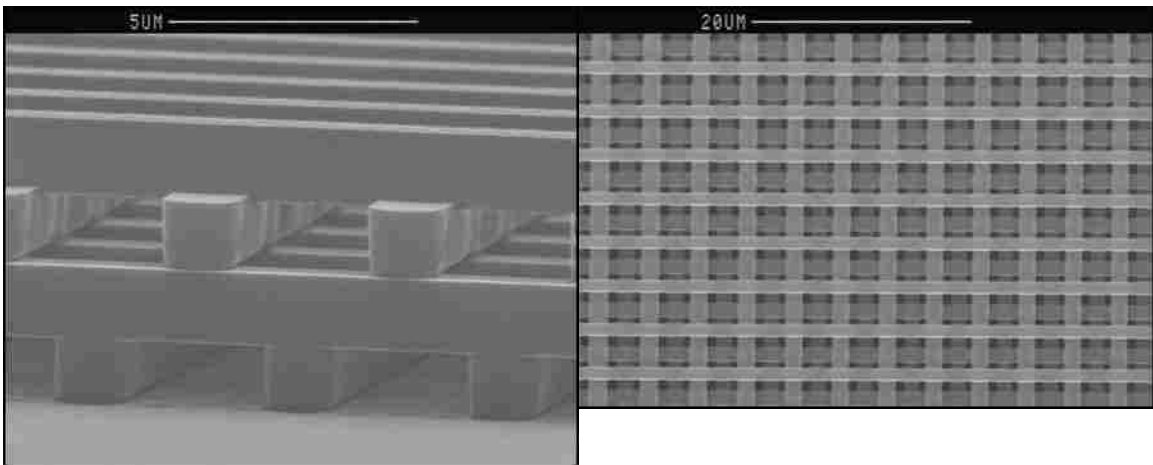
are parallel to each other with a pitch of  $d$ . The orientations of the axes are rotated by  $90^\circ$  between adjacent layers. Between every other layer, the rods are shifted relative to each other by  $0.5d$ . The resulting structure has face-centered-tetragonal (f.c.t.) lattice symmetry. For the special case of  $c/d = 1.414$ , the lattice can be derived from a face-centered-cubic (f.c.c.) unit cell with a basis of two rods. This layered structure can also be derived by replacing the  $\langle 110 \rangle$  chains of atoms in a diamond structure crystal with rods.

The process involves the repetitive deposition and etching of multiple dielectric films. Within each layer,  $\text{SiO}_2$  is first deposited, patterned, and etched to the desired depth. The resulting trenches are then filled with polycrystalline silicon or similar dielectric material. Following this, the surface of the wafers are planarized using chemical mechanical polishing, and the process is then repeated. After processing all desired levels, the wafer is immersed in a  $\text{HF}/\text{H}_2\text{O}$  solution for the final  $\text{SiO}_2$  removal.<sup>6</sup>

Some of the issues with the woodpile technique are the requirement of sub- $\mu\text{m}$  precision placement, plus complicated and expensive multi-step processing. Alignment of each layer needs to be within a fraction of the period, with an alignment step for each layer. At least four alignment steps are required in order to obtain a single photonic

crystal period, and at least seventeen different processes steps are required in order to obtain a single photonic crystal period using the standard techniques of silicon microelectronics.

The first woodpile three-dimensional photonic crystal was manufactured by S. Y. Lin and group at Sandia National Laboratories. An example of a woodpile photonic crystal made out of polycrystalline silicon with a bandgap at  $11\mu\text{m}$  is shown in Figure 9. Another approach to fabricating woodpile structure has been reported by Deying Xia, who utilized silica nanoparticles self-assembled around photoresist patterns using spin coating. After multiple layers are formed, the photoresist pattern is removed through a high temperature calcination process.<sup>13</sup>



**Figure 9** – Example of 3D Woodpile Photonic Crystals cross-section SEM & top-down SEM images.

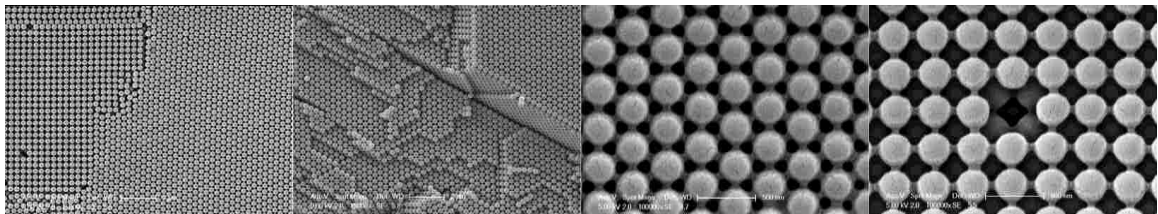
## Artificial Opals

Three-dimensional photonic crystals made by colloidal solution of uniform spheres are referred to as artificial opal photonic crystals, because the self-organized spheres obtained reproduces the structure of natural opals. Usually a colloidal solution of

latex, PMMA, or silica spheres are ordered through a centrifugal force, or by slow evaporation of the solvent forcing the spheres to settle out of solution.

The spheres will crystallize inside the lattice with the minimal potential energy, i.e. inside the f.c.c. lattice. However the f.c.c. lattice is unfortunately very close to the energy of the hexagonal close packed h.c.p. lattice. This tends to cause significant stacking defects in artificial opals, which is one of the main fabrication issues. The orientation of the “crystallized” lattice of spheres can be forced by pre-structuring the substrate where the sedimentation takes place. The other main issue of artificial opals is that the spheres are usually made from low dielectric constant materials; therefore the photonic crystals don’t have a complete bandgap. This can be solved by using the inverse opal technique. Inverse opal is a process that infiltrates a photonic crystal with a high index media, such as silicon, therefore allowing for a complete bandgap and is discussed in detail in Chapter 6.

Examples of opal photonic crystals made of 364nm diameter PMMA spheres are shown in Figure 10. As is seen in Figure 10 artificial opals commonly have many defects such as missing spheres, lattice mismatch, and packing errors. In one of the images of the colloidal photonic crystal, the image exhibits domains of both (111) and (100) orientations.<sup>14</sup>



**Figure 10** – Examples of 3D opal Photonic Crystals.

## **Overview**

The remainder of this dissertation will focus on the modeling, fabricating, and measuring of three-dimensional photonic crystals made by interferometric lithography. Three-dimensional photonic crystals with embedded waveguides, plus future prospects for three-dimensional photonic crystals made by interferometric lithography are also a focal point of this dissertation. It is possible to fabricate a wide variety of three-dimensional photonic crystals made by interferometric lithography along with additional processing steps that exhibit a complete bandgap. These three-dimensional photonic crystals can contain embedded omnidirectional bandgap restricted waveguides.

Different approaches to fabricating photonic crystals (in one, two, and three-dimensions) using interferometric lithography, is examined in Chapter 2. Chapter 2 contains mathematical models for each of the different interferometric lithography methods of fabricating photonic crystals.

A fabrication technique to create waveguides embedded in the photonic crystals, using two different exposing wavelengths for creating the waveguides and photonic crystal, is introduced in Chapter 3. Finally the chapter presents a fabrication technique to embed the waveguides inside the photonic crystal.

The experimental fabrication of three-dimensional photonic crystals is presented in Chapter 4. Three different experimental setups for making three-dimensional photonic crystals are presented. Simulated photoresist profiles of experimental three-dimensional photonic crystals are generated and plotted, followed by actual photoresist profile SEM images of experimentally fabricated three-dimensional photonic crystals. Comparisons of the modeled and experimental photoresist profiles are concluded. Chapter 4 finishes

on fabricated three-dimensional photonic crystals containing waveguides and their photoresist profile SEM images.

Chapter 5 is focused on the optical properties of the three-dimensional photonic crystals fabricated in Chapter 4. Optical models of three-dimensional photonic crystals are simulated, producing photonic crystal band diagrams. Chapter 5 continues with FTIR measurements and presents transmission and reflection plots of the three-dimensional photonic crystals fabricated in Chapter 4. The FTIR measurements are then compared to the simulated photonic crystal band diagrams.

The dissertation concludes in Chapter 6 on the accomplishments of the interferometric lithography three-dimensional photonic crystals, and the embedded waveguides. The prospects and limitations of the photonic crystals are given in Chapter 6. Ways to overcome some of the limitations are discussed. An example of a three-dimensional photonic crystal with a 26% complete bandgap is simulated, utilizing interferometric lithography, with further infiltration of a high index material. Chapter 6 finishes with direction on future studies for interferometric lithography three-dimensional photonic crystals.

The Appendices contain the programs used to generate the calculation, simulation, and plots of the data used in this dissertation. They also contain all the different process flow sheets used in the fabrication of the interferometric lithography three-dimensional photonic crystals. The programs for the equipment used in the fabrication of the interferometric lithography three-dimensional photonic crystals, are also found in the Appendices.

**CHAPTER 2**  
**APPROACHES TO INTERFEROMETRIC LITHOGRAPHY**  
**FABRICATION OF PHOTONIC CRYSTALS**

***Introduction to Interferometric Lithography***

Interferometric lithography (IL) has been used for years to produce holographic gratings. Interferometric lithography has the capability of producing gratings down to  $\lambda/4n$  half-pitch, where  $n$  is the index of refraction of the exposure medium ( $n = 1$  for air).<sup>15</sup> Interferometric lithography has a large depth-of-focus with great uniformity when forming gratings on photoresist-coated wafers. Most important of all, using interferometric lithography there is no need to use a mask or lens system to produce very small pitch structures. This allows interferometric lithography to facilitate inexpensive large-area fabrication capabilities for sub-micrometer pitch periodic features. Interferometric lithography typically involves the use of a small number of coherent optical beams incident from different directions on a 2D film (thin photoresist layer  $\ll \lambda$ ) or 3D film (thick photoresist layer  $\gg \lambda$ ) to produce an interference pattern whose intensity distribution is recorded in the photoresist layer and is later transferred (developed) by thermal or chemical processes. In the literature this concept has been variously referred to as holographic lithography, interference lithography, and interferometric lithography which is the description adopted in this dissertation. The result is a periodic pattern with either a single period (two-beam interference) or multiple periods which can have different orientations in two and three dimensions.<sup>16</sup>

This chapter goes into detail on the theory and modeling of interferometric lithography. The fabrication of photonic crystals using interferometric lithography is explained.

## ***Modeling Interferometric Lithography Approach to Photonic Crystals***

Interferometric lithography has been used for a long time in manufacturing one and two-dimensional periodic structures. Its low cost and simplicity makes it a versatile technique for building photonic crystals. Interferometric lithography uses two or more plane waves of light to create a sinusoidal intensity pattern at the intersection of the plane waves. The sinusoidal intensity pattern is then typically used to expose photoresist.

The theory and modeling of interferometric lithography detailed in this section is broken down into one-dimensional, two-dimensional, and three-dimensional interferometric lithography. For each case of interferometric lithography, single-exposure techniques and multiple-exposure techniques are explained and modeled. The interferometric lithography models are then applied to the fabrication of photonic crystals in photoresist films.

### **One-Dimensional Interferometric Lithography**

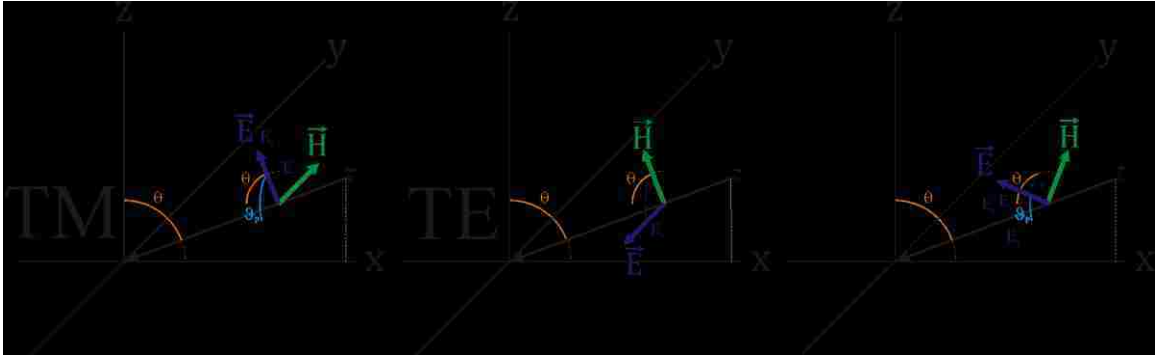
In order to make one-dimensional structures using interferometric lithography only two plane waves of mutually coherent light are needed. As the name implies, some form of interferometer is used to split a single coherent beam into two mutually coherent beams. An exposure plane is then placed at the intersection of the two beams. There are



three conditions that must be met in order for interference of the two beams to occur. The first condition is polarization. Only the collinear parts of the two beams' electric fields contribute to the interference pattern. The greatest degree of interference occurs when using linearly polarized light, specifically when using TE linearly polarized light. The second condition that must be met for interference is frequency. To produce a stationary interference pattern the two electric fields must have the same frequency for the duration of the exposure. Otherwise the phase front of one beam will drift in relation to the phase front of the other beam, and the interference pattern will wash out. For interference to occur without shifts during the exposure, the optical path length difference of the two beams must be less than the temporal coherence of the light beam. The third condition needed for interference is spatial coherence length. More specifically the phase fluctuations across the interfering beams are slowly varying compared to the average phase front of each beam during the exposure time period, creating a stationary interference pattern. For interference to occur without shifts during the exposure, the stationary wavefront across the two superimposed beams must be less than the spatial coherence length of the light beam.<sup>17</sup>

Modern Photoresists for the semiconductor industry have been engineered to have a highly nonlinear response to light intensity. For positive tone photoresist, in locations where the light intensity is above the exposure threshold, the photoresist is removed during development while the photoresist remains everywhere else. Similarly for negative tone photoresist, the photoresist remains after development where the light intensity is above the exposure threshold and the photoresist is removed everywhere else. Thus knowing the irradiance pattern of the exposing beams it is possible to derive an

approximation to the final photoresist pattern. The irradiance pattern is given by summing of the electric fields for each beam at the exposure plane and taking the square of the resulting amplitude. Transverse Electric (TE) mode beams are ideal for interferometric lithography, since the standing wave pattern formed with TE polarized light have the largest ratio of maximum to minimum values of the standing wave otherwise known as the standing wave ratio (SWR). In some situations it may not be possible to use TE polarized light and the polarization state or angle must be taken into account. Figure 11 is a plot of the transverse electric and magnetic vectors of a uniform plane wave in the  $xz$ -plane with linear polarization in an unbounded medium at an oblique angle  $\theta$  for TE polarized, TM polarized, and polarized at angle  $\vartheta_p$ .



**Figure 11** – linearly polarized plane wave at an arbitrary angle  $\theta$ .  
a) TM mode. b) TE mode. c) Linearly polarized at angle  $\vartheta_p$ .

The following formulas present the intensity pattern for one-dimensional interferometric lithography. The electric field for a forward propagating beam of light in the  $xz$ -plane with arbitrary polarization (refer to Figure 11-c) is defined as follows:

$$\vec{E} = A\{-\cos(\vartheta_p)\hat{y} + \sin(\vartheta_p) [-\cos(\theta)\hat{x} + \sin(\theta)\hat{z}]\} \cdot e^{ik[\sin(\theta)x + \cos(\theta)z]} \quad (2.1)$$

$$\vec{H} = \frac{A}{n}\{-\sin(\vartheta_p)\hat{y} + \cos(\vartheta_p) [-\cos(\theta)\hat{x} + \sin(\theta)\hat{z}]\} \cdot e^{ik[\sin(\theta)x + \cos(\theta)z]} \quad (2.2)$$

With  $A$  being the electric field amplitude,  $\theta$  being the angle of incidence of the plane wave onto the exposure plane,  $k$  is the wave number ( $k = 2\pi \cdot n/\lambda$ ),  $n$  is the refractive index of the medium ( $n = 1$  for air),  $\lambda$  is the exposure beam wavelength, and  $\vartheta_p$  is the polarization angle. The polarization angle  $\vartheta_p$  is the angle of the linearly polarized electric field from the  $xy$ -plane, with  $\vartheta_p = 0$  for TE polarized light, no electric field in the direction of propagation, and  $\vartheta_p = \pi/2$  for TM polarized light, no magnetic field in the direction of propagation. Since photoresist responds to the intensity ( $|E|^2$ ), the rest of the equations in this dissertation will concentrate on just the  $E$ -fields and not the  $H$ -fields. The simplified  $E$ -fields, from equation 2.1, for both TE linearly polarized ( $\vartheta_p = 0$ ) and TM linearly polarized ( $\vartheta_p = \pi/2$ ) at the  $z = 0$  plane are given below.

$$\vec{E}_{\text{TE}} = -A\hat{y} \cdot e^{ik \sin(\theta)x} \quad (2.3)$$

$$\vec{E}_{\text{TM}} = A[-\cos(\theta)\hat{x} + \sin(\theta)\hat{z}] \cdot e^{ik \sin(\theta)x} \quad (2.4)$$

For one-dimensional interferometric lithography, two forward propagating beams of light from opposing  $x$ -directions are required to form an interference or standing wave pattern. The following formulas give the intensity pattern for one-dimensional interferometric lithography.

$$\vec{E}_1 = A_1\{-\cos(\vartheta_{p_1})\hat{y} + \sin(\vartheta_{p_1})[-\cos(\theta_1)\hat{x} + \sin(\theta_1)\hat{z}]\} \cdot e^{ik[\sin(\theta_1)x + \cos(\theta_1)z]} \quad (2.5)$$

$$\vec{E}_2 = A_2\{-\cos(\vartheta_{p_2})\hat{y} + \sin(\vartheta_{p_2})[-\cos(\theta_2)\hat{x} + \sin(\theta_2)\hat{z}]\} \cdot e^{ik[\sin(\theta_2)x + \cos(\theta_2)z]} \quad (2.6)$$

$$\vec{E} = \vec{E}_1 + \vec{E}_2 \quad (2.7)$$

$$\begin{aligned} \vec{E} = & A_1 \{-\cos(\vartheta_{P_1})\hat{y} + \sin(\vartheta_{P_1})[-\cos(\theta_1)\hat{x} + \sin(\theta_1)\hat{z}]\} \cdot e^{ik[\sin(\theta_1)x + \cos(\theta_1)z]} + \\ & A_2 \{-\cos(\vartheta_{P_2})\hat{y} + \sin(\vartheta_{P_2})[-\cos(\theta_2)\hat{x} + \sin(\theta_2)\hat{z}]\} \cdot e^{ik[\sin(\theta_2)x + \cos(\theta_2)z]} \end{aligned} \quad (2.8)$$

$E$  in the above equation 2.8 is the total electric field at the exposure plane. For the generalization of the intensity equations the notation  $\vec{E} = A \cdot \tilde{E}$  will be used from here on.

The photoresist responds to the irradiance of the  $E$ -field, and defined as:

$$I = \frac{1}{2} |\vec{E} \cdot \vec{E}^*| = \frac{1}{2} |\vec{E}|^2 = \frac{1}{2} |A \cdot \tilde{E}|^2 \equiv \frac{|A_x \cdot \tilde{E}_x|^2 + |A_y \cdot \tilde{E}_y|^2 + |A_z \cdot \tilde{E}_z|^2}{2} \quad (2.9)$$

The irradiance for a one-dimensional interferometric lithography exposure is given as:

$$\begin{aligned} I = & \frac{1}{2} \left\{ \left| -A_1 \sin(\vartheta_{P_1}) \cos(\theta_1) \cdot e^{ik[\sin(\theta_1)x + \cos(\theta_1)z]} - A_2 \sin(\vartheta_{P_2}) \cos(\theta_2) \cdot \right. \right. \\ & \left. \left. e^{ik[\sin(\theta_2)x + \cos(\theta_2)z]} \right|^2 + \right. \\ & \left. \left| -A_1 \cos(\vartheta_{P_1}) \cdot e^{ik[\sin(\theta_1)x + \cos(\theta_1)z]} - A_2 \cos(\vartheta_{P_2}) \cdot e^{ik[\sin(\theta_2)x + \cos(\theta_2)z]} \right|^2 + \right. \\ & \left. \left| A_1 \sin(\vartheta_{P_1}) \sin(\theta_1) \cdot e^{ik[\sin(\theta_1)x + \cos(\theta_1)z]} + A_2 \sin(\vartheta_{P_2}) \sin(\theta_2) \cdot e^{ik[\sin(\theta_2)x + \cos(\theta_2)z]} \right|^2 \right\} \end{aligned} \quad (2.10)$$

For interferometric lithography the best exposure contrast results when both coherent beams have the same electric field amplitude ( $A_1 = A_2$ ). This is normally the case if both beams were evenly split from the same source beam, and the optical systems are equivalent. Since the irradiance contributions from both beams are equal, let  $I_1 = I_2 = I_0 = \frac{1}{2}|A_0|^2$ . For TE polarization the intensity formula equation 2.9 simplifies to the following:

$$I = \frac{1}{2} |\vec{E}|^2 = I_0 \left| e^{ik \sin(\theta_1)x} + e^{ik \sin(\theta_2)x} \right|^2 \quad (2.11)$$

And for the most common case of  $\theta = \theta_1 = -\theta_2$  the intensity formula simplifies further to:

$$I = I_0 \left| [2 \cos\{k \sin(\theta)x\}] \right|^2 \quad (2.12)$$

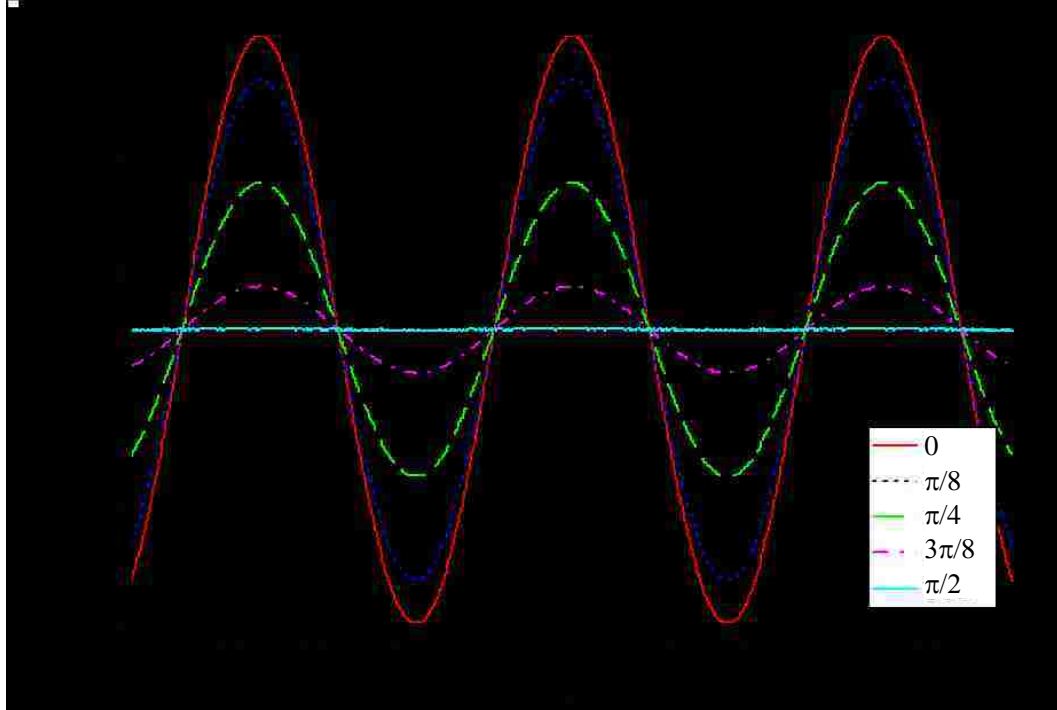
$$I = 4I_0 \cos^2\{k \sin(\theta)x\} \quad (2.13)$$

$$I = 2I_0 [1 + \cos\{2k \sin(\theta)x\}] \quad (2.14)$$

The extreme values of the intensity function  $I$  are given by the following equation 2.15.

$$I = \begin{cases} 4I_0, & x = \frac{(2m)\pi}{k \sin(\theta)} \\ 0, & x = \frac{(2m-1)\pi}{2k \sin(\theta)} \end{cases} \quad (m = 0, \pm 1, \pm 2, \pm 3, \dots) \quad (2.15)$$

As can be seen from equation 2.15, for TE polarized light the interference term of the irradiance equation quadruples the intensity by causing total constructive interference when the two beams are in-phase, while diminishing the intensity by causing total destructive interference when the two beams are out-of-phase



**Figure 12** – Two-beam interference intensity plot as a function of polarization angle  $\mathcal{G}_p$  with a  $NA \equiv n \cdot \sin(\theta) = 0.7$ .

The irradiance equation 2.10 for interferometric lithography is plotted in Figure 12. The plot was made by varying angle of polarization from a full TE state to a full TM state. It can be seen from Figure 12, the effect polarization can have on the standing wave ratio (SWR). TE polarized light ( $\mathcal{G}_p = 0$ ) has the maximum contrast possible, which is always the case, but for the specific case of  $NA \equiv n \cdot \sin(\theta) = 0.7$ , TM polarized light ( $\mathcal{G}_p = \pi/2$ ) has a zero contrast. For TM polarized light the SWR depends on the exposing beam angle  $\theta$ , and approaches zero as the exposing beams angle  $\theta$  approaches  $45^\circ$  in the resist ( $NA = n_r \sqrt{2}/2$ ). Therefore it is best to use TE polarized light for interferometric lithography if possible.

The pitch ( $\Lambda$ ) of the sinusoidal interference irradiance pattern is given as

$$\Lambda = \frac{\lambda}{n[\sin(\theta_1) + \sin(\theta_2)]} \quad (2.16)$$

In the special case where the normal to the surface bisect the angle between the two coherent beams such that  $\theta_1=\theta_2=\theta$  the pitch formula simplifies to

$$\Lambda = \frac{\lambda}{2n \sin(\theta)} = \frac{\lambda}{2 \cdot NA} \quad (2.17)$$

Thus when using interferometric lithography, the photoresist is exposed with a sinusoidal irradiance pattern with a pitch defined by equation 2.16. As the angle between the two beams increases, the pitch decreases until the minimum half-pitch resolution of  $R = \frac{\lambda}{4n}$  is reached at grazing incidence.

This analysis is easily extended to a full three-dimensional photoresist model of this two-beam interferometric lithography via using the original irradiance formula.

$$\begin{aligned} I(x, y, z) = & \\ & \frac{(2A)^2}{2} \left\{ \left| -\sin(\vartheta_{P_1}) \cos(\theta_1) \cdot e^{ik[\sin(\theta_1)x + \cos(\theta_1)z]} - \sin(\vartheta_{P_2}) \cos(\theta_2) \cdot e^{ik[\sin(\theta_2)x + \cos(\theta_2)z]} \right|^2 + \right. \\ & \left| -\cos(\vartheta_{P_1}) \cdot e^{ik[\sin(\theta_1)x + \cos(\theta_1)z]} - \cos(\vartheta_{P_2}) \cdot e^{ik[\sin(\theta_2)x + \cos(\theta_2)z]} \right|^2 + \\ & \left. \left| \sin(\vartheta_{P_1}) \sin(\theta_1) \cdot e^{ik[\sin(\theta_1)x + \cos(\theta_1)z]} + \sin(\vartheta_{P_2}) \sin(\theta_2) \cdot e^{ik[\sin(\theta_2)x + \cos(\theta_2)z]} \right|^2 \right\} \end{aligned} \quad (2.18)$$

This represents the intensity of light in the photoresist, neglecting the effect of Fresnel reflections at the resist top and bottom interfaces. In practice the incoming intensity can be increased to compensate for the reduced intensity transmitted into the photoresist due to Fresnel reflections, and an anti-reflection coating (ARC) is normally used at the resist bottom interface, therefore making the assumption reasonably valid. For simulation, the electric field amplitude for each beam is normalized to a value of unity. Using a Heaviside function ( $\Phi$ ) to approximate the non-linear response of the

developed photoresist pattern, gives a very good first approximation to the final photoresist pattern.

$$\Phi(m) = \begin{cases} 0, & m < 0 \\ 1, & m \geq 0 \end{cases} \quad (2.19)$$

$$ResistPattern(x, y, z) = \Phi\{I(x, y, z) - ResistThreshold\} \quad (2.20)$$

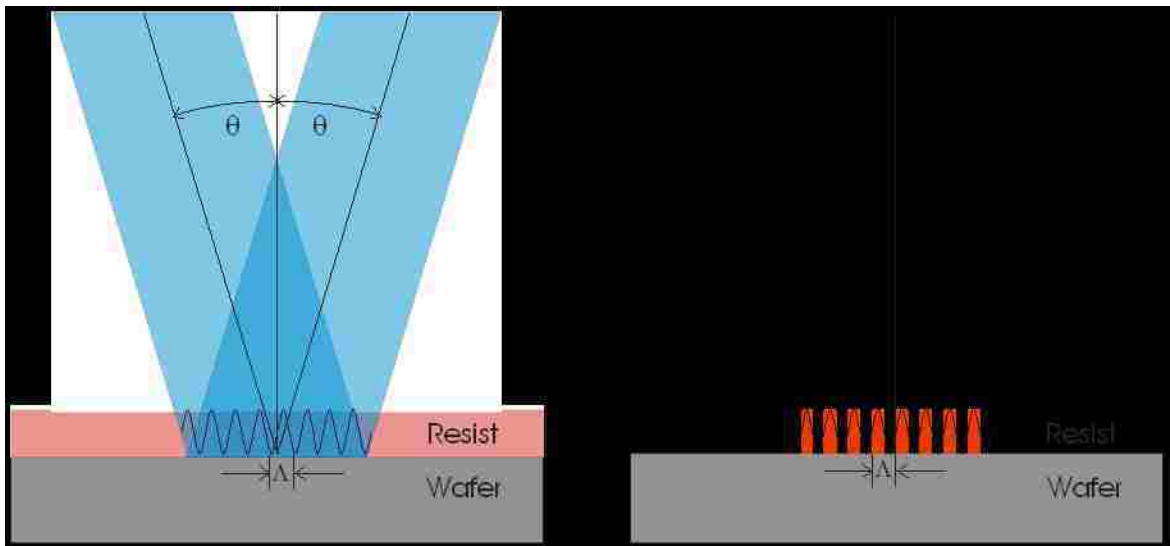
$$ResistPattern(x, y, z) =$$

$$\begin{aligned} & \Phi\left(\frac{1}{4}\left\{\left|-\sin(\vartheta_{P_1})\cos(\theta_1) \cdot e^{ik[\sin(\theta_1)x+\cos(\theta_1)z]} - \sin(\vartheta_{P_2})\cos(\theta_2) \cdot e^{ik[\sin(\theta_2)x+\cos(\theta_2)z]}\right|^2 + \right. \right. \\ & \left. \left|-\cos(\vartheta_{P_1}) \cdot e^{ik[\sin(\theta_1)x+\cos(\theta_1)z]} - \cos(\vartheta_{P_2}) \cdot e^{ik[\sin(\theta_2)x+\cos(\theta_2)z]}\right|^2 + \right. \\ & \left. \left. \left|\sin(\vartheta_{P_1})\sin(\theta_1) \cdot e^{ik[\sin(\theta_1)x+\cos(\theta_1)z]} + \sin(\vartheta_{P_2})\sin(\theta_2) \cdot e^{ik[\sin(\theta_2)x+\cos(\theta_2)z]}\right|^2\right\} - \right. \\ & \left. ResistThreshold\right) \end{aligned} \quad (2.21)$$

The resulting photoresist pattern function has a value of one where the Intensity function has a value greater than the *ResistThreshold* value, and a value of zero where the intensity function has a value less than the *ResistThreshold* value. Therefore for negative tone photoresist the  $x, y, z$  locations that yield a value of one represent where the photoresist remains and similarly an  $x, y, z$  locations that yield a value of zero represent where the photoresist is developed away, and opposite for positive tone photoresist. Often, but not always, the *ResistThreshold* is set to 50%, which yields equal sized lines and spaces. If the *ResistThreshold* is set to greater than 50%, the result is an overexposed image with larger spaces than lines for positive tone photoresist. Likewise if the *ResistThreshold* is set to less than 50%, the result is an underexposed image with larger lines than spaces for positive tone photoresist. Figure 13 contains a diagram that demonstrates two-beam interference lithography during exposure and after photoresist



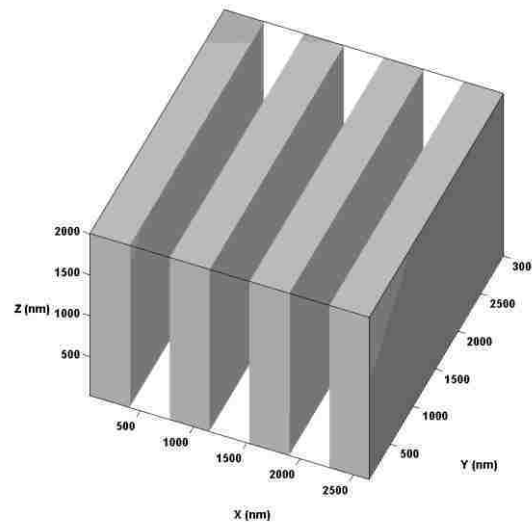
development, using a *ResistThreshold* set to 50%. A 3D plot of the photoresist pattern function for one-dimensional interferometric lithography is seen in Figure 14, for a *ResistThreshold* = 50%, an interference angle of  $\theta = \theta_1 = -\theta_2 = 8^\circ$ , TE polarization angle of  $\vartheta_p = 0$ , photoresist index of  $n_r = 1.7$ , and exposure wavelength of  $\lambda = 355$  nm.



**Figure 13** – Two-beam interference during exposure & after photoresist development.

The 3D plot in Figure 14 shown below has well defined lines with square edges oriented perpendicular to the X direction. In reality the lines edges are a bit rounded, the sidewalls are not perfectly smooth and flat, and the achievable ratio of the line height to width is limited. Substrate reflection can cause standing waves in the resist sidewalls, this can be significantly or completely removed by the commonly use of a bottom anti-reflection coating (BARC) under the resist. There can also be chemical interactions between the resist and substrate that cause the lines to have footing or notching, which can also be eliminated by the use of a proper BARC. Underexposed lines may have photoresist bridging between them, and overexposed lines may exhibit line height reduction and rounding. A complete development treatment of the photolithography

process that takes into account these optical and chemical effects can be found in commercial programs such as SAMPLE or PROLITH.<sup>18</sup> But this Heaviside function approach is a very good approximation, and it is shown later that it works very well for the simulation of three-dimensional photonic crystal structures. The normalized standing wave ratio for the intensity  $SWR = \frac{I_{max} - I_{min}}{I_{max} + I_{min}}$  for this photoresist pattern is  $SWR = 100\%$ , which is achieved only when using TE polarized light (although at  $\theta = 8^\circ$  the SWR difference between TE and TM is only 0.97%).



**Figure 14** – 1D interference lithography photoresist pattern.

## Two-Dimensional Interferometric Lithography

In order to create two-dimensional patterns an additional sinusoidal interference pattern is introduced to the exposure. Otherwise it is similar to one-dimensional interferometric lithography with the same basic requirements. There are two methods that can be taken to add the additional sinusoidal interference pattern. The first method is

a single exposure with additional beams of exposing light. The second method is multiple two-beam exposures.

## Single Exposure

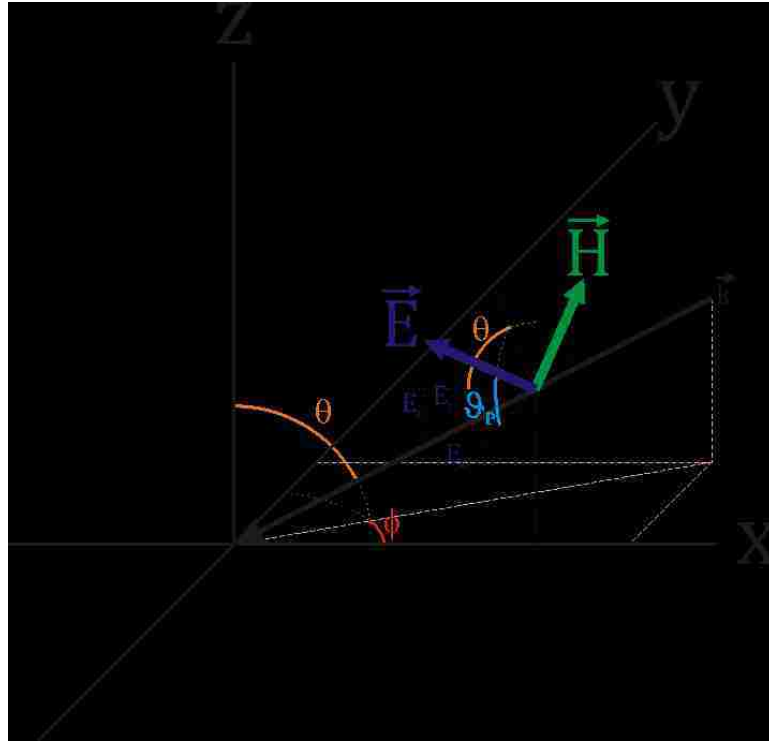
To expose two-dimensional patterns in a single exposure requires that three or more plane waves of coherent light are used to create the interference pattern. Unlike two-beam interferometric lithography used to create one-dimensional structures, where the phase between the two exposure beams only determines the placement of the pattern and its alignment to the underlying structure, the phase of each plane wave of the three or more beams must be controlled at the exposure plane. If the phase is not controlled there are additional unwanted interference patterns due to higher order cross terms, in addition to the pattern placement and alignment. These higher order interference patterns need to be considered in the modeling. The following formula is the electric field equation for each plane wave in the two-dimensional interferometric lithography.

$$\begin{aligned} \vec{E}_n = & \\ & A_n \{ \cos(\vartheta_{P_n}) [\sin(\varphi_n)\hat{x} - \cos(\varphi_n)\hat{y}] + \\ & \sin(\vartheta_{P_n}) [-\cos(\theta_n)\sin(\varphi_n)\hat{x} - \cos(\theta_n)\cos(\varphi_n)\hat{y} + \sin(\theta_n)\hat{z}] \} \cdot \\ & e^{-ik[\sin(\theta_n)\cos(\varphi_n)x + \sin(\theta_n)\sin(\varphi_n)y + \cos(\theta_n)z]} \cdot e^{i\delta_n} \end{aligned}$$

$$n = 1, 2 \dots \#\_of\_Beams. \quad (2.22)$$

For maximum contrast the condition of  $A_1 = A_2 = A_n = A$  in the photoresist needs to be met, and is normally the case if each beam is evenly split from a single source beam taking into account losses from beam optics, Fresnel reflection, etc. These equations are similar to the one-dimensional case, but with the addition of the  $\varphi$  (rotation) to the  $\theta$

(angle) for the x and y coefficients terms plus a  $\delta$  (phase) term for each beam. Figure 15 shows the geometry for a single linearly polarized plane wave with an arbitrary orientation to the exposure plane. When combined with other similarly linearly polarized plane waves results in two-dimensional or three-dimensional interferometric lithography.



**Figure 15** – linearly polarized plane wave at an arbitrary angle  $\theta$  and rotation  $\phi$ .

The intensity pattern for single exposure two-dimensional interferometric lithography is given as follows.

$$I = \frac{1}{2} \left| \sum_{n=1}^{\text{\#\_of\_Beams}} \vec{E}_n \right|^2 = \frac{(nA)^2}{2} \left( |\tilde{E}_{1x} + \tilde{E}_{2x} + \dots + \tilde{E}_{nx}|^2 + |\tilde{E}_{1y} + \tilde{E}_{2y} + \dots + \tilde{E}_{ny}|^2 + |\tilde{E}_{1z} + \tilde{E}_{2z} + \dots + \tilde{E}_{nz}|^2 \right) \quad (2.23)$$

Similar to the modeling of the one-dimensional interferometric lithography case, a simple three-dimensional photoresist model of this two-dimensional single exposure interferometric lithography can be performed. For the simulation the electric field amplitude for all beams is normalized to a value of  $1/n$ , assuming that each beam comes from the same source with the intensity evenly split among each beam. Using the same Heaviside step function with an appropriate photoresist threshold to yield a photoresist pattern function given as:

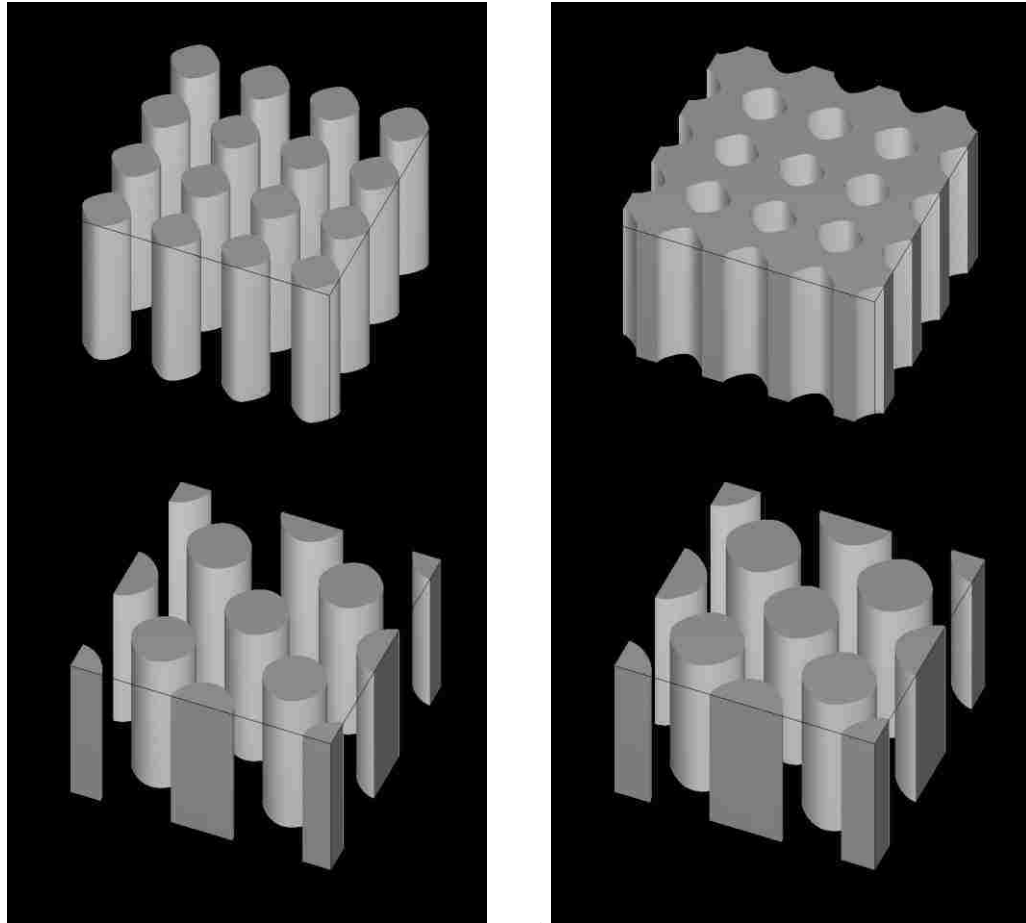
$$\begin{aligned}
ResistPattern(x, y, z) = & \\
\Phi \left( \frac{1}{\#\_of\_Beams} \sum_{n=1}^{\#\_of\_Beams} \{ & [ [\cos(\vartheta_{P_n}) \sin(\varphi_n) - \sin(\vartheta_{P_n}) \cos(\theta_n) \cos(\varphi_n)] \cdot \right. \\
e^{ik[\sin(\theta_n) \cos(\varphi_n)x + \sin(\theta_n) \sin(\varphi_n)y + \cos(\theta_n)z] + i\delta_n} & \left. \right)^2 + \\
[ [-\cos(\vartheta_{P_n}) \cos(\varphi_n) - \sin(\vartheta_{P_n}) \cos(\theta_n) \sin(\varphi_n)] \cdot e^{ik[\sin(\theta_n) \cos(\varphi_n)x + \sin(\theta_n) \sin(\varphi_n)y + \cos(\theta_n)z] + i\delta_n} & \left. \right)^2 + \\
|\sin(\vartheta_{P_n}) \sin(\theta_n) \cdot e^{ik[\sin(\theta_n) \cos(\varphi_n)x + \sin(\theta_n) \sin(\varphi_n)y + \cos(\theta_n)z] + i\delta_n}|^2 & \left. \right\} - ResistThreshold \Big)
\end{aligned} \tag{2.24}$$

A single exposure multiple beam two-dimensional interference lithography pattern typically has the limitation of not being able to use TE polarized light for each of its beams. For interference to occur, a single light source is used to generate all the interference beams, and it is usually not possible to rotate the polarized state of the source beam to TE polarization for each generated interference beam. Typically for a four beam exposure, the beams on the  $x$ -axis (so-defined) use TE polarized light  $\vartheta_P = 0^\circ$  and the beams on the  $y$ -axis use TM polarized light  $\vartheta_P = 90^\circ$ . Another option is to use light that has a polarization angle of  $\vartheta_P = 45^\circ$  on all four beams. At large pitches this will not have

a significant impact on the patterning, but as the pitch decreases the contrast loss previously mentioned will have an increasingly negative influence on the pattern.

For a large pitch case of  $n=4$ ,  $\theta_n=(-1)^n \cdot 8^\circ$ ,  $\phi_n=(n-1) \cdot 90^\circ$ ,  $\vartheta_{P_n}=(n-1)(\pi/2)$ ,  $\delta_n=(n-1)(\pi/2)$  {case a & b} and  $\delta_n=0$  {case c & d},  $n_r=1.7$ ,  $\lambda=355$  nm, and *ResistThreshold* = 62% {case a & c} and *ResistThreshold* = 38% {case b & d}, the resulting 3D photoresist plots for the four cases are shown in Figure 16. For a four beam single exposure to get equal post hole ratio requires a *ResistThreshold* = 50%. A threshold > 50% yields a pattern of posts and a threshold < 50% yields a pattern of holes. In practice when the *ResistThreshold*  $\approx$  50% the result is a mixture of holes and posts due to indeterminate variations in processing. For equal size holes and intervals *ResistThreshold* = 33.3%, and equal size posts and spaces *ResistThreshold* = 66.6%.

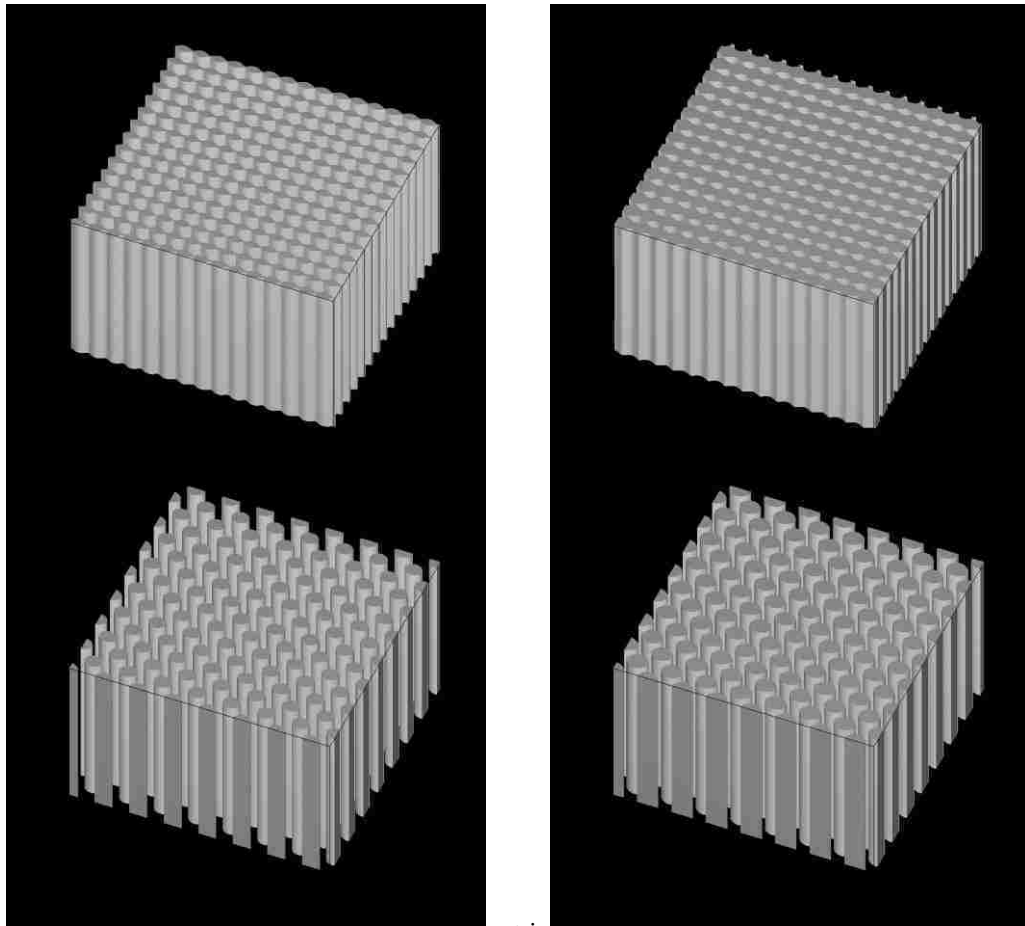
The 3D plots show in some cases a square grid of posts and in other cases a square grid of holes. If the phase is kept the same in all exposures the grid is rotated by  $45^\circ$  with the pitch increasing by  $\sqrt{2}$ , as seen in Figure 16 cases c and d. In addition when the phase is kept the same in all exposures, holes are not easily achieved. These simulation results for a single four beam exposure with the  $\pi/2$  phase change between exposing beams have a standing wave ratio of *SWR*=98%, and when all the exposing beams have the same phase a standing wave ratio of *SWR*=100% results.



**Figure 16** – A 2D single exposure interferometric lithography photoresist patterns with  $\theta=8^\circ$ .  
**a) & b)**  $\pi/2$  phase difference between beams      **c) & d)** Same phase difference between all beams  
**a) & c)** *ResistThreshold* = 62%      **b) & d)** *ResistThreshold* = 38%

In order to see the effects of using both TE polarized beams and TM polarized beams in the same single exposure, the beam angles need to be increased. If the exposing angle is increased by a factor of four from  $\theta_n=(-1)^n \cdot 8^\circ$  to  $\theta_n=(-1)^n \cdot 32^\circ$ , and the previous simulation are rerun, then the resulting four plots are shown in Figure 17. These 3D plots start to show the effect of using both TE polarized beams and TM polarized beams in the single exposure. The simulation results for a single four beam exposure with the  $\pi/2$  phase difference change between exposing beams have the post and holes elongated on the x-axis, and standing wave ratio reduced from a  $SWR=98\%$  to a  $SWR=72\%$ . When all

the exposing beams have the same phase the posts are still round, and a standing wave ratio of  $SWR=100\%$  still results. The worst case occurs when the exposing beam angle is at  $45^\circ$  in the photoresist medium. Figure 17 illustrates how both beam phase and polarization affect the final photoresist pattern profile.



**Figure 17** – A 2D single exposure interferometric lithography photoresist patterns with  $\theta=32^\circ$ .

**a) & b)**  $\pi/2$  phase difference between beams

**c) & d)** Same phase difference between all beams

**a) & c)**  $ResistThreshold = 62\%$

**b) & d)**  $ResistThreshold = 38\%$

## Multiple Exposures

A simpler method for making two-dimensional structures is to use two-beam interferometric lithography with multiple-exposures. This eliminates the need to control the phase between all the beams at the exposure plane. Using multiple-exposures works



due to the fact that photoresist responds to the sum of the intensity of all exposures and the total intensity of all exposures determines the developed pattern. Therefore in order to make photoresist posts on a square grid for example, performs one partial exposure of lines in the  $x$  direction using two-beam interferometric lithography, followed by a second partial exposure of lines in the  $y$  direction. The sum of the two exposures creates posts at the intersection of the  $x$  and  $y$  line nulls. This is usually done by using a single two-beam interferometer setup and rotating the photoresist sample at the exposure plane between exposures. This also allows for the use of only TE polarized light for all exposures. The formula for multiple-exposure is similar to that for single exposure, except that instead of summing all the electric fields and squaring it for the intensity, the intensities of the multiple-exposures are summed. With each exposure being the squared sum of two-beam electric fields. The electric field for the first and second exposure is given as follows.

$$\begin{aligned}
\vec{E}_{\text{exp}_1} = & \\
& A_1 \{ \cos(\vartheta_{P_1}) [-\sin(\varphi_1)\hat{x} - \cos(\varphi_1)\hat{y}] + \\
& \sin(\vartheta_{P_1}) [-\cos(\theta_1)\cos(\varphi_1)\hat{x} + \sin(\theta_1)\cos(\varphi_1)\hat{y} + \sin(\theta_1)\hat{z}] \} \cdot \\
& e^{ik[\sin(\theta_1)\cos(\varphi_1)x + \sin(\theta_1)\sin(\varphi_1)y + \cos(\theta_1)z]} + \\
& A_2 \{ \cos(\vartheta_{P_2}) [-\sin(\varphi_1)\hat{x} - \cos(\varphi_1)\hat{y}] + \\
& \sin(\vartheta_{P_2}) [-\cos(\theta_2)\cos(\varphi_1)\hat{x} + \sin(\theta_2)\cos(\varphi_1)\hat{y} + \sin(\theta_2)\hat{z}] \} \cdot \\
& e^{ik[\sin(\theta_2)\cos(\varphi_1)x + \sin(\theta_2)\sin(\varphi_1)y + \cos(\theta_2)z]}
\end{aligned} \tag{2.25}$$

$$\begin{aligned}
\vec{E}_{\text{exp}_2} = & \\
& A_1 \{ \cos(\vartheta_{P_1}) [-\sin(\varphi_2)\hat{x} - \cos(\varphi_2)\hat{y}] + \\
& \sin(\vartheta_{P_1}) [-\cos(\theta_1)\cos(\varphi_2)\hat{x} + \sin(\theta_1)\cos(\varphi_2)\hat{y} + \sin(\theta_1)\hat{z}] \} \cdot \\
& e^{ik[\sin(\theta_1)\cos(\varphi_2)x + \sin(\theta_1)\sin(\varphi_2)y + \cos(\theta_1)z]} + \\
& A_2 \{ \cos(\vartheta_{P_2}) [-\sin(\varphi_2)\hat{x} - \cos(\varphi_2)\hat{y}] + \\
& \sin(\vartheta_{P_2}) [-\cos(\theta_2)\cos(\varphi_2)\hat{x} + \sin(\theta_2)\cos(\varphi_2)\hat{y} + \sin(\theta_2)\hat{z}] \} \cdot \\
& e^{ik[\sin(\theta_2)\cos(\varphi_2)x + \sin(\theta_2)\sin(\varphi_2)y + \cos(\theta_2)z]}
\end{aligned} \tag{2.26}$$

For maximum contrast the condition of  $A_1=A_2=A$  in the photoresist needs to be met, which is the case when two equal intensity beams are at the same angle normal to the exposure plane. The intensity pattern for multiple-exposure two-dimensional interferometric lithography is given as follows.

$$\begin{aligned}
I = \frac{1}{2} \left( |\vec{E}_{\text{exp}_1}|^2 + |\vec{E}_{\text{exp}_2}|^2 \right) = \\
2A^2 \left\{ \left( |\tilde{E}_{\text{exp}_1x}|^2 + |\tilde{E}_{\text{exp}_1y}|^2 + |\tilde{E}_{\text{exp}_1z}|^2 \right) + \left( |\tilde{E}_{\text{exp}_2x}|^2 + |\tilde{E}_{\text{exp}_2y}|^2 + |\tilde{E}_{\text{exp}_2z}|^2 \right) \right\}
\end{aligned} \tag{2.27}$$

Because the phase is not important for multiple-exposure two-dimensional structures, except for alignment to underlying structures, the  $\delta$  term has been dropped for now. For a Manhattan grid structure  $\phi_1=0^\circ$  and  $\phi_2=90^\circ$ , and similarly for a hexagonal structure  $\phi_1=0^\circ$  and  $\phi_2=120^\circ$ . For a two-dimensional interferometric lithography pattern it is possible to do three or more exposures but in many cases it is only necessary to do two exposures. If more than two exposures are needed then the equations used for

multiple exposure three-dimensional interferometric lithography, described in a following section, will need to be used.

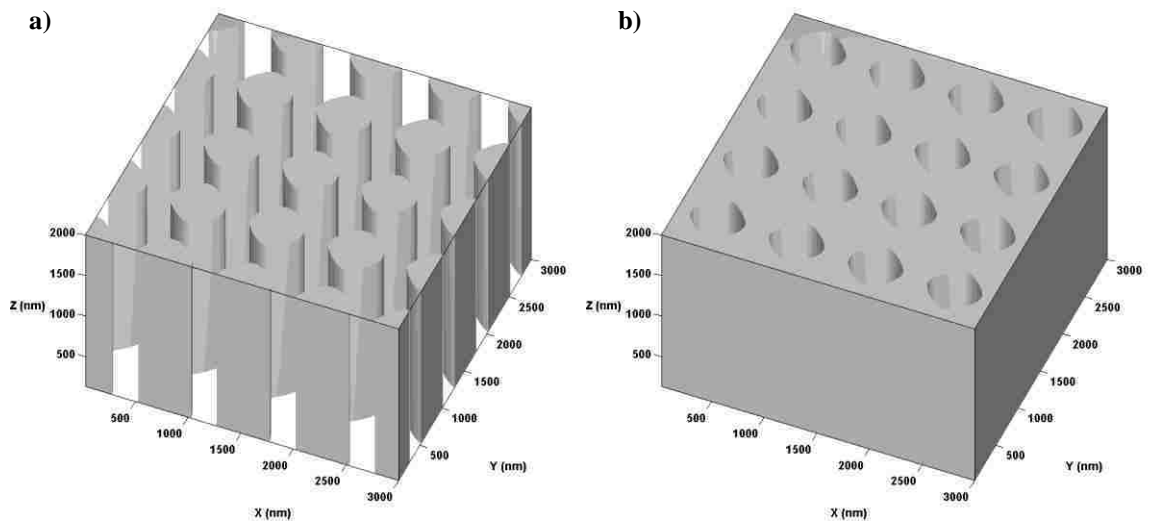
Again a simple three-dimensional photoresist model of this two-dimensional multiple-exposure interferometric lithography can be performed. For the simulation the intensity for all exposures is normalized to a value of  $\frac{1}{2}$ , which assumes each of the two exposures has the same exposure dose. Using the same Heaviside step function to yield a photoresist pattern function gives:

$$\begin{aligned}
ResistPattern(x, y, z) = & \\
& \Phi \left( \frac{1}{4} \left\{ \left[ \left[ -\cos(\vartheta_{P_1}) \sin(\varphi_1) - \sin(\vartheta_{P_1}) \cos(\theta_1) \cos(\varphi_1) \right] \cdot e^{ik[\sin(\theta_1) \cos(\varphi_1)x + \sin(\theta_1) \sin(\varphi_1)y + \cos(\theta_1) z]} + \right. \right. \\
& \left. \left[ -\cos(\vartheta_{P_2}) \sin(\varphi_1) - \sin(\vartheta_{P_2}) \cos(\theta_2) \cos(\varphi_1) \right] \cdot e^{ik[\sin(\theta_2) \cos(\varphi_1)x + \sin(\theta_2) \sin(\varphi_1)y + \cos(\theta_2) z]} \right]^2 + \\
& \left[ \left[ -\cos(\vartheta_{P_1}) \cos(\varphi_1) - \sin(\vartheta_{P_1}) \cos(\theta_1) \sin(\varphi_1) \right] \cdot e^{ik[\sin(\theta_1) \cos(\varphi_1)x + \sin(\theta_1) \sin(\varphi_1)y + \cos(\theta_1) z]} + \right. \\
& \left. \left[ -\cos(\vartheta_{P_2}) \cos(\varphi_1) - \sin(\vartheta_{P_2}) \cos(\theta_2) \sin(\varphi_1) \right] \cdot e^{ik[\sin(\theta_2) \cos(\varphi_1)x + \sin(\theta_2) \sin(\varphi_1)y + \cos(\theta_2) z]} \right]^2 + \\
& \left| \sin(\vartheta_{P_1}) \sin(\theta_1) \cdot e^{ik[\sin(\theta_1) \cos(\varphi_1)x + \sin(\theta_1) \sin(\varphi_1)y + \cos(\theta_1) z]} + \sin(\vartheta_{P_2}) \sin(\theta_2) \cdot \right. \\
& \left. e^{ik[\sin(\theta_2) \cos(\varphi_1)x + \sin(\theta_2) \sin(\varphi_1)y + \cos(\theta_2) z]} \right|^2 \left. \right\} + \\
& \left[ \left[ -\cos(\vartheta_{P_1}) \sin(\varphi_2) - \sin(\vartheta_{P_1}) \cos(\theta_1) \cos(\varphi_2) \right] \cdot e^{ik[\sin(\theta_1) \cos(\varphi_2)x + \sin(\theta_1) \sin(\varphi_2)y + \cos(\theta_1) z]} + \right. \\
& \left. \left[ -\cos(\vartheta_{P_2}) \sin(\varphi_2) - \sin(\vartheta_{P_2}) \cos(\theta_2) \cos(\varphi_2) \right] \cdot e^{ik[\sin(\theta_2) \cos(\varphi_2)x + \sin(\theta_2) \sin(\varphi_2)y + \cos(\theta_2) z]} \right]^2 + \\
& \left[ \left[ -\cos(\vartheta_{P_1}) \cos(\varphi_2) - \sin(\vartheta_{P_1}) \cos(\theta_1) \sin(\varphi_2) \right] \cdot e^{ik[\sin(\theta_1) \cos(\varphi_2)x + \sin(\theta_1) \sin(\varphi_2)y + \cos(\theta_1) z]} + \right. \\
& \left. \left[ -\cos(\vartheta_{P_2}) \cos(\varphi_2) - \sin(\vartheta_{P_2}) \cos(\theta_2) \sin(\varphi_2) \right] \cdot e^{ik[\sin(\theta_2) \cos(\varphi_2)x + \sin(\theta_2) \sin(\varphi_2)y + \cos(\theta_2) z]} \right]^2 + \\
& \left| \sin(\vartheta_{P_1}) \sin(\theta_1) \cdot e^{ik[\sin(\theta_1) \cos(\varphi_2)x + \sin(\theta_1) \sin(\varphi_2)y + \cos(\theta_1) z]} + \sin(\vartheta_{P_2}) \sin(\theta_2) \cdot \right. \\
& \left. e^{ik[\sin(\theta_2) \cos(\varphi_2)x + \sin(\theta_2) \sin(\varphi_2)y + \cos(\theta_2) z]} \right|^2 \left. \right\} - ResistThreshold \Big)
\end{aligned} \tag{2.28}$$

For  $\theta_1=8^\circ$ ,  $\theta_2=-8^\circ$ ,  $\varphi_1=0^\circ$ ,  $\varphi_2=90^\circ$ ,  $\vartheta_{P_1}=\vartheta_{P_2}=0^\circ$ ,  $n=1.7$ ,  $\lambda=355$  nm, and  $ResistThreshold = 62\%$  {case a} and  $ResistThreshold = 38\%$  {case b}, the 3D photoresist

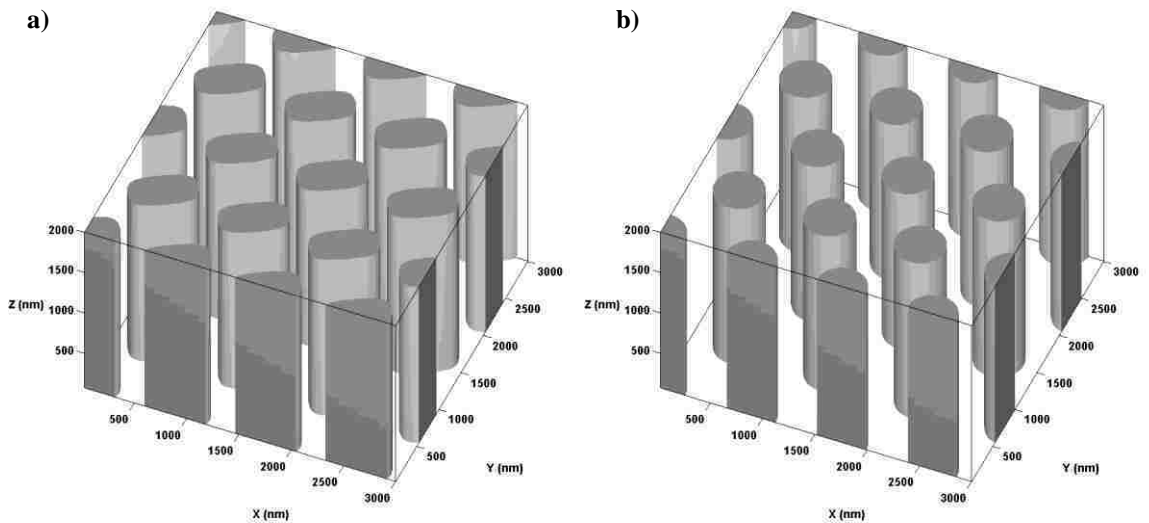
plot found in Figure 18 results. For a multiple beam two-dimensional exposure to get equal post hole ratio requires a  $ResistThreshold = 50\%$ , just as in the one-dimensional case. A threshold  $> 50\%$  yields a pattern of posts, a threshold  $< 50\%$  yields a pattern of holes, and in practice when the  $ResistThreshold \approx 50\%$  the result is a mixture of holes and posts due to indeterminate variations in processing. For equal size holes and intervals  $ResistThreshold = 33.3\%$ , and equal size posts and spaces  $ResistThreshold = 66.6\%$ .

The final result is very similar to the single exposure two-dimensional case, yielding a well-defined square grid of posts. But in the multiple-exposure case the phase between the plane waves need not be controlled except to align to additional features on the wafer, and the interferometer setup is simpler and can readily implement the use of only TE polarized light.



**Figure 18** – A 2D multiple-exposure interferometric lithography photoresist patterns.  
**a)** Posts ( $ResistThreshold = 62\%$ ) **b)** Holes ( $ResistThreshold = 38\%$ )

For the case of creating post or holes on a hexagonal grid, when doing two exposure the post or holes come out as ovals as is shown for posts in Figure 19 a). The best contrast is still obtained when the two exposure intensities are the same. If the ratio of the two exposures is changed, the size of the oval post or holes will vary and the angle of the oval will slightly vary, but the overall shape and orientation will mainly remain the same. In practice though the photoresist posts and holes tend to have a rounder profile as opposed to oval, especially if the pitch is near or below the exposing wavelength. In order to achieve truly round post or holes on a hexagonal grid, three exposures are necessary as is shown for posts in Figure 19 b). Figure 19 use the same simulation parameters as in the previous two-dimensional square grid example found in Figure 18, except for the rotation angle and number of exposures (two exposures for case a, and three exposures for case b), with  $\theta_1=8^\circ$ ,  $\theta_2=-8^\circ$ ,  $\phi_1=0^\circ$ ,  $\phi_2=120^\circ$ ,  $\phi_3=240^\circ$  {case b only},  $\mathcal{G}_{P1}=\mathcal{G}_{P2}=0^\circ$ ,  $n=1.7$ ,  $\lambda=355$  nm, and  $ResistThreshold = 62\%$ .



**Figure 19** – A 2D hexagonal multiple-exposure interferometric lithography photoresist patterns.  
**a)** Two-Exposure Posts    **b)** Three-Exposure Posts

## Three-Dimensional Interferometric Lithography

Creating three-dimensional crystals is much more complex. The process has all the issues associated with two-dimensional interferometric lithography, but with the additional constraint of dealing with variation in the Z plane. There are phase shifts of the sinusoidal interference pattern in the Z direction. Traditionally three-dimensional interferometric lithography is done using a single exposure with four or more plane waves. However just as was the case with its two-dimensional counterpart, it can also be done using multiple-exposures of two-beam interferometric lithography.

### Single Exposure

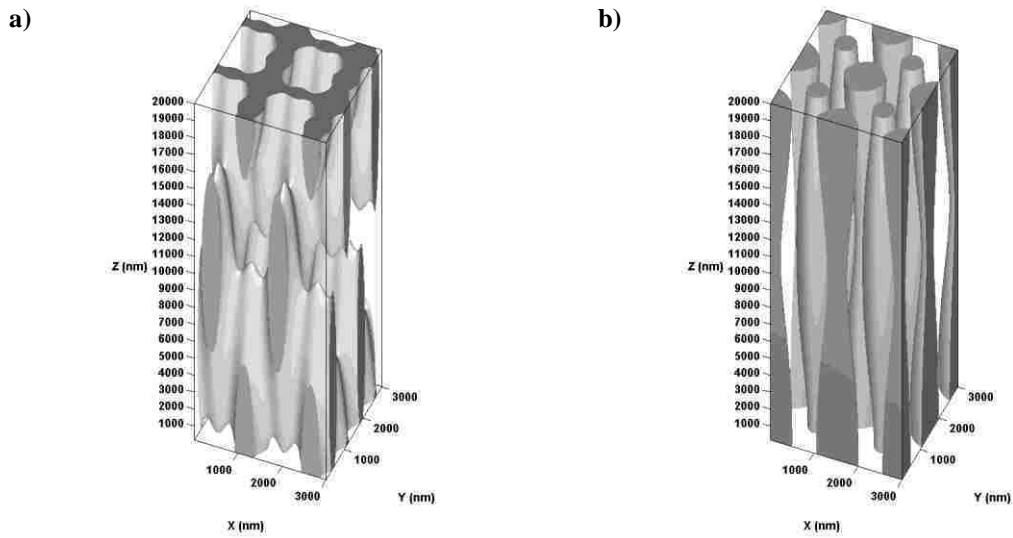
To create three-dimensional structures with single exposure interferometric lithography requires three or more optical plane waves. Typically four or five plane waves are used. In addition there are additional interference cross-terms from the multiple exposure beams, which may give rise to an unwanted exposure intensity bias. Unlike two-dimensional interferometric lithography where, at the exposure plane, it may be possible to adjust the phase to avoid the unwanted interference cross-terms, in the three-dimensional case except under very special conditions it is impossible to avoid the cross terms. The same formulas used for the single exposure two-dimensional case are used for the single exposure three-dimensional case. The electric field equations for each plane wave in three-dimensional interferometric lithography are found in equation 2.19 thru equation 2.21 found on page 23. Again for maximum contrast the condition of  $A_1 = A_2 = A_n = A$  in the photoresist needs to be met. It may be necessary to adjust the intensity for exposure beams of varying angles, to compensate for varying Fresnel reflections off

the surface of the photoresist, in order to maintain the condition of  $A_1=A_2=A_n=A$  in the photoresist. The intensity pattern for single exposure three-dimensional interferometric lithography is given as follows.

$$I = \frac{1}{2} \left| \sum_n^{\text{\#\_of\_Beams}} \vec{E}_n \right|^2 = \frac{(nA)^2}{2} \left( \left| \tilde{E}_{1x} + \tilde{E}_{2x} + \dots + \tilde{E}_{nx} \right|^2 + \left| \tilde{E}_{1y} + \tilde{E}_{2y} + \dots + \tilde{E}_{ny} \right|^2 + \left| \tilde{E}_{1z} + \tilde{E}_{2z} + \dots + \tilde{E}_{nz} \right|^2 \right) \quad (2.29)$$

This equation is the same as the two dimensional case. Looking at 3D photoresist model of this three-dimensional single exposure interferometric lithography is very similar for the two-dimensional case, but now the  $z$ -dimension needs to be considerably larger to see the variation in the  $z$ -direction ( $A_x = A_y = 2.551 \mu\text{m}$  &  $A_z = 62.211 \mu\text{m}$ ). Just as in the two-dimensional case the simulation electric field amplitude for all beams is normalized to a value of  $1/n$ . Using the same Heaviside step function to yield a photoresist pattern function, which is the same as for the two-dimensional case, is given in equation 2.24 on page 28.

For  $n=5$ ,  $\theta_n=(-1)^n \cdot 8^\circ$  &  $\theta_5=0^\circ$ ,  $\phi_n=(n-1) \cdot 90^\circ$ ,  $\vartheta_{pn}=(n-1)(\pi/2)$  {case a} and  $\delta_n=0$  {case b}, and  $n_{resist}=1.7$ ,  $\lambda=355 \text{ nm}$ , and  $ResistThreshold = 50\%$  the 3D photoresist plot found in Figure 20. If  $|\theta|$  is the same for all of the beams (therefore no normal incidence beam) then the result is the same as for the single exposure two-dimensional case. In a change from the previous photoresist model plots the  $z$ -axis is increased by a factor of 10 to show the details of the structure. The  $x$  &  $y$ -axes are not on the same scale as the  $z$ -axis in the 3D photoresist plot.



**Figure 20** – 3D five beam single exposure interferometric lithography photoresist patterns.

a)  $\pi/2$  phase difference between beams.      b) Phase difference same between all beams.

Here the true three-dimensional nature of the crystal can be seen. Unlike the perfect cube shape dielectric function illustrated in the introduction, the crystal constantly varies in all the directions. By traversing along a cut in the crystal in any axis direction the photoresist periodically goes from solid to missing back to solid, similarly as it did in the  $x$  and  $y$  directions for the two-dimensional crystals. Another thing to note that the pitch is significantly different in the  $z$  direction than it is in the  $x$  and  $y$  directions. Additionally when the phase difference between all beams are the same, it is very hard to get the interlinking structure that results when there is a  $\pi/2$  phase difference between the  $x$ -axis and  $y$ -axis beams. If the exposure dose or resist threshold is reduced, in the case of the phase difference between all beams are the same, eventually results in a solid structure with periodic voids in it, however in practice it would be extremely difficult to develop such a structure, since there is no path for the developer to access the isolated voids. This is a result of the fact that as the photoresist develops, there would be no path



formed to wash away the broken down material through, but instead the broken down material would have to diffuse through the undeveloped solid photoresist material in order to create the voids.

## **Multiple Exposures**

A process for creating a three-dimensional structure that takes advantage of multiple exposure two-beam interferometric lithography is introduced in this work. Instead of trying to create the three-dimensional structure in a single exposure, multiple two-beam exposures are summed up to create a final three-dimensional pattern. However unlike the case with multiple-exposure two-dimensional lithography, an additional condition must be met. The incident angle and rotation between the exposures must be tightly controlled. For both one and two-dimensional interferometric lithography, the z-plane can be ignored due to the resist thicknesses being much less than the z-pitch or in other words the depth-of-focus is very large. To a first order of approximation (resist thickness  $\ll \Lambda_z \gg \Lambda_x \approx \Lambda_y$ ) this is true. But obviously this is not the case for three-dimensional patterning. Thus the exposure plane needs to be the same between each exposure to within a small percentage of the Z pitch. The following formula presents the electric field equations for each exposure in three-dimensional interferometric lithography. The first two exposure terms are the same as for multiple-exposure two-dimensional interferometric lithography.

$$\begin{aligned}
\vec{E}_{\text{exp}_n} = & \\
& A_1 \{ \cos(\vartheta_{P_1}) [-\sin(\varphi_n)\hat{x} - \cos(\varphi_n)\hat{y}] + \\
& \sin(\vartheta_{P_1}) [-\cos(\theta_1)\cos(\varphi_n)\hat{x} + \sin(\theta_1)\cos(\varphi_n)\hat{y} + \sin(\theta_1)\hat{z}] \} \cdot \\
& e^{ik[\sin(\theta_1)\cos(\varphi_n)x + \sin(\theta_1)\sin(\varphi_n)y + \cos(\theta_1)z]} + \\
& A_2 \{ \cos(\vartheta_{P_2}) [-\sin(\varphi_n)\hat{x} - \cos(\varphi_n)\hat{y}] + \\
& \sin(\vartheta_{P_2}) [-\cos(\theta_2)\cos(\varphi_n)\hat{x} + \sin(\theta_2)\cos(\varphi_n)\hat{y} + \sin(\theta_2)\hat{z}] \} \cdot \\
& e^{ik[\sin(\theta_2)\cos(\varphi_n)x + \sin(\theta_2)\sin(\varphi_n)y + \cos(\theta_2)z]} \\
& n = 1, 2 \dots \#\_of\_Exposures \tag{2.30}
\end{aligned}$$

For maximum contrast the condition of  $A_1=A_2=A$  in the photoresist needs to be met. And just like the two-dimensional multiple-exposure case, we sum the intensities of each two-beam exposure. For three-dimensional patterns three or more exposures are necessary. The intensity pattern for multiple-exposure three-dimensional interferometric lithography is given as follows.

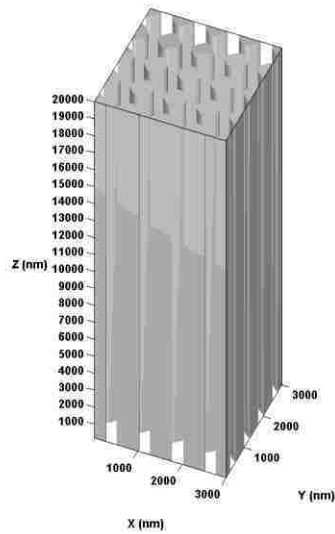
$$I = \sum_{n=1}^{\#\_of\_Exposures} \frac{1}{2} |\vec{E}_{\text{exp}_n}|^2 = \frac{4A^2}{\#\_of\_Exposures} \left( |\vec{E}_{\text{exp}_1}|^2 + |\vec{E}_{\text{exp}_2}|^2 + \dots + |\vec{E}_{\text{exp}_n}|^2 \right) \tag{2.31}$$

The phase between each of the beams does not need to be taken into account, except for alignment to other structures on the wafer. But it is very important that the exposure beam angles  $\theta_1$  and  $\theta_2$  do not change during any rotation ( $\phi_1 \dots \phi_n$ ), as this would cause a change in pitch along the  $xy$ -plane, which is the same as a tilt in the exposure plane. Tilt in the exposure plane will be examined in further detail in the next section.

A 3D photoresist model of this three-dimensional multiple-exposure interferometric lithography is examined. For the simulation the intensity for all exposures is normalized to a value of  $1/n$ , this assumes that each exposure has the same exposure dose. Using the same Heaviside step function to yield a photoresist pattern function given as:

$$\begin{aligned}
ResistPattern(x, y, z) = & \\
& \Phi \left( \frac{1}{4} \sum_{n=1}^{\#\_of\_Exposures} \left[ \left[ -\cos(\vartheta_{P_1}) \sin(\varphi_n) - \sin(\vartheta_{P_1}) \cos(\theta_1) \cos(\varphi_n) \right] \cdot \right. \right. \\
& e^{ik[\sin(\theta_1) \cos(\varphi_n)x + \sin(\theta_1) \sin(\varphi_n)y + \cos(\theta_1)z]} + \left[ -\cos(\vartheta_{P_2}) \sin(\varphi_n) - \sin(\vartheta_{P_2}) \cos(\theta_2) \cos(\varphi_n) \right] \cdot \\
& e^{ik[\sin(\theta_2) \cos(\varphi_n)x + \sin(\theta_2) \sin(\varphi_n)y + \cos(\theta_2)z]} \left. \right]^2 + \\
& \left[ -\cos(\vartheta_{P_1}) \cos(\varphi_n) - \sin(\vartheta_{P_1}) \cos(\theta_1) \sin(\varphi_n) \right] \cdot e^{ik[\sin(\theta_1) \cos(\varphi_n)x + \sin(\theta_1) \sin(\varphi_n)y + \cos(\theta_1)z]} + \\
& \left[ -\cos(\vartheta_{P_2}) \cos(\varphi_n) - \sin(\vartheta_{P_2}) \cos(\theta_2) \sin(\varphi_n) \right] \cdot e^{ik[\sin(\theta_2) \cos(\varphi_n)x + \sin(\theta_2) \sin(\varphi_n)y + \cos(\theta_2)z]} \left. \right]^2 + \\
& \left| \sin(\vartheta_{P_1}) \sin(\theta_1) \cdot e^{ik[\sin(\theta_1) \cos(\varphi_n)x + \sin(\theta_1) \sin(\varphi_n)y + \cos(\theta_1)z]} + \right. \\
& \left. \sin(\vartheta_{P_2}) \sin(\theta_2) \cdot e^{ik[\sin(\theta_2) \cos(\varphi_n)x + \sin(\theta_2) \sin(\varphi_n)y + \cos(\theta_2)z]} \right|^2 - ResistThreshold \Big)
\end{aligned} \tag{2.32}$$

If  $n=4$ ,  $\theta_n=(-1)^n \cdot 8^\circ$ ,  $\phi_n=(n-1) \cdot 90^\circ$ ,  $\vartheta_{P_n}=0^\circ$ ,  $\delta_n=0$ ,  $n_{resist}=1.7$ ,  $\lambda=355$  nm, and  $ResistThreshold = 62\%$  results in the 3D photoresist plot found in Figure 21. Similarly to the previous three-dimensional photoresist model plot the  $z$ -axis is increased by a factor of 10 to show the details of the structure. The  $x$  &  $y$ -axes are not on the same scale of the  $z$ -axis in the 3D photoresist plot.



**Figure 21** – 3D multiple-exposures interferometric lithography photoresist pattern.

$$\text{On-axis exposure } \Lambda_z = \infty$$

Here the three-dimensional structure of the multiple-exposure interferometric lithography photonic crystal is the same as the two-dimensional interferometric lithography photonic crystal. The reason for the three-dimensional structure being the same as the two-dimensional structure is that, when the exposure beam angles are of the same magnitude and symmetric around the  $z$ -axis ( $|\theta_1| = |\theta_2|$ ), the pitch in the  $z$ -direction is infinite. The next section explains a method that addresses controlling the pitch in the  $z$ -direction.

### **Independent Control of $z$ -Direction Periodicity**

The one issue that is quickly seen in the three-dimensional interferometric lithography is that the  $z$  pitch is usually much larger than the  $x$  and  $y$  pitch. For the single exposure approach it is very difficult to get the  $z$  pitch similar to the  $x$  and  $y$  pitch, and typically involves larger wavelengths comparable to the  $(x, y)$  pitch for which the

photoresist may not be sensitive. However in the multiple-exposure approach it is much simpler to get the  $z$  pitch similar to or the same as the  $x$  and  $y$  pitch.

In single exposure interferometric lithography the pitch in all three directions is affected by the angle of each plane-wave beam and the exposure wavelength. In order to get the  $x$ ,  $y$ , and  $z$  pitch to be similar in size, requires that the exposure beam angle  $\theta$  be as close as possible to  $90^\circ$ , and the exposure wavelength be as close to the desired pattern pitch dimension. For example, if the desired photonic crystal pitch is 750 nm then the exposure wavelength needs to be 750 nm. This is difficult because this requires a photoresist that is sensitive at that wavelength, and if the desired pitch changes than the photoresist may also need to change.

The main advantage of the multiple-exposure interferometric lithography approach to three-dimensional structures is the much greater flexibility to independently control the dimensions of the three-dimensional structures along each axis. The  $x$ -pitch and  $y$ -pitch of the pattern in the exposure plane is controlled by the angle between the two exposure beams  $2\theta_A$ . The  $z$ -pitch of the pattern, perpendicular to the exposure plane, is controlled by the angle of the intercept between the two beams to the normal of the exposure plane  $\psi$ , see Figure 22 and Figure 23.

If both exposure beams are tilted together off normal to the exposure plane ( $\psi \neq 0$ ) the interference pattern in the photoresist is tilted. Also as a result of Snell's law the plane waves of light are bent at the photoresist interface, see Figure 22. For a vertical interference pattern ( $\psi = 0$ )  $\theta_1 = -\theta_2$ , but if  $\theta_1$  &  $\theta_2$  are offset by a fixed angle there is a shift in the interference pattern angle  $\psi_c$ . The following formulas give the relations

between the plane-wave beam angles in the air and in the photoresist as well as some of the defined pitches.

$$\theta_{1.PR} = \text{asin} \left[ \frac{\sin(\theta_1)}{n_r} \right] \quad (2.33)$$

$$\theta_{2.PR} = \text{asin} \left[ \frac{\sin(\theta_2)}{n_r} \right] \quad (2.34)$$

$$\psi = \frac{\theta_1 + \theta_2}{2} \quad (2.35)$$

$$\theta_{\Delta} = \frac{\theta_2 - \theta_1}{2} \quad (2.36)$$

$$\psi_c = \frac{\theta_{1.PR} + \theta_{2.PR}}{2} \quad (2.37)$$

$$\theta_{\Delta.PR} = \frac{\theta_{1.PR} - \theta_{2.PR}}{2} \quad (2.38)$$

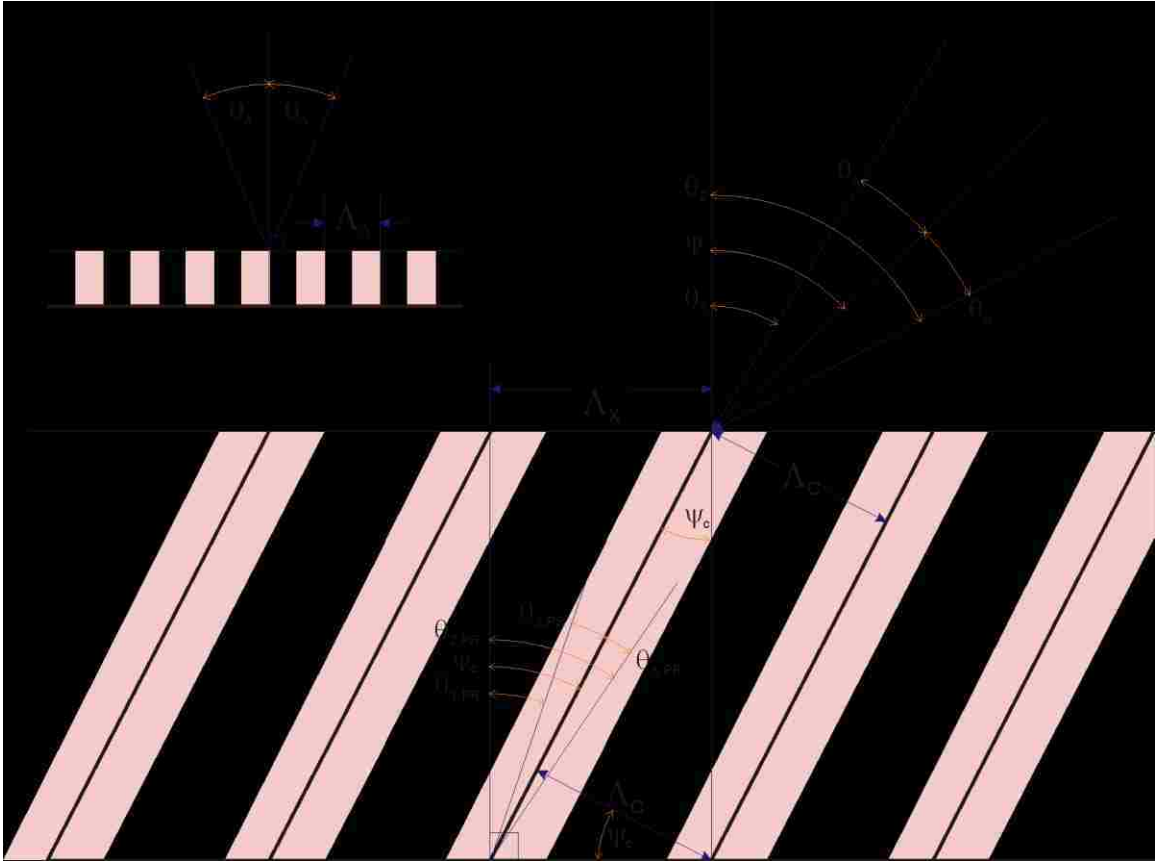
$$\Lambda_x = \Lambda_{x.air} = \Lambda_{x.PR} = \frac{\lambda}{\sin(\theta_2) - \sin(\theta_1)} = \frac{\lambda}{n_r \cdot [\sin(\theta_{2.PR}) - \sin(\theta_{1.PR})]} \quad (2.39)$$

$$\Lambda_c = \Lambda_x \cdot \cos(\psi_c) = \frac{\lambda}{2 \cdot n_r \cdot \sin(\theta_{\Delta.PR})} \quad (2.40)$$

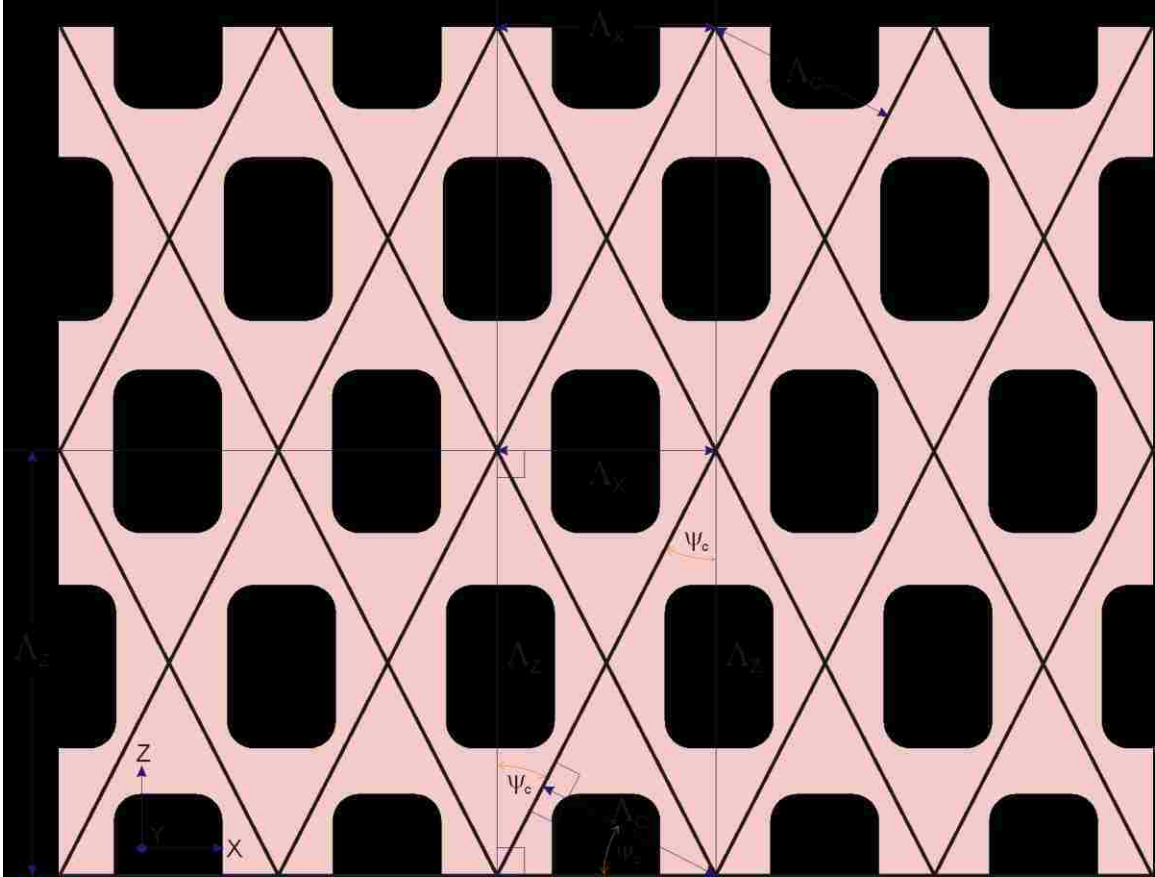
If three or more exposures with the tilted interference pattern are combined the result is a three-dimensional pattern that has a shortened  $z$ -pitch. The following Figure 22 and Figure 23 show the slice view of a three-dimensional pattern, in addition to an additional pitch definition  $\Lambda_z$ . The following is the formula for the pitch in the  $z$ -direction.

$$\Lambda_z = \frac{\Lambda_x}{\tan(\psi_c)} \quad (2.41)$$

If  $\psi_c = 45^\circ$  then  $\Lambda_x = \Lambda_z$ . This is important if symmetrical three-dimensional photonic crystals are desired.



**Figure 22** – Definitions of plane-wave beam angles in the air and in the photoresist.  
For on-axis and off-axis exposures.



**Figure 23** – Cross-section of a three-dimensional pattern and pitch definitions.

To better understand the relation and parameter space for the  $z$ -pitch compared to the transverse pitches, an plot of available  $z$ -pitches versus available  $x$  ( $y$ ) pitches for an exposure wavelength of  $\lambda=355\text{nm}$  and photoresist index of refraction  $n_r=1.3$ , is presented in Figure 24. In this plot the solid red line represents the  $z$ -pitch versus transverse pitch for on-axis single-exposure three-dimensional interferometric lithography photonic crystals. The cyan colored area represents the combinations of  $z$ -pitches versus transverse pitches achievable with off-axis multiple-exposure three-dimensional interferometric lithography photonic crystals. The  $45^\circ$  green dashed line represents a symmetrical photonic crystal ( $z$ -pitch =  $x$ -pitch). As the refractive index of the



photoresist increases, the area of achievable pitches (cyan colored area) decreases due to the reduction of the beam angle in the resist from Snell's law.

Looking at the extreme limits of achievable pitches on each, for off-axis illumination multiple-exposure three-dimensional interferometric lithography photonic crystals, we notice that the minimum  $z$ -pitch =  $\frac{\lambda}{\tan[\frac{1}{2}-\text{asin}(\frac{1}{n_r})]}$  occurs when  $\theta_\Delta = 45^\circ$  and  $\psi = 45^\circ$ , the minimum  $x$ -pitch =  $\lambda/2$  occurs when  $\theta_\Delta \rightarrow 90^\circ$  and  $\psi \rightarrow 0^\circ$ , the maximum  $z$ -pitch  $\rightarrow \infty$  occurs when  $\theta_\Delta \rightarrow 0^\circ$  and  $\psi \rightarrow 0^\circ$ , the maximum  $x$ -pitch  $\rightarrow \infty$  occurs when  $\theta_\Delta \rightarrow 0^\circ$  and  $\psi \rightarrow 90^\circ$ . The minimum symmetrical pitch achievable is  $\frac{\lambda}{1-n_r\sqrt{1-\frac{1}{n_r^2}}}$  which occurs when  $\psi_c = 45^\circ$ . The use of immersion will improve this plot even further by reducing the Snell's law deviations on entering the photoresist, which is further examined in Chapter 6.

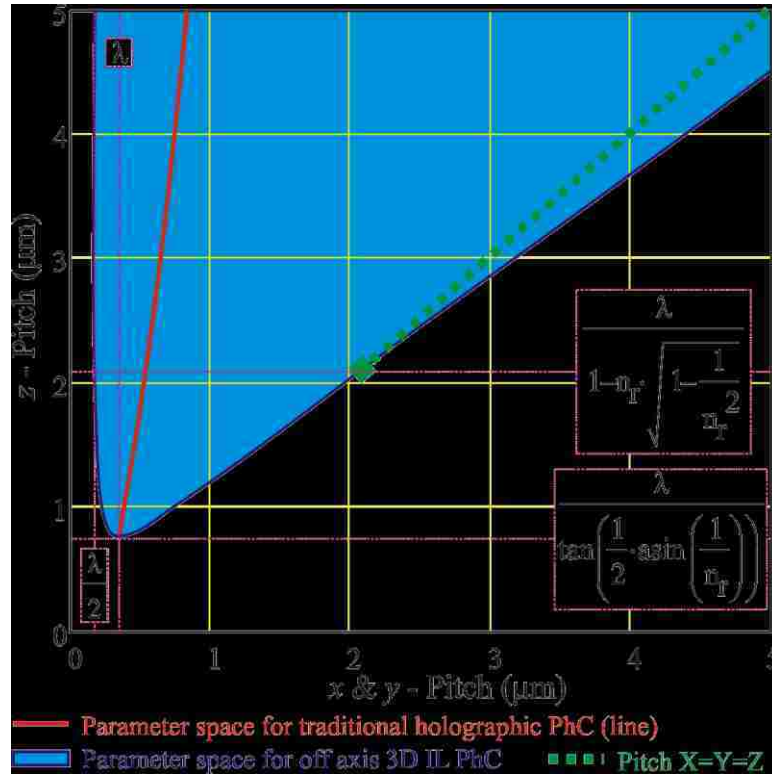
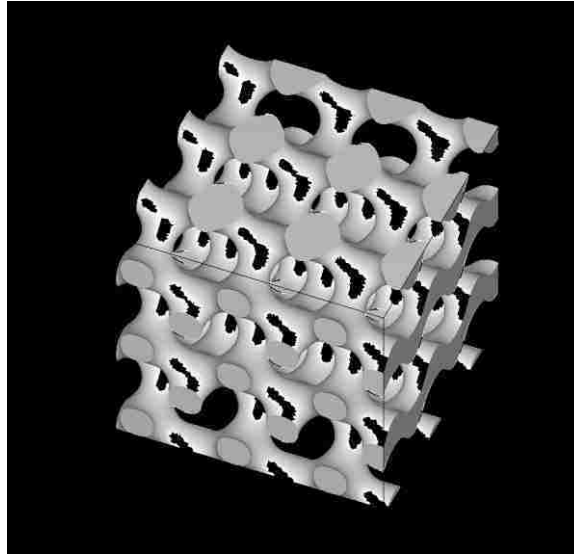


Figure 24 – Photonic crystal pitch parameter space.

$\lambda=355\text{nm}$ ,  $n_r=1.3$  Red line single exposure PhC, cyan shaded area multiple exposure PhC.

If the same 3D photoresist model of a three-dimensional multiple-exposure interferometric lithography used to create Figure 21 is used again, but with interference beam angles that have been offset by a fixed amount, we can see how the  $z$  pitch is reduced. For  $n=4$ ,  $\phi_n=(n-1)\cdot 90^\circ$ ,  $\vartheta_{pn}=0$ ,  $\delta_n=(n-1)(\pi/2)$ ,  $n_{resist}=1.7$ ,  $\lambda=355\text{ nm}$ , and  $ResistThreshold = 62\%$  with  $\theta_A=8^\circ$ ,  $\psi=45^\circ$  such that  $\theta_1=37^\circ$ ,  $\theta_2=53^\circ$  the 3D photoresist plot found in Figure 25 results. The crystal has an  $x$ -pitch of  $1.804\ \mu\text{m}$  and a  $z$ -pitch of  $3.695\ \mu\text{m}$ .



**Figure 25** – 3D multiple-exposure interferometric lithography photore resist pattern with tilted incident beams.

This three-dimensional photore resist pattern is much more symmetric than the single-exposure interferometric lithography pattern or the multiple-exposure interferometric lithography pattern with the interference beam angles normal to the exposure plane. This off-axis exposure advantage that the multiple-exposure interferometric lithography approach allows, gives much greater flexibility to independently control the dimensions of the 3D structures along each of the individual axis. Therefore this multiple-exposure interferometric lithography approach was used to create the three-dimensional photonic crystals demonstrated in the remainder of this dissertation.

## CHAPTER 3

### WAVEGUIDE FABRICATION

Three-dimensional photonic crystals have unique optical properties which can be utilized in applications such as optical filters, mirrors, and optical coupling. Many photonic crystals applications however involve the use of waveguides in the crystal. A waveguide is designed to transport waves within a frequency band of interest across a path. Waveguides in photonic crystals can: guide light around sharp bends, filter light, split or mix light into multiple waveguides, contain waveguides with optical isolators, and form optical coupled cavities.<sup>19</sup> Waveguides in a photonic crystal can also possess non-linear optical properties if the crystal contains material that have an optical Kerr effect or a nonlinear susceptibility  $\chi^{(2)}$  that can be used for optical computing applications.<sup>3,20,21</sup>

The formation of a waveguide in a photonic crystal is accomplished by introducing defects in the crystal lattice, usually a linear two-dimensional defect. Such defect can be a missing row of nodes, or filled in row of voids. The row of defects doesn't even have to be completely missing or filled in, they can be just a ratio change in node to void size compared to the surrounding volume in the crystal. In other words say a row of larger nodes compared to all surrounding nodes. This is very similar to using dopants in a semiconductor crystal to introduce defects to the atomic lattice for modifying the semiconductor crystal electrical properties.

The use of three-dimensional photonic crystals with embedded waveguides has a great potential for applications, due to the possibility of a three-dimensional photonic

crystal having a full bandgap. Waveguides in a three-dimensional photonic crystal with a full bandgap can allow for lossless wave guiding properties. One of the important issues hindering applications that use optical devices being made out of three-dimensional photonic crystal is due to the ability to produce three-dimensional photonic crystals with internal waveguides. Most techniques for embedding waveguides into a photonic crystal involve either forming the defects or waveguide when building the photonic crystal one layer at a time, or by a direct write, two-photon method used for typical holographic photonic crystals. In all cases the embedded waveguide formation is a tedious and slow serial process.<sup>22</sup>

The novel fabrication process used in this dissertation and outlined in the following section can utilize current semiconductor manufacturing tools and practices. It allows for a mass manufacturing approach to waveguide formation in photonic crystals.

### ***Two Wavelength Approach to Waveguide Fabrication***

The novel approach taken in this dissertation to fabricate a waveguide uses two different exposing wavelengths in the same photoresist film. The first wavelength is used to fabricate the photonic crystal, and the second wavelength is used to fabricate the waveguides. Both exposures are done in the same layer of photoresist material used to make the device.

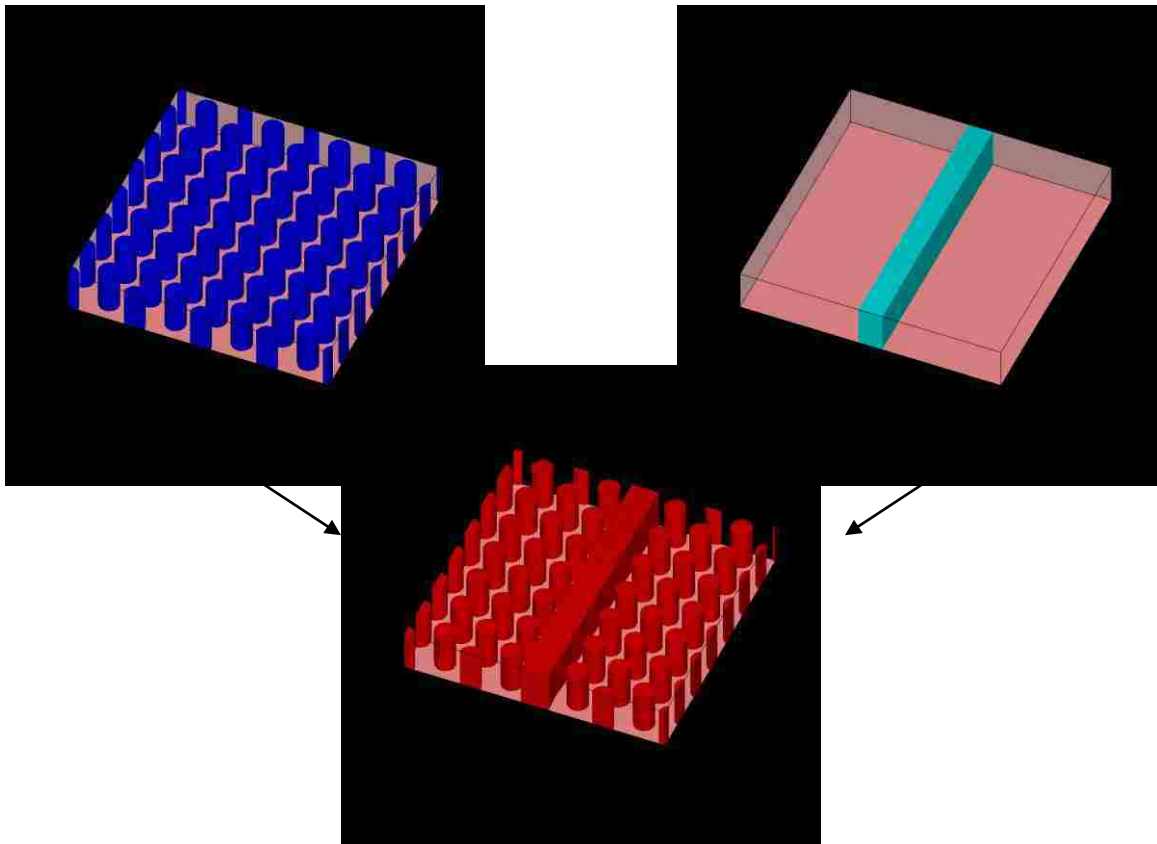
### **Fabrication Technique**

The fabrication process for the two-wavelength approach is as follows. An anti-reflective coating (ARC) is deposited on the photonic crystal substrate. This ARC is used

to minimize the reflection of the exposing light off of the substrate. The ARC can either be a dielectric layer or a spun on organic layer, the latter being used exclusively for the photonic crystals fabricated for this dissertation. A very thick layer of photoresist is then spun atop ARC. This thick photoresist layer becomes the body of the photonic crystal. The photoresist is then baked to drive out solvents and crosslink the photoresist into a film on the ARC coated substrate. The photoresist is exposed to light utilizing one of the interferometric lithography techniques previously described to create photonic crystals. This is immediately followed by an exposure at a different wavelength, using a standard lithography technique to define the waveguide defect path. Once the photoresist is exposed at both wavelengths it receives a post exposure bake followed by a development step. The result is a photoresist pattern which is the functional sum of the two different wavelength exposures, and when done properly becomes a photonic crystal with embedded waveguide. Figure 26 illustrates this process, the first plot (a) is of the latent image in the photoresist during the exposing of a two-dimensional photonic crystal of posts or rods at the first wavelength, the second plot (b) is of the latent image in the photoresist during the exposing of the waveguide at the second wavelength, and the final plot (c) is the developed photoresist pattern on the substrate of a two-dimensional photonic crystal of post with a waveguide.

The lateral size of the waveguide defect is a direct function of the waveguide mask pattern size plus waveguide exposure dose. The example illustrated in Figure 26, since the waveguide extends completely through the photo resist layer, could have been achieved with a single wavelength and even a single exposure, but as the concept of this

technique is expanded upon it is possible to create waveguides that cannot be achieved with a single exposure wavelength.

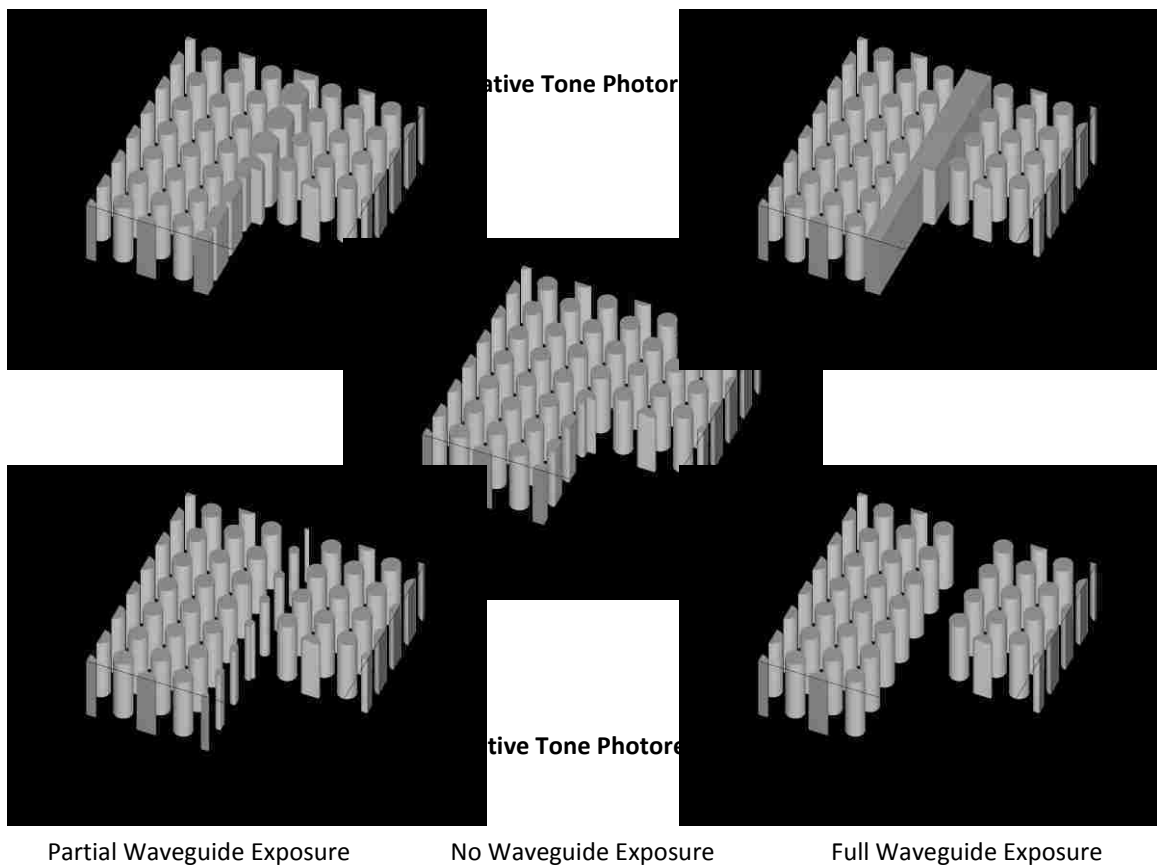


**Figure 26** – Two-wavelength fabrication of waveguide in photonic crystal.

## Photoresist Requirements

In order for this two-wavelength process to work, the photoresist must be sensitive to the light at both wavelengths. Many chemically amplified photoresists used in the semiconductor industry are sensitive to light over a large range of wavelengths. For instance a negative I-line photoresist that could be used to make a photonic crystal may be sensitive to 248 nm light that could be used to make the waveguide. Similarly a positive 248 nm photoresist that could be used to make a photonic crystal may be sensitive to 193 nm light that could be used to make the waveguide. In most cases the

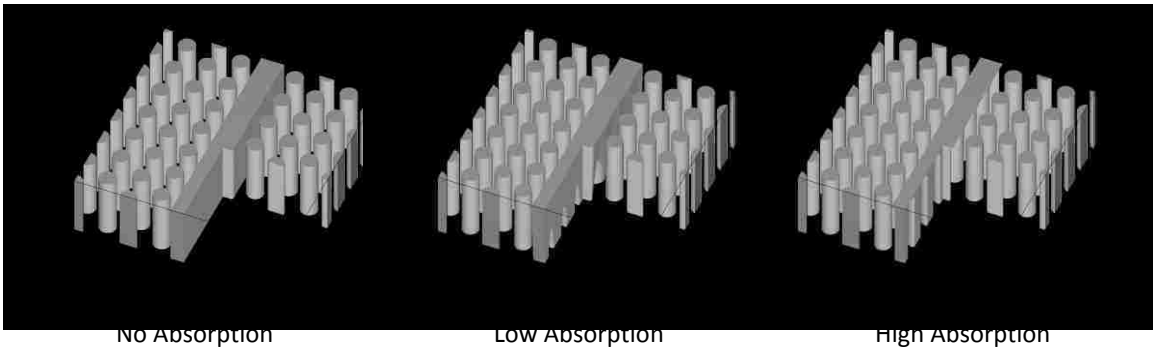
photoresist has the same tone for both wavelengths but this is not a requirement. For example a photoresist usually acts as either a positive material or negative material at both wavelengths, but the process steps could be modified to produce similar results if the photo resist has a positive tone response and one wavelength and a negative tone at the other wavelength. Figure 27 shows several models of a 2D photonic crystal of posts in a hexagonal pattern exposed in 2  $\mu\text{m}$  of photoresist with various waveguide exposures in both positive tone and negative tone photoresist at the waveguide exposure wavelength. The bottom right quadrant of the plots has been cutout to better show the cross-section of the waveguide.



**Figure 27** – 2D photonic crystal of posts, with various waveguide exposures.



It is not necessary but is usually beneficial if the photoresist photo-response is different at the two exposure wavelength, which will be demonstrated hereafter. For the photonic crystal exposure the photoresist should be very transparent and have a highly nonlinear response curve at the exposing wavelength. Most photoresist are very transparent and nonlinear at their design wavelength. But for the waveguide exposure the transparency of the photoresist at the exposing wavelength can play an important role. If the photoresist is very transparent at the waveguide exposure wavelength then the waveguide extends through the full thickness of the photoresist. This is normally the desired case for two-dimensional photonic crystal. In the case where the waveguide extends the full thickness of the photoresist it is possible to have the waveguide exposure wavelength be the same as the photonic crystal exposure wavelength. However if the photoresist is highly absorptive at the waveguide exposure wavelength, then the waveguide only exists on the surface of the crystal. By tailoring the absorption of the photoresist at the waveguide exposure wavelength, it is possible to control how thick a waveguide is formed. Figure 28 shows several models of two-dimensional photonic crystals exposed in 2  $\mu\text{m}$  of negative tone photoresist at the waveguide exposure wavelength, with the absorption of the photoresist varying from nearly transparent to highly absorptive at the waveguide exposure wavelength. Control of the waveguide thickness is important for three-dimensional photonic crystals.



**Figure 28** – Waveguide in a photonic crystal of posts, with various amounts of photoresist absorption at the waveguide exposure wavelength. Waveguide thickness is proportional to photoresist absorption.

### ***Embedded Waveguides***

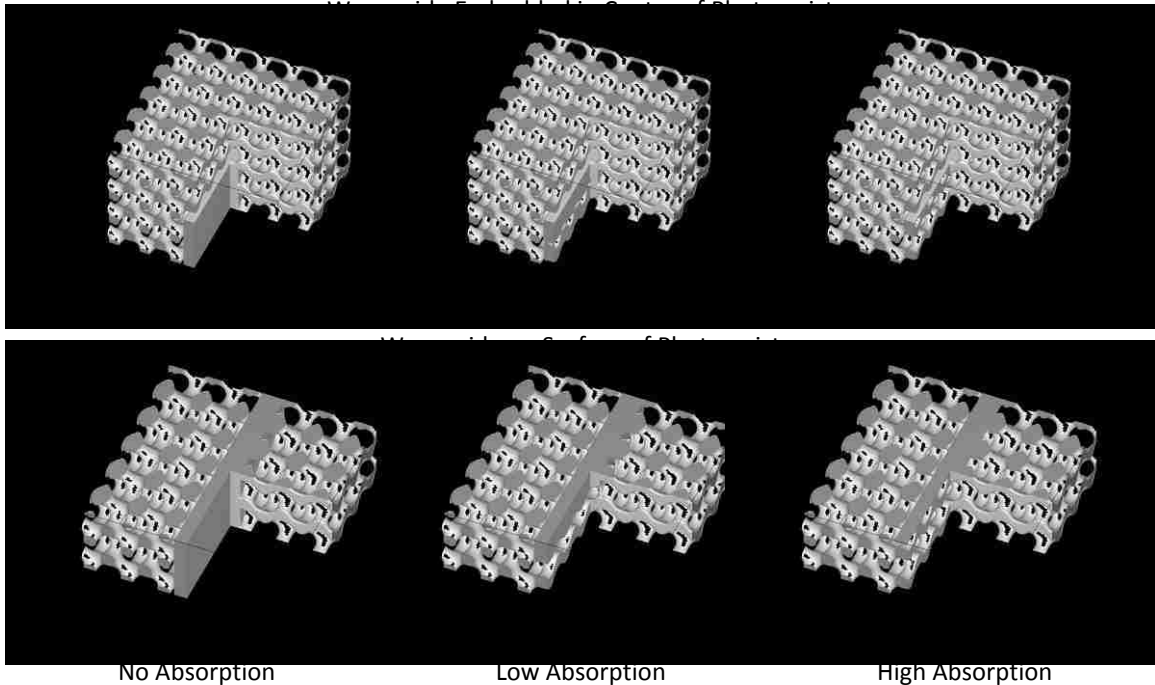
In three-dimensional photonic crystals it is desirable to have full three-dimensional confinement of the waveguide, and not have a slab waveguide that extends throughout the crystal thickness. As this allows light to leak from the waveguide at its top and bottom boundaries, and is highly multimode. If the waveguide is fabricated as previously described with the photoresist being partially absorptive at the waveguide exposure wavelength, then the three dimensional photonic crystal has a waveguide at the surface. However this still allows light to leak from the waveguide at the surface. What is desired is to have a waveguide that is embedded in the middle of the crystal.

### **Fabrication Technique**

Another novel fabrication technique used in this dissertation that expands on the previous waveguide manufacturing process that allows for the embedding of the waveguide is as follows. Instead of exposing the waveguides on the surface of the photonic crystal, the waveguides are exposed in the middle of the photonic crystal. This is still possible to do with a single photonic crystal interferometric lithography exposure

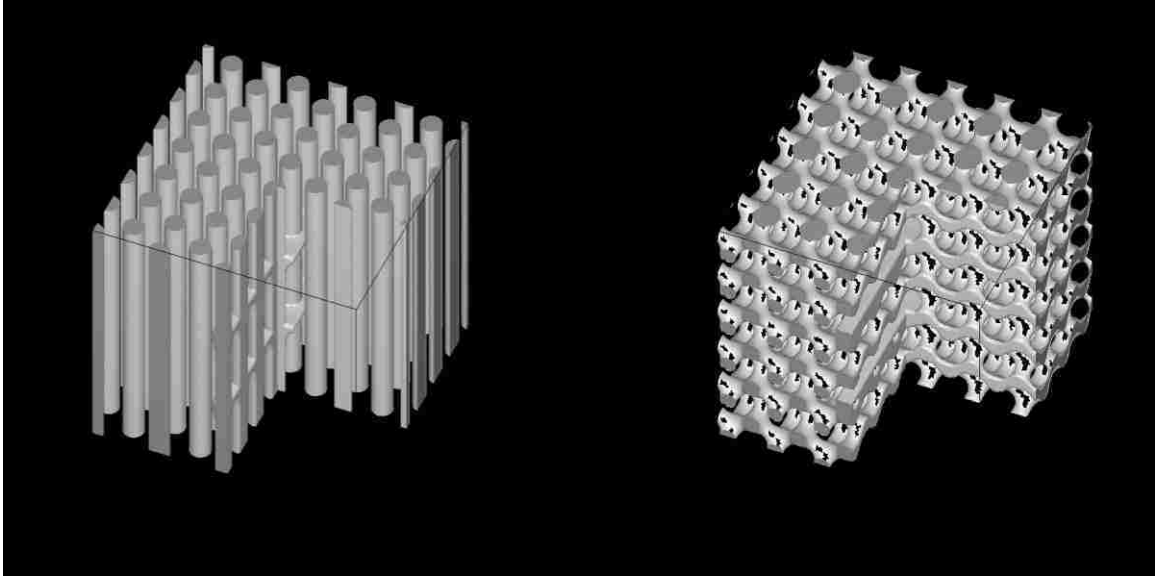
step and a single waveguide lithography exposure step. The trick is to use two layers of photoresist. First a single thick layer of photoresist is spun on to the anti-reflective coated substrate, and baked. The waveguide is then exposed on the surface of this photoresist layer using a wavelength that is strongly absorbed by the photoresist. Next without any further processing a second layer of thick photoresist is spun on to the first layer of photoresist. Now the two layers of photoresist are exposed using the three-dimensional interferometric lithography technique at a wavelength that is very transparent to the photoresist. Now that the two layers of photoresist are exposed at the photonic crystal wavelength with the first layer being exposed at the waveguide wavelength, the photoresist receives a post exposure bake. Then the full two layer photoresist stack is developed. The result is a photoresist pattern that is a combination of two different wavelength exposures, and when done properly becomes a photonic crystal with embedded waveguides. The lateral size of the waveguide defect is a direct function of the waveguide mask pattern size plus waveguide exposure dose, and the thickness of the waveguide is a direct function of the photoresist absorption at the waveguide exposure wavelength plus waveguide exposure dose. Figure 29 shows several models of three-dimensional photonic crystal exposures that are negative tone at the waveguide exposure wavelength, with the absorption of the photoresist varying from nearly transparent to highly absorptive at the waveguide exposure wavelength. The three lower model plots illustrate the waveguides on the surface of a single  $2\ \mu\text{m}$  layer of photoresist. This is the same as Figure 27 in the previous section, but with three-dimensional photonic crystals instead of two-dimensional photonic crystals. The three upper model plots illustrate waveguides embedded in the middle of a  $4\ \mu\text{m}$  layer of photoresist made from two  $2\ \mu\text{m}$

layers of photoresist spun on top of each other with the waveguide exposure done in between the coats.



**Figure 29** – Waveguide on the surface and embedded in the center of 3D photonic crystals, with various amounts of photoresist absorption at the waveguide exposure wavelength.

This technique can be expanded to more than two layers. It is possible to fabricate a layer of embedded waveguides patterns that are  $1/3$  from the bottom of the photonic crystal and a layer of embedded waveguides patterns that  $2/3$  from the bottom of the photonic crystal using a three-layer process, as is seen in Figure 30. With some clever processing it is even possible to make vertical waveguides between the two embedded waveguide layers using a via exposure patterning step done on the second photoresist layer. This via pattern exposure could be done either by using a high dose at the waveguide exposure wavelength, or using a third exposure wavelength with a lower photoresist absorption than the waveguide exposure wavelength. This will be important for the integration of optical circuits fabricated into photonic crystals.



**Figure 30** – Two embedded waveguides in a photonic crystal of posts, and in 3D photonic crystal.

## Photoresist Requirements

In order for the waveguide embedding technique to work the photoresist must meet special requirements. The first requirement is that the photoresist has the right absorption at the waveguide exposure wavelength to allow a waveguide that is thick enough for wave propagation but not too thick that it reaches too close to the photonic crystal boundary to avoid wave propagation leakage or becomes multimode.

The second requirement is that when coating the second layer of photoresist it does not adversely affect the first layer of photoresist. This is a stringent requirement that can be upset by multiple undesirable chemical interaction issues.

One source of potential problems that can arise when coating the second layer of photoresist is that the casting solvent for the second photoresist layer dissolves the first layer of photoresist during the coat process. The result is a new single layer of photoresist composed of material from both the first layer of photoresist and the second

layer of the photoresist. If some of the material in the first layer of photoresist is exposed during a waveguide exposure, then some of that exposed material is mixed into the new layer of photoresist during the second coat process, and causes undesirable effects. Therefore a photoresist must be chosen that doesn't dissolve in the casting solvent once coated and baked.

Another source for potential problems, which can arise during the coating of the second layer of photoresist, is that if any exposed part of the first layer of photoresist during the coat process is dissolved or developed by the casting solvent of the photoresist. This is less likely to happen if the second layer of photoresist is coated without any post exposure baking of the first layer of photoresist.

Still another source of potential problems is if there is a contamination effect caused on the surface of the first layer of photoresist. This contamination effect could cause the first layer of photoresist to develop differently than the second layer during development.

There likely will be other photoresist issues that need to be considered than the ones listed here in order to achieve satisfactory embedded waveguides. However as is demonstrated in the next chapter, there are photoresists available that impart the right characteristics to make three-dimensional photonic crystals with embedded waveguides.

## CHAPTER 4

### EXPERIMENTAL FABRICATION OF 3D PHOTONIC CRYSTALS

#### *Introduction to Experimental Fabrication of 3D Photonic Crystals*

This chapter goes into the details of the photonic crystals that were experimentally fabricated. The next section describes several approaches to making photonic crystals using the multiple-exposure interferometric lithography technique. One of the approaches is then selected and used for fabricating three-dimensional photonic crystals. The following section contains photoresist profiles generated using the three-dimensional photonic crystal models made by the multiple-exposure interferometric lithography technique from Chapter 2. The photoresist modeled profiles are used for comparing to the photoresist profiles obtained by SEM images of experimentally fabricated three-dimensional photonic crystal. Photonic crystals made by 355 nm exposures in negative photoresist and photonic crystals made by 244 nm exposures in positive photoresist are presented. The last section contains scanning electron microscope images of the fabricated three-dimensional photonic crystals with waveguides. Images of three-dimensional photonic crystals with waveguides, both at the surface of the photonic crystal and embedded in the center of the photonic crystal, are presented. In the first case of waveguides on the surface of the photonic crystal there are images in both negative and positive photoresist.<sup>23</sup>

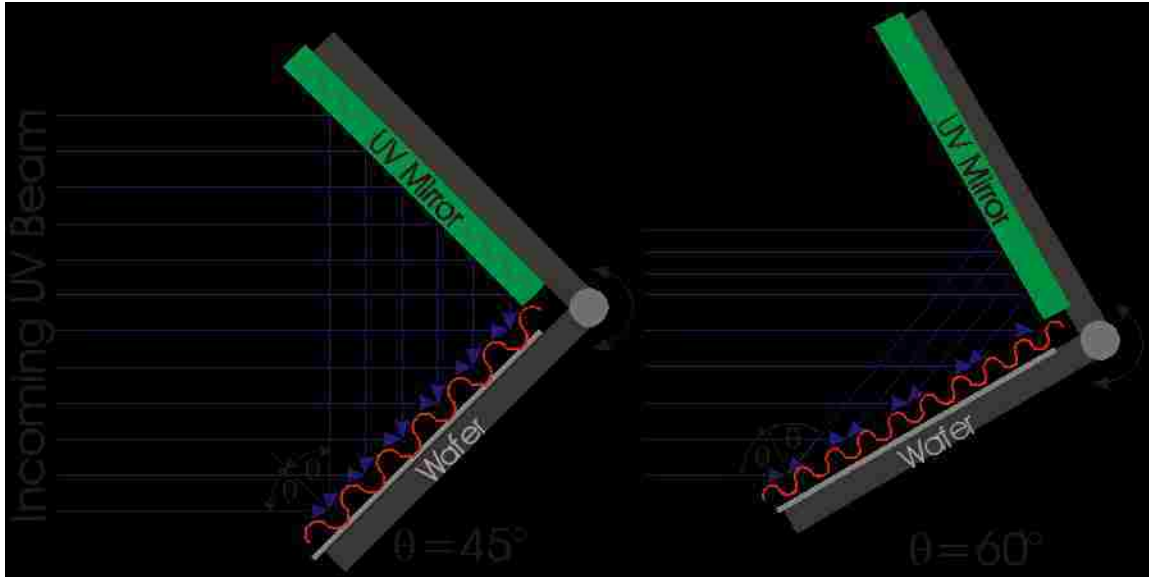
## ***Experimental Approaches***

This section describes several experimental setups that were built to fabricate three-dimensional photonic crystals using the multiple-exposure interferometric lithography technique. The first setup is based on a Fresnel mirror interferometer. The second setup is based on phase mask interferometer. And a final third setup is based on a Michelson interferometer. The advantages and disadvantages of each setup are discussed. The Michelson interferometer setup is used to create the experimental three-dimensional photonic crystals presented later in this dissertation.

### **Fresnel Mirror Interferometer**

A Fresnel corner cube mirror interferometer is one of the simplest interferometers, it usually consist of just a mirror mounted  $90^\circ$  to a wafer chuck on a rotation stage. Figure 31 illustrates how the corner cube mirror folds half of the incoming UV beam onto the wafer to form a sinusoidal interference pattern on the surface of the wafer. In a corner cube interferometer the angle of the incoming beam to the wafer is equal to the angle of the beam reflected off the corner mirror to the wafer ( $\theta_l = \theta_r$ ), see Figure 31. The period of the grating exposed in the photoresist is given by  $\Lambda = \frac{\lambda}{2 \cdot n \cdot \sin(\theta)}$  ( $n = 1$  for exposure in air). Therefore rotating the corner cube interferometer with respect to the incoming UV beam sets the period. With this arrangement the two beams are always symmetrically incident on the wafer for any given pitch ( $\theta_1 = -\theta_2$ ).



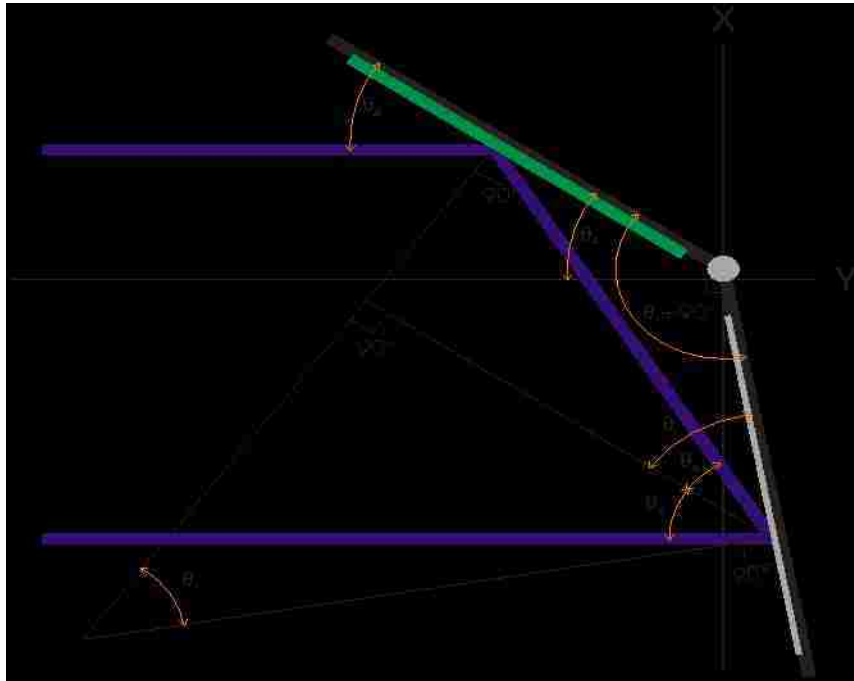


**Figure 31** – Fresnel corner cube mirror interferometer diagram.

One issue with using a Fresnel mirror is that the difference in the two path lengths increases the further the exposing location is from the edge of the mirror at the exposure stage (the inside corner of the cube). If the path length difference is greater than the coherence length there is no interference pattern just light with uniform intensity exposing the sample.

For three-dimensional structures there is the need to offset the two incident beams from normal. This is achieved by modifying the Fresnel mirror interferometer. Instead of having the interferometer setup as a corner cube with the mirror  $90^\circ$  from the exposure plane, the mirror is offset. The offset angle ( $\theta_i$ ) of the mirror from  $90^\circ$  in turn offsets the two exposure beam angles the same amount from normal to the wafer exposure plane. Figure 32 illustrates a Fresnel mirror interferometer used for off-incidence exposures with all notable angles labeled, which is also relatively inexpensive and easy to setup. The rotating of the whole interferometer to the angle of the incoming beam sets the angle

between the two beams ( $\theta_\Delta$ ), and thus the pitch  $\Lambda_X = \frac{\lambda}{n \cdot [\sin(\theta_i + \theta_\Delta) - \sin(\theta_i - \theta_\Delta)]}$  same as for a regular Fresnel corner cube interferometer. By rotating the sample in the exposure plane ( $\phi$ ) between exposures it is possible to make three-dimensional interferometric lithography patterns on this setup.



**Figure 32** – Fresnel mirror interferometer with offset incident beams diagram, used for making PhCs.

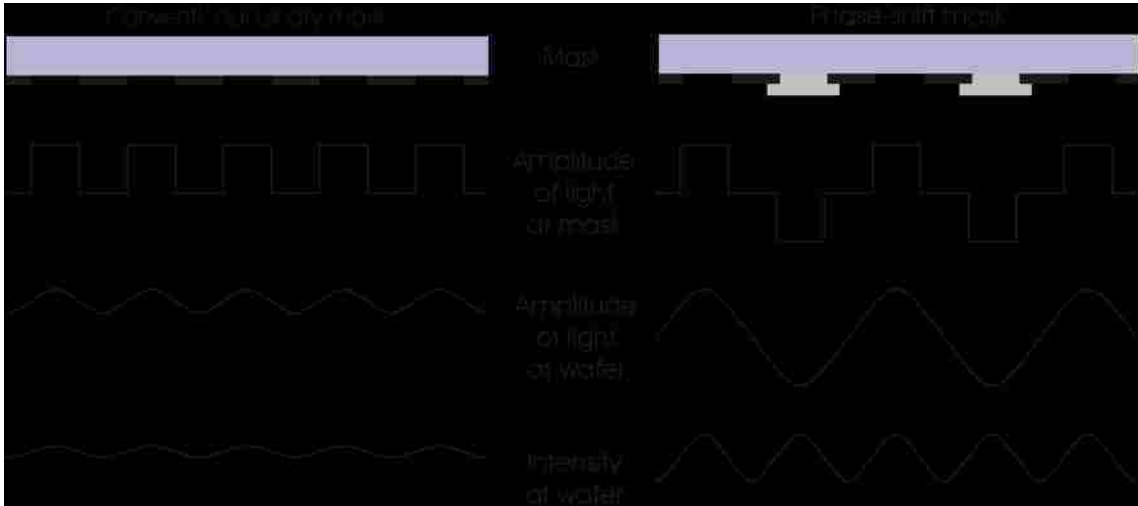
A second issue that arises when doing tilted exposure needed for three-dimensional patterning is that the two beams intercept the photoresist surface at different angles ( $\theta_1 \equiv \theta_i + \theta_\Delta \neq \theta_2 \equiv \theta_i - \theta_\Delta$ ). This causes a difference in the amount of light transmitted into the photoresist for each beam, due to the different Fresnel reflection of each beam off the surface of the photoresist, and different beam sizes intercepting the surface of the photoresist. The beam reflected off the mirror will be elongated more in the grating direction ( $x$ -axis) than the direct incoming beam to the sample by a factor of  $\cos(\theta_\Delta)$ . The difference between the amounts of light electric field amplitude in the

photoresist from each beam ( $A_1 - A_2$ ) increases as the offset incident angle ( $\theta$ ) increases, and as the pitch  $\Lambda_x = \frac{\lambda}{n \cdot [\sin(\theta_i + \theta_\Delta) - \sin(\theta_i - \theta_\Delta)]}$  decreases. This in turn causes a reduction in the interference pattern contrast. For three-dimensional photonic crystals where large offset incident angles ( $\theta_i$ ) are desired, the loss of contrast can be problematic. The only way to solve this is to adjust the left and right beam intensities to account for the intensity of the incoming beam incident to the substrate only, and the intensity of the beam reflecting off the mirror to compensate for the different beam shapes and Fresnel reflectance of the light electric field amplitude into the photoresist.

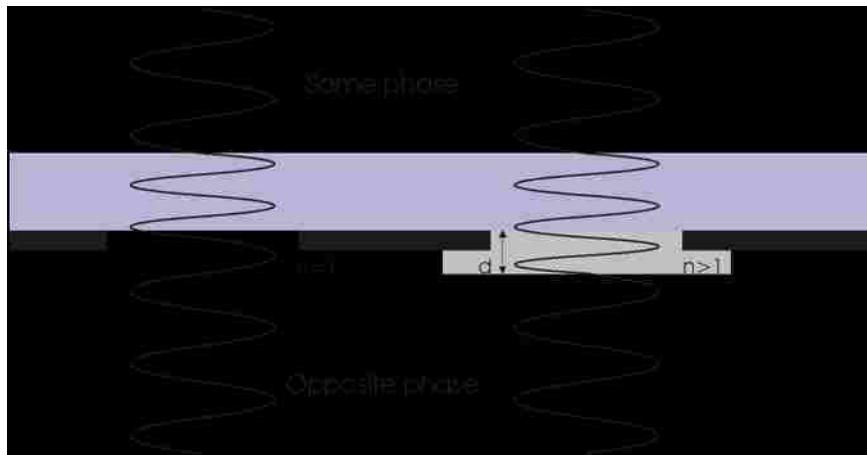
## Phase Mask Interferometer

A phase mask interferometer setup uses a special phase mask to split an incident beam into two or more beams. Phase-shift masks modulate both the amplitude and phase of the electromagnetic light wave as it passes through the mask. In comparison a transmission mask made of chrome on quartz controls only the amplitude of the light wave. Shifting the phase of the light wave  $180^\circ$  is equivalent to changing the sign of the light wave amplitude, see Figure 33. In order to shift the phase of the light  $180^\circ$  an extra layer is added to the mask to create an optical path difference of  $\lambda/2$  between the phase-shift layer mask openings and the non-phase shifted mask openings. The required thickness for the phase-shift layer is given as  $d = \frac{\lambda}{2(n-1)}$  ( $n$  is the refractive index of the shifter material) see Figure 34. This causes the zero-order light transmitted thru the phase shifter part of the mask to destructively interfere with the light passing through the non-phase shifted part of the mask. When there is no normal incident beam then the

grating pitch width in the photoresist is half the size of the grating pitch on the mask  $\Lambda_{resist} = 1/2 \Lambda_{PM}$ , thus frequency doubling the grating period.



**Figure 33** – Comparison of imaging through a conventional binary mask and an alternating shifter PSM.

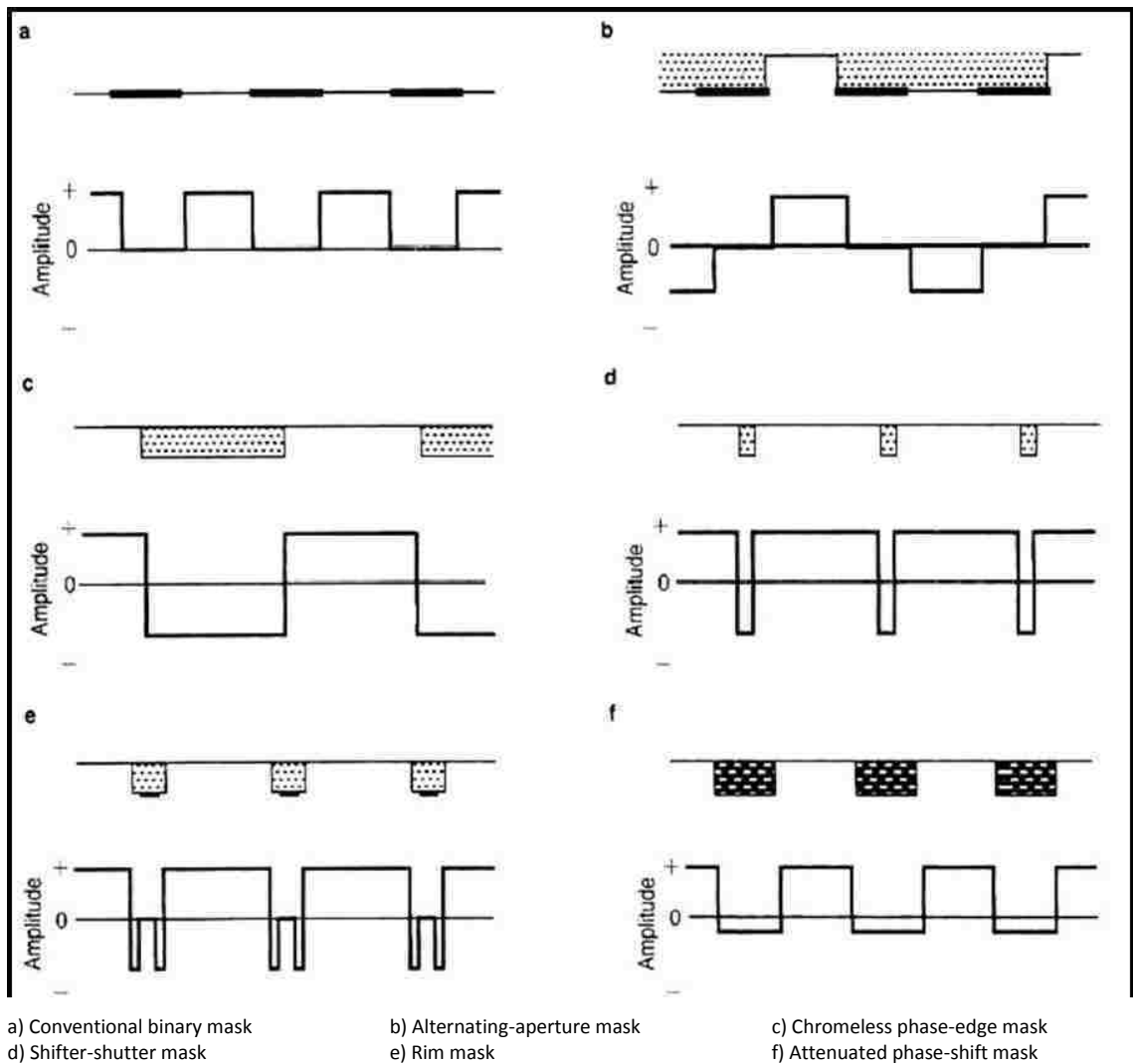


**Figure 34** – Phase-shift mask with phase shifting layer  $d=\lambda/2(n-1)$ .

For fine features on a mask the intensity profile at the wafer is reduced, but by using PSM the contrast is greatly increased.<sup>24</sup>

There are several types of phase-shift mask, Alternating shifter PSM (also known as Levenson-Shibuya), chromeless phase edge PSM, outrigger PSM, rim PSM, and attenuated PSM see Figure 35. All PSM can be placed into two categories: frequency

doubling ‘strong’ PSM, and edge contrast enhancement ‘weak’ PSM.<sup>25</sup> The ‘strong’ phase-shift masks consist of alternating shifter, and chromeless phase edges.



Thick black region represents opaque material  
Dashed regions represents 180° phase shift layer  
“Brick-like” shading represents partially transmitting material with 180° phase shift.

**Figure 35** – Examples of various phase-shift masks.<sup>25</sup>

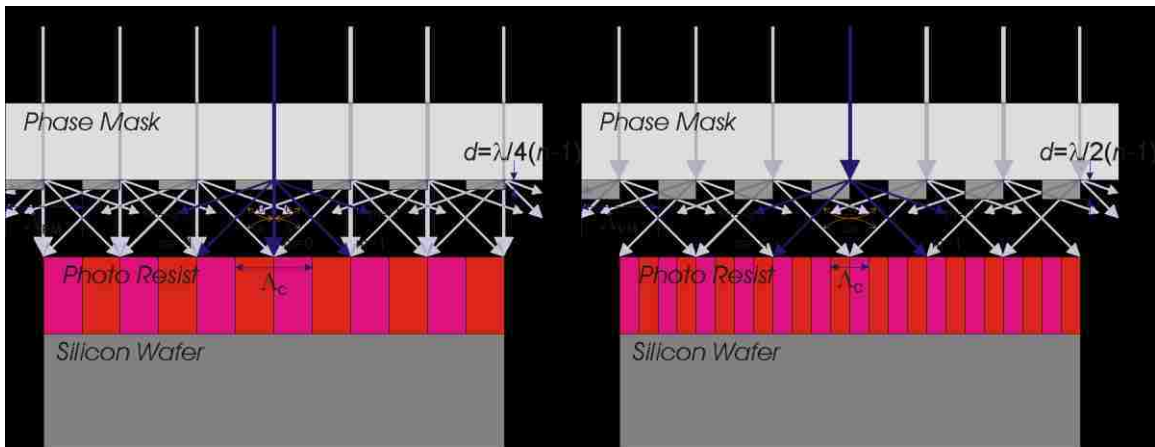
Strong PSM operates by alternating the phase of adjacent features on the mask, thus doubling the spatial frequency. In other words the mask transmittance function has a period which is twice the period to be printed on the wafer, thus they are referred to as “frequency doubling” PSM. Strong PSM does not provide any enhancement for non-

dense or isolated features. Strong PSM provides the greatest improvement but is limited in practicality for general lithography. The ‘weak’ phase-shift masks consist of Outrigger, Rim, and Attenuated PSM. Weak PSM operates by adding a sub-resolution phase shifter to the edges of features on the mask. The image produced by the sub-resolution phase shifters is not printed on the wafer but they enhance the edge contrast of the feature of interest. Weak PSM are most effective for non-dense or isolated features.

A chromeless strong PSM is best suited for use in an interferometer. This is due to the need of creating diffracted orders of plane waves from a dense grating for use as the beams in the interferometer. Therefore the chromeless phase-edge mask is only considered from this point on.

The angle of the beams that are diffracted from the phase mask is a function of the pitch of the phase mask and is defined by  $\theta_m = \sin^{-1} \left( \frac{m \cdot \lambda}{\Lambda_{PM}} \right)$  ( $m$  being the order of the diffracted beam, and  $\Lambda_{PM}$  being the pitch of the phase mask). The intensity of the zero-order beam is a function of the phase shifter thickness, and the duty cycle of the pitch, also known as the line space ratio. If the phase shifter deviates from shifting the phase of the light  $180^\circ$ , creating an optical path difference of  $\lambda/2$  between the phase-shift mask openings and the non-phase shifted mask openings, then a zero-order is present. When there is a zero-order then the grating pitch in the photoresist is the same period as the grating pitch on the mask  $\Lambda_{resist} = \Lambda_{PM}$ , instead of being halved as is the case when there is no zero-order present  $\Lambda_{resist} = \frac{1}{2} \Lambda_{PM}$ . By adjusting the thickness of the phase shifter between 0 and  $\lambda/4$  the intensity of the zero-order varies. This is important for off-axis illumination.

Two or more beams are then used to create the interference pattern as seen in Figure 36. In order to create three-dimensional photonic crystals it is necessary to offset the diffracted beams from normal. This is accomplished by either tilting the sample or using off axis illumination on the phase mask, which is clearly different from conventional phase masks used for general lithography. The angle of the beams that are diffracted from the phase mask with off-axis illumination is now defined as  $\theta_m = \sin^{-1} \left( \sin(\theta_i) + \frac{m \cdot \lambda}{\Lambda_{PM}} \right)$  ( $m$  being the order of the diffracted beam, and  $\theta_i$  is the angle of the off axis illumination beam). The three-dimensional photonic crystals are formed using the interference from the tilted zero and negative first orders. The positive orders are diffracted away from the mask. This is illustrated in Figure 37 of a phase mask interferometer used for off incident exposures with all notable angles labeled.

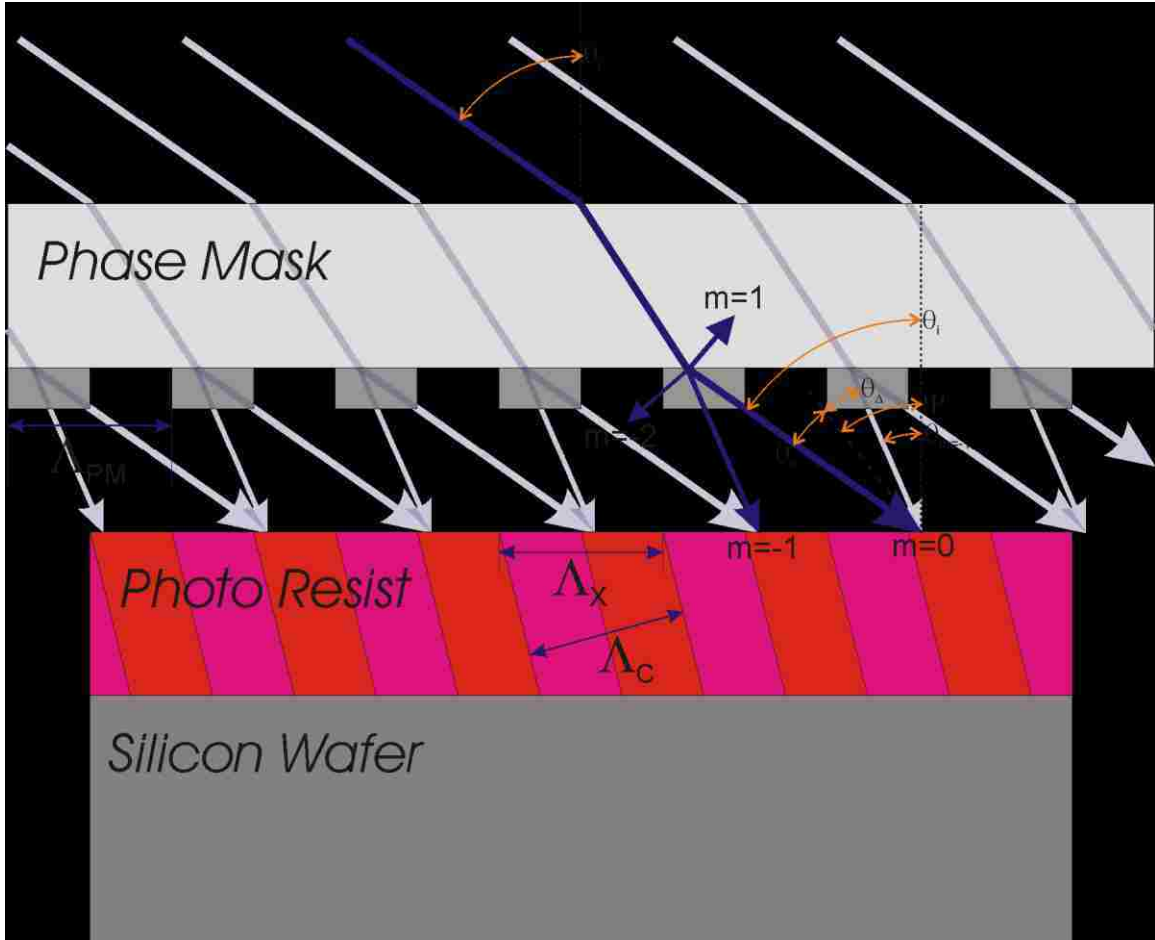


**Figure 36** – Phase mask interferometer, with zero-order and without zero-order.

There can be issues with secondary reflections off the surface of the photoresist that reflect and diffract off the phase mask and back into the sample at undesired angles. This can be reduced or eliminated by using a top anti-reflection coating on the surface of

the photoresist. It can also be eliminated by inserting a lens system between the phase mask and photoresist sample.

The pitch of the pattern in the photoresist is now defined as follows referring to Figure 37 for the definition of the angles and pitches. Figure 22 is also useful to refer to for angle of the beams in air and in the photoresist.



**Figure 37** – Phase mask interferometer with off-axis illumination diagram, used for making PhCs.

$$\theta_{m=0} = \theta_i \quad (3.1)$$

$$\theta_{m=-1} = \sin^{-1} \left[ \sin(\theta_i) - \frac{\lambda}{\Lambda_{PM}} \right] \quad (3.2)$$

$$\theta_{1,PR} = \sin^{-1} \left[ \frac{\sin(\theta_{m=-1})}{n_r} \right] = \sin^{-1} \left[ \frac{\Lambda_{PM} \cdot \sin(\theta_i) - \lambda}{n_r \cdot \Lambda_{PM}} \right] \quad (3.3)$$



$$\theta_{2.PR} = \sin^{-1} \left[ \frac{\sin(\theta_{m=0})}{n_r} \right] = \sin^{-1} \left[ \frac{\sin(\theta_i)}{n_r} \right] \quad (3.4)$$

$$\theta_{\Delta.PR} = \frac{\theta_{2.PR} - \theta_{1.PR}}{2} \quad (3.5)$$

$$\Lambda_C = \frac{\lambda}{2 \cdot n_r \cdot \sin(\theta_{\Delta.PR})} = \frac{1}{2} \cdot \frac{\lambda}{n_r \cdot \sin \left\{ \frac{1}{2} \sin^{-1} \left[ \frac{\sin(\theta_i)}{n_r} \right] - \frac{1}{2} \sin^{-1} \left[ \frac{1}{n_r} \left( \sin(\theta_i) - \frac{\lambda}{\Lambda_{PM}} \right) \right] \right\}} \quad (3.6)$$

$$\Lambda_X = \Lambda_{PM} \quad (3.7)$$

The angle of the tilted photoresist pattern is defined as follows.

$$\theta_c = \frac{\theta_{1.PR} + \theta_{2.PR}}{2} = \frac{1}{2} \cdot \left\{ \sin^{-1} \left[ \frac{\Lambda_{PM} \cdot \sin(\theta_i) - \lambda}{n_r \cdot \Lambda_{PM}} \right] + \sin^{-1} \left[ \frac{\sin(\theta_i)}{n_r} \right] \right\} \quad (3.8)$$

It is more useful to rearrange these equations to determine the strong phase mask pitch ( $\Lambda_{PM}$ ) and off-axis angle of incident illumination ( $\theta_i$ ) for a given photonic crystal pitch ( $\Lambda_C$ ) and crystal angle ( $\theta_c$ ). The following equation gives the definition needed to do such calculations.

$$\theta_{\Delta.PR} = \sin^{-1} \left( \frac{\lambda}{2 \cdot n_r \cdot \Lambda_C} \right) \quad (3.9)$$

$$\theta_{1.PR} = \theta_c - \theta_{\Delta.PR} \quad (3.10)$$

$$\theta_{2.PR} = \theta_c + \theta_{\Delta.PR} \quad (3.11)$$

$$\theta_{m=-1} = \sin^{-1} [n_r \cdot \sin(\theta_{2.PR})] \quad (3.12)$$

$$\theta_i = \sin^{-1} [n_r \cdot \sin(\theta_{1.PR})] \quad (3.13)$$

$$\Lambda_{PM} = \frac{\lambda}{\sin(\theta_i) - \sin(\theta_{m=-1})} \quad (3.14)$$

The photoresist is exposed under the phase mask, and rotated between exposures to carry out the three-dimensional interferometric lithography process.

A issue that arises when doing tilted exposure needed for three-dimensional patterning is that the two beams intercept the photoresist surface at different angles ( $\theta_1 \equiv$

$\theta_1 \neq \theta_2 \equiv \theta_1 - 2\theta_\Delta$ ). Just as in the Fresnel interferometer, this causes an issue with the amount of light transmitted into the photoresist, due to different Fresnel reflection of each beam off the surface of the photoresist. Similarly, the difference between the amounts of electric field amplitude in the photoresist from each beam ( $A_1 - A_2$ ) increases as the offset incident angle ( $\theta_i$ ) increases and as the pitch ( $\Lambda_x$ ) decreases. This in turn causes a reduction in the interference pattern contrast. For three-dimensional photonic crystals where large offset incident angles ( $\theta_i$ ) are desired, the loss of contrast can be problematic. One way to solve this is to adjust the phase shifter thickness to reduce the zero-order intensity so the electric field amplitude in the photoresist from the zero-order and the -1 order is the same ( $A_1 = A_2$ ).

Phase mask interferometric lithography can be done as a proximity lithography process as illustrated in Figure 36 and Figure 37. It can also be done via contact lithography or by using a photolithography stepper. When using a photolithography stepper the two requirements on the stepper are 1) the ability to do off-axis monopole illumination of the phase mask, and 2) a high enough numerical aperture ( $NA = \sin\theta$ ) to allow both the high angle zero-order and -1 order to pass through the lens system ( $NA_{stepper} \geq \sin\theta_{m=0}$ ).

One issue with phase-shift masks is that they are very costly to make due to the patterning of an additional shifter layer and the tight tolerances of the shifter layer thickness across the mask. In addition a different mask may need to be fabricated for each exposure in the multiple-exposure interferometric lithography process, especially if used on a photolithography stepper. It is not necessary if the exposure tool can rotate the

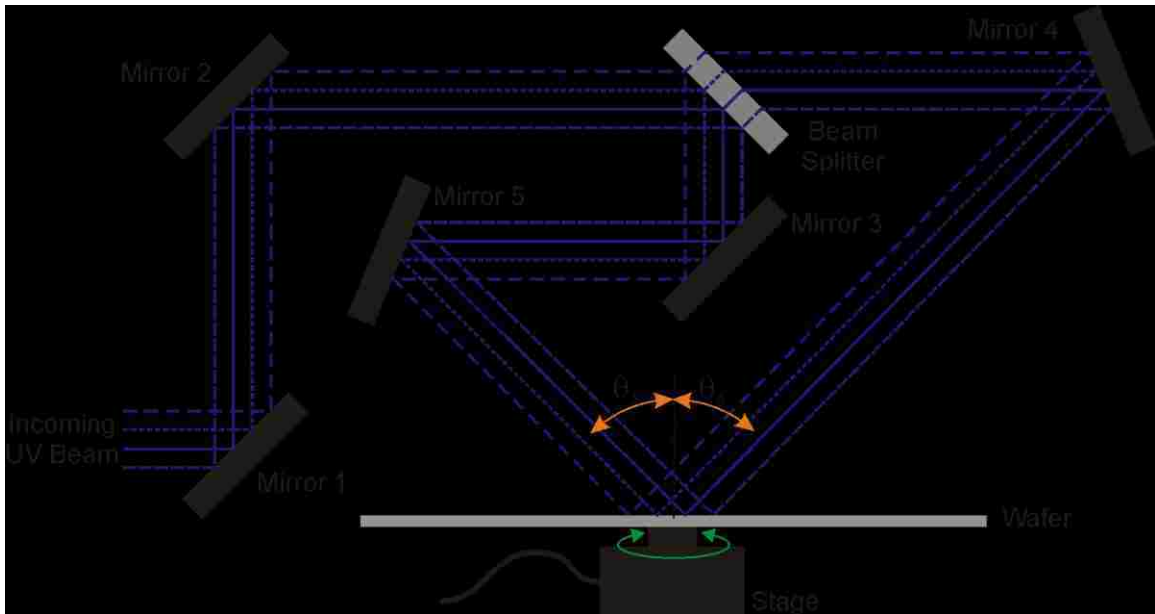
wafer between exposures and adjust the masking of the exposure field to match the rotated field on the wafer; however this is normally not the case for most commercial lithography exposure tools, which have a very limited wafer rotation capability. Plus different masks are needed for each lithography pitch desired.

## **Michelson Interferometer**

The Michelson interferometer is the final exposure setup to be considered, and the interferometer used for the rest of this dissertation. The Michelson interferometer is the most complex of the three interferometer setups examined. The Michelson interferometer uses a 50/50 beamsplitter to split an exposing beam into two beams of equal intensity. The two beams are reflected off mirrors and onto an exposure stage. The mirrors are placed appropriately for the needed exposure angles and path lengths. Figure 38 shows an illustration of a Michelson interferometer typically used for one-dimensional and two-dimensional interferometric lithography. In this interferometer the angle of the two beams are set to  $\theta_\Delta = \theta_1 = -\theta_2$ . The period of the grating exposed in the photoresist is given by  $\Lambda = \frac{\lambda}{2 \cdot n \cdot \sin(\theta_\Delta)}$  ( $n = 1$  for exposure in air).

One of the main advantages of the Michelson interferometer is that the beamsplitter and mirror 3 in Figure 38 can be moved left or right such that the path length of beam 1 is equal to the path length of beam 2. Having the same path length of both beams maximizes the interference pattern contrast and allows a large exposure area even when using a laser with a short temporal coherence. The incoming beam is split in such a way that the two exposure beams overlay each other with the same orientation, in other words the same photon that was split at the beamsplitter interferes with itself at the

exposure plane. This is very useful for making large exposure areas even if the light source has a small transverse coherence, such as is the case with an eximer laser.

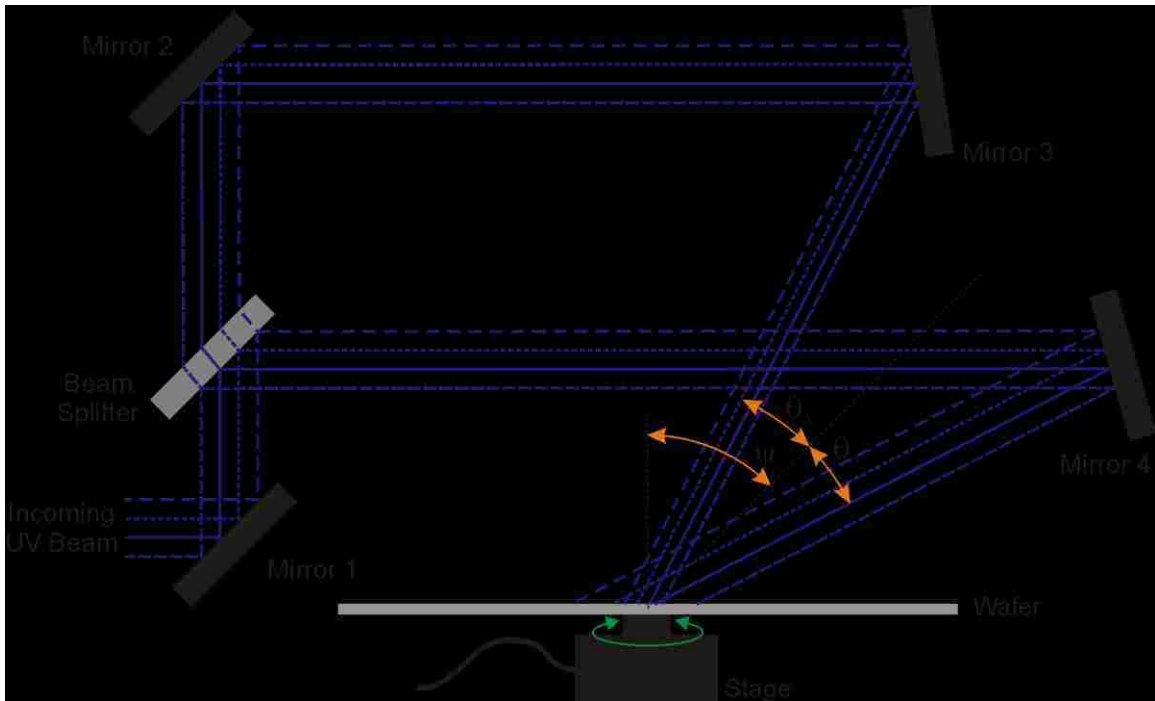


**Figure 38** – Standard Michelson interferometric lithography setup.

One of the main disadvantages of the Michelson interferometer is that each time the pitch is changed the beamsplitter and mirrors need to be moved and realigned. Another issue stems from the fact that the optical path lengths are relatively large compared to the previous two interferometer setups. The requirement of all the optics to be stable during the exposure becomes exponentially harder to maintain as the optical path lengths increases. It is necessary that there are no vibrations among any of the optical mounts, or air turbulence in the beam paths during the exposure. Care must be taken to ensure that this is the case, either by the use of good optical mounting design or short exposure time or a combination of both.

For three-dimensional structures there is the need to offset the two incident beams from normal. This is quite straightforward for the Michelson interferometric lithography

setup. The mirrors need to be rearranged in a fashion that has the two beams offset from the normal to the exposure plane, as is seen in Figure 39.



**Figure 39** – Michelson interferometric lithography setup with off-axis illumination, used for making PhCs.

The mirror 2 and mirror 3 in Figure 38 can be moved up or down such that the path length of beam 1 is equal to the path length of beam 2. The pitch of the photoresist pattern and angle of the interference pattern in the photoresist is given in equation 2.33 to equation 2.41 on page 45.

An issue when tilting the exposure beams off-axis from the normal to the exposure plane, is that the exposure area of each beam is not the same in the grating direction. This can be seen in Figure 39, as the beam off mirror 4 exposes a wider part of the wafer compared to the beam off mirror 3. An aperture right at the exposure plane can be used to block the unwanted non-overlapping portions of exposure light. There still exists the issue that the interference contrast of the two beams could be reduced, if the

mismatch of the two beams exceeds the light source spatial (transverse) coherence. A pair of cylindrical lenses can be used in the second beam path, to shrink the beam in the one dimension by the necessary amount to match the first beam. This will prevent unwanted exposure from non-overlap beams and ensure high contrast interference by maintaining spatial overlay.

## Beam Intensity Ratio Control

The intensity of the beam off of mirror 4 in Figure 39 always needs to be larger than the intensity of the beam off of mirror 3. To determine the amount to reduce the first beam, it is necessary to calculate the power reflected off of the photoresist and transmitted power into the photoresist from each beam. This is accomplished with the following equations for s-polarized light (TE polarization),  $R$  being the percent reflected power and  $T$  being the percent transmitted power.

$$R_{s.1} = \frac{\sin^2(\theta_{1.air} - \theta_{1.PR})}{\sin^2(\theta_{1.air} + \theta_{1.PR})} = \frac{\sin^2\left\{\theta_i - \theta_\Delta - \sin^{-1}\left[\frac{\sin(\theta_i - \theta_\Delta)}{n_r}\right]\right\}}{\sin^2\left\{\theta_i - \theta_\Delta + \sin^{-1}\left[\frac{\sin(\theta_i - \theta_\Delta)}{n_r}\right]\right\}} \quad (3.15)$$

$$R_{s.2} = \frac{\sin^2(\theta_{2.air} - \theta_{2.PR})}{\sin^2(\theta_{2.air} + \theta_{2.PR})} = \frac{\sin^2\left\{\theta_i + \theta_\Delta - \sin^{-1}\left[\frac{\sin(\theta_i + \theta_\Delta)}{n_r}\right]\right\}}{\sin^2\left\{\theta_i + \theta_\Delta + \sin^{-1}\left[\frac{\sin(\theta_i + \theta_\Delta)}{n_r}\right]\right\}} \quad (3.16)$$

$$T_{s.1} = 1 - R_{s.1} \quad (3.17)$$

$$T_{s.2} = 1 - R_{s.2} \quad (3.18)$$

The power in the first beam needs to be reduced by the ratio of the two transmitted powers from each beam into the photoresist.

$$P_1 = \frac{T_{s.2}}{T_{s.1}} \% \quad P_2 = 100\% \quad (3.19)$$

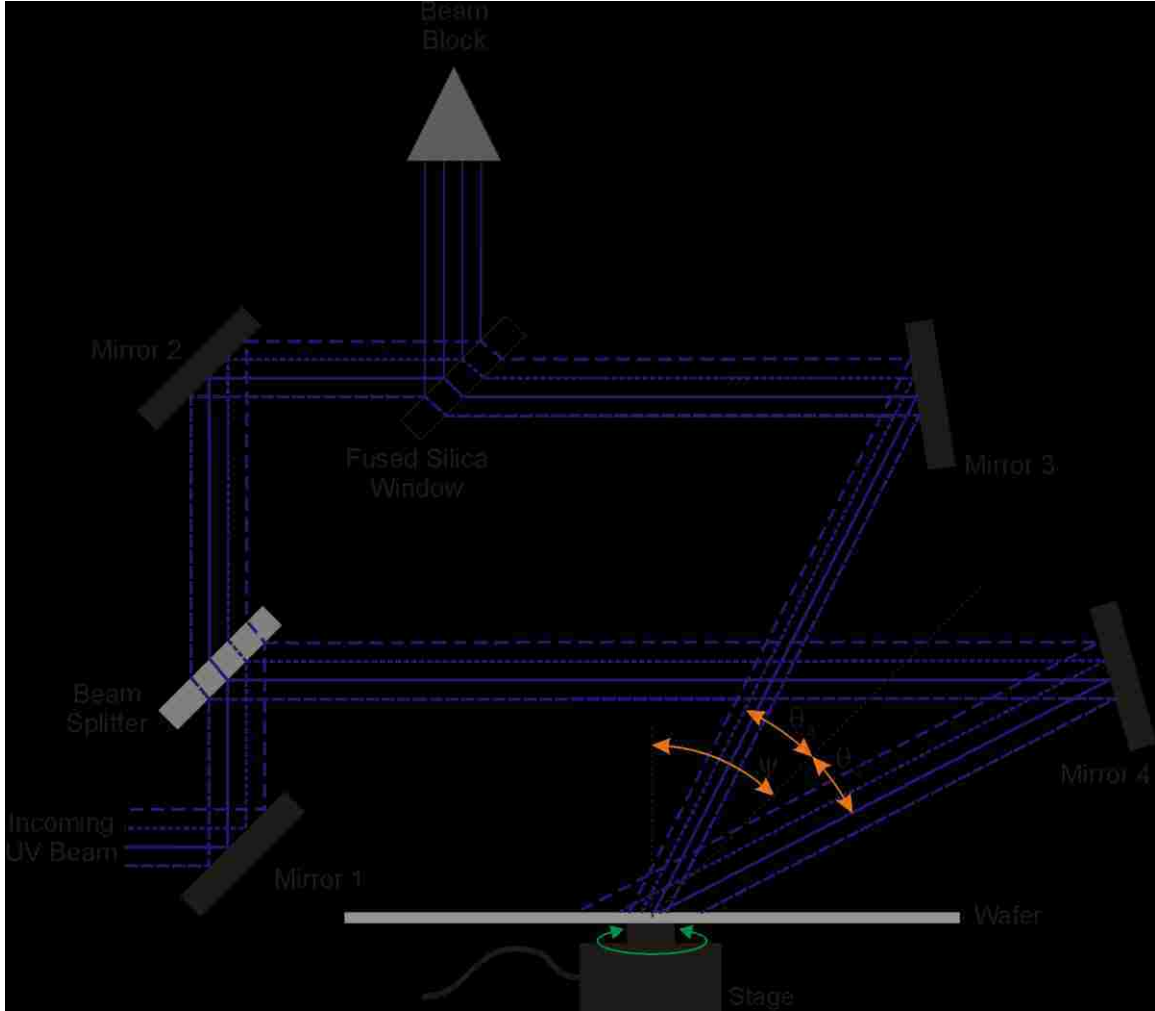
This causes the reduced power of the first beam to have the same transmitted power into the photoresist as the second beam does.

$$P_{1.PR} \equiv P_1 \cdot T_{s.1} = P_{2.PR} \equiv P_2 \cdot T_{s.2} \quad (3.20)$$

This can be achieved in several ways or a combination of them. The simplest method is to use a beamsplitter with the correct ratio needed for each beam. However the beamsplitter with such a ratio may not exist, or be very costly to manufacture.

The next method uses mirrors with a lower reflection for mirror 2 and mirror 3 than that of mirror 4. If the right set of mirrors are used, than the correct ratio can be achieved. However, given the problem of requiring the correct ratio of reflections, the mirrors needed for such a ratio may not exist. Also mirrors with lower reflection absorb some of the light, which can cause unwanted thermal changes to the mirrors during exposure.

Another method uses a fused silica window placed in the path of the first beam at an angle. A small amount of light reflects off the surface of the window due to Fresnel reflection. By adjusting the angle of the window the amount of light reflected is changed. Figure 40 show the Michelson interferometric lithography setup with the Fresnel reflection window.



**Figure 40** – Michelson interferometric lithography setup with off-axis illumination, and beam intensity ratio compensator. This setup allows for matching the beam intensities in the photoresist.

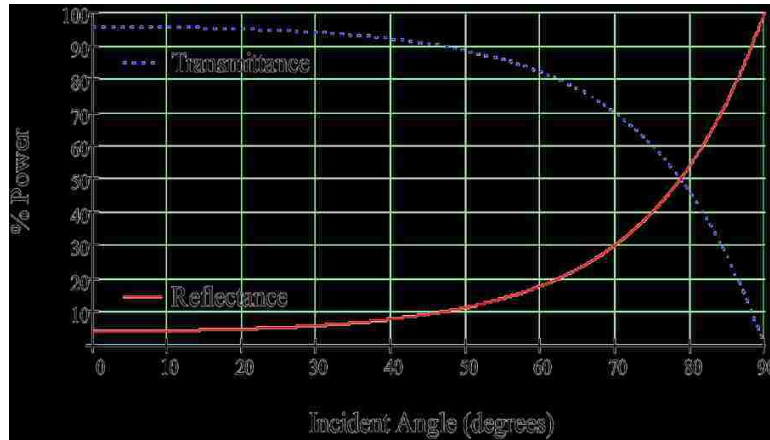
The following equations give the reflected and transmitted power of s-polarized light off the front surface of the window with an incident angle  $\theta_i$  and an index of refraction  $n_w$ .

$$R_{s,1} = \frac{\sin^2(\theta_{1,air} - \theta_{1,w})}{\sin^2(\theta_{1,air} + \theta_{1,w})} = \frac{\sin^2\left\{\theta_i - \sin^{-1}\left[\frac{\sin(\theta_i)}{n_w}\right]\right\}}{\sin^2\left\{\theta_i + \sin^{-1}\left[\frac{\sin(\theta_i)}{n_w}\right]\right\}} \quad (3.21)$$

$$T_s = 1 - R_s$$



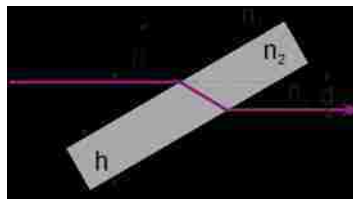
Figure 41 is a plot of the transmittance and reflectance off the front surface of a window as a function of the incident angle. The reflectance does not become large until relatively large incident angles are approached. This requires a very large window, which might not be practical. But using this Fresnel reflection window in conjunction with one of the previous methods allows for fine control of the beam power.



**Figure 41** – Reflectance and transmittance off a window surface with an index of refraction  $n_w = 1.5$

The window also displaces the beam. The amount of the displacement  $d$  is given by the following equation, and is determined by the thickness  $h$ , index of refraction  $n_2$ , and angle  $\theta$  of the window relative to the beam path.

$$d = h \cdot \sin(\theta) \cdot \left[ 1 - \frac{\cos(\theta)}{\sqrt{\left(\frac{n_1}{n_2}\right)^2 - \sin^2(\theta)}} \right] \quad (3.22)$$



**Figure 42** – Beam displacement from an optical flat window.

The window should have an anti-reflective (AR) coating on the backside to prevent unwanted interference pattern in the beam from secondary reflections off the backside of the window. A better method is to use a window with a small wedge (1° - 3°) between the front and back surfaces. This prevents any unwanted secondary reflections from interfering with the primary beam. It is also recommended to use a beamsplitter on a wedged flat for the same reason.

## Stage Control

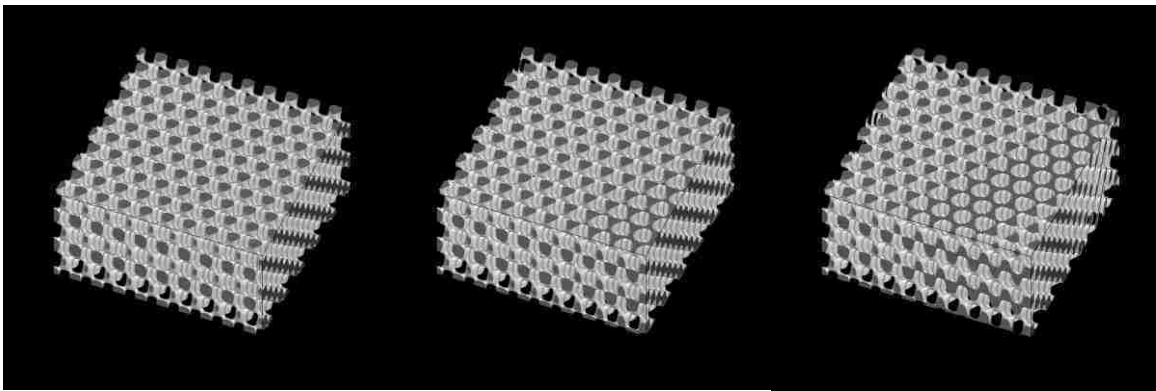
The rotation of the exposure stage between exposures needs to be tightly controlled in three-dimensional interferometric lithography. If the rotation is off there is a phase variation along the crystal planes, the same is true for tilt variations. The greater the rotation is off, the larger the phase variation is. This will cause a moiré affect on the surface of the photonic crystal, which can be seen from the simulations in Figure 43. The plotted top surface of the photonic crystal is only 10 μm on a side, and with just a 1° error of rotation it can be seen the phase of the crystal at the top left corner is different than the phase at the bottom right corner. And with a 2° error there is a full phase cycle across every 12.9 μm length of the crystal surface. The pitch of the moiré ( $\Lambda_{m,\alpha}$ ) can be calculated if the crystal pitch ( $\Lambda_x$ ) and angle error ( $\alpha$ ) is known by the following equation:

$$\Lambda_{m,\alpha} = \frac{1}{2} \cdot \sqrt{\frac{-2\Lambda_x^2}{\cos \alpha - 1}} \quad (3.23)$$

By rearranging the equation the maximum error in the rotation angle ( $\alpha$ ) allowed can be determined by knowing the crystal pitch ( $\Lambda_x$ ) and setting the minimum moiré pitch ( $\Lambda_{m,\alpha}$ ) using the following equation.

$$\alpha = \cos^{-1} \left( \frac{2 \cdot \Lambda_{m,\alpha}^2 - \Lambda_x^2}{2 \cdot \Lambda_{m,\alpha}^2} \right) \quad (3.24)$$

If a photonic crystal has a 1  $\mu\text{m}$  pitch and the minimum moiré pitch of 1 cm is desired then the rotation accuracy between exposures needs to be better than 0.0029°.



**Figure 43** – Phase errors along the photonic crystal due to rotation misalignment.

The use of high precision rotation stages commercially available should allow for accuracies needed for large area exposures. It is recommended to use a high precision stepper motor driven stage, or even better is a motorized rotation stage with an optical encoder feedback. The Michelson interferometric lithography setup used in this dissertation has a Newport URM-80A-CCHL rotation stage with 0.001° accuracy, and does not utilize any other method of rotational feedback. A 0.001° accuracy corresponds to a full moiré fringe every 5.145 cm.

## Phase Control

One very stringent requirement for three-dimensional interferometric lithography is that phase of the intensity pattern created by the interference beams between each exposure needs to be tightly controlled, as was stated in Chapter 2. This is accomplished by stringently controlling the rotation between exposure, the incident angle of each exposure, and the Z-position of the exposure plane of each exposure. The rotation control has already been discussed, deviations in the incident angle or exposure plane between exposures result in similar phase variations. A deviation in the exposure plane angle is the same as a deviation in the angle  $\Psi$  (the intercept between the two exposing beams to the normal of the exposure plane). Therefore the tilt error angle ( $\delta\Psi$ ) cause a change in the exposure pitch. The moiré pitch ( $\Lambda_{m,\delta\Psi}$ ) results from the phase variation of the two different exposure pitches. The pitch of the moiré ( $\Lambda_{m,\delta\Psi}$ ) is calculated by the following equations:

$$\Lambda_{m,\delta\Psi} = \frac{2\Lambda_1\Lambda_2}{\Lambda_2 - \Lambda_1} = \frac{2\lambda}{\sin(\Psi + \theta_\Delta) - \sin(\Psi - \theta_\Delta) - \sin(\Psi + \theta_\Delta + \delta\Psi) + \sin(\Psi - \theta_\Delta + \delta\Psi)} \quad (3.25)$$

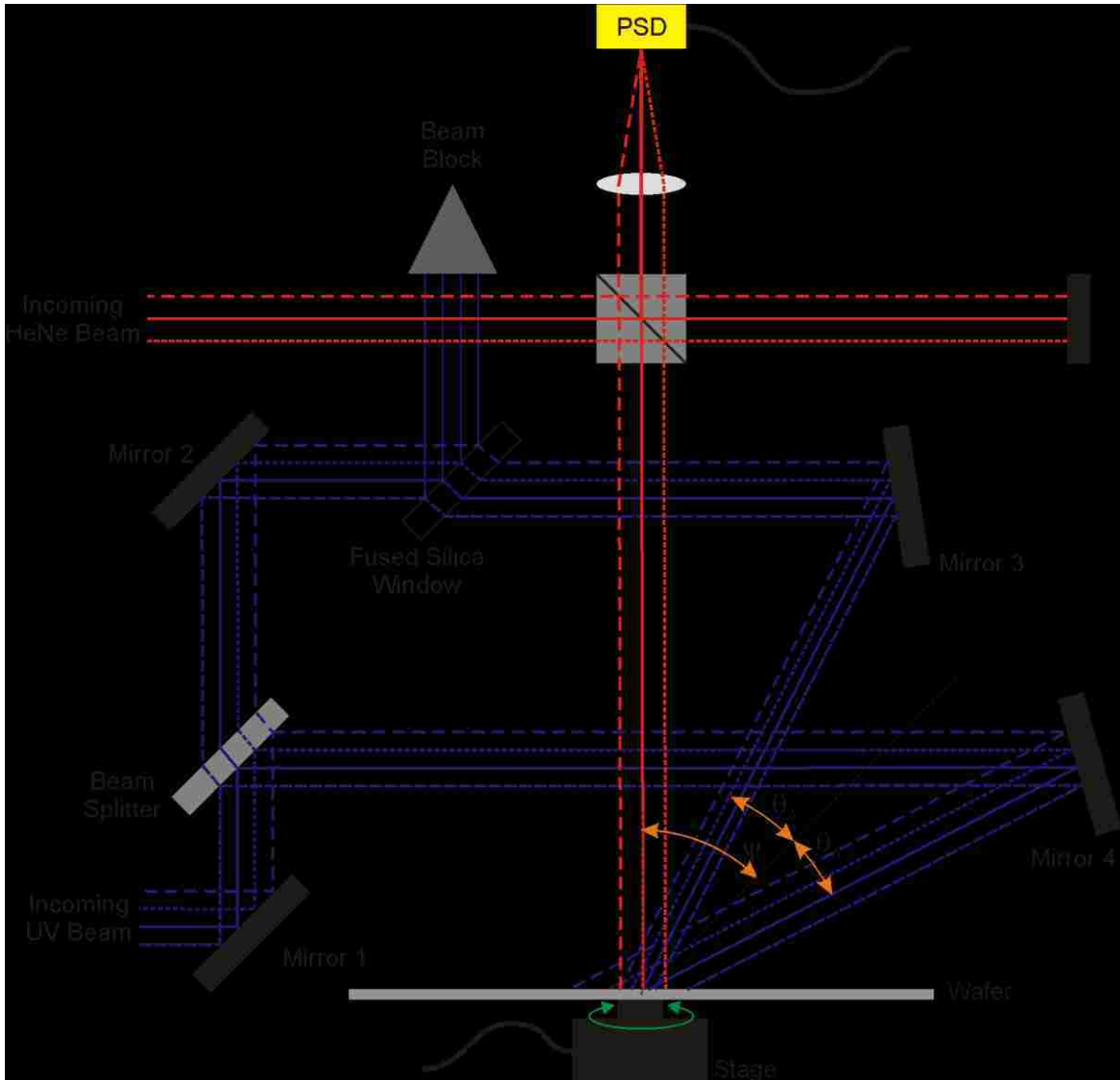
By rearranging the equation the maximum error in the tilt angle ( $\delta\Psi$ ) allowed can be determined by knowing the exposure wavelength ( $\lambda$ ), angles  $\Psi$ , angle  $\theta_\Delta$ , and setting the minimum moiré pitch ( $\Lambda_{m,\delta\Psi}$ ) using the following equation.

$$\delta\Psi = \cos^{-1} \left( \frac{\Lambda_{m,\delta\Psi} \cdot \sin \theta_\Delta \cdot \cos \Psi - \lambda}{\Lambda_{m,\delta\Psi} \cdot \sin \theta_\Delta} \right) - \Psi \quad (3.26)$$

For the photonic crystal experimentally made in this dissertation to have a minimum moiré pitch of 1 cm then the tilt accuracy between exposures needs to be better than  $0.035^\circ$ .

A second interferometer is used to monitor the incident angle and Z-height of the exposure plane for each exposure, and to provide feedback to control the exposure plane. When the wafer stage is level to the monitoring interferometer a spherical phase front zero-order centered fringe pattern is formed, similar to a bull's-eye mark. As tilt is introduced into the wafer stage the center fringe moves and the number of rings in the fringe pattern increases accordingly, until the center fringe moves out of the beam path and only parts of many rings are seen. As the wafer stage moves up and down in the z-direction the center zero-order fringe will undergo a sinusoidal change from light to dark.

By using an interferometer with one leg perpendicular to the exposure plane, it is possible to detect in real time any angular or displacement of the exposure plane to within submicron accuracy. Even on the best rotation stages during rotation there can still be a few arc minutes of angular deviation and microns of vertical displacement. Such a feedback phase control interferometer used in conjunction with a Michelson interferometric lithography setup is shown in Figure 44.



**Figure 44** – Michelson interferometric lithography setup with off-axis illumination, beam intensity ratio compensator and phase control interferometer. Complete setup necessary for making PhCs.

The interferometer has a reference leg with an optically flat stationary reference mirror, and a measurement leg with the exposure substrate or wafer as the measurement mirror. A lens on the output leg of the interferometer is used to create interference Haidinger fringes<sup>26</sup> focused onto a two-dimensional Position Sensitive Detector (PSD) used to measure the angular deviation and vertical displacement of the exposure substrate.

A HeNe laser is used as the light source for the phase control interferometer. The HeNe laser wavelength is sufficiently long that a UV sensitive photoresist is not exposed by the HeNe light. This is important as the HeNe light is propagating through the photoresist and reflected off the exposure substrate.

Pico-motors or piezo-motors on the stage that hold the exposure substrate, which is connected on top of the rotation stage, can be used to correct any angular and vertical displacement. By using the interferometer in a feedback loop to the motors on the stage it is possible to maintain the incident angle via holding the zero-order fringe on the center of the PSD and exposure plane height constant via keeping the zero-order fringe at max intensity during rotation and between all exposures, to the accuracy of the interferometer and motors.

This Michelson interferometric lithography setup illustrated in Figure 44 was used for all of the exposures discussed in the rest of this dissertation. A photograph of the experimental photonic crystal Michelson interferometric lithography setup used for this dissertation is shown in Figure 45. Some of the important optical components and angles are labeled, the transparent blue line represents the UV exposing beam, and the transparent red line represents the HeNe alignment beam.

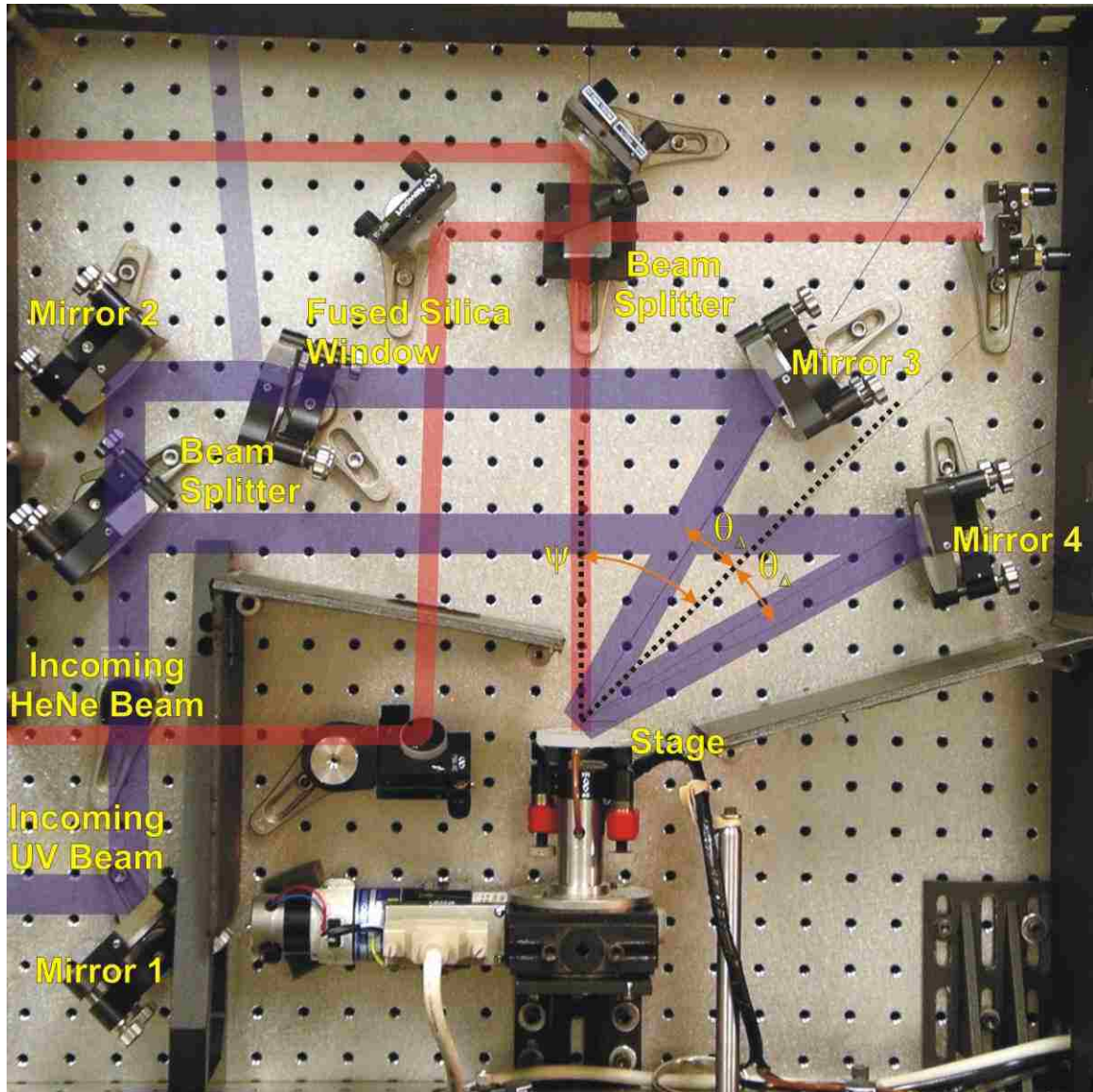


Figure 45 – Experimental PhC Michelson interferometric lithography setup.

### ***3D Photonic Crystal Photoresist Profile Models***

This section examines models of the photoresist profiles of the three-dimensional photonic crystals that are made using this Michelson interferometric lithography setup. The modeling is performed using a MATLAB program based on equation 2.32 found on Page 42, for which the MATLAB source code M-file is given in Appendix B. These



models generate three-dimensional plots of the photoresist profiles, which are used to compare to Scanning Electron Microscope (SEM) images of actual three-dimensional photonic crystals experimentally produced.

The model assumes negative tone photoresist but can be applied to both positive and negative tone photoresist if the photoresist has small absorption through the thickness of the photoresist. The same three-dimensional photonic crystal structure are produced for both positive tone and negative tone photoresist if the exposure dose is set correctly, and the photoresist has no absorption at the exposure wavelength. The model however does take into account the photoresist absorption. To make the model valid for positive tone photoresist the output values of the Heaviside function  $\Phi$  need to be reversed.

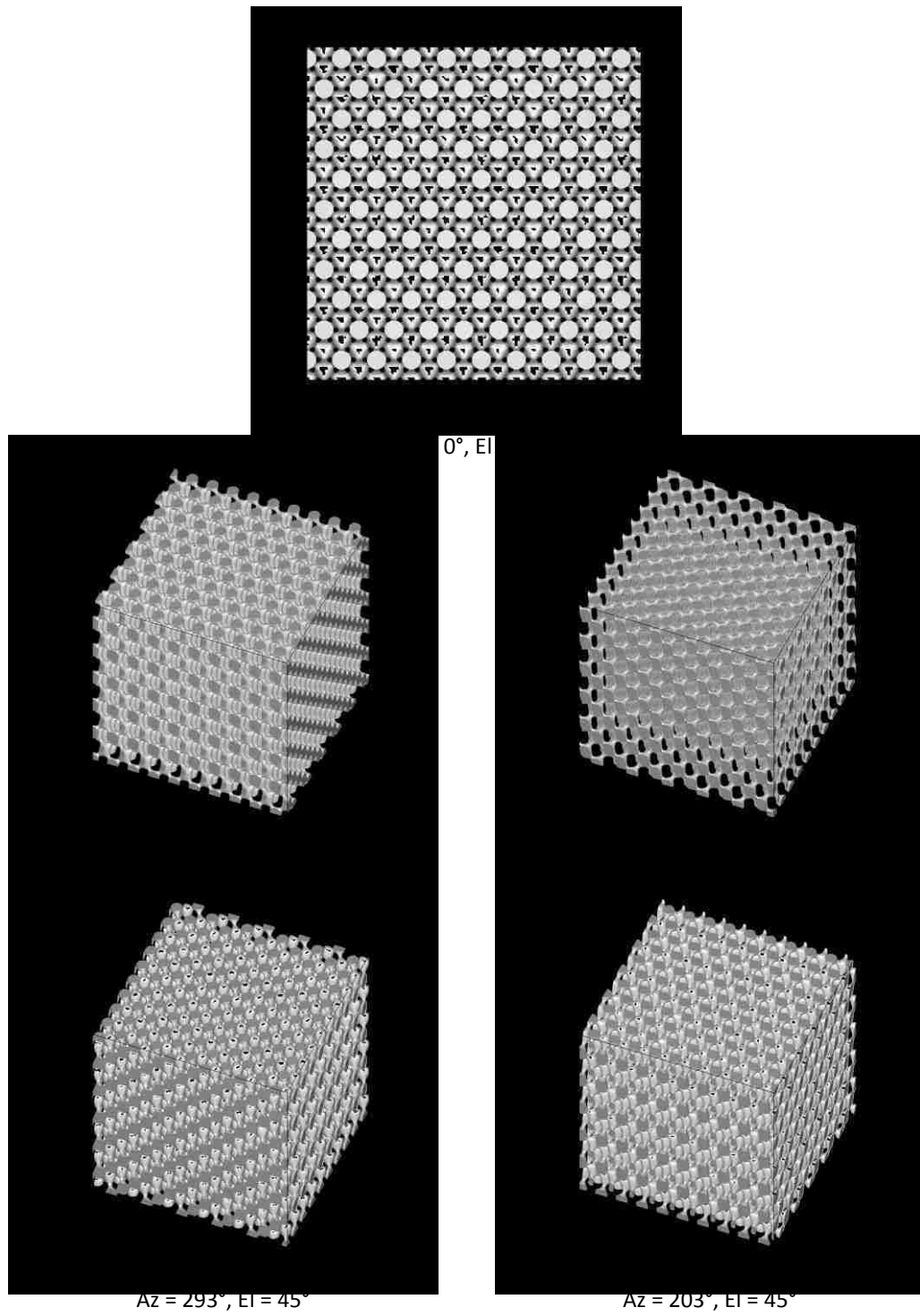
### **Three Exposures (120° rotation)**

The first case to look at is three-dimensional photonic crystal made by three separate two-beam exposures with 120° rotation between exposures. The input parameters for the model are given in Table 1.

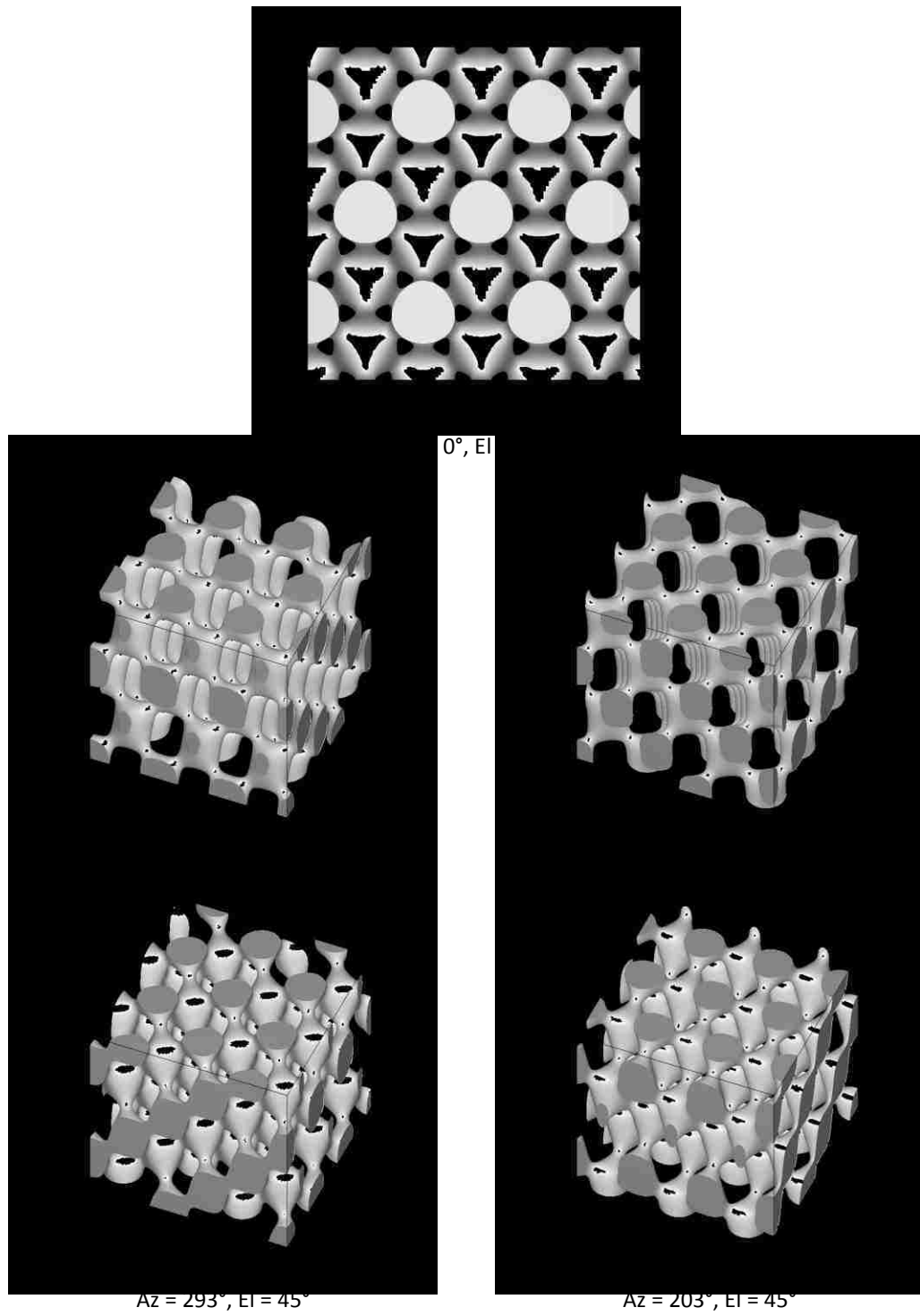
<b>Description</b>	<b>Label</b>	<b>Value</b>
Vacuum wavelength - $\lambda$ (nm)	lambda	355
Index of photoresist - $n_r$	n	1.7
Polarization Angle – $\vartheta$ (deg)	theta_pol	0
The delta angle of the exposing beam from the crystal angle in the photoresist - $\theta_{\Delta PR}$ (deg)	theta_del	7.458
Crystal angle in the photoresist - $\psi_c$ (deg)	psi_c	26.348
The angle rotation between exposures - $\phi_{\Delta}$ (deg)	phi_del	120
The phase shift between exposures - $\delta$ (deg)	phase	0
The number of separate exposures needed to make the crystal - $n$	n_exp	3
The photoresist exposure threshold - <i>ResistThreshold</i>	threshold	0.62
Set the delta between axes tick marks (nm)	tick_del	2000 & 500
Set the output array size in the X direction	array_size_X	128
Set the output array size in the Y direction	array_size_Y	128
Set the output array size in the Z direction	array_size_Z	128
X model region size (nm)	max_x	10000 & 3000
Y model region size (nm)	max_y	10000 & 3000
Z model region size (nm)	max_z	10352 & 3000

**Table 1** – Modeling parameters for a 3-exposure 3D photonic crystal

The results of the model are seen in Figure 46, with close up views in Figure 47.



**Figure 46** – Models of 3D photonic crystal, made using 3-exposure interferometric lithography.



**Figure 47** – Close up of 3D photonic crystal models, made using 3-exposure interferometric lithography.

The hexagonal symmetry of the surface <111> plane of the photonic crystal is clearly seen.

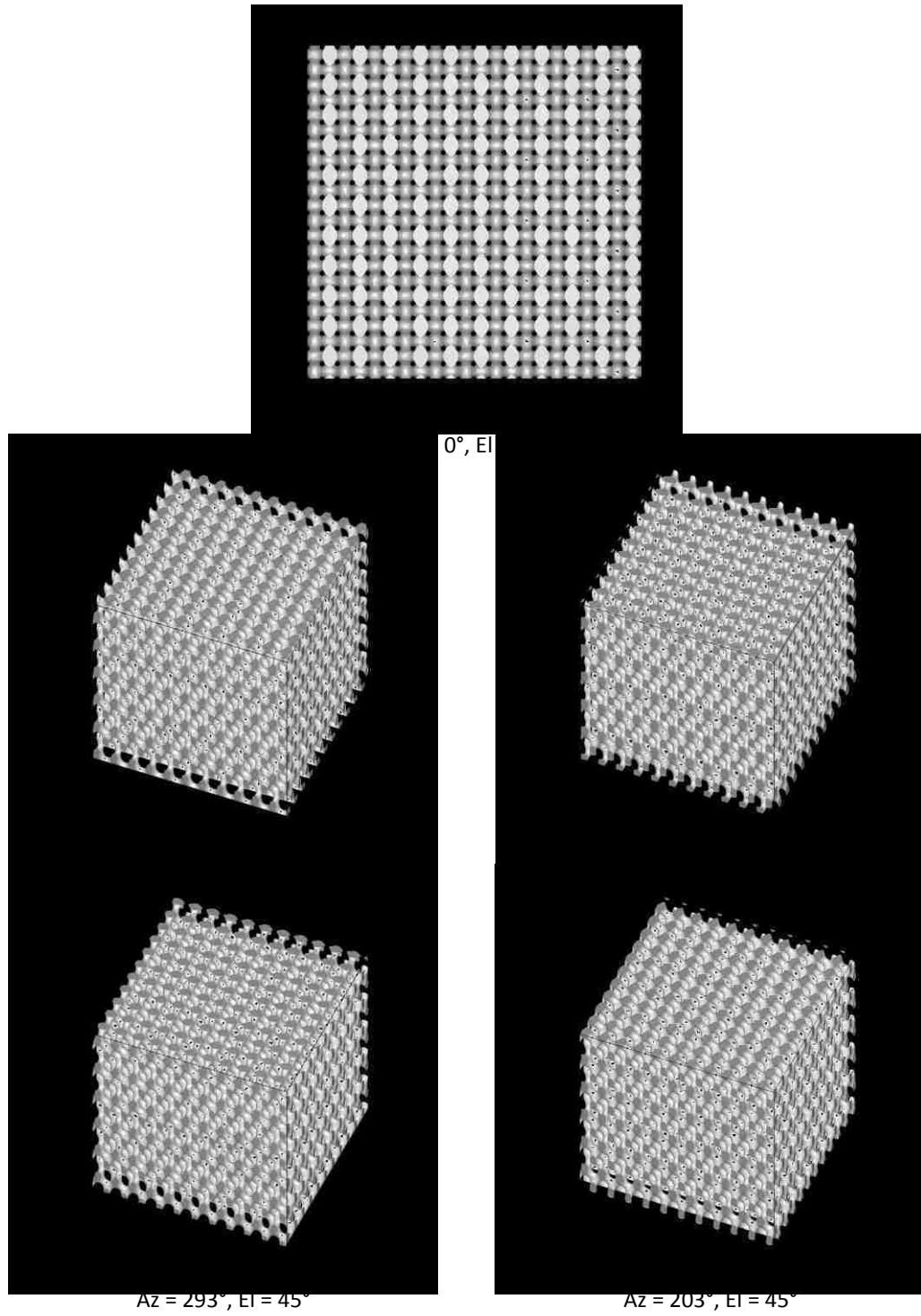
### Four Exposures (90° rotation)

The next case to look at is three-dimensional photonic crystal made by four separate two-beam exposures with 90° rotation between exposures. There is a phase shift of  $\pi/2$  between each exposure. The input parameters for the model are given in Table 2.

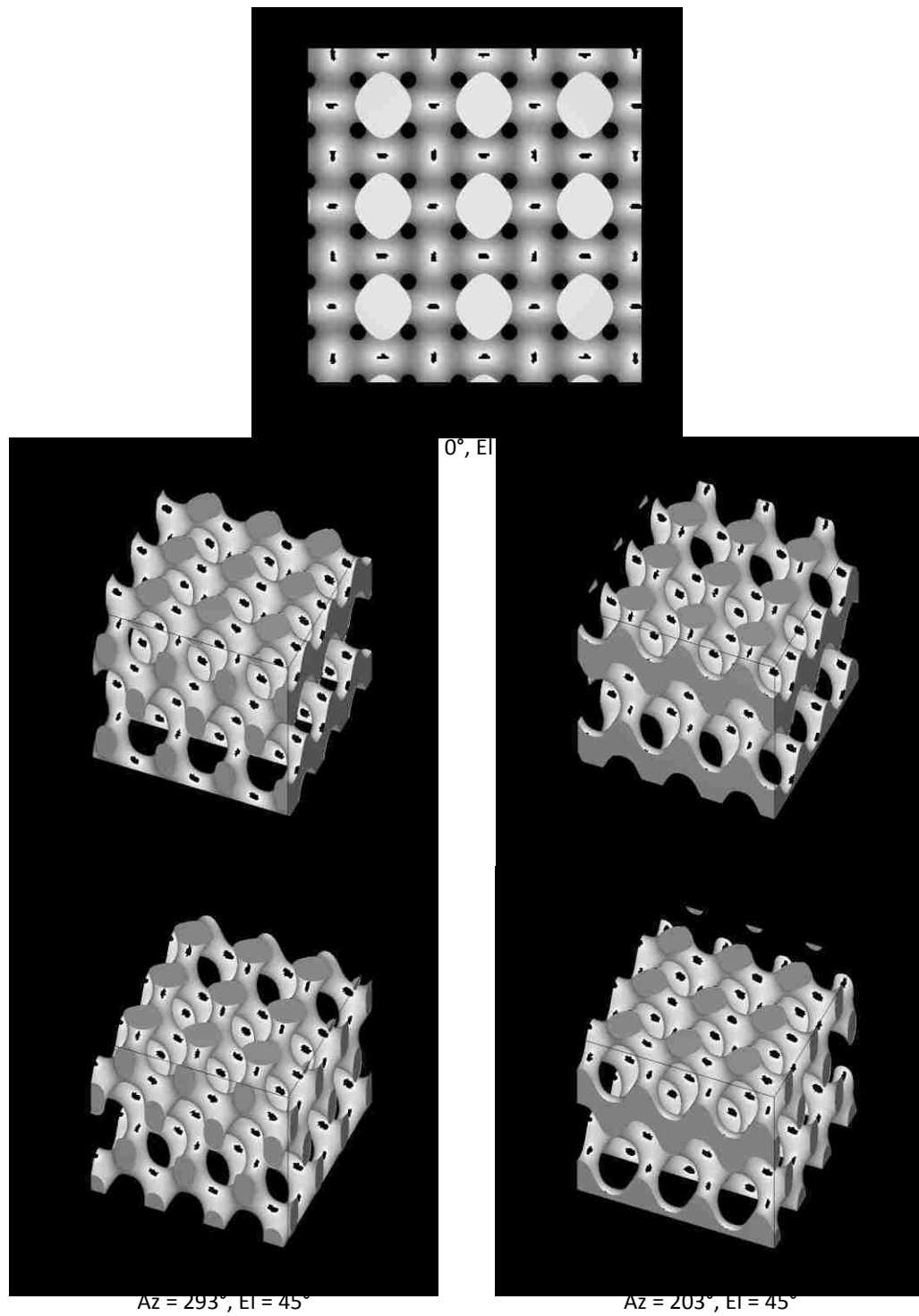
Description	Label	Value
Vacuum wavelength - $\lambda$ (nm)	lambda	355
Index of photoresist - $n_r$	n	1.7
Polarization Angle – $\vartheta$ (deg)	theta_pol	0
The delta angle of the exposing beam from the crystal angle in the photoresist - $\theta_{\Delta PR}$ (deg)	theta_del	7.458
Crystal angle in the photoresist - $\psi_c$ (deg)	psi_c	26.348
The angle rotation between exposures - $\phi_{\Delta}$ (deg)	phi_del	90
The phase shift between exposures - $\delta$ (deg)	phase	pi/2
The number of separate exposures needed to make the crystal - $n$	n_exp	4
The photoresist exposure threshold - <i>ResistThreshold</i>	threshold	0.62
Set the delta between axes tick marks (nm)	tick_del	2000 & 500
Set the output array size in the X direction	array_size_X	128
Set the output array size in the Y direction	array_size_Y	128
Set the output array size in the Z direction	array_size_Z	128
X model region size (nm)	max_x	10000 & 3000
Y model region size (nm)	max_y	10000 & 3000
Z model region size (nm)	max_z	10352 & 3000

**Table 2** – Modeling parameters for a 4-exposure 3D photonic crystal

The results of the model are seen in Figure 48, with close up views in Figure 49.



**Figure 48** – Models of 3D photonic crystal, made using 4-exposure interferometric lithography.



**Figure 49** – Close up of 3D photonic crystal models, made using 4-exposure interferometric lithography.

The square symmetry of the surface <100> plane of the photonic crystal can be seen. The rods in the photonic crystal structure take the shape of a saddle connecting the nodes. Therefore the  $z$  cut-plane will show ovals in the  $x$ -direction, to circles at a node center, to ovals in the  $y$ -direction as the  $z$  cut-plane traverses the  $z$ -direction.

### Six Exposures (60° rotation)

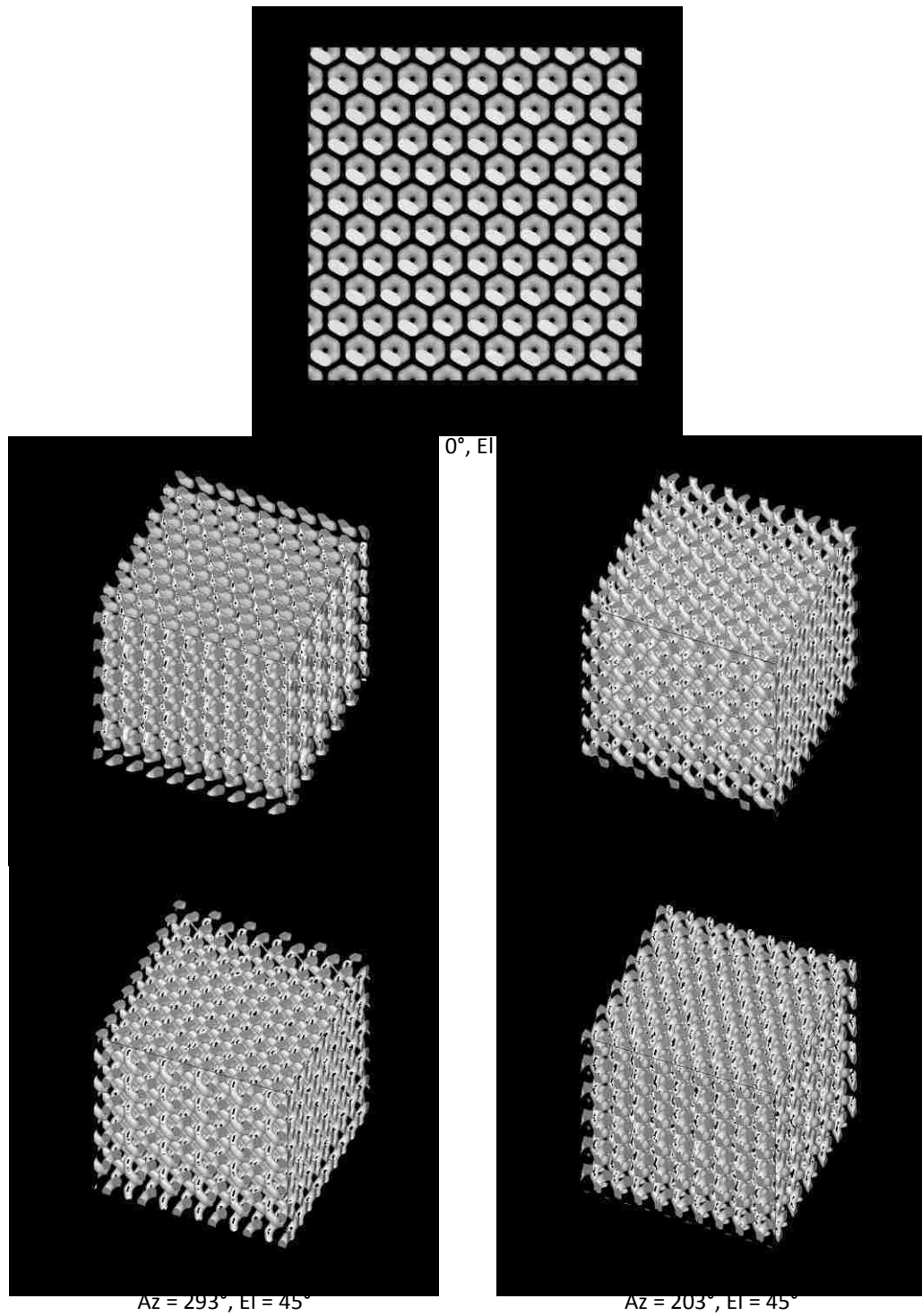
The last case to examine is three-dimensional photonic crystal made by six separate two-beam exposures with 60° rotation between exposures. There is a phase shift of  $\pi/3$  between each exposure. The input parameters for the model are given in Table 3.

Description	Label	Value
Vacuum wavelength - $\lambda$ (nm)	lambda	355
Index of photoresist - $n_r$	n	1.7
Polarization Angle - $\vartheta$ (deg)	theta_pol	0
The delta angle of the exposing beam from the crystal angle in the photoresist - $\theta_{\Delta PR}$ (deg)	theta_del	7.458
Crystal angle in the photoresist - $\psi_c$ (deg)	psi_c	26.348
The angle rotation between exposures - $\phi_A$ (deg)	phi_del	60
The phase shift between exposures - $\delta$ (deg)	phase	pi/3
The number of separate exposures needed to make the crystal - $n$	n_exp	6
The photoresist exposure threshold - <i>ResistThreshold</i>	threshold	0.62 & 0.38
Set the delta between axes tick marks (nm)	tick_del	2000 & 500
Set the output array size in the X direction	array_size_X	128
Set the output array size in the Y direction	array_size_Y	128
Set the output array size in the Z direction	array_size_Z	128
X model region size (nm)	max_x	10000 & 3000
Y model region size (nm)	max_y	10000 & 3000
Z model region size (nm)	max_z	10352 & 3000

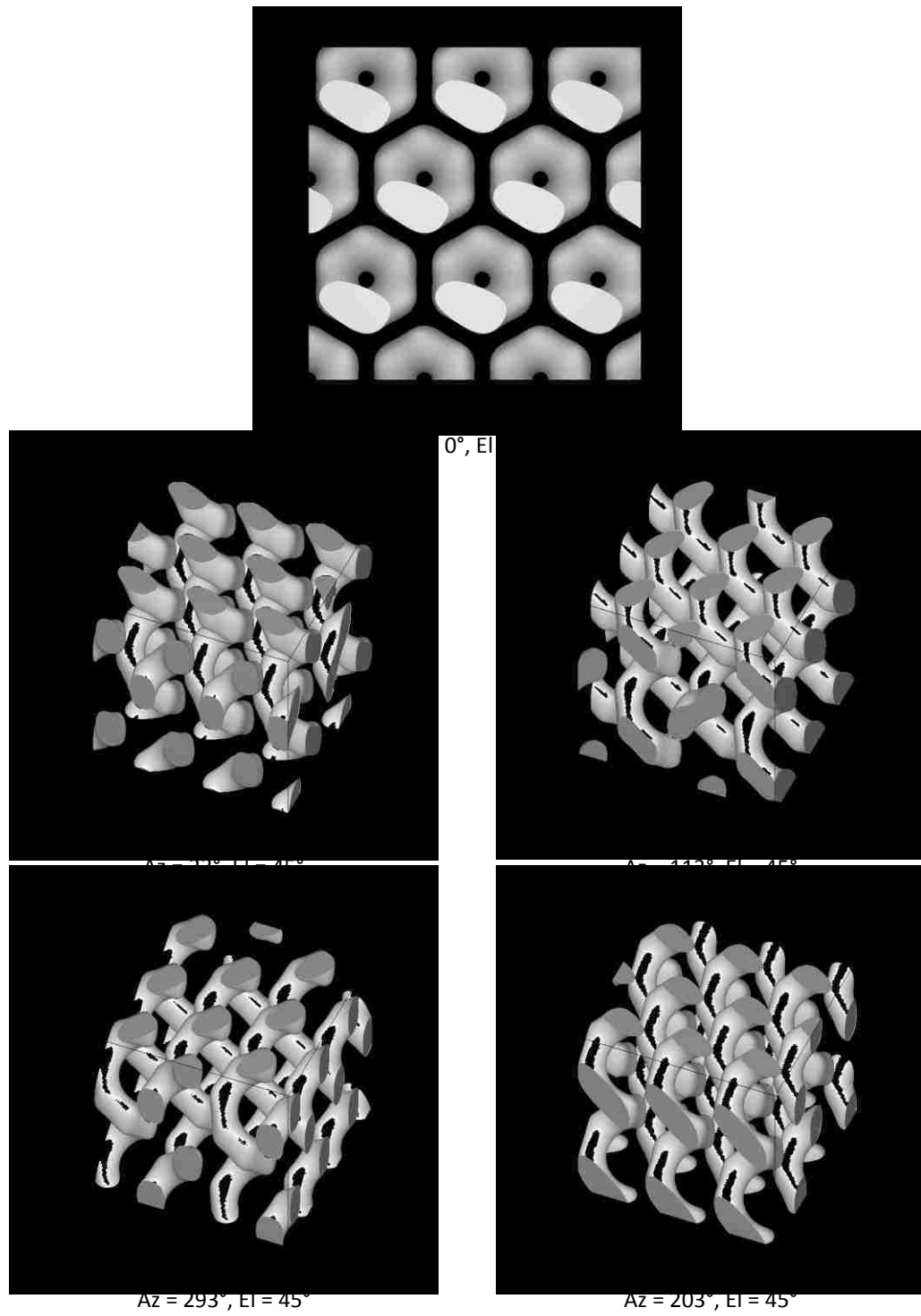
**Table 3** – Modeling parameters for a 6-exposure 3D photonic crystal

The results of the model with a photoresist exposure resist threshold of 62% are seen in Figure 50, with close up views in Figure 51.



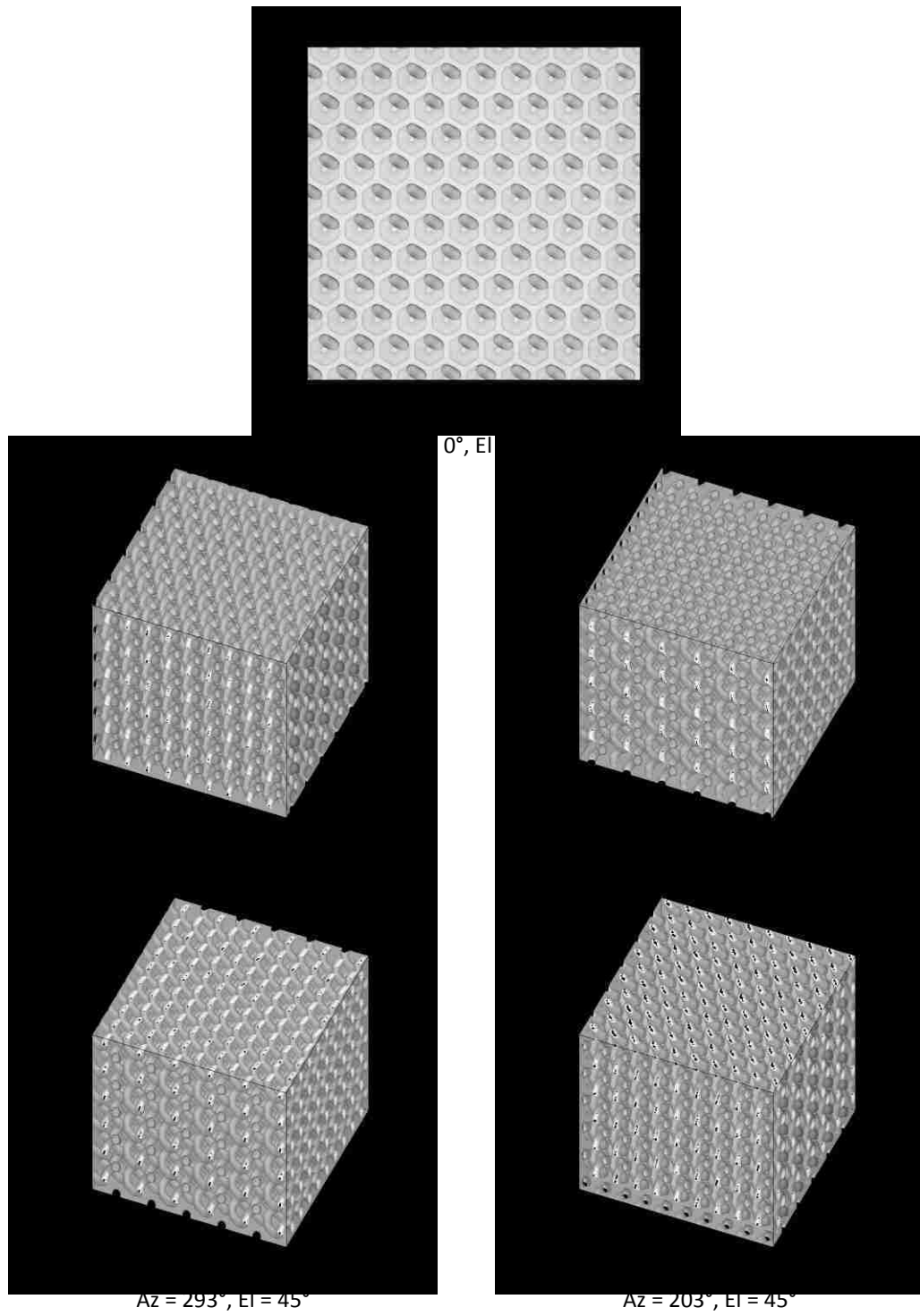


**Figure 50** – Models of 3D photonic crystal, made using 6-exposure interferometric lithography with a resist threshold of 62%.

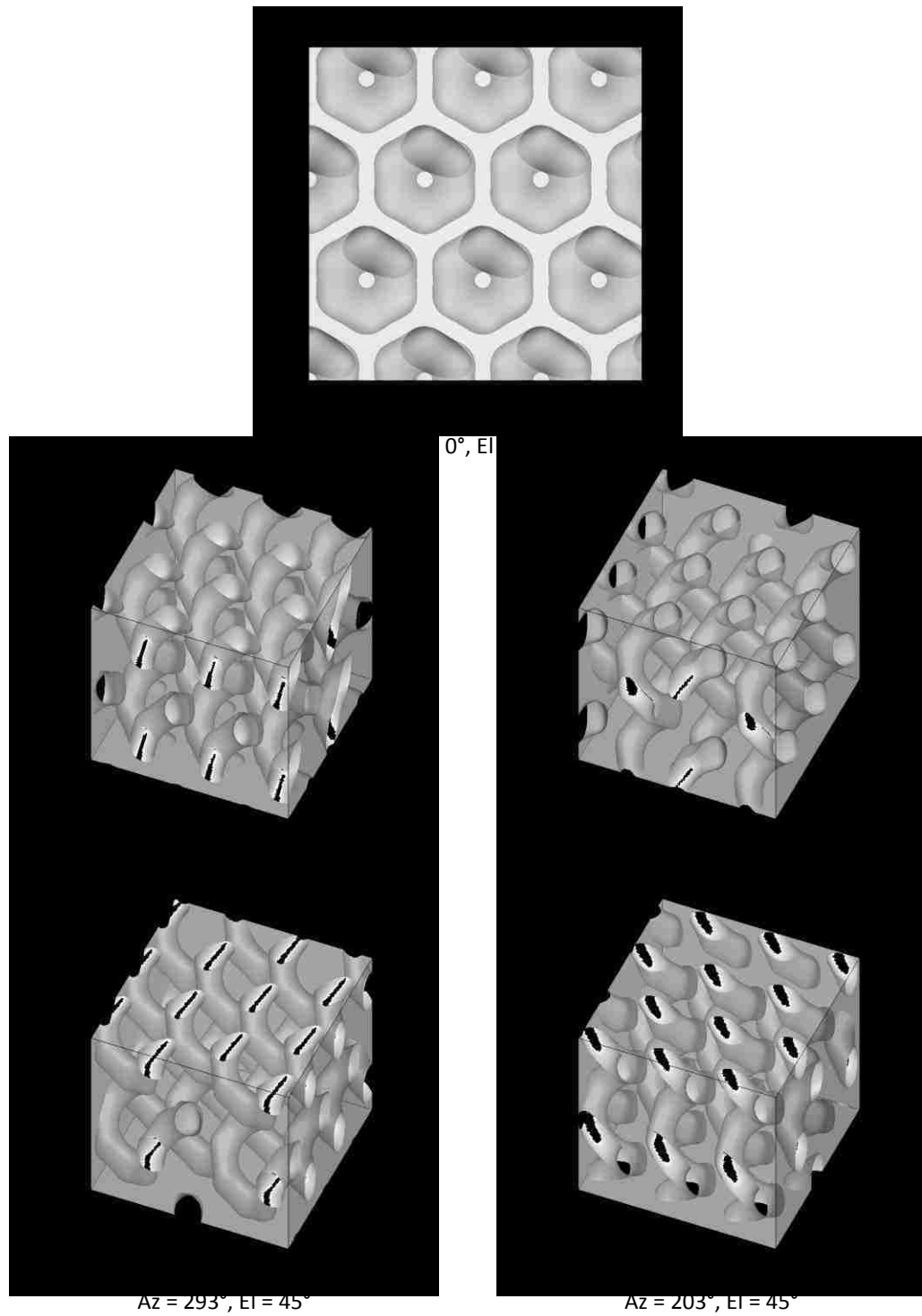


**Figure 51** – Close up of 3D photonic crystal models, made using 6-exposure interferometric lithography with resist threshold of 62%.

The six-exposure photonic crystals create coil-spring like helical structures (sometimes referred to as chiral structures). These structures have very useful optical applications including: circular polarizer, optical diodes, and/or poor-man's optical isolators.<sup>27,28</sup> Traditionally these helical structures have been formed using either glancing angle deposition (GLAD) a technique based on physical vapor deposition that employs oblique angle deposition conditions, or direct laser writing a technique based on multi-photon absorption and pin-pointed focusing of laser light using a high magnification objective to write directly into photoresist.<sup>29,30</sup> Both of these methods are slow and tedious for fabricating helical structures over large areas. By using the off-axis Michelson interferometric interferometer technique producing similar helical structures over large area is rapid in comparison. The helical pillar photoresist structures will be very prone to collapsing during development due to the surface tension applied on the high aspect ratio with small substrate contact area of the photoresist during the drying step of the development process. The inverse of these helix pillar structures can be obtained by lowering the exposure dose. Utilizing an exposure resist threshold of 38% instead of 62% in the simulation results in the models seen in Figure 52, with close up views in Figure 53. The solid resist structure of the model is made semitransparent to view the inner detail of the resulting helical holes in photoresist photonic crystal structure.



**Figure 52** – Models of 3D photonic crystal, made using 6-exposure interferometric lithography with a resist threshold of 38%.



**Figure 53** – Models of 3D photonic crystal close up, made using 6-exposure interferometric lithography with resist threshold of 38%.

This inverse photonic crystal structure will not exhibit any issues with pattern collapse, and can be used as a mandrel for filling with a high index material of optical interest. More details on the use of the photoresist as mandrel for higher index material are given in Chapter 6.

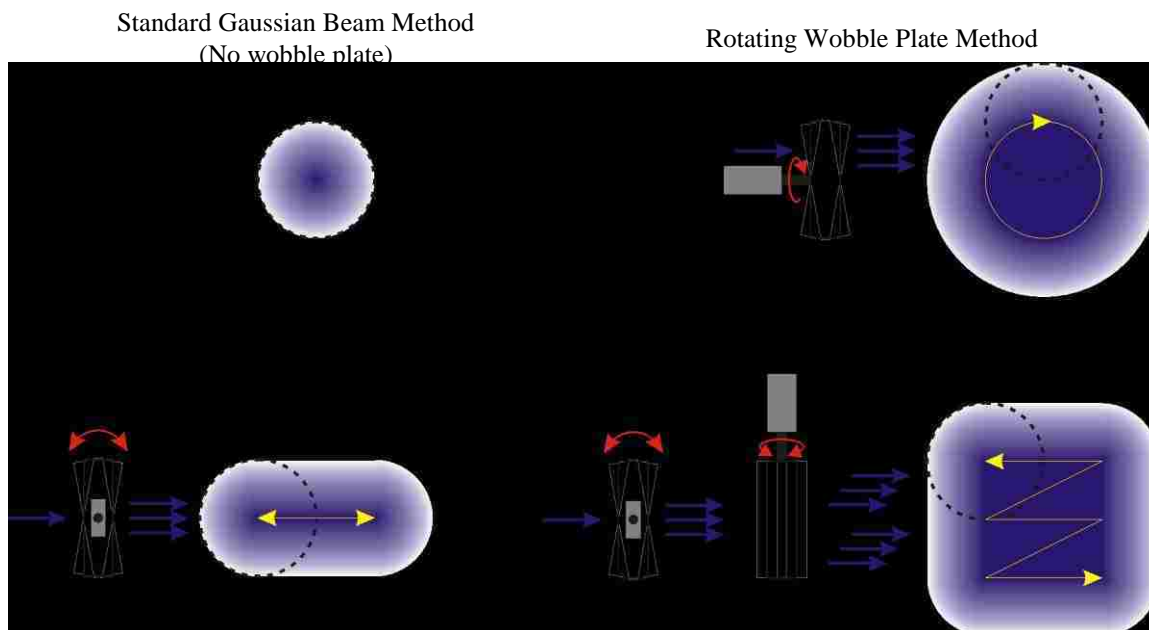
### ***Experimental 3D Photonic Crystal SEM Images***

This section provides the results achieved using a Michelson interferometer arrangement multiple-exposure interferometric lithography experimental setup to create three-dimensional photonic crystals. There are four primary components to the experimental layout used to perform interferometric lithography in this paper.

The first is the light source, which for 355 nm is a “Coherent Infinity 40-100” laser system. The source laser is a Nd:YAG pulsed laser followed by nonlinear crystals to generate a third harmonic 355-nm output beam. The third harmonic is generated by frequency doubling the 1064-nm fundamental Nd:YAG wavelength to 532 nm with a BBO crystal, and then frequency mixing the fundamental 1064 nm with the 532 nm to generate the 355-nm wavelength with a second BBO crystal. The laser beam is a ¼ inch in diameter at the output of the laser, and the laser pulse duration is ~2 ns. The exposure light is TE-polarized (s-polarized) light at the interferometer. The 244 nm light source is a “Coherent Sabre FRED” argon-ion laser. The laser uses an argon-ion cw 488 nm fundamental, with an intra-cavity frequency doubling BBO crystal generating the 244 nm output. The laser output light is rotated to TE-polarized (s-polarized) light at the interferometer.

The next primary components are the wobble optics. The use of wobble optics is a technique that significantly improves the uniformity across large areas. Since the beam intensities vary over a fixed area of exposure, physical displacement of the two interfering beams over the exposure area while maintaining their mutual coherence will average out the effects of the intensity variation. This is accomplished by inserting wobble plate optics before the beam is expanded. The wobble optics consists of a plane-parallel window mounted on a scanner, which tilts the window. The result is that the beams are shifted and scanned across the exposure area. Since the interference path is defined independent of the wobble, the fringes are unaffected. The only requirement on speed is that the beam raster be fast compared with the total exposure time (not the pulse duration). The amount of beam displacement is given by the equation 3.22 on page 80, and is the same one used for the beam displacement of the Fresnel reflection windows in the section on beam intensity ratio control. The beam displacement is determined by the thickness, index of refraction, and angle of the window relative to the beam path.

The displacement is magnified as the beam is expanded in the exposure setup. Four common wobble plate geometries are shown in Figure 54 as plots of beam intensity over a wafer for each of the given geometries. The wobble optics used to create the three-dimensional photonic crystals in this dissertation are scanning wobble plates consisting of two 1/2-inch UV grade fused silica windows 3/8-inch thick, one on a horizontal scanner and the other on a vertical scanner.



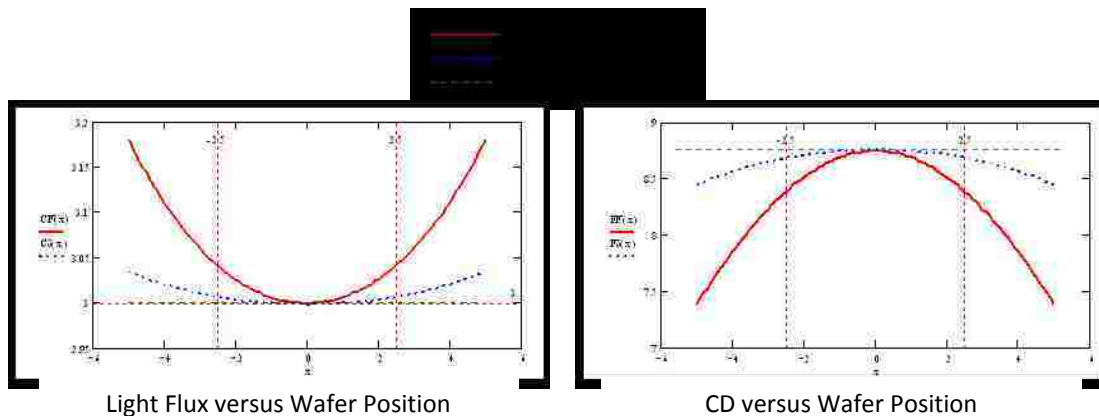
**Figure 54** – Wobble plate geometries, used for averaging out beam inhomogeneities.

The speed at which the wobble plates are scanned needs to be set such that the scanning completes at least one full cycle within the duration of the exposure. It is best to have the scanning complete ten to one-hundred cycles within the duration of the exposure time, especially if the laser source has intensity fluctuation within the duration of the exposure time in order to average out the fluctuation over many wobble scanning cycles. If the source laser is a pulsed laser, then the scanning cycles speed should be an order of magnitude slower than the source laser repetition rate. The laser repetition rate and wobble scanning cycle rate should not be an even multiple of each other, to further average out any cyclical intensity fluctuations. Simply stated in order to achieve good intensity averaging, the laser pulse duration is a fraction of the wobble optics scanning cycle duration which is a fraction of the exposure duration. For the experimental setup used to create the 355 nm exposed photonic crystals, the laser repetition rate was set to



100 Hz, the wobble optics scanning rate was set to 1.9 Hz, and the exposure duration was on the order of 10 to 20 seconds (0.10 to 0.05 Hz).

The impact of the wobble plate can be incorporated into the modeling of beam intensity and CD versus position on a wafer. Figure 55 shows the resulting laser intensity (a cut across the beam center, left) and CD uniformity (right). In each case the solid red curve is without the wobble plate, the dotted blue curve represents the improved uniformity with the rotating wobble plate, and the dashed green curve represents the further improved uniformity with the scanning wobble plate. The central exposure fluence must be increased by a factor of  $\sim 2$  to account for the reduced intensity effects of averaging out the beam in the center, but the uniform exposure area is dramatically increased using the laser power more efficiently. The modeling is based on simple Gaussian beam profiles, but wobble can be useful for averaging out other beam inhomogeneities.



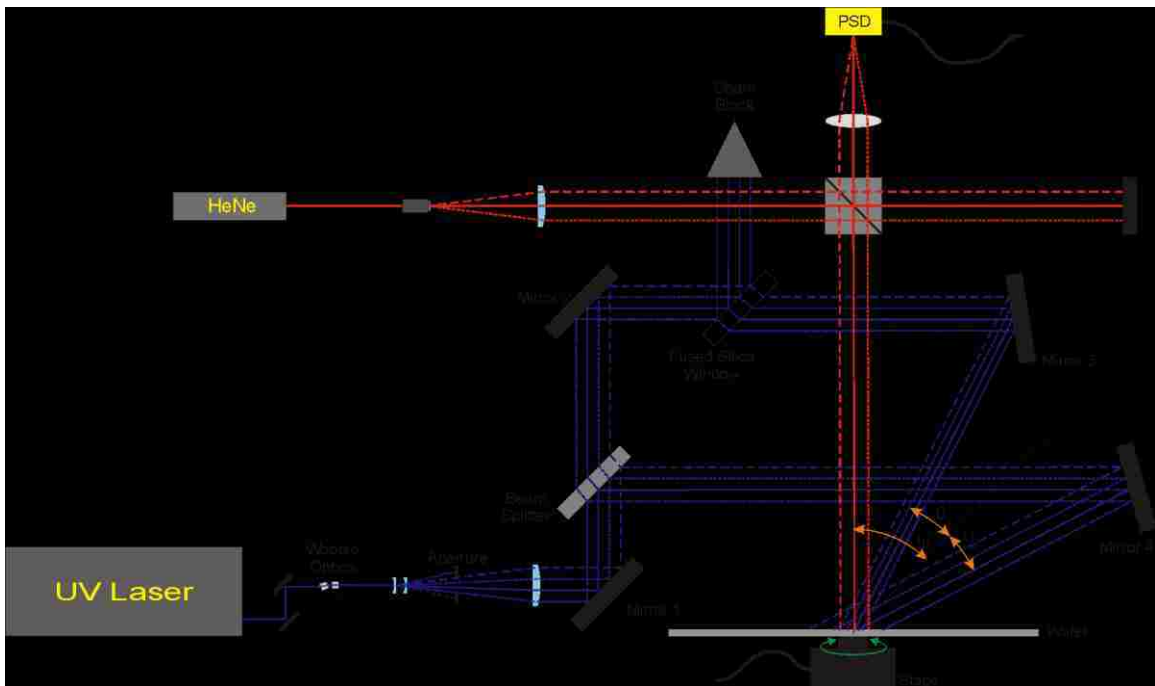
**Figure 55** – Modeled effect wobble optics have on beam intensity and CD across a wafer.

The third primary component used is a beam expander. The beam expander uses three lenses made of a UV grade fused silica. The first two lenses are 1.0-inch diameter Plano-concave (negative) lenses with a focal length of  $-50$  mm, used to expand the beam.

There is a round aperture located in the expanding beam that sets the beam size and allows only the uniform center section of the beam to pass on. The third lens is 5.787-inches diameter Plano-convex (positive) lens with a focal length of 1109 mm, used to re-collimate the expanded beam. All lenses have antireflection coatings on both surfaces. By using two weaker expanding lenses, in lieu of a single stronger expanding lens, there is less distortion and some control over the expansion magnification and collimation of the beam. By using a Galilean telescope design with a negative beam expanding lens and a positive beam collimating lens, the telescope has a virtual focal point. This is important for pulsed UV lasers, because if the laser beam passes through a real focal point in air the high fluences of the short pulses will rapidly heat the air causing beam distortions. If the fluencies are very high ( $> 2 \times 10^{13} \text{ W/cm}^2$ ), as in the case with the “Coherent Infinity 40-100” laser used, the result is laser-induced breakdown of air molecules. This will cause significant turbulence in air that will distort the wave front of the propagating beam. Using a Galilean telescope design avoids the possibility of laser beam induced distortion. The beam expander expands the ¼-inch beam to a usable beam aperture diameter of about one-inch. One advantage of having the exposing field aperture in the expanding beam is that diffracted light from the edges of the aperture will not be collimated by the final lens with the main exposing beam. In addition the further from the exposing plane the aperture is, the less the influence of the diffracted light at the exposure plane.

The fourth and last primary component in the experimental layout is the Michelson interferometer described in the previous section for three-dimensional multiple-exposure interferometer lithography. A photograph of the experimental Michelson interferometer was shown in Figure 45 of the previous section. The following

Figure 56 is a diagram of the full experimental layout used to produce three-dimensional photonic crystals. A beam aperture is placed between the telescoping optics of the beam expander. The aperture passes the averaged uniform intensity part (sweet spot) of the wobbled beam, and sets the maximum exposure field size and shape (not including the distortion from the off-axis beam angles). Again because the aperture is inside the beam expander the diffraction fringes off the edges of the aperture will not be in collimation with the expanded beam, this minimizes the impact of the diffraction at the exposure plane. A second aperture could be placed within a wavelength away from the exposure plane to define the final exposure field and eliminate any diffraction along the edge of the exposure field; this however was not implemented in the present experimental setup.



**Figure 56** – Michelson interferometric lithography setup used to produce 3D photonic crystals.  
Blue is exposure system, red is tilt/rotation interferometer monitor.

## 355 nm Exposure in Negative Photoresist

This section shows Scanning Electron Microscope images of the three-dimensional photonic crystals made using the multiple-exposure interferometer lithography setup. The first section focuses on the photonic crystals made using a three-exposure process that creates a three-dimensional photonic crystal with hexagonal symmetry. The second section shows the images of photonic crystals made using a four-exposure process that creates a three-dimensional photonic crystal with rectangular symmetry.

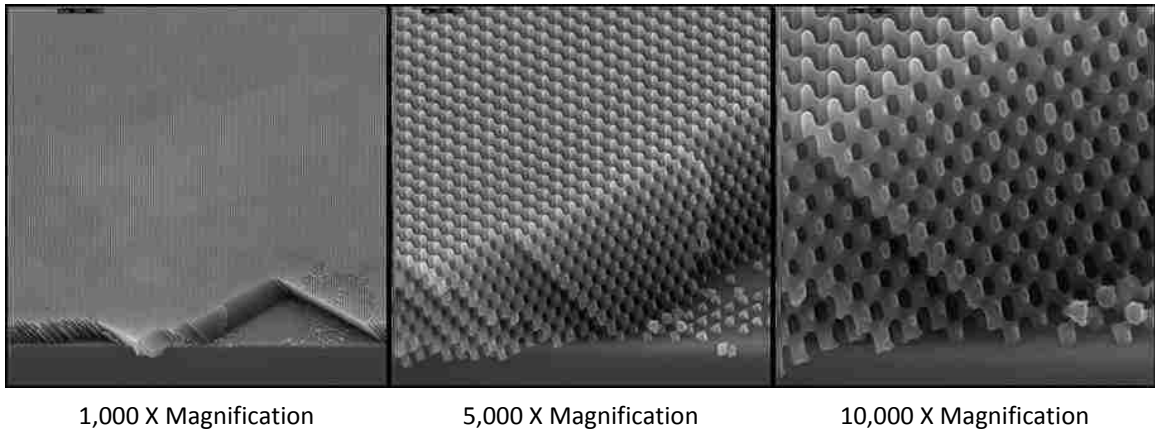
The fabrication process is as follows. A silicon wafer is used as a substrate. The wafer is then coated with a bottom anti-reflective coating (ARC) and baked. This bottom ARC is used to prevent unwanted reflection of the exposure light from the silicon substrate. The 72 nm thickness of the ARC needed for minimum reflections is calculated using the MathCAD program found in Appendix A. The next step is coating a thin adhesion layer. A thin layer, ~100 nm, of negative photoresist is spun on, baked, flood exposed and used as the adhesion layer. By flood exposing the negative photoresist the photoresist is not removed during development, and remains with the bottom ARC as a film coating the substrate. Without using the adhesion layer, it has been observed in SEM images that the photonic crystal pulls away in areas from the bottom ARC during development. This is most likely due to stresses in the photonic crystal, which occur as a result of some shrinkage of the exposed negative photoresist. A thick, 7.4  $\mu\text{m}$ , layer of negative photoresist is applied, and since it is the same material as the adhesion layer, sticks to the adhesion layer. The thick negative photoresist becomes the material of the photonic crystal. After the thick photoresist is coated and baked, it is exposed using the

Michelson interferometric lithography setup with off-axis illumination to create three-dimensional photonic crystals. Once exposed, the silicon wafer is post-exposure baked (PEB) to crosslink the exposed photoresist polymers. The photoresist on the silicon wafer is then developed by spraying a puddle of the strong base tetramethylammonium hydroxide (TMAH) on the photoresist in a spinner using a dynamic process, the develop recipe for the spinner is found in Appendix F. The photoresist is developed with the unexposed photoresist dissolving away and the exposed cross-linked photoresist remaining. The silicon wafer and photoresist is rinsed in de-ionized (DI) water and spin-dried with nitrogen (blow-off from LN<sub>2</sub> to avoid any water vapor contamination). The final result is the three-dimensional photonic crystal made of negative photoresist on a thin film of negative photoresist and bottom ARC on a silicon wafer.

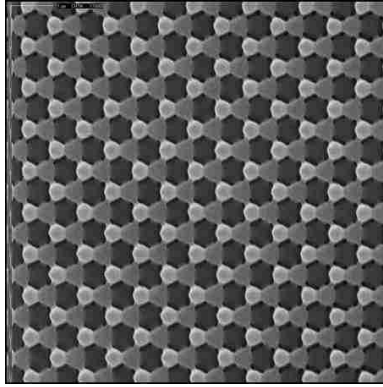
### **Three Exposures at 355 nm (120° rotation)**

The process flow and parameters for the single negative photoresist layer 355 nm three-exposure three-dimensional photonic crystals are found in Table 8 of Appendix C. Scanning electron microscope images of the three-dimensional photonic crystal in 355 nm negative photoresist made from this three-exposure process are shown in Figure 57 and Figure 58. In Figure 57 the silicon wafer substrate is cleaved for cross-section and it can be seen that the photonic crystal on the surface is also cleaved along its crystal planes. The photonic crystal is very uniform over the 10- $\mu\text{m}^2$  area imaged; the overall size was  $\sim 2 \text{ cm}^2 \times 7 \text{ }\mu\text{m}$  high. For the top-down SEM images in Figure 58, three periods down into the crystal are visible. The top down SEM clearly shows the hexagonal symmetry of the surface  $\langle 111 \rangle$  plane of the three-exposure photonic crystal. There is some small

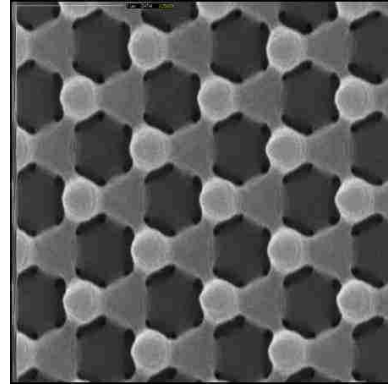
variations from the surface to bottom of the photonic crystal, which should not be confused with the variation of the nodes due to the photonic crystal cleave angle. The variation in the photonic crystal pore size is likely due to variation in exposure dose versus photoresist depth from absorption of the actinic wavelength in the photoresist, and to a smaller extent from developer diffusion and concentration fluctuations during developing. Across the photonic crystal area there are phase shifts along the surface every ~3-8 mm, which appear as faint fringes on the photonic crystal to the naked eye. These phase shifts are from variations of the exposure plane due to wafer flatness. The void sizes in the crystal structure vary slightly from edge to edge of the 2-cm<sup>2</sup> photonic crystal mostly due to exposure variation.



**Figure 57** – 45° cross-section SEM images of defect free 3D photonic crystal over large areas, made using 3-exposure interferometric lithography at 355 nm.



10,000 X Magnification



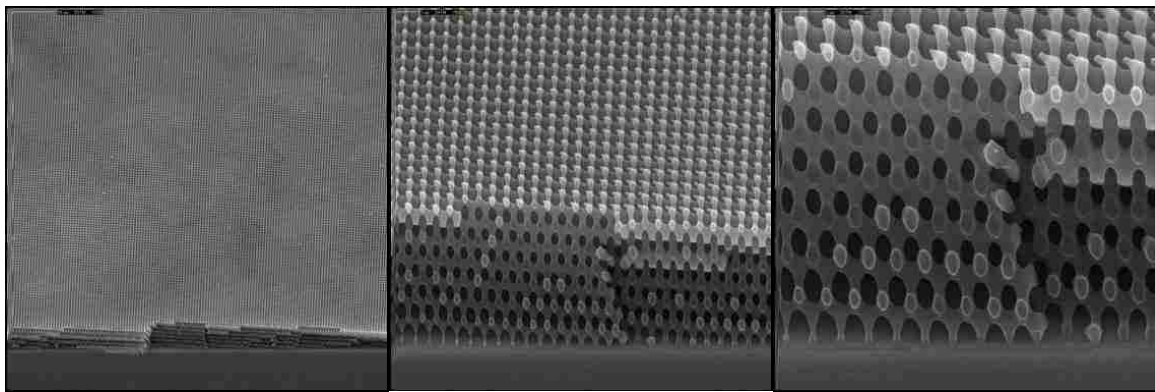
25,000 X Magnification

**Figure 58** – Top-down SEM images of defect free 3D photonic crystal over large areas, made using 3-exposure interferometric lithography at 355nm.

### **Four Exposures at 355 nm (90° rotation)**

The four-exposure three-dimensional photonic crystal fabrication is very similar to the three-exposure process. The main difference is the additional exposure, which makes the rotational and wafer tilt alignments more critical. The process flow and parameters for the single negative photoresist layer 355 nm four-exposure three-dimensional photonic crystals are found in Table 9 of Appendix C. The scanning electron microscope images of the three-dimensional photonic crystal in 355 nm negative photoresist made from this four-exposure process are shown in Figure 59 and Figure 60. In Figure 59 the silicon wafer substrate is cleaved for cross-section and it can be seen that the photonic crystal on the surface also cleaved along its crystal planes which are slightly out of alignment with the silicon cleavage plane. The photonic crystal is noticeably very uniform over the  $10\mu\text{m}^2$  area imaged, which is much harder to achieve in a four-exposure photonic crystal; again the overall size was  $\sim 2\text{ cm}^2$ , however there is visible phase variation across the surface of the crystal with the center of the crystal having approximately a 4 mm diameter of constant phase. For the top-down SEM images in

Figure 61, four periods down into the crystal are visible. The phase variation across the photonic crystal is due to tilt variations between exposures, and from the flatness of the silicon wafer substrate compared to the exposure plane. The top down SEM in Figure 60 clearly shows the expected square symmetry of the surface  $\langle 100 \rangle$  plane of the four-exposure photonic crystal. As previously mentioned the variation in the photonic crystal pore size is likely due to variation in exposure dose versus photoresist depth from light absorption in the photoresist, and to a smaller extent from developer diffusion and concentration fluctuations during developing.



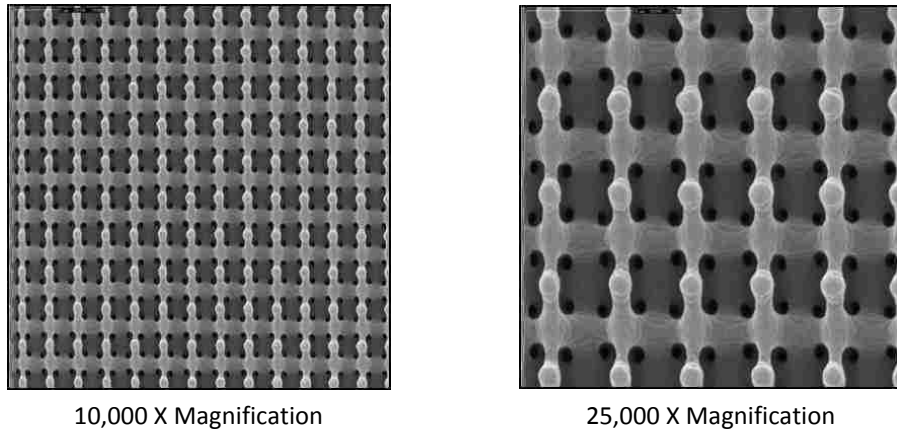
1,000 X Magnification

5,000 X Magnification

10,000 X Magnification

**Figure 59** – 45° cross-section SEM images of defect free 3D photonic crystal over large areas, made using 4-exposure interferometric lithography at 355 nm.





**Figure 60** – Top-down SEM images of defect free 3D photonic crystal over large areas, made using 4-exposure interferometric lithography at 355nm.

### **244 nm Exposure in Positive Photoresist**

The 244 nm exposure process for exposing the photonic crystals is very similar to the 355 nm exposure photonic crystals. The wavelength of the exposing light is obviously changed, as well as the tone of the photoresist going from a negative 355 nm photoresist to a positive 244 nm photoresist. The other change is the absence of an adhesion layer as the bottom ARC is now sufficient as the adhesion layer for the photoresist.

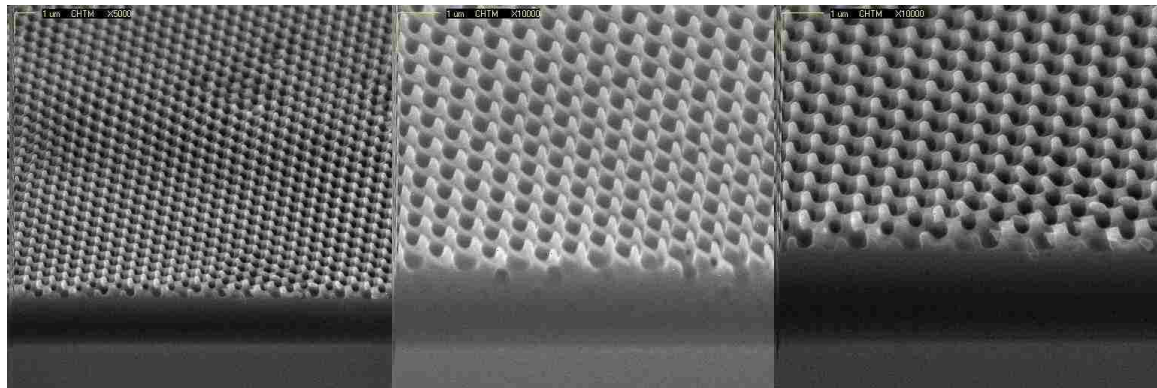
The experimental setup is the same as for the 355 nm exposure, with the 355 nm dielectric mirrors being swapped out with 244 nm dielectric mirrors. The 244 laser beam is directed into the setup beam path using a kinematic mirror mount placed in the beam line in front of the wobble optics. The beam expander lenses are move forward a few mm to adjust for the wavelength change and keep the beam collimated. Everything else including the beam angles was kept the same for the 244 nm exposures of the three-dimensional photonic crystals. This will cause the periodic pitch on the 244 nm exposed photonic crystals to be reduced from the 355 nm exposed photonic crystals.

The fabrication process is as follows. A silicon wafer is used as a substrate. The wafer is then coated with a bottom anti-reflective coating (ARC) and baked. This bottom ARC is used to prevent unwanted reflection of the exposure light from the silicon substrate, and as an adhesion layer for the photoresist to the substrate. The 65 nm thickness of the ARC needed for minimum reflections is calculated using a MathCAD program found in Appendix A. A thick 1.3  $\mu\text{m}$  layer of positive photoresist is applied, and baked. A second thick 1.3  $\mu\text{m}$  layer of positive photoresist is subsequently applied, and baked. These two layers of positive photoresist become the material of the photonic crystal. The 2.6  $\mu\text{m}$  of photoresist is exposed using the Michelson multiple-exposure interferometric lithography setup to create three-dimensional photonic crystals. Once exposed the silicon wafer is post exposure baked (PEB) to scission the exposed crosslink photoresist polymers. The silicon wafer is then developed by spraying a puddle of the strong base TMAH on the photoresist in a spinner in a dynamic process, the develop recipe for the spinner is found in Appendix F. The photoresist is developed with the exposed photoresist dissolving away and the unexposed crosslink photoresist remaining. The silicon wafer and photoresist is rinsed in de-ionized (DI) water and spin-dried with nitrogen (blow-off from  $\text{LN}_2$  to avoid any water vapor contamination). The final result is the three-dimensional photonic crystal made of positive photoresist on a thin film of bottom ARC on a silicon wafer.

### **Three Exposures at 244 nm (120° rotation)**

The process flow and parameters for the single positive photoresist layer 244 nm three-exposure three-dimensional photonic crystals are found in Table 10 of Appendix C.

Scanning electron microscope images of the three-dimensional photonic crystal in 244 nm positive photoresist made from this three-exposure process are shown in Figure 61 and Figure 62. It can be seen in these images that the photonic crystal does not extend throughout the photoresist thickness. In the images shown, and on other image samples not shown, of the 244 nm exposed photonic crystals there are only about three to four periods of the crystal structure. On inspection of Figure 61 it is seen that as the exposure dose is increased the same number of periods exist in both exposures, but the amount of undeveloped photoresist under the photonic crystal is reduced as the exposure dose increases. This is the result of the photoresist film being too absorptive at the exposure wavelength. As the exposing beam exposes the top of the photoresist film with the proper dose to form a photonic crystal, the bottom of the photoresist film is underexposed and does not develop away, due to the amount of light being absorbed by the photoresist. If the dose is further increased to properly expose the bottom of the photoresist film necessary to form a photonic crystal, the top of the photoresist film is overexposed and completely develops away. This can be fixed by using a different 244 nm photoresist with a lower absorption coefficient. However no photoresist with a lower absorption coefficient were readily available at the time of the experiment formulated with a spin on thickness necessary for the multi-layer three-dimensional photonic crystal.

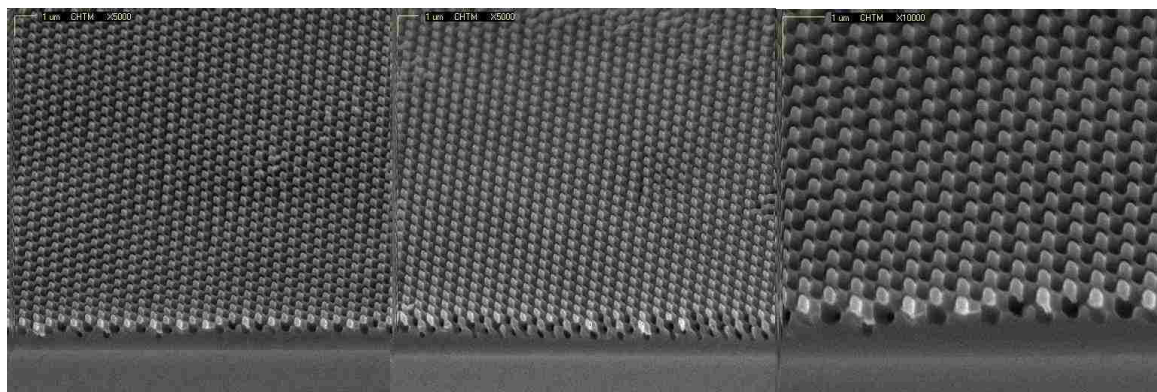


5,000 X Magnification

10,000 X Magnification

10,000 X Magnification

**15 Seconds Exposures**



5,000 X Magnification

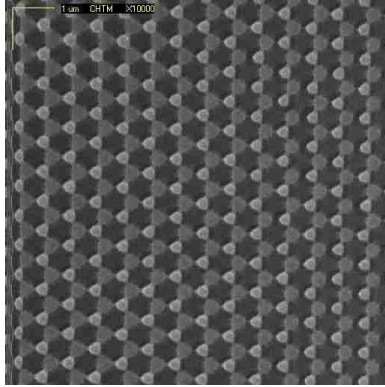
5,000 X Magnification

10,000 X Magnification

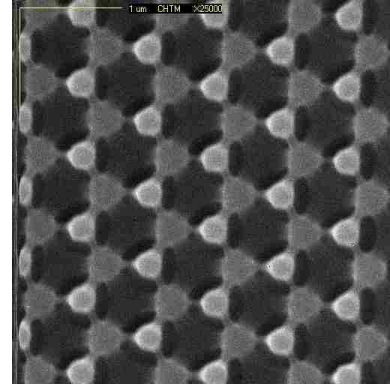
**25 Seconds Exposures**

**Figure 61** – 45° cross-section SEM images of 3D photonic crystal over large areas, made using 3-exposure interferometric lithography at 244 nm.

The top-down SEM images of the 244 nm three-exposure photonic crystal in Figure 62 appear equivalent to the top-down SEM images of the 355 nm three-exposure photonic crystals found in Figure 58. This demonstrates that although the tone of the photoresist changed from negative tone to positive tone, with the proper exposure parameters the same photonic crystal can be achieved.



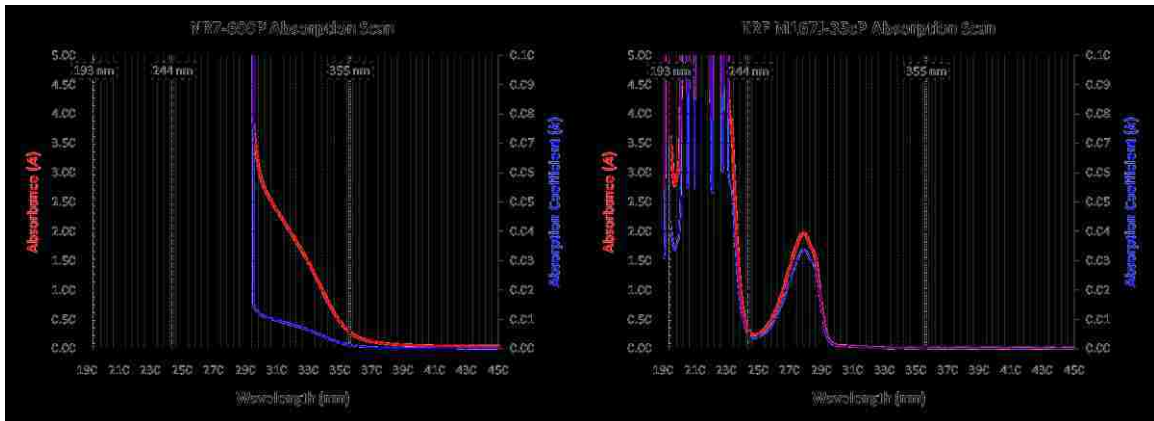
10,000 X Magnification



25,000 X Magnification

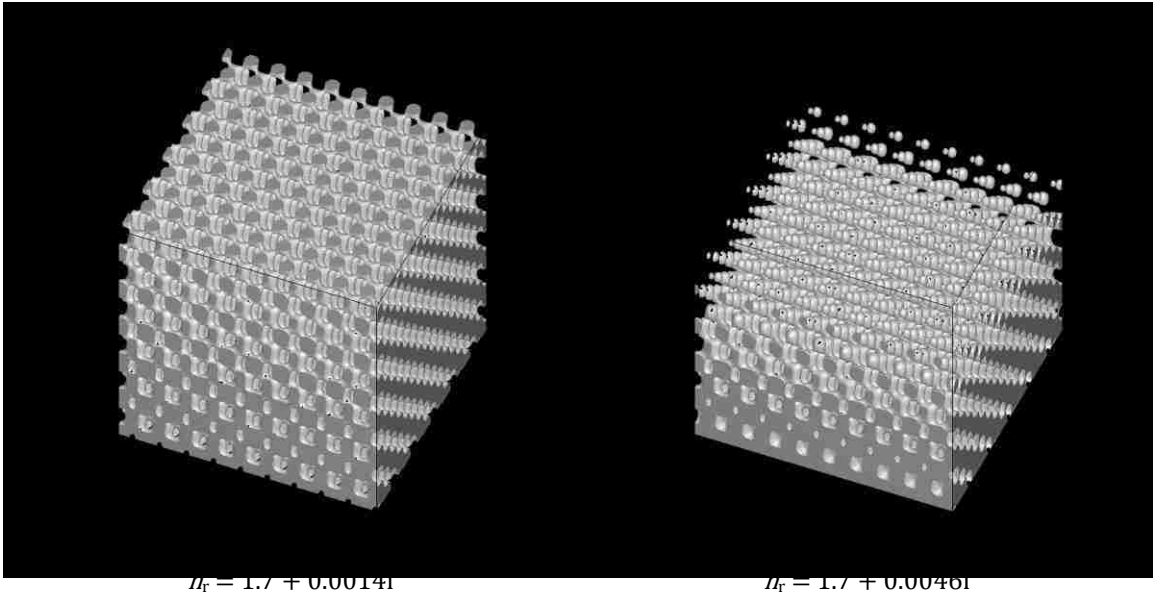
**Figure 62** – Top-down SEM images of 3D photonic crystal over large areas, made using 3-exposure interferometric lithography at 244nm.

An absorption plot of the 355 nm Futurrex NR7 photoresist and the 244 nm JSR KRF M167J photoresist are shown in Figure 63. The absorbance of unexposed Futurrex NR7 photoresist at 355 nm is  $A_{355} = 0.3057$  for a 6 μm film thickness corresponding to an absorption coefficient of  $k = 0.0014$ , and similarly the absorbance of unexposed JSR KRF M167J photoresist at 244 nm is  $A_{244} = 0.3099$  for a 1.3 μm film thickness corresponding to an absorption coefficient of  $k = 0.0046$ . Upon comparison the difference in the two photoresist absorption at their exposure wavelength is significant.



**Figure 63** – Absorption Scan of Unexposed NR7 and KRF M167J photoresists.

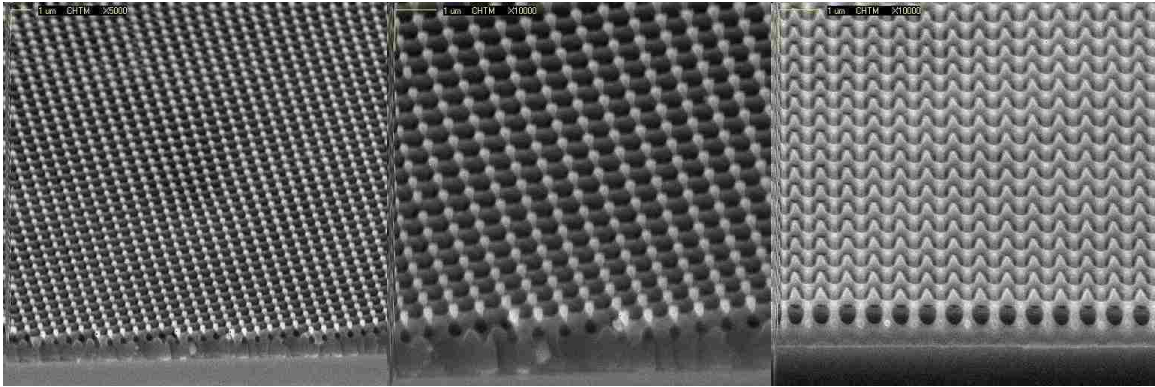
A simulation of the same three-dimensional photonic crystal exposed in two different photoresist films one with a refractive index of  $n_r = 1.7 + 0.0014i$  and the other with  $n_r = 1.7 + 0.0046i$  is shown in Figure 64. By examining the images in Figure 64 the size of the nodes increases and the voids decrease as a function of depth into the photoresist for both photoresist cases due to absorption. However as the absorption of the photoresist increases the rate at which the nodes and voids change in size as a function of depth into the photoresist also increases. In the simulation of the photonic crystal with an  $n_r = 1.7 + 0.0046i$  there are nodes floating in space that would be washed away during development and individual voids in the bottom bulk of the photoresist that would not be developed out during development, leaving at most five periods of definite photonic crystal structure. This explains why the NR7 photoresist is seen having up to fifteen periods of crystal structure compared to the KRF M167J photoresist having only up to four periods of crystal structure. It also explains why a very transparent photoresist is necessary for fabrication of three-dimensional photonic crystals.



**Figure 64** – Simulation of 3D photonic crystal in photoresist of varying absorption.  
The number of PhC periods in the z-direction is proportional to photoresist absorption.

### Four Exposures at 244 nm (90° rotation)

The four-exposure three-dimensional photonic crystal fabrication is very similar to the three-exposure process. The main difference is the additional exposure, which makes the rotational and wafer tilt alignments more critical. The process flow and parameters for the single positive photoresist layer 244 nm four-exposure three-dimensional photonic crystals are as found in Table 11 of Appendix C. Scanning electron microscope images of the three-dimensional photonic crystal in 244 nm positive photoresist made from this four-exposure process are shown in Figure 65 and Figure 66. Similar to the three-exposure 244 nm photonic crystals the four-exposure 244 nm photonic crystals only contain about three period of crystal structure in the photoresist. This small number of photonic crystal period again is due to the higher absorption of the 244 nm photoresist used.



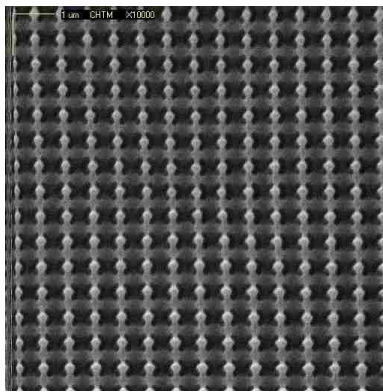
5,000 X Magnification

10,000 X Magnification

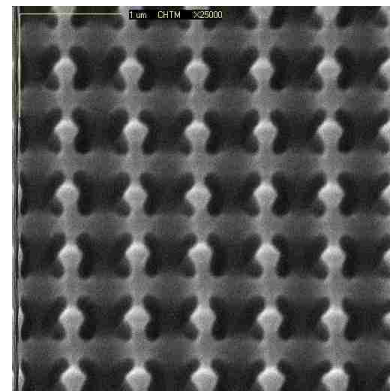
10,000 X Magnification

**Figure 65** – 45° cross-section SEM images of 3D photonic crystal over large areas, made using 4-exposure interferometric lithography at 244 nm.

The top-down SEM images of the 244 nm four-exposure photonic crystal found in Figure 66 appears equivalent to the top-down SEM images of the 355 nm four-exposure photonic crystals found in Figure 60. Demonstrating that although the tone of the photoresist changed from negative tone to positive tone, with the proper exposure parameters the same photonic crystal can be achieved.



10,000 X Magnification



25,000 X Magnification

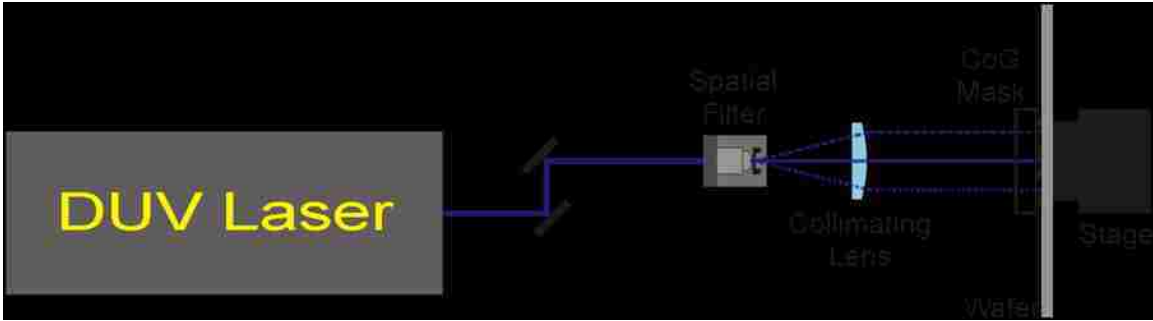
**Figure 66** – Top-down SEM images of 3D photonic crystal over large areas, made using 4-exposure interferometric lithography at 244nm.



### ***3D Photonic Crystal with Waveguides SEM Images***

This section provides the results achieved for three-dimensional photonic crystals with integrated waveguides. The first sections show the results of a photonic crystal with the waveguide on the top surface of the photonic crystal. The second section shows the results of a photonic crystal with the waveguide embedded in the center of the crystal. The Michelson interferometer multiple-exposure interferometric lithography setup described and used in the previous section is also used to create three-dimensional photonic crystals described in this section.

In order to create the waveguides a second exposure setup is used. The waveguide exposure setup operates at a shorter wavelength than the Michelson interferometer multiple-exposure interferometric lithography setup. The waveguide exposure setup is a simple contact lithography system, which uses a chrome-on-glass photo mask. The photo mask contains the desired waveguide pattern on a 1X scale to the photonic crystal. The wafer with the thick photoresist is placed on the exposure chuck; the chuck is then moved in contact to the photo mask with the chrome side facing the photoresist. The photoresist is subsequently exposed to an expanded beam of the waveguide exposure light source at the waveguide exposure wavelength. A diagram of the waveguide exposure setup is shown in Figure 67.



**Figure 67** – Waveguide contact mask lithography setup.

One issue with the contact mask lithography setup is the potential for contamination. If there is a particle on the mask it could transfer to the photoresist during the contact exposure, and vice-versa a particle in the photoresist could transfer to the mask during the contact exposure creating a temporary or permanent defect on the mask. The possibility of scratching the mask is also a concern. After several contact exposures the contact mask will need to be replaced. This can be avoided by using a photolithography stepper, however photolithography steppers are considerably more expensive to acquire, and were not available for this work.

### **Waveguide at the Surface of 3D Photonic Crystal**

This section shows Scanning Electron Microscope images of three-dimensional photonic crystals with waveguides at the top surface of the photonic crystal, made using the multiple-exposure interferometric lithography setup plus waveguide exposure setup. The first section focuses on the photonic crystals made using a three-exposure process that creates a three-dimensional photonic crystal exposed at 355 nm and waveguides exposed at 244 nm in negative photoresist. The second section show the images of photonic crystals made using a three-exposure process that creates a three-dimensional

photonic crystal exposed at 244 nm and waveguides exposed at 193 nm in positive photoresist.

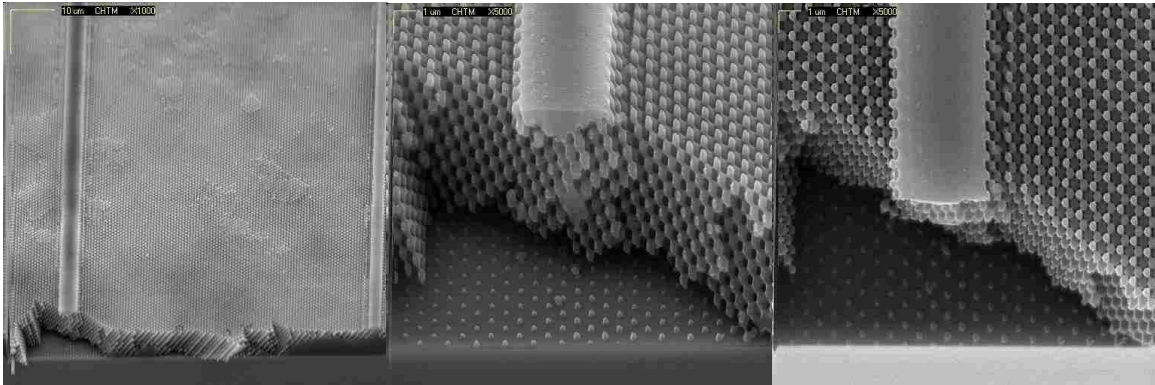
The fabrication process is the same as in the previous section, with an additional exposure on the waveguide exposure setup. This exposure is done right after the photoresist is exposed using the Michelson multiple-exposure interferometric lithography setup to create three-dimensional photonic crystals. Once exposed on both exposure setups, the silicon wafer is post exposure baked (PEB) as before.

### **355 nm PhC Exposure with 244 nm Waveguide Exposure in Negative Photoresist**

The three-dimensional photonic crystals with waveguides at the surface made in negative tone photoresist, used a three-exposure multiple-exposure interferometric lithography process, but it could have simply used a four-exposure process. The Michelson multiple-exposure interferometric lithography setup 355 nm light source is a “Coherent Infinity 40-100” laser, and the waveguide contact mask lithography setup 244 nm light source is a “Coherent Sabre FRED” argon ion laser. The process flow and parameters for the single negative photoresist layer 355 nm three-exposure three-dimensional photonic crystals with a 244 nm exposure surface waveguides are found in Table 12 of Appendix C.

The Waveguides in negative photoresist is the presence of photoresist forming a solid line on the photonic crystal. Because the waveguide is an undevelopable crosslinked photoresist, during the development of the photonic crystal the developer need to diffuse around and through the photoresist waveguide in order to develop the

underlying photonic crystal structure. This did not seem to impose any issues in the successful formation of the three-dimensional photonic crystal with waveguides. The scanning electron microscope images of the three-dimensional photonic crystal in 355 nm negative photoresist made from the three-exposure photonic crystal process with waveguides on the surface are seen in Figure 68.

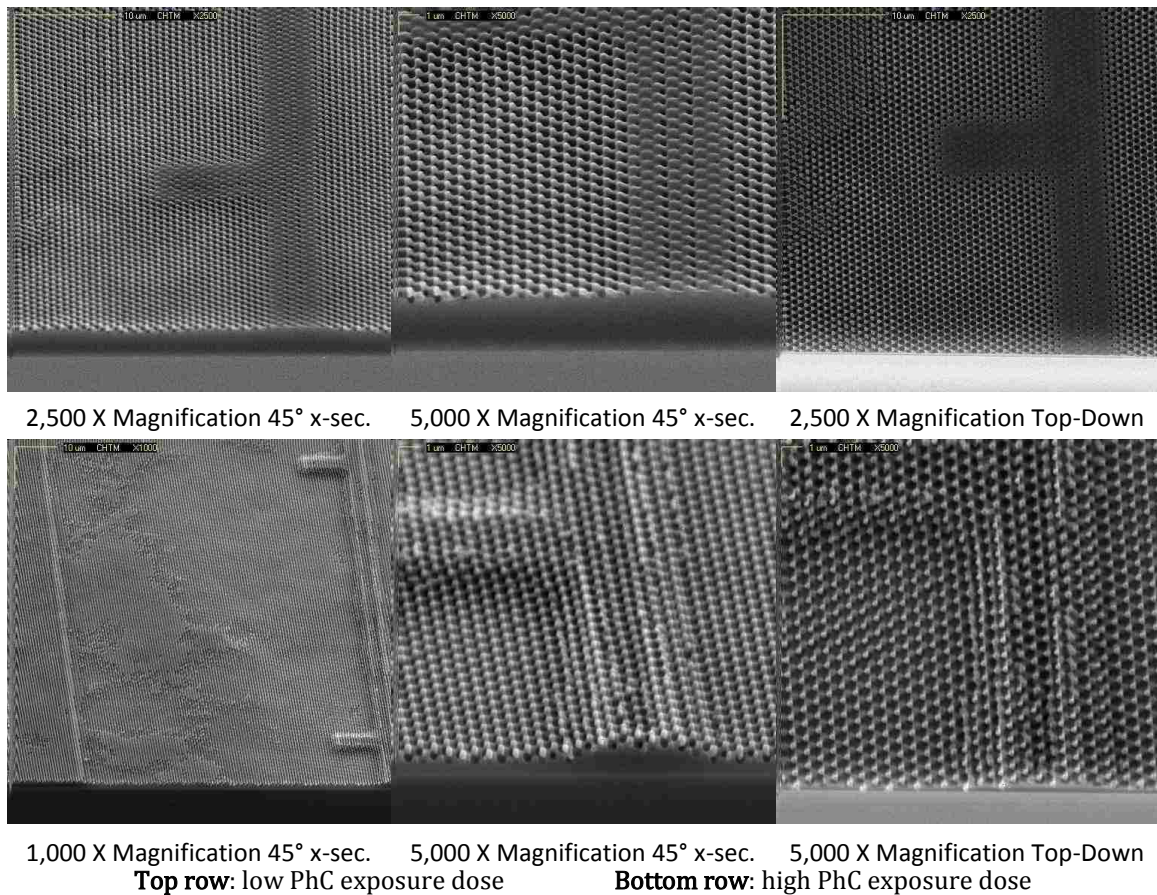


1,000 X Magnification 45° x-sec. 5,000 X Magnification 45° x-sec. 5,000 X Magnification Top-Down  
**Figure 68** – Cross-section SEM images of 355 nm 3-exposure 3D photonic crystal, with 244 nm surface waveguides in negative photoresist.

## **244 nm PhC Exposure with 193 nm Waveguide Exposure in Positive Photoresist**

As discussed in the previous section, the three-dimensional photonic crystals with waveguides at the surface made in positive tone photoresist, used a three-exposure multiple-exposure interferometric lithography process, but again it could have just the same used a four-exposure process. The Michelson multiple-exposure interferometric lithography setup 244 nm light source is a “Coherent Sabre FRED” argon ion laser, and the waveguide contact mask lithography setup 193 nm light source is a “Cymer ELX-5400A” eximer laser. The process flow and parameters for the positive photoresist layer

244 nm three-exposure three-dimensional photonic crystals with a 193 nm exposure surface waveguides are found in Table 13 of Appendix C. The Waveguides in positive photoresist should correspond to the absence of photoresist forming a trench on the photonic crystal, however the photoresist appears to act as a negative resist at the very high 193 nm exposure doses used. The scanning electron microscope images of the three-dimensional photonic crystal in 244 nm positive photoresist made using this three-exposure photonic crystal process with waveguides on the surface are show in Figure 69.



**Figure 69** – Cross-section SEM images of 244 nm 3-exposure 3D photonic crystal, with 193 nm surface waveguides in positive photoresist.

As was previously seen in the 244 nm exposed three-dimensional photonic crystals only about three periods of the photonic crystal structure are present in the

photoresist. The waveguide formed by the 193 nm exposure is clearly seen in Figure 69. The 193 nm exposure caused the photoresist to require a higher 244 nm exposure dose to clear the photonic crystal structure, and is why there is additional photoresist remaining where the waveguide exposure was present.

## **Waveguide Embedded in the Center of 3D Photonic Crystal**

This section shows scanning electron microscope images of the three-dimensional photonic crystals with waveguides embedded in the center of the photonic crystal, made using the multiple-exposure interferometric lithography setup plus waveguide exposure setup. Photonic crystals were made using a three-exposure process creating a three-dimensional photonic crystal exposed at 355 nm and embedded waveguides exposed at 244 nm in negative photoresist. The fabrication process is similar to the previous section, with additional photoresist coating step(s). After the final bottom layer(s) photoresist post application bake (PAB) only the waveguide exposure is performed. Once exposed using the waveguide exposure setup, the silicon wafer with the first photoresist layer undergoes a post exposure bake (PEB). Now the additional photoresist coating step is performed. Once the final layer of photoresist is spun on and post application bake (PAB) is performed, then the three-dimensional photonic crystal exposure is performed throughout the composite multi-layer photoresist stack using the Michelson interferometer multiple-exposure interferometric lithography setup. Finally a post exposure bake (PEB) is carried out and the wafer processed through development same as before.

This process requires at least two and possibly more photoresist coat steps. The waveguides are exposed halfway through the photoresist coating process, thus embedding them into the photoresist stack. The three-dimensional photonic crystal is exposed after the photoresist coating process, exposing the full photoresist stack. The full photoresist stack is developed in a single step, developing the photonic crystal and waveguide at the same time. This process can be expanded to multiple layers of embedded waveguides with more photoresist coat steps and waveguide exposure steps.

### **355 nm PhC Exposure with 244 nm Waveguide Exposure in Negative Photoresist**

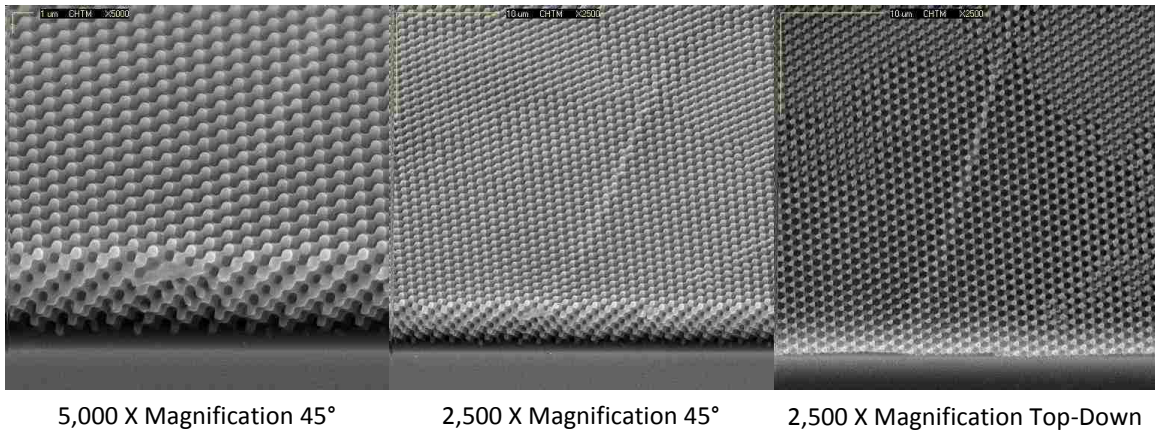
The embedded waveguide process requires at least two coating steps of photoresist, with one layer of photoresist placed on top of another layer of photoresist. This multilayer photoresist stack required quite a bit of experimenting and optimization, in order to achieve the required processing parameters. The first negative photoresist examined was MicroChem Corp. "SU-8 2000". Although it is possible to make three-dimensional photonic crystals in a single layer of SU-8, it cannot be used for embedding waveguides between two layers of SU-8. This is due to the fact that when coating a second layer of SU-8 the casting solvent for the photoresist completely dissolves the first layer of photoresist and mixes its contents with the contents of the second layer coating. This creates a new single layer of thicker SU-8, but not twice as thick with two distinct layers stacked on top of each other. And if a waveguide is exposed into the first layer of SU-8 it is destroyed during the coating of the second layer of SU-8.

The negative photoresist that is used to make embedded waveguide is Futurrex NR7. This negative photoresist has two advantages compared to SU-8. The first is that it uses an aqueous developer (TMAH) that is commonly used in industry, as opposed to solvent base developer that gives off carcinogenic flammable fumes. The more important advantage is that the casting solvent does not dissolve the photoresist once the photoresist has been post application baked. Nonetheless, achieving a very good three-dimensional photonic crystal throughout the two layer photoresist stack required quite a bit of process optimization. A designed of experiment (DOE) was performed on the following condition to optimize the photonic-crystal manufacturing process with NR7: PAB temperature, PAB time, PEB temperature, PEB time, developer normality (strength), and develop time. The DOE was performed on two-dimensional photonic crystals of holes in two layers of 12  $\mu\text{m}$  thick NR7. It is easier to evaluate the quality of a two-dimensional crystal. The DOE was performed on both NR7 negative photoresist and a newer NR71 photoresist. The DOE results of the NR7 photoresist formulation were more promising, and therefore the NR7 photoresist was chosen. A smaller refined DOE was subsequently performed using three-dimensional photonic crystals for determining the final optimized conditions. The final optimized conditions are quite far from the recommended conditions for the NR7 photoresist used for standard lithography, and can be found in Table 14 of Appendix C.

Just as in the previous section, three-dimensional photonic crystals with embedded waveguides were made using a negative tone photoresist, with a three-exposure interferometric lithography process. However, it could have used a four-exposure process. The process flow and parameters for the two negative photoresist layer



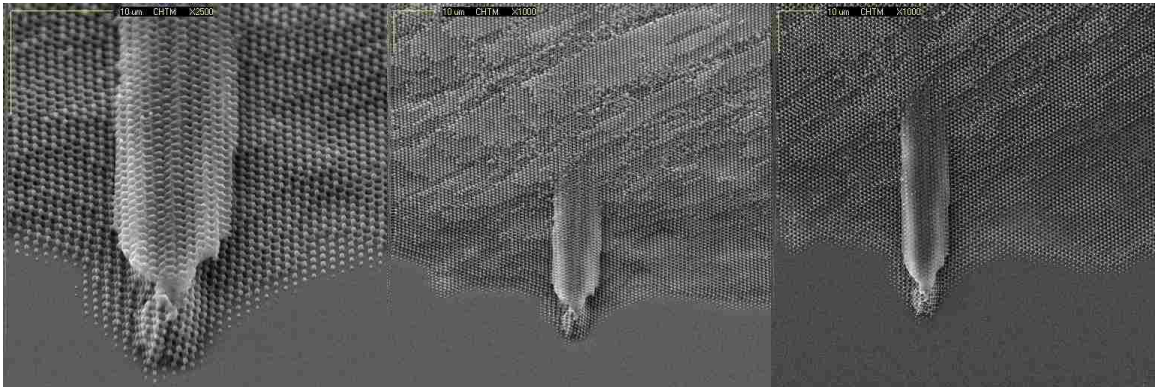
355 nm three-exposure three-dimensional photonic crystals with a 244 nm exposure embedded waveguides are found in Table 14 of Appendix C. The waveguides in the negative photoresist correspond to a line of photoresist thru the photonic crystal. As with the previous surface waveguides, the embedded waveguide is undevelopable crosslinked photoresist, and during the development of the photonic crystal the developer needed to diffuse around and through the photoresist waveguide in order to develop the underlying photonic crystal structure. This did not seem to impose any issues in the successful formation of the three-dimensional photonic crystal with embedded waveguides. The scanning electron microscope images of the three-dimensional photonic crystal in 244 nm positive photoresist made using this three-exposure photonic crystal process with the waveguides embedded in the middle are show in Figure 70.



**Figure 70** – Cross-section SEM images of 355 nm 3-exposure 3D photonic crystal, with 244 nm embedded waveguides in positive photoresist.

The  $\sim 1 \mu\text{m}$  waveguide is barely visible in the SEM image, as there are just a few missing voids in the cross-section of the photonic crystal. Due to some charging from the e-beam of the embedded waveguide, it is barely noticeable through the surface of the photonic crystal in the SEM images shown in Figure 70. To improve viewing the embedded

waveguides in the photonic crystal, a post process etch-back was used to reveal individual layers of the photonic crystal and waveguide, as is shown in Figure 71. The waveguide has more photoresist substance too it and therefore etches slower in the etch-back procedure. This allows the waveguide to protrude from the receding etched photonic crystal layers. Figure 71 showing a  $\sim 10 \mu\text{m}$  wide waveguide clearly demonstrate that the waveguide is embedded in the middle of the photonic crystal.



2,500 X Magnification 45° x-sec.    1,000 X Magnification 45° x-sec.    1,000 X Magnification Top-Down

**Figure 71** – Cross-section SEM images of 355 nm 3-exposure 3D PhC, with 244 nm embedded waveguides in positive photoresist, after a wet chemical etch-back of the PhC cleaved cross-section to reveal the embedded waveguide.

## CHAPTER 5

### 3D PHOTONIC CRYSTAL OPTICAL PROPERTIES

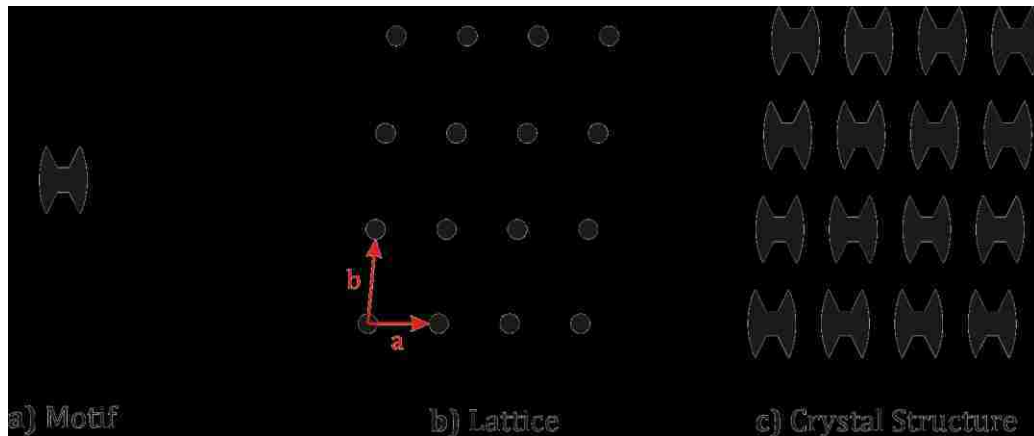
#### ***Introduction to 3D Photonic Crystal Optical Properties***

This chapter is focused on the optical properties of the photonic crystals presented in the previous chapter. The next section presents the crystallographic structure classification of the photonic crystals. With the photonic crystal family and system identified the unit cell of the photonic crystal is derived and used for modeling. The following section contains the modeling results for the photonic crystal optical properties. The band diagram models are plotted using a simulation model that computes definite-frequency eigenstates (harmonic modes) of Maxwell's equations in periodic dielectric structures for arbitrary wave-vectors. Following that section is a section that contains transmission and reflection plots made by measurements of the photonic crystals fabricated in the previous chapter, using a Fourier Transform Infrared (FTIR) spectrometer. The measured transmission and reflection plots are compared to the modeled band diagram plots. All the models and measurements are done for three-exposure and four-exposure three-dimensional photonic crystals made using the multiple-exposure interferometric lithography process.

#### ***Photonic Crystal Structural Classification and Unit Cell***

To model the optical properties of the photonic crystal a representation of the photonic crystal unit cell is first needed. This is accomplished using a MatLAB program to create a three-dimensional representation of the photonic crystal unit cell medium, by

defining an index of refraction matrix of the unit cell. First the unit cell of the photonic crystal must be determined, and to do this the photonic crystal structure must be classified. A crystal structure is a regular arrangement of atoms or molecules. More specifically a crystal structure contains a motif which is the unit cell of a three-dimensional crystal that is repeated over a net of points called a lattice for a three-dimensional crystal, refer to Figure 72.<sup>31</sup> The space lattice of a crystal describes how the motif of a crystal is repeated over three-dimensional space. The basis of the lattice is the set of vectors that describe the direction and distance of lattice points relative to an arbitrary crystal origin, in Figure 72 the basis vectors are shown and labeled in red on the diagram of a two-dimensional lattice.



**Figure 72** – A periodic 2D pattern consisting of a motif and lattice.

All three-dimensional crystal can be classified into 7 crystal systems according to their point groups, and into 7 lattice systems according to their Bravais lattices. A lattice system is a class of lattices with the same point group. In three dimensions there are seven lattice systems: triclinic, monoclinic, orthorhombic, tetragonal, rhombohedral (often confused with the trigonal crystal system), hexagonal, and cubic. The lattice system of a crystal or space group is determined by its lattice but not always by its point

group. A crystal system is a class of point groups. Two point groups are placed in the same crystal system if the sets of possible lattice systems of their space groups are the same. For many point groups there is only one possible lattice system, and in these cases the crystal system corresponds to a lattice system and is given the same name. However, for the five point groups in the trigonal crystal class there are two possible lattice systems for their point groups: rhombohedral or hexagonal. In three dimensions there are seven crystal systems: triclinic, monoclinic, orthorhombic, tetragonal, trigonal, hexagonal, and cubic. The crystal system of a crystal or space group is determined by its point group but not always by its lattice. A crystal family also consists of point groups and is formed by combining crystal systems whenever two crystal systems have space groups with the same lattice. In three dimensions a crystal family is almost the same as a crystal system (or lattice system), except that the hexagonal and trigonal crystal systems are combined into one hexagonal family. In three dimensions there are six crystal families: triclinic, monoclinic, orthorhombic, tetragonal, hexagonal, and cubic. The crystal family of a crystal or space group is determined by either its point group or its lattice, and crystal families are the smallest collections of point groups with this property. The relation between three-dimensional crystal families, crystal systems, and lattice systems is shown in Table 4.<sup>32</sup>

Crystal family	Crystal system	Required symmetries of point group	point groups	space groups	Bravais lattices	Lattice system
Triclinic		None	2	2	1	Triclinic
Monoclinic		1 twofold axis of rotation or 1 mirror plane	3	13	2	Monoclinic
Orthorhombic		3 twofold axes of rotation or 1 twofold axis of rotation and two mirror planes.	3	59	4	Orthorhombic
Tetragonal		1 fourfold axis of rotation	7	68	2	Tetragonal
Hexagonal	Trigonal	1 threefold axis of rotation	5	7	1	Rhombohedral
	Hexagonal	1 sixfold axis of rotation		18	1	Hexagonal
Cubic		4 threefold axes of rotation	7	27		
Cubic		4 threefold axes of rotation	5	36	3	Cubic
<b>Total: 6</b>	<b>7</b>		<b>32</b>	<b>230</b>	<b>14</b>	<b>7</b>

**Table 4** – The relation between 3D crystal families, crystal systems, and lattice systems.

When the crystal systems are combined with the various possible lattice centering: body centering, face centering, base centering; we arrive at the Bravais lattices. They describe the geometric arrangement of the lattice points, and thereby the translational symmetry of the crystal. In three dimensions, there are 14 unique Bravais lattices which are distinct from one another in translational symmetry. All crystalline materials recognized until now (not including quasicrystals) fit in one of these arrangements. The fourteen three-dimensional lattices, classified by crystal system, are shown in Table 5. The Bravais lattices are sometimes referred to as space lattices.<sup>32</sup>

The crystal structure consists of the same group of atoms or nodes, the basis, positioned around each and every lattice point. This group of atoms or nodes therefore repeats indefinitely in three dimensions according to the arrangement of one of the 14 Bravais lattices. The characteristic rotation and mirror symmetries of the group of atoms or unit cell, is described by its crystallographic point group.<sup>32</sup>

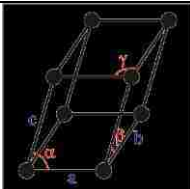
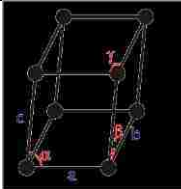
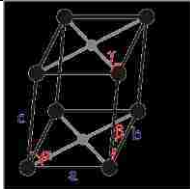

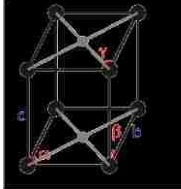
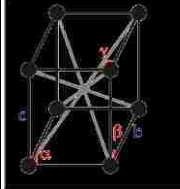
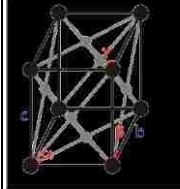
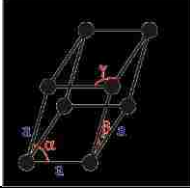
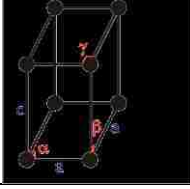
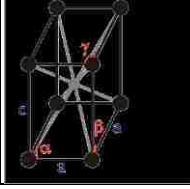
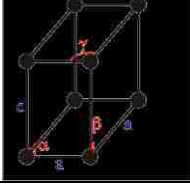
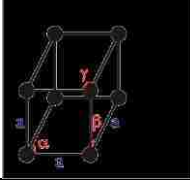
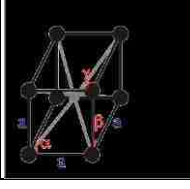
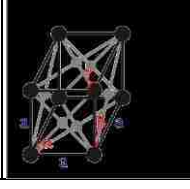
The 7 lattice systems <i>From least to most symmetric</i>	The 14 Bravais Lattices			
1. triclinic, or <i>anorthic</i> (a) $a \neq b \neq c$ $\alpha \neq 90^\circ$ $\beta \neq 90^\circ$ $\gamma \neq 90^\circ$	primitive (aP) 			
2. monoclinic (m) $a \neq b \neq c$ $\alpha \neq 90^\circ$ $\beta = \gamma = 90^\circ$	primitive (mP) 	base-centered (mC) 		
3. orthorhombic (o) $a \neq b \neq c$ $\alpha = \beta = \gamma = 90^\circ$	primitive (oP) 	base-centered (oC) 	body-centered (oI) 	face-centered (oF) 
4. rhombohedral (R) $a = b = c$ $\alpha = \beta = \gamma \neq 90^\circ$	primitive (R) 			
5. tetragonal (t) $a = b \neq c$ $\alpha = \beta = \gamma = 90^\circ$	primitive (tP) 	centered (tI) 		
6. hexagonal (h) $a = b \neq c$ $\alpha = \beta = 90^\circ$ $\gamma = 120^\circ$	primitive (hP) 			
7. cubic (c) $a = b = c$ $\alpha = \beta = \gamma = 90^\circ$	primitive (cP) 	body-centered (cI) 		face-centered (cF) 

Table 5 – The 14 3D Bravais Lattices

The crystallographic point group or crystal class is the mathematical group comprising the symmetry operations that leave at least one point unmoved and that leave the appearance of the crystal structure unchanged. These symmetry operations include: reflection, which reflects the structure across a reflection plane; rotation, which rotates the structure a specified portion of a circle about a rotation axis; inversion, which changes the sign of the coordinate of each point with respect to a center of symmetry or inversion point; and improper rotation, which consists of a rotation about an axis followed by an inversion. Rotation axes (proper and improper), reflection planes, and centers of symmetry are collectively called symmetry elements. There are 32 possible crystal classes. Each one can be classified into one of the seven crystal systems.<sup>32</sup>

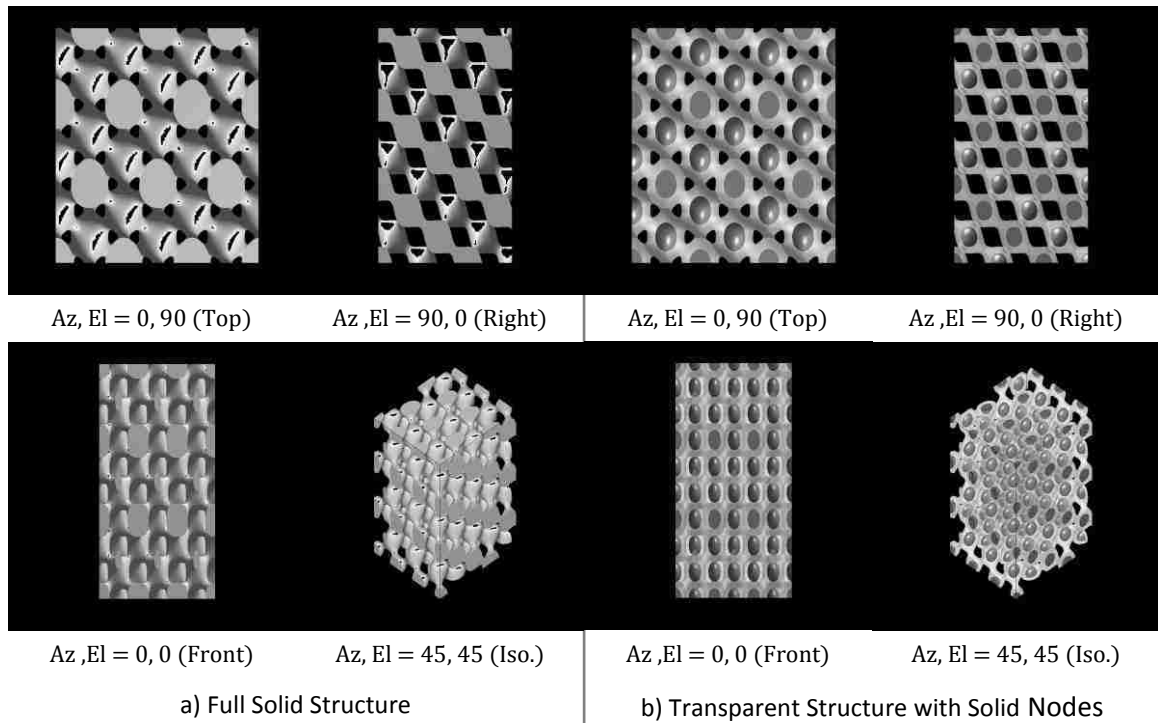
The space group of the crystal structure is composed of the translational symmetry operations in addition to the operations of the point group. These include: pure translations, which move a point along a vector; screw axes, which rotate a point around an axis while translating parallel to the axis; and glide planes, which reflect a point through a plane while translating it parallel to the plane. There are 230 distinct space groups.<sup>32</sup>

The next subsections will classify the photonic crystals of interest in this dissertation according to this crystallography classification. The unit cell will then be identified and modeled. The unit cell will be transposed into reciprocal space according to its Brillouin zone.



## Three-Exposure Photonic Crystal Unit Cell

The first step in determining the three-exposure photonic crystal unit cell is to determine what Bravais lattice the crystal uses. The photonic crystal can be viewed as a periodic pattern of nodes and rods, analogous to atoms and bonds of a semiconductor crystal. It is the location of the photonic crystal nodes, or semiconductor crystal atoms that determine the Bravais lattice. By only looking at the three-exposure photonic crystal made by multiple exposure interferometric lithography shown in Figure 73 (a) it is difficult to determine the Bravais lattice, and very difficult to isolate the unit cell. However if we look just at the nodes of the photonic crystal by making the surface of the photonic crystal model transparent and showing the nodes as a darker solid surface inside the photonic crystal structure, as shown in Figure 73 (b) it becomes much easier to identify the Bravais lattice.

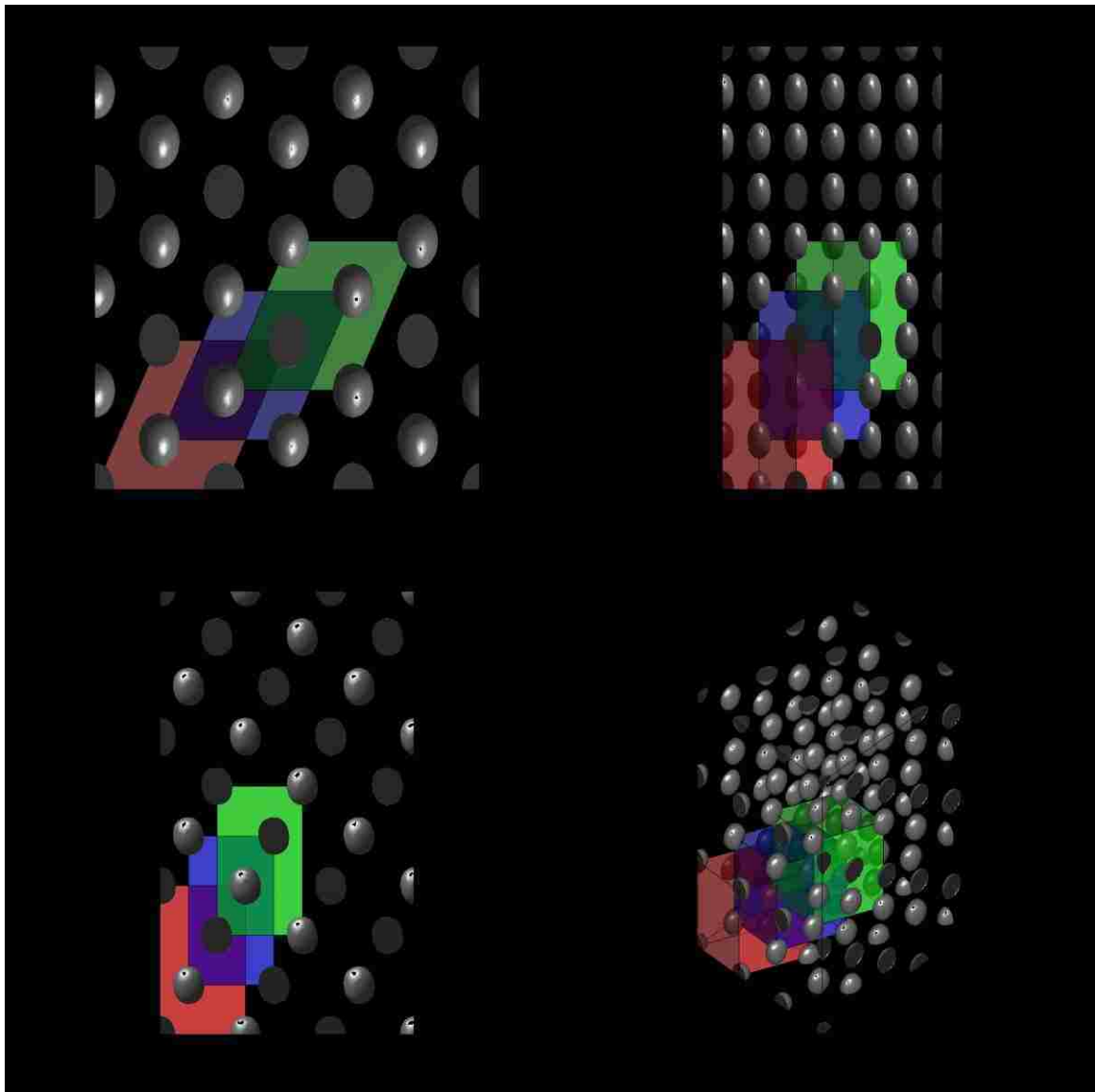


**Figure 73** – Three-exposure 3D photonic crystal structures, used for identifying unit cell.

We also know the period of the photonic crystal made by multiple exposure interferometric lithography in the  $x$  and  $z$  Cartesian coordinates from the exposure beam angles according to Equation 2.39 and Equation 2.41 on page 45. The basis  $(a, b, c)$  of the Bravais lattice in the orthorhombic, tetragonal, and cubic lattice systems are aligned to the axis of the Cartesian coordinate system  $(x, y, z)$  such that  $\vec{a} = ax$ ,  $\vec{b} = by$ ,  $\vec{c} = cz$ ,  $\alpha \equiv \angle \vec{a}\vec{c} = 90^\circ$ ,  $\beta \equiv \angle \vec{b}\vec{c} = 90^\circ$ ,  $\gamma \equiv \angle \vec{a}\vec{b} = 90^\circ$ . For the photonic crystal made by multiple exposure interferometric lithography, the magnitude of the  $a$  and  $b$  basis is equal to the photonic crystal period in the  $x$ -direction, such that  $|a| = |b| = \Lambda_x$ . Similarly the magnitude of the  $c$  basis is equal to the photonic crystal period in the  $z$  direction, such that  $|c| = \Lambda_z$ . For the photonic crystal made by multiple exposure interferometric lithography, the angle  $\alpha$  between the  $a$  and  $c$  basis is  $90^\circ$ , and the angle  $\gamma$  between the  $a$  and  $b$  basis is equal to the rotation angle  $\phi$  between exposures. For the three-exposure photonic crystal experimentally made by interferometric lithography used in this dissertation  $\Lambda_x = 898$  nm,  $\Lambda_z = 1813$  nm, and  $\phi = 120^\circ$ , therefore the crystal basis  $|a| = |b| = 898$  nm  $\neq$   $|c| = 1813$  nm,  $\alpha = \beta = 90^\circ$ , and  $\gamma = 120^\circ$ . Based on these considerations it is recognized that the experimentally made three-exposure photonic crystal is a hexagonal lattice system.

At first glance though it looks as if there might be some form of centering as all of the nodes don't lie on the primitive hexagonal lattice sites; however there are no Bravais lattice centering types for the hexagonal lattice system. Upon close inspection what is happening is that the photonic crystal contains interpenetrating hexagonal primitive lattices. This is similar to the diamond lattice which contains two interpenetrating cubic

face-centered lattices offset by  $1/4$  of the unit cell in each dimension. For the case of three-exposure photonic crystal experimentally made by interferometric lithography used in this dissertation there are three interpenetrating hexagonal primitive lattices offset by a  $0$ ,  $1/3$  and  $2/3$  of the unit cell respectively in each dimension. Thus the motif of the three-exposure photonic crystal structure consists of a single hexagonal primitive lattice plus two partial hexagonal primitive lattices. This is easily seen in Figure 74 of the three-exposure photonic crystal with only the nodes displayed, and with the primary unit cell highlighted in red plus the secondary offset unit cell highlighted in blue and the third offset unit cell highlighted in green.



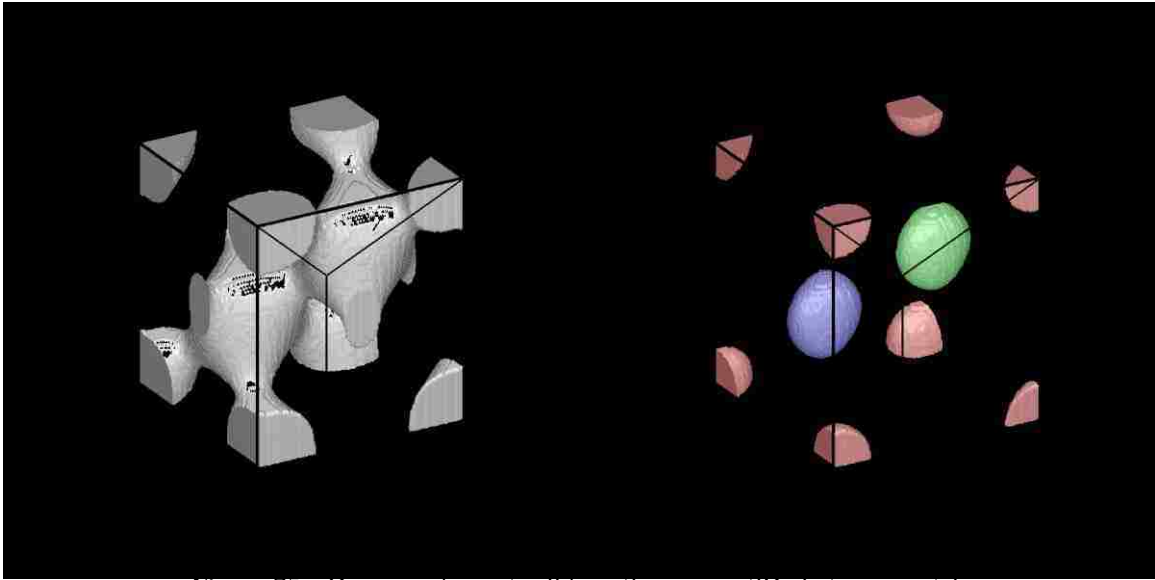
Az, El = 0, 0 (Front)

Az, El = 45, 45 (Iso.)

**Figure 74** – 3-exposure 3D PhC nodes, with primary unit cell in highlighted in red, plus interpenetrating unit cells highlighted in blue and green.

The unit cell for the photonic crystal experimentally made by three-exposure interferometric lithography is the primary hexagonal primitive unit cell highlighted in red shown in Figure 74. The single unit cell representations of the three-beam exposure three-dimensional photonic crystal is depicted in Figure 75 with the full photonic crystal

structure (Figure 75 a) that was used for optical modeling, and with the photonic crystal nodes only colored corresponding to the interleaved unit cell (Figure 75 b).

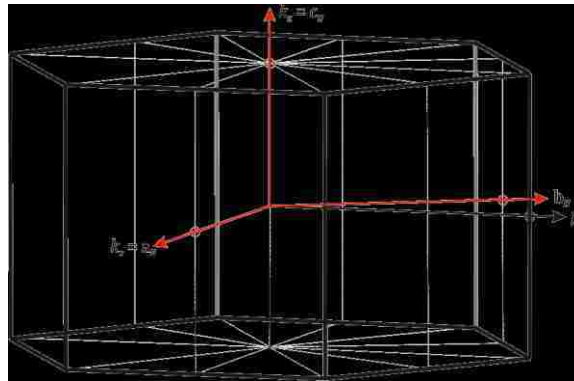


**Figure 75** – Diagram of a unit cell for a 3-exposure 3D photonic crystal.

By looking at Figure 75 it is easily identified that the unit cell contains 3 nodes;  $1/6$  of a *red* node at the four obtuse corners, plus  $1/12$  of a *red* node at the four acute corners, plus of full *blue* node from the corner of the first interleaved unit cell  $1/3$  up the unit cell diagonal, plus a second full *green* node from the corner of the second interleaved unit cell  $2/3$  up the unit cell diagonal ( $4 \times 1/6 + 4 \times 1/12 + 1 + 1 = 3$ ).

For the optical modeling is it necessary to know the Brillouin zone of the photonic crystal and corresponding critical k-vectors points. The first Brillouin zone is a uniquely defined primitive cell in reciprocal space. The boundaries of this cell are given by planes related to points on the reciprocal lattice. The importance of the Brillouin zone stems from the Bloch wave description of waves in a periodic medium, in which it is found that the solutions can be completely characterized by their behavior in a single Brillouin zone. This is what is done in the MPB modeling software that will be used to evaluate the

photonic crystal band diagrams in the next section. Taking surfaces at the same distance from one element of the lattice and its neighbors, the volume included is the first Brillouin zone. Another definition is as the set of points in k-space that can be reached from the origin without crossing any Bragg plane. There are also second, third, etc., Brillouin zones, corresponding to a sequence of disjoint regions (all with the same volume) at increasing distances from the origin. As a result, the first Brillouin zone is often called simply the Brillouin zone. The Brillouin zone for a hexagonal Bravais lattice is shown in Figure 76, with the unit vectors shown in red.



**Figure 76** – Brillouin zone for the hexagonal unit cell.

Critical points are several points of high symmetry in the Brillouin zone that are of special interest. These are the k-point sets that will be mapped on the band diagram, due to their high symmetry. In order to determine the Brillouin zone critical k-points, the symmetry and geometry of the photonic crystal must be known. This requires determining the photonic crystal point and space groups. The hexagonal lattice system has 12 point groups and 45 space groups as given in Table 4. The interleaved unit cells and rod between the nodes break some of the symmetry of the hexagonal unit cell.

The first step is to determine the point group. Point groups are formed by set of symmetry operation of reflection, rotation, improper rotation, and inversion that are compatible with the 14 Bravais lattices. The hexagonal lattice system has 12 point groups out of the total 32 crystallographic point groups. The point group will be determined by counting the ways in which the symmetry element can be combined to form a single closed set. The first symmetry operation is the proper rotation. For the three-exposure photonic crystal there is a primary three-fold axis of rotation along the [111] direction of the unit cell. This makes the photonic crystal part of the trigonal crystal system, which drops the point group down to 5 point groups from 12 point groups (the 5 point groups being  $\mathbf{3}$ ,  $\bar{\mathbf{3}}$ ,  $\mathbf{32}$ ,  $\mathbf{3m}$ , and  $\bar{\mathbf{3}}\frac{2}{m}$ ).

The symmetries of the 5 point groups of the trigonal crystal system are given as follows. The first trigonal point group  $\mathbf{3}$  has only a three-fold rotational symmetry around the primary [111] rotation axis. The second trigonal point group  $\bar{\mathbf{3}}$  has a three-fold rotational symmetry around the primary [111] rotation axis, with inversion symmetry along the primary rotation axis. The third trigonal point group  $\mathbf{32}$  has a three-fold rotational symmetry around the primary [111] rotation axis, and two-fold rotational symmetry along the tertiary  $[1\bar{1}0]$  rotation axis, which is perpendicular to the primary [111] axis. The fourth trigonal point group  $\mathbf{3m}$  has a three-fold rotational symmetry around the primary [111] rotation axis, containing a rotational mirror plane along the primary axis. The fifth and last trigonal point group  $\bar{\mathbf{3}}\frac{2}{m}$  has a three-fold rotational symmetry around the primary [111] rotation axis, with inversion symmetry along the

primary rotation axis, and a two-fold rotational symmetry along the tertiary  $[1\bar{1}0]$  rotation axis with a mirror plane perpendicular to the tertiary axis.

For the three-exposure photonic crystal there are no secondary or tertiary axes of proper or improper rotation. Thus the remaining point groups are  $\mathbf{3}$ ,  $\bar{\mathbf{3}}$ ,  $\mathbf{3m}$ . The next symmetry operator is inversion symmetry, in which there is an equivalent structure imaged thru the unit cell origin perpendicular to the primary axis of rotation such that for nodes at point  $x, y, z$  there exists equivalent nodes at  $-x, -y, -z$ . The three-exposure photonic crystal does exhibit such inversion symmetry and thus is part of the  $\bar{\mathbf{3}}$  point groups. The last operation is reflection in which there is a mirror plane perpendicular to a principal axis. The three-exposure photonic crystal does not have any reflection symmetry. The three-exposure photonic crystal is a member of the  $\bar{\mathbf{3}}$  point group.

The second step is to determine the space group. The space groups takes the point group symmetries and translates them along the Bravais lattice via one of three translational symmetries operation: pure translation, screw axis, and glide planes. For the  $\bar{\mathbf{3}}$  point group there are only two space groups  $\mathbf{P}\bar{\mathbf{3}}$  and  $\mathbf{R}\bar{\mathbf{3}}$ . However for the hexagonal lattice system only the  $\mathbf{P}\bar{\mathbf{3}}$  space group exists. The  $\mathbf{R}\bar{\mathbf{3}}$  space group is for the rhombohedral lattice system. The experimentally made three-exposure photonic crystal is a member of the  $\mathbf{P}\bar{\mathbf{3}}$  space group (international space group #147).

Knowing the three-exposure photonic crystal is part of space group #147, the critical  $k$ -points and necessary unique  $k$ -vectors to calculate over the Brillouin can be simply calculated or looked up.<sup>33</sup> The following Table 6 lists the critical  $k$ -points for the



hexagonal Brillouin zone, and Figure 77 shows a diagram of the hexagonal Brillouin zone with all k-points labeled.

Symbol	Coordinates	Description
$\Gamma$	0, 0, 0	Center of the Brillouin zone
A	0, 0, 1/2	Center of a hexagonal face
H	2/3, 1/3, 1/2	Corner Point
K	2/3, 1/3, 0	Middle of an edge joining two rectangular faces
L	1/2, 0, 1/2	Middle of an edge joining a hexagonal and a rectangular faces
M	1/2, 0, 0	Center of a rectangular face
$\Delta$	0, 0, 0 < z < 1/2	Points along the line between the $\Gamma$ and A points
R	0 < x < 1/2, 0, 1/2	Points along the line between the $\Delta$ and A points
Q	0 < x < 2/3, 0 < y < 1/2, 1/2	Points along the line between the H and A points
U	1/2, 0, 0 < z < 1/2	Points along the line between the M and L points
P	2/3, 1/3, 0 < z < 1/2	Points along the line between the K and H points
S	1/2 < x < 2/3, 0 < y < 1/3, 1/2	Points along the line between the $\Delta$ and H points
T	1/2 < x < 2/3, 0 < y < 1/3, 0	Points along the line between the M and K points
$\Lambda$	0 < x < 2/3, 0 < y < 1/3, 0	Points along the line between the $\Gamma$ and K points

Table 6 – Critical points of the hexagonal Brillouin zone.

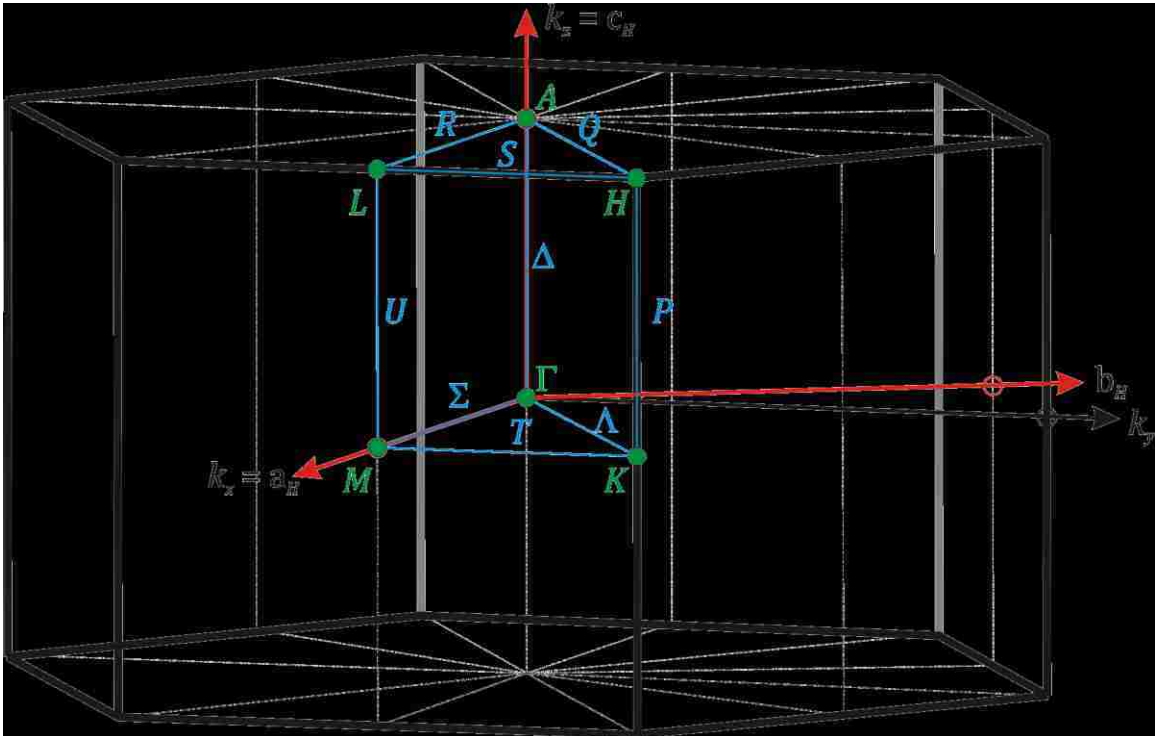
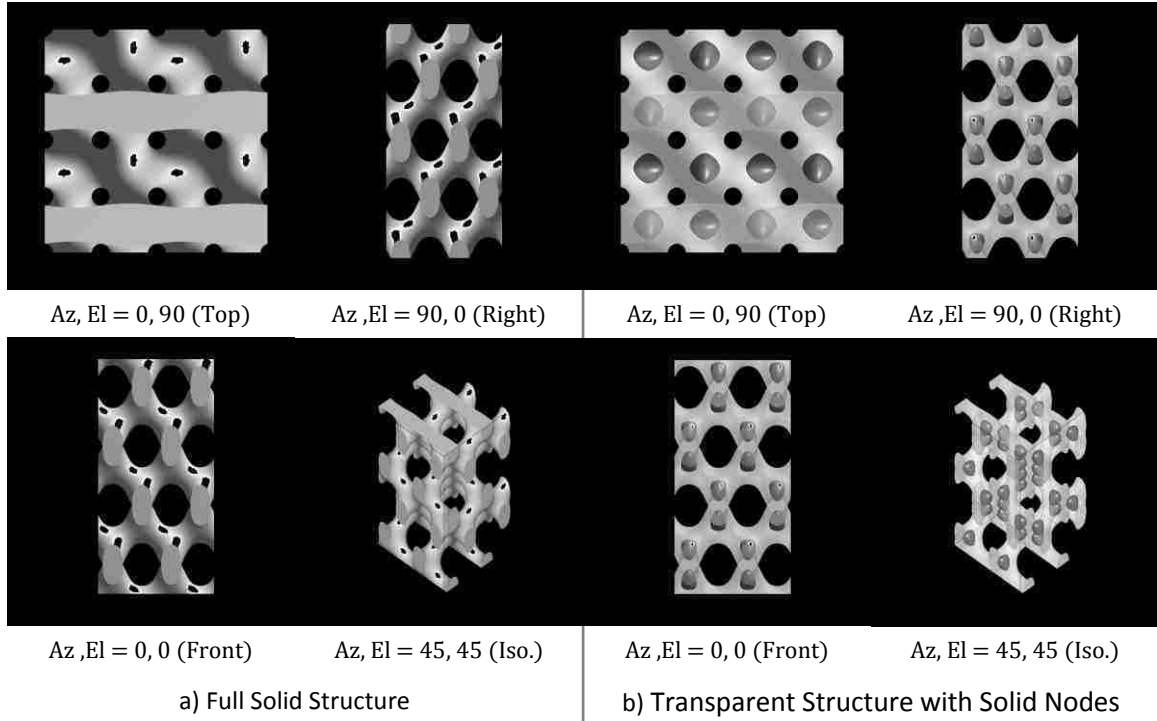


Figure 77 – Brillouin zone for the hexagonal unit cell with labeled k-points.

With the unit cell shown in Figure 75, the space group determined to be international space group #147, and the Brillouin zone with all the associated k-point determined shown in Figure 77, it is possible to run optical simulations on the three-exposure interferometric lithography photonic crystal model.

### **Four-Exposure Photonic Crystal Unit Cell**

Just like the three-exposure photonic crystal the first step is to determine what Bravais lattice the crystal uses. By only looking at the four-exposure photonic crystal made by multiple exposure interferometric lithography shown in Figure 78 (a) it is difficult to determine the Bravais lattice type it is, and very difficult to isolate the unit cell from the figure. However if we look just at the nodes of the photonic crystal by making the surface of the photonic crystal model transparent and showing the node as a darker solid surface inside the photonic crystal structure, as shown in Figure 73 (b) it becomes much easier to identify the Bravais lattice.

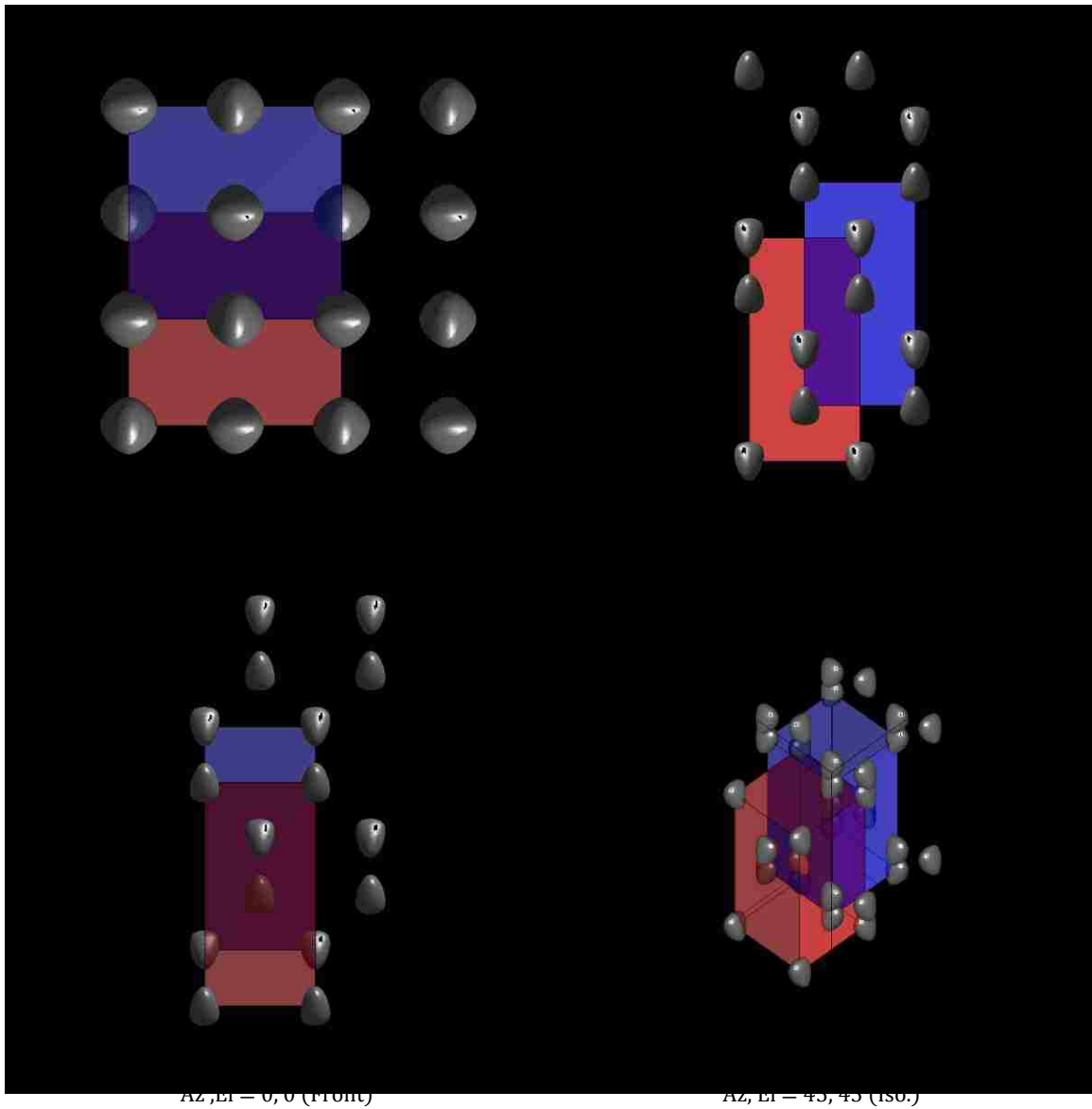


**Figure 78** – Four-exposure 3D photonic crystal structures, used for identifying unit cell.

We also know the period of the photonic crystal made by multiple exposure interferometric lithography in the  $x$  and  $z$  Cartesian coordinates from the exposure beam angles according to Equation 2.39 and Equation 2.41 on page 45. For the four-exposure photonic crystal experimentally made by interferometric lithography used in this dissertation  $\Lambda_x = 898$  nm,  $\Lambda_z = 1813$  nm, and  $\phi = 90^\circ$ , therefore the crystal basis  $|a| = |b| = 898$  nm  $\neq$   $|c| = 1813$  nm,  $\alpha = \beta = \gamma = 90^\circ$ . Based on these numbers it is recognized that the experimentally made four-exposure photonic crystal is a tetragonal lattice system.

At first glance though it looks as if there might be some form of centering as all of the nodes don't lie on the primitive tetragonal lattice sites; and there is a Bravais lattices centering type for the tetragonal lattice system, the tetragonal centered lattice. There is no distinction between body-centered and face-centered tetragonal Bravais lattices, because by changing the tetragonal face-centered lattice orientation the result is a smaller

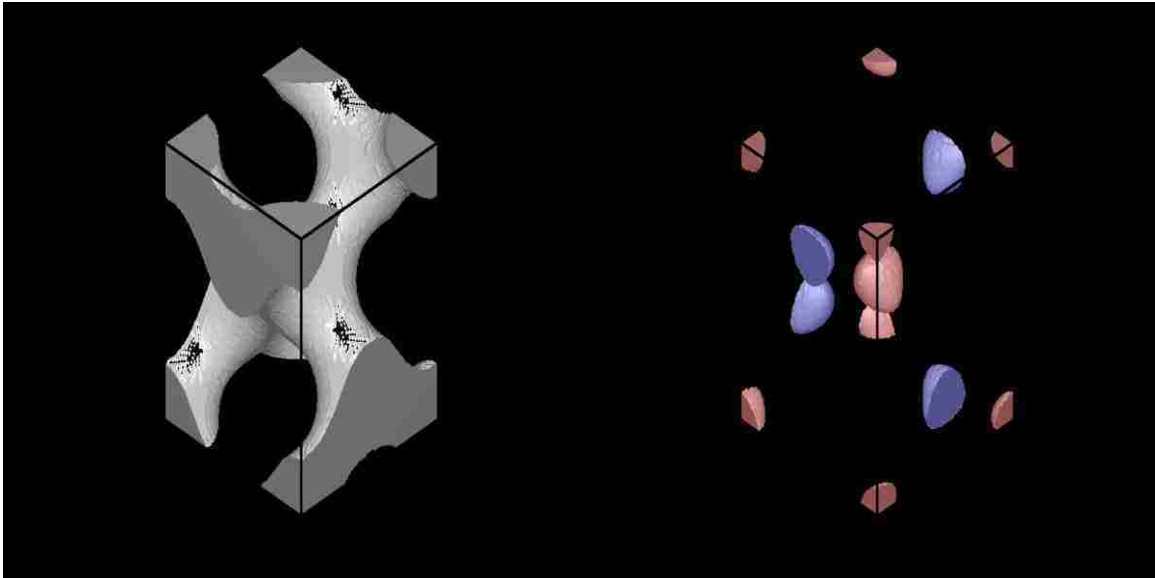
tetragonal body-centered lattice and is therefore not a unique lattice upon itself. For the four-exposure experimental photonic crystal there are nodes that line up with the tetragonal centered Bravais lattice, however not all of the nodes do. Similar to the three-exposure experimental photonic crystal, upon close inspection what is happening is that the photonic crystal contains interpenetrating tetragonal centered lattices. Just like the diamond lattice which contains two interpenetrating cubic face-centered lattices offset by  $1/4$  of the unit cell in each dimension. For the case of the four-exposure photonic crystal experimentally made by interferometric lithography used in this dissertation there are two interpenetrating tetragonal centered lattices offset by a  $1/2bx$ , and  $1/4cz$  of the unit cell. This offset is not along the diagonal of the unit cell, as in the case of the diamond unit cell or previous three-exposure photonic crystal, but along a portion of the  $yz$  face that is not along on the  $yx$  face diagonal. Thus the motif of the four-exposure photonic crystal structure consists of a single tetragonal centered lattice plus a partial tetragonal centered lattice. This is easily shown in Figure 79 of the four-exposure photonic crystal with only the nodes displayed, and with the primary unit cell highlighted in red and the secondary offset unit cell highlighted in blue.



**Figure 79** – 4-exposure 3D PhC nodes, with primary unit cell in highlighted in red, plus interpenetrating unit cell highlighted in blue.

The unit cell for the photonic crystal experimentally made by four-exposure interferometric lithography is the primary tetragonal centered primitive unit cell highlighted in red shown in Figure 79. The single unit cell representations of the four-beam exposure three-dimensional photonic crystal is depicted in Figure 80 with the full photonic crystal structure (Figure 80 a) that was used for optical modeling, and with the

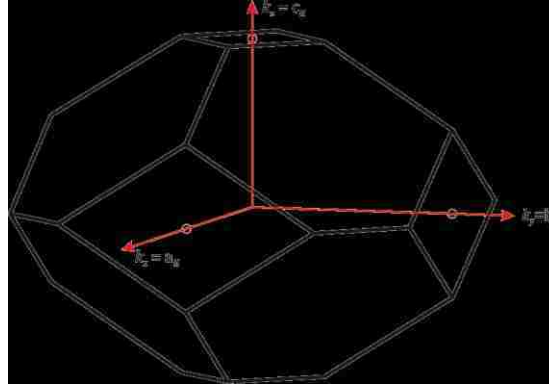
photonic crystal nodes only colored corresponding to the interleaved unit cell (Figure 80 b).



**Figure 80** – Diagram of a unit cell for a 4-exposure 3D photonic crystal.

By looking at Figure 80 it is easily identified that the unit cell contains 4 nodes; an  $1/8$  of a *red* node at each of the eight corners, plus one full *red* node in the center of the unit cell, plus half a *blue* node each from two corners of the interleaved unit cell, and plus half a *blue* node each from the center nodes of the interleaved unit cells ( $8 \times 1/8 + 1 + 2 \times 1/2 + 2 \times 1/2 = 4$ ).

For the optical modeling is it necessary to know the Brillouin zone of the photonic crystal and corresponding critical k-vector points. The Brillouin zone for a tetragonal centered Bravais lattice is shown in Figure 81, with the unit vectors shown in red. This Brillouin zone is in the shape of a truncated octahedron.



**Figure 81** – Brillouin zone for the tetragonal centered unit cell.

In order to determine the Brillouin zone critical k-points, the symmetry and geometry of the photonic crystal must be known. This requires determining the photonic crystal point and space groups. The tetragonal lattice system has 7 point groups and 68 space groups as given in Table 4. The interleaved unit cells and rod between the nodes break some of the symmetry of the tetragonal centered unit cell.

The first step is to determine the point group. Point groups are formed by set of symmetry operation of reflection, rotation, improper rotation, and inversion that are compatible with the 14 Bravais lattices. The tetragonal lattice system has 7 point groups out of the total 32 crystallographic point groups (the 7 point groups being  $4$ ,  $\bar{4}$ ,  $\frac{4}{m}$ ,  $422$ ,  $4mm$ ,  $\bar{4}2m$ , and  $\frac{4}{m} \frac{2}{m} \frac{2}{m}$ ). The point group will be determined by counting the ways in which the symmetry element can be combined to form a single closed set.

The symmetries of the 7 point groups of the tetragonal crystal system are given as follows. The first tetragonal point group  $4$  has only a four-fold rotational symmetry around the primary  $[001]$  rotation axis. The second tetragonal point group  $\bar{4}$  has a four-fold rotational symmetry around the primary  $[001]$  rotation axis with inversion symmetry

along the primary rotation axis. The third tetragonal point group  $\frac{4}{m}$  has a four-fold rotational symmetry around the primary [001] rotation axis with a mirror plane perpendicular to the primary axis. The fourth tetragonal point group **422** has a four-fold rotational symmetry around the primary [001] rotation axis and two-fold rotational symmetry along the secondary  $\langle 100 \rangle$  and tertiary  $\langle 110 \rangle$  rotation axes. The fifth tetragonal point group **4mm** has a four-fold rotational symmetry around the primary [001] rotation containing two rotating perpendicular mirror planes along the primary axis. The sixth tetragonal point group  $\bar{4}2m$  has a four-fold rotational symmetry around the primary [001] rotation axis with inversion symmetry along the primary rotation axis, and two-fold rotational symmetry along the secondary  $\langle 100 \rangle$  axis with mirror planes bisecting the two-fold axis. The seventh and last tetragonal point group  $\frac{4}{m} \frac{2}{m} \frac{2}{m}$  has a four-fold rotational symmetry around the primary [001] rotation axis with a mirror plane perpendicular to the primary axis, and two-fold rotational symmetry along the secondary  $\langle 100 \rangle$  and tertiary  $\langle 110 \rangle$  rotation axes with corresponding perpendicular mirror planes.

The first symmetry operation is the proper rotation. For the four-exposure photonic crystal there is a primary four-fold axis of rotation along the [001] direction of the unit cell. There are two secondary two-fold axis of rotations along the  $\langle 100 \rangle$  and  $\langle 110 \rangle$  direction. This drops the point group down to 2 point groups from 7 point groups (the two point groups being **422**, and  $\frac{4}{m} \frac{2}{m} \frac{2}{m}$ ). For the four-exposure photonic crystal there are also perpendicular mirror planes coinciding with each proper rotation axis. The four-exposure photonic crystal is therefore a member of the  $\frac{4}{m} \frac{2}{m} \frac{2}{m}$  (or **4/mmm** in shorthand notation) point group.



The second step is to determine the space group. The space groups takes the point group symmetries and translates them along the Bravais lattice via one of three translational symmetries operation: pure translation, screw axis, and glide planes. For the  $\frac{4}{m} \frac{2}{m} \frac{2}{m}$  point group there are 20 space groups. However for the tetragonal centered Bravais lattice only 4 space group exist (the four space groups being  $\mathbf{I} \frac{4}{m} \frac{2}{m} \frac{2}{m}$ ,  $\mathbf{I} \frac{4}{m} \frac{2}{c} \frac{2}{m}$ ,  $\mathbf{I} \frac{4_1}{a} \frac{2}{m} \frac{2}{d}$ , and  $\mathbf{I} \frac{4_1}{a} \frac{2}{c} \frac{2}{d}$ ). These are known as the non-symmorphic space groups. These space groups are formed by combining the  $\frac{4}{m} \frac{2}{m} \frac{2}{m}$  point group with screw-rotations and/or glide planes. The four-exposure photonic crystal exhibits screw rotation only around the point group primary proper rotation axis, and thus making the space group either  $\mathbf{I} \frac{4_1}{a} \frac{2}{m} \frac{2}{d}$  or  $\mathbf{I} \frac{4_1}{a} \frac{2}{c} \frac{2}{d}$ . For each axis that exhibits a glide plane the mirror plane letter is replaced by the appropriate glide plane letter. Because the four-exposure photonic crystal has a interpenetrating unit cell formed by copying the primary tetragonal centered lattice along glide planes on the x-axis and z-axis only, with no glide plane along the y-axis. The experimentally made four-exposure photonic crystal is a member of the  $\mathbf{tI} \frac{4_1}{a} \frac{2}{m} \frac{2}{d}$  space group, otherwise known as the **tI4/amd** space group (international space group #141).

Knowing the three-exposure photonic crystal is part of space group #141, the critical  $k$ -points and necessary unique  $k$ -vectors to calculate over the Brillouin can be simple calculated or looked up.<sup>33</sup> The following Table 7 lists the critical  $k$ -points for the hexagonal Brillouin zone, and Figure 82 shows a diagram of the hexagonal Brillouin zone with all  $k$ -points labeled.

Symbol	Coordinates	Description
$\Gamma$	0, 0, 0	Center of the Brillouin zone
M	0, 0, 1/2	Center of a square face on c axis
X	0, 1/2, 0	Center of a square face on a or b axis
N	1/4, 1/4, 1/4	Center of hexagonal face
P	0, 1/2, 1/4	Corner point joining three edges
R	1/4, 1/2, 0	Corner point joining three edges
G	1/4, 1/4, 1/2	Corner point joining three edges
S	1/8, 1/8, 1/2	Middle of an edge joining a hexagonal and a square face
T	0, 0, 1/4	Middle of line between the $\Gamma$ and M points
$\Delta$	0, 0 < y < 1/2, 0	Points along the line between the $\Gamma$ and X points
$\Lambda$	0, 0, 0 < z < 1/2	Points along the line between the $\Gamma$ and A points
$\Sigma$	0 < x < 1/2, 0 < y < 1/2, 0	Points along the line between the $\Gamma$ and $S_0$ points
U	0, 0 < y < 1/4, 1/2	Points along the line between the M and G points
F	0 < x < 1/8, 0 < y < 1/8, 1/2	Points along the line between the K and H points
Q	1/4, 1/4 < y < 1/2, 1/4	Points along the line between the N and P points
W	0, 1/2, 0 < z < 1/4	Points along the line between the X and P points
Y	0 < x < 1/4, 1/2, 0	Points along the line between the X and R points

Table 7 – Critical points of the tetragonal centered Brillouin zone.

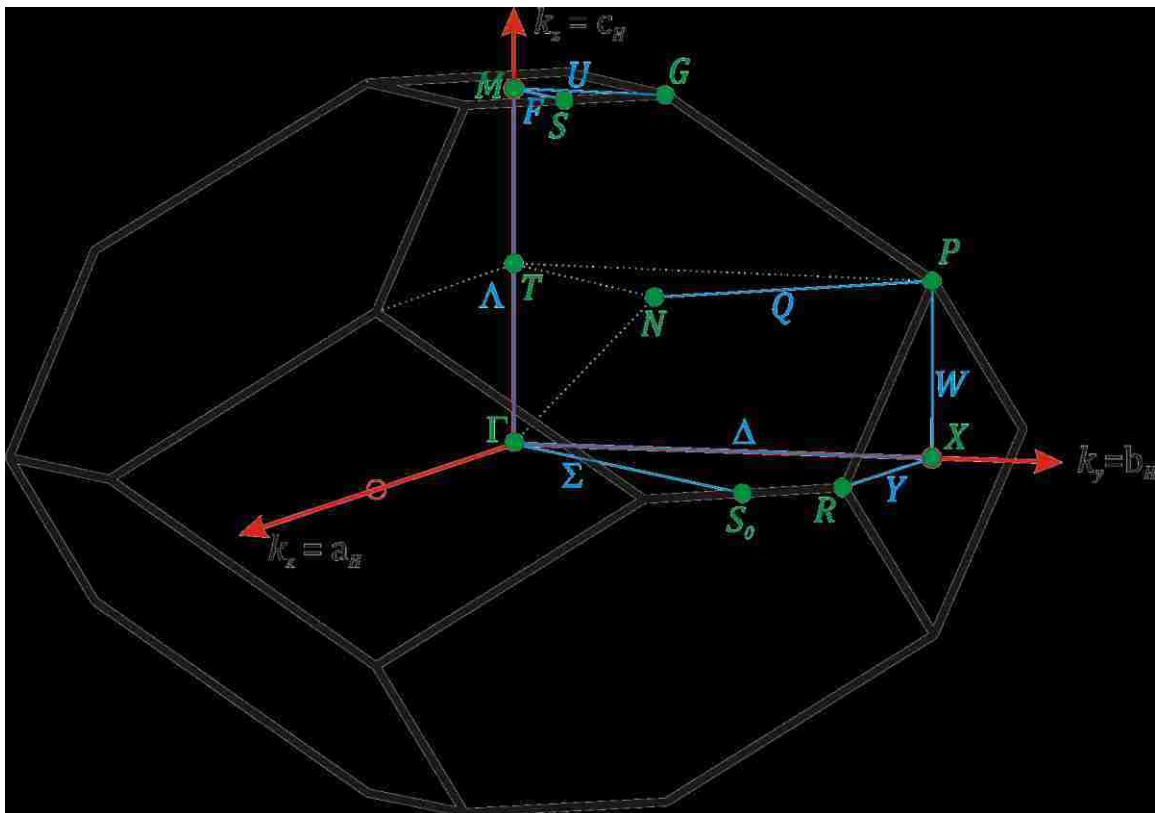


Figure 82 – Brillouin zone for the tetragonal centered unit cell with labeled  $k$ -points.

With the unit cell shown in Figure 80, the space group determined to be international space group #141, and the Brillouin zone with all the associated k-point determined shown in Figure 82, it is possible to run optical simulations on the three-exposure interferometric lithography photonic crystal model.

### ***Band Diagrams of the Photonic Crystals***

With the photonic crystal basis and unit cell known it is possible to model the optical properties of the photonic crystal. An open source photonic crystal modeling software package was used. The MIT Photonic-Bands (MPB) package is a free program for computing the band structures (dispersion relations) and electromagnetic modes of periodic dielectric structures, on both serial and parallel computers. It was developed by Steven G. Johnson at MIT along with the Joannopoulos Ab Initio Physics group.

“MPB” uses a plane wave expansion computational technique that computes definite-frequency eigenstates (harmonic modes) of Maxwell's equations in periodic dielectric structures for arbitrary wave-vectors<sup>34</sup>. The next section uses MPB for calculating the photonic crystal band diagrams.

The band diagram models are generated for photonic crystals made by both three-beam and four-beam multiple-exposure interferometric lithography. The MPB software uses a matrix defining the photonic crystal unit cell defined in the previous section as an input to the photonic crystal simulator software, in addition to a script file that describes the crystal basis, the k-vectors of its Brillouin zone, and simulation parameters.

The unit cells of the photonic crystals that were depicted in Figure 75 and Figure 80 were entered into the simulation software as files containing an epsilon matrix, which

is a four-dimensional matrix of  $X$ ,  $Y$ ,  $Z$ , and  $n^2$ . Where the value  $n$  equals 1.0 for the voids of the photonic crystal, and equals the square of the index of refraction of the photoresist ( $n_r = 1.7$ ) that makes the solid part of the photonic crystal. The matrix is generated using the MatLAB program found in Appendix J, which creates the matrix in a HDF5 file named “epsilon.m” that is used by MPB modeling software

The script files “MPB3Exp3DPhC.ctf” and “MPB4Exp3DPhC.ctf” for executing the MPB program are also found in Appendix K. The scrip file is run by using the command line syntax “mpb *ScriptFile.ctf* >& *OutputFile.out*”. The output of MPB is piped to the output file name given. The band diagram data is found in the output file on lines that precede with the word “freqs”. To create a text file of just the band diagram data the command “grep freqs *OutputFile.out* > *BandData.dat*” is issued. The *BandData.dat* file is a comma delaminated text file of the band diagram, which is then imported into a spreadsheet program and graphed. If the photonic crystal simulation find a bandgap it is also found in the output file on lines that precede with the word “Gap”. To create a text file of just the bandgap regions data the command “grep Gap *OutputFile.out* > *BandgapData.dat*” is issued. It may be worthy to note that even on a modern high speed computer workstation it take several hours just to compute the band diagram of a single three-dimensional photonic crystals presented in this section.

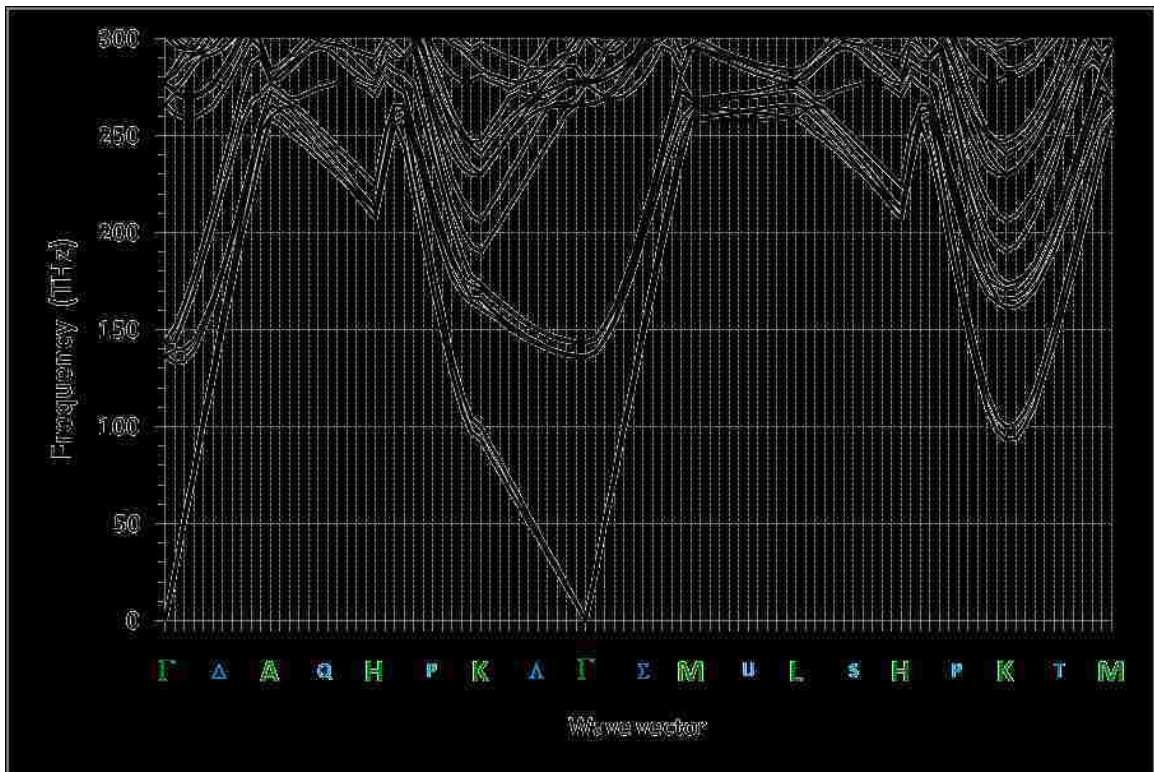
The following two sections will present the simulated MPB band diagram data for both the three-exposure and four-exposure photonic crystal models, based on the experimentally made photonic crystals used in this dissertation. Additional band diagram data will also be presented and compared to FTIR measurements made on the experimental photonic crystals.

## Three-Exposures Photonic Crystal Band Diagram

The band diagram for a three-exposure three-dimensional photonic crystal is generated using the following Linux commands:

- `mpb MPB3Exp3DPhC.ctf >& MPB3Exp3DPhC.out`
- `grep freqs MPB3Exp3DPhC.out > MPB3Exp3DPhC.dat`

The “MPB3Exp3DPhC.ctf” script file for executing the MPB program is found in Appendix K. The band diagram for a three-exposure three-dimensional photonic crystal is shown in Figure 83.



**Figure 83** – Band gap diagram for 3-exposure photonic crystal.

As is seen in Figure 83 there is not a complete bandgap for this photonic crystal. The critical  $k$ -points of high symmetry are listed along the horizontal axis in green, with the lines of high symmetry listed in cyan. There is no complete bandgap, in part because

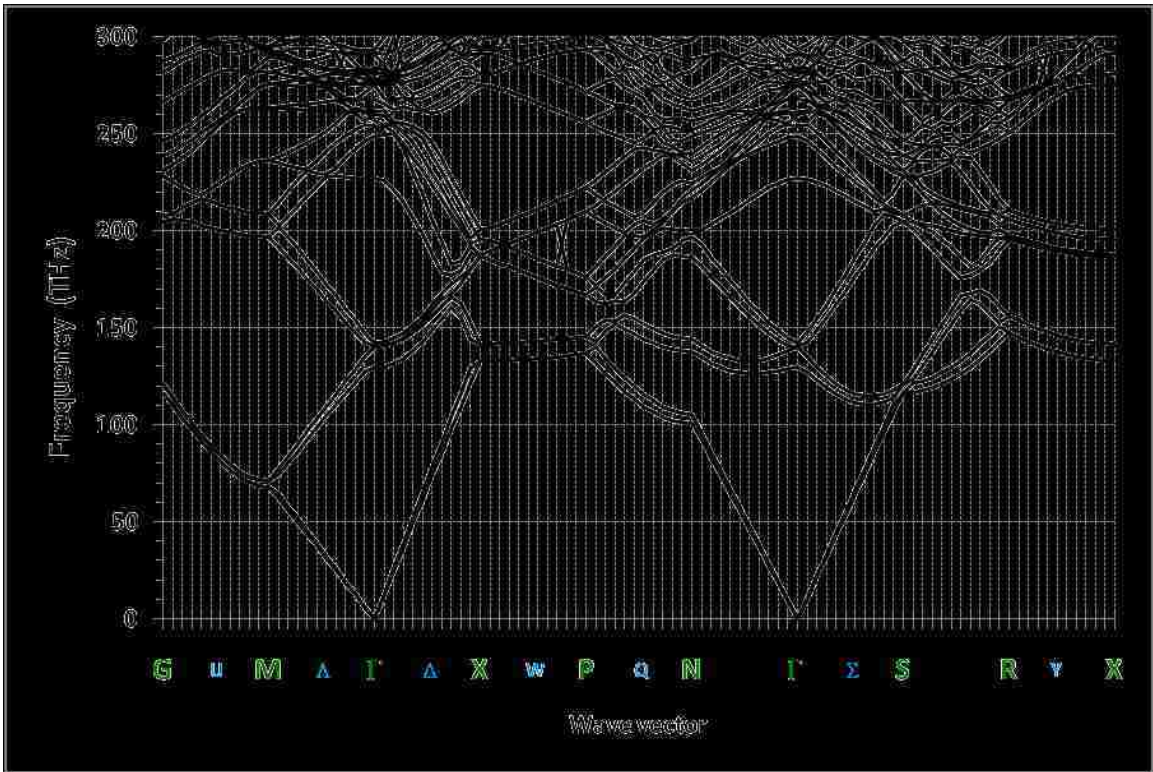
the index difference between the solid and void parts of the photonic crystal is not large enough. There are only a partial bandgaps along particular  $k$ -vectors. There are post fabrication methods that increase the photonic crystal refractive index contrast to solve this initial limitation, which are presented in Chapter 6.

## **Four-Exposures Photonic Crystal Band Diagram**

The band diagram for a four-exposure three-dimensional photonic crystal is generated using the following Linux commands:

- `mpb MPB4Exp3DPhC.ctf >& MPB4Exp3DPhC.out`
- `grep freqs MPB4Exp3DPhC.out > MPB4Exp3DPhC.dat`

The “MPB4Exp3DPhC.ctf” script file for executing the MPB program is found in Appendix K. The band diagram for a four-exposure three-dimensional photonic crystal is shown in Figure 84.



**Figure 84** – Band gap diagram for 4-exposure photonic crystal.

As is seen in Figure 84 there is not a complete bandgap for this photonic crystal either. The critical  $k$ -points of high symmetry are listed along the horizontal axis in green, with the lines of high symmetry listed in cyan. There is no complete bandgap, in part because the index difference between the solid and void parts of the photonic crystal are not large enough. There are only a partial bandgaps along particular  $k$ -vectors. There are post fabrication methods that increase the photonic crystal refractive index contrast to solve this limitation, which are presented in Chapter 6.

### **3D Photonic Crystals FTIR Measurements**

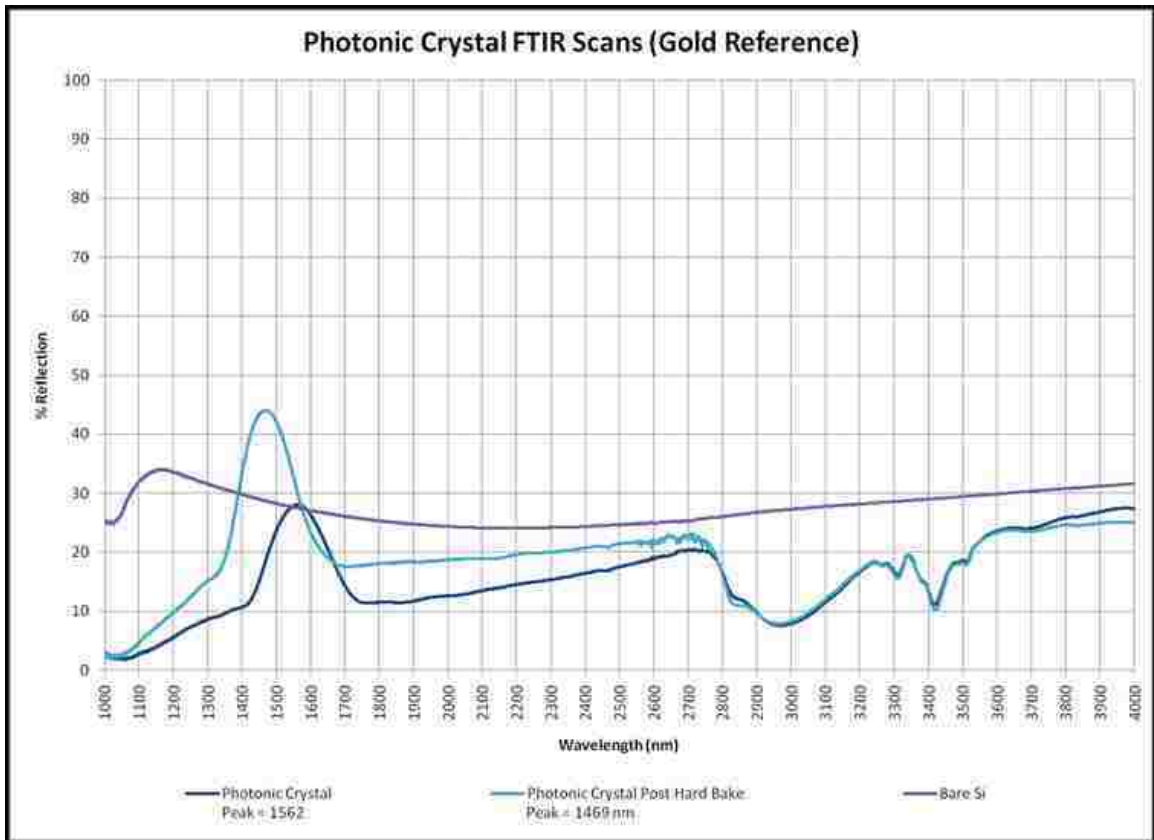
Some of the experimentally made photonic crystals were fabricated on double-sided polished silicon wafers. These wafers are transparent in the infrared, allowing the measurements of infrared light transmitted through and reflected off of the three-dimensional photonic crystals. Using a Nicolet Magna-IR 760 FTIR spectrometer the normal incident reflection and transmission curves were collected for the experimental three-dimensional photonic crystals. The FTIR is setup using a quartz beam-splitter and a DTGS detector with a KBr window. The transmission measurements were made with the IR light incident normal to the wafer plane. The reflection measurements were made using a jig, consisting of three mirrors and sample holder, placed in the FTIR transmission beam-path such that the IR light is incident  $7^\circ$  off-axis to the wafer plane. The first section of plots is for the three-exposure process that creates a three-dimensional photonic crystal with a hexagonal symmetry of the surface  $\langle 111 \rangle$  plane. The second section of plots is for the four-exposure process that creates a three-dimensional photonic crystal with rectangular symmetry of the surface  $\langle 100 \rangle$  plane.

#### **Three-Exposures Transmission & Reflection Plots**

The first set of plots will be of three-dimensional photonic crystals made using three-exposure interferometric lithography. The photonic crystal stack and process parameters are the same as the one used in the previous chapter and are given in Table 8 of Appendix C. The reflection measurement used a gold coated silicon wafer as the reflectance reference measurement, in other words the reflectance off of the photonic crystals on a silicon wafer is compared to the reflectance off of a gold coated silicon wafer. The



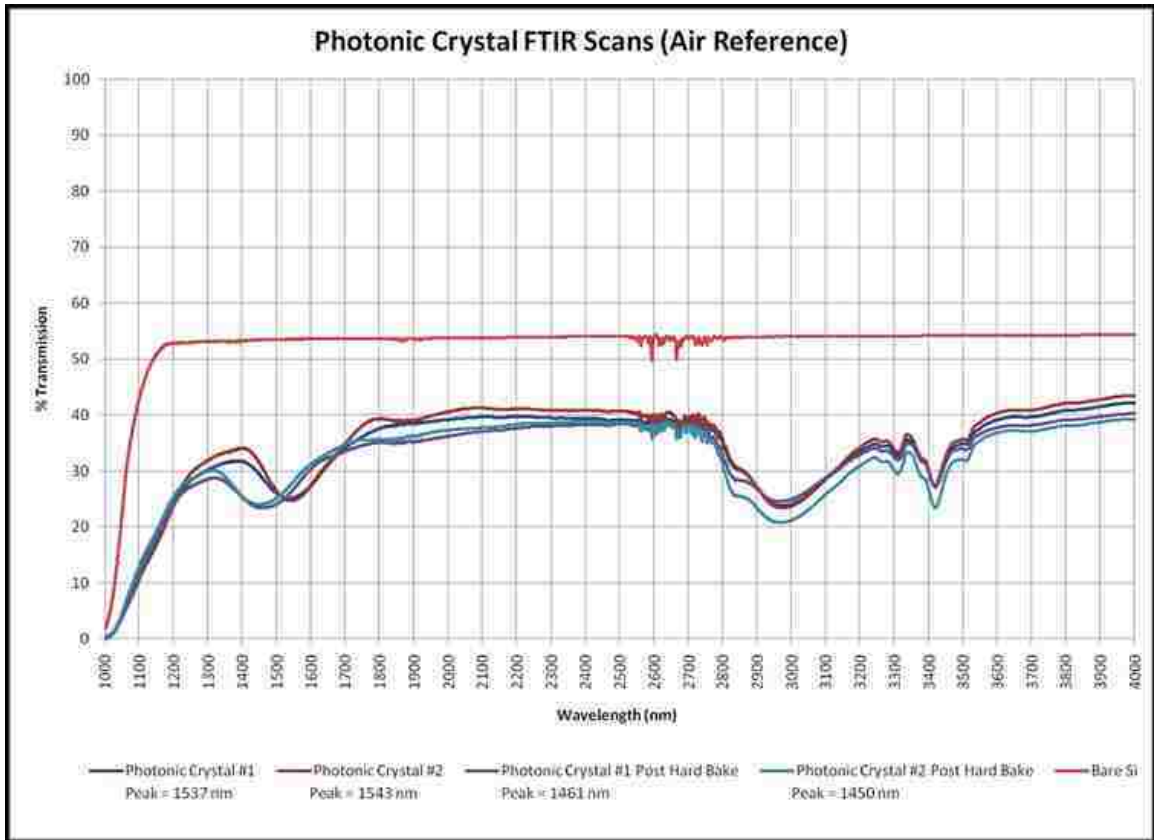
reflection curves for these photonic crystals are plotted in Figure 85. There are two different measurements plotted of the same sample. The second measurements of the photonic crystal were made after an additional hard bake at 130°C, causing the photoresist to further cross-link providing some small shrinkage mostly in the Z crystal direction (normal to the substrate). Also a bare silicon wafer was measured for reference.



**Figure 85** – 3-exposure photonic crystal FTIR scan reflection plots.

The transmission measurement used air as the reflectance reference measurement, in other words the transmittance through the photonic crystals on a silicon wafer is compared to the transmittance through air. The Transmission curves for these photonic crystals are plotted in Figure 86. There are four different transmission measurements

plotted. Two different samples made under the same processing conditions were measured. Same as with the reflection plots, additional measurements of the same photonic crystals were made after an additional hard bake at 130°C. A bare silicon wafers was measured for reference.



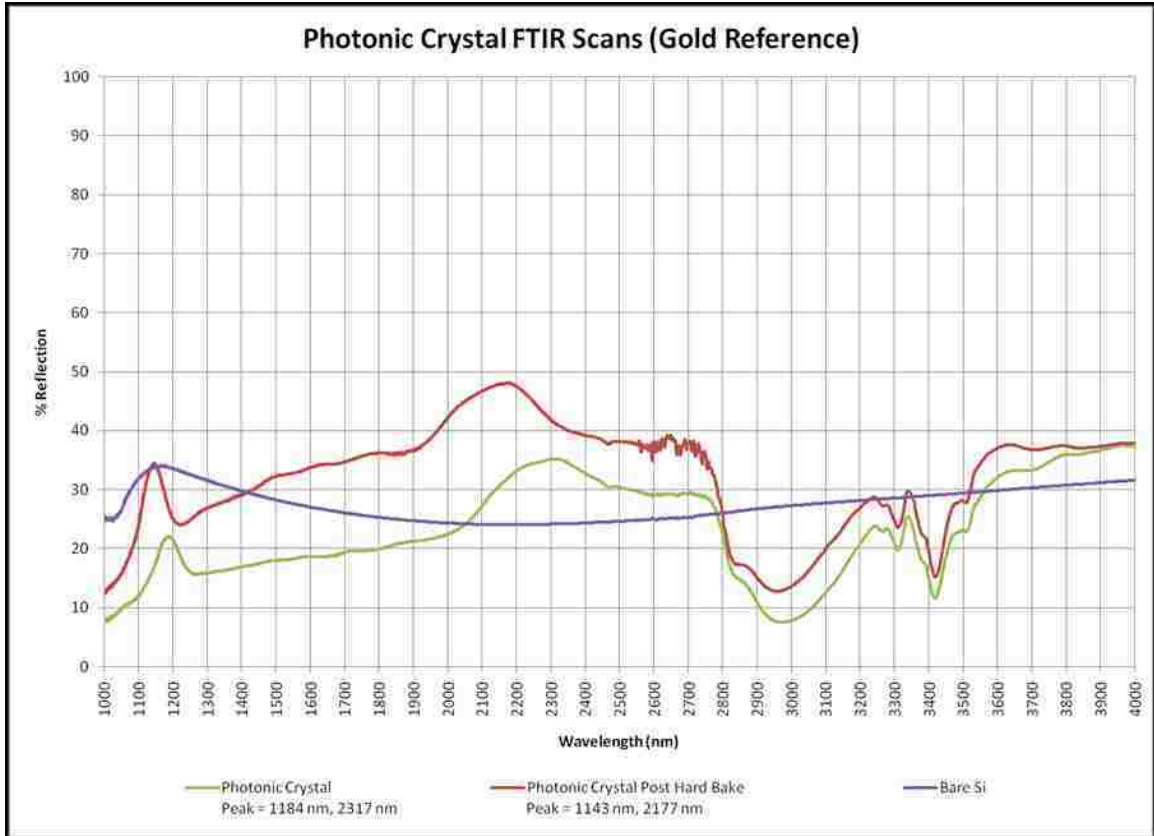
**Figure 86** – 3-exposure photonic crystal FTIR scan transmission plots.

From inspection of the reflection and transmission plots there are higher reflection peaks and a lower transmission notches around the 1550nm wavelength that corresponds to standard optical telecommunication wavelengths. Also the effect of a post processing hard bake is a shift in the wavelength spectrum to lower wavelengths, most likely due to shrinkage of the photoresist. On all of the transmission plots the transmittance drop off

significantly at 1200 nm wavelength, because the silicon wafer substrate becomes absorptive at this wavelength and becomes completely opaque at 1000 nm wavelength.

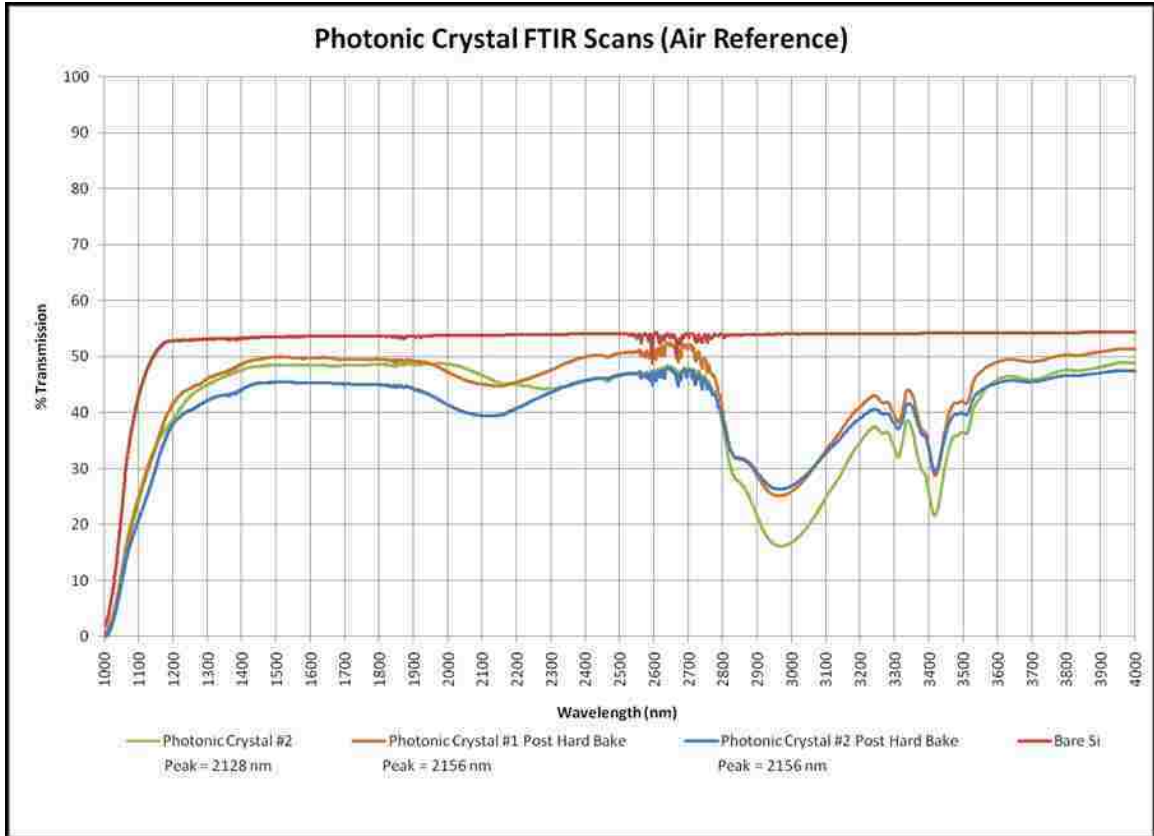
### **Four-Exposures Transmission & Reflection Plots**

The first set of plots will be of three-dimensional photonic crystals made using four-exposure interferometric lithography. The photonic crystal stack and process parameters are the same as the one used in the previous chapter and are given in Table 9 of Appendix C. The reflection measurement used a gold coated silicon wafer as the reflectance reference measurement, in other words the reflectance off of the photonic crystals on a silicon wafer is compared to the reflectance off of a gold coated silicon wafer. The reflection curves for these photonic crystals are plotted in Figure 87. There are two different measurements plotted of the same sample. The second measurements of the photonic crystal were made after an additional hard bake at 130°C, causing the photoresist to further cross-link and some small shrinkage mostly in the Z crystal direction (normal to the substrate). Also a bare silicon wafer was measured for reference.



**Figure 87** – 4-exposure photonic crystal FTIR scan reflection plots.

The transmission measurement used air as the reflectance reference measurement, in other words the transmittance through the photonic crystals on a silicon wafer is compared to the transmittance through air. The Transmission curves for these photonic crystals are plotted in Figure 88. There are three different transmission measurements plotted. Two different samples made under the same processing conditions were measured. Same as with the reflection plots, additional measurements of the same photonic crystals were made after an additional hard bake at 130°C. A bare silicon wafers were measured for reference.



**Figure 88** – 4-exposure photonic crystal FTIR scan transmission plots.

From inspection of the reflection and transmission plots there are higher reflection peaks and a lower transmission notches around 2140nm. Also the effect of a post processing hard bake is a shift in the wavelength spectrum to lower wavelengths, most likely due to shrinkage of the photoresist. On all of the transmission plots the transmittance drop off significantly at 1200 nm wavelength, because the silicon wafer substrate becomes absorptive at this wavelength and becomes completely opaque at 1000 nm wavelength.

## ***Comparison of Measurements to Models***

It is possible to simulate transmission and reflection models of the photonic crystal using finite-difference time-domain (FDTD) electromagnetic simulation software. This is accomplished by taking Maxwell's equations and evolves them over time within some finite computational region. These computations are very involved and normally take days to execute running in parallel over networked workstation clusters. There are many different free and commercial FDTD software packages available, many of which are listed at "[http://en.wikipedia.org/wiki/Finite-difference\\_time-domain\\_method](http://en.wikipedia.org/wiki/Finite-difference_time-domain_method)".

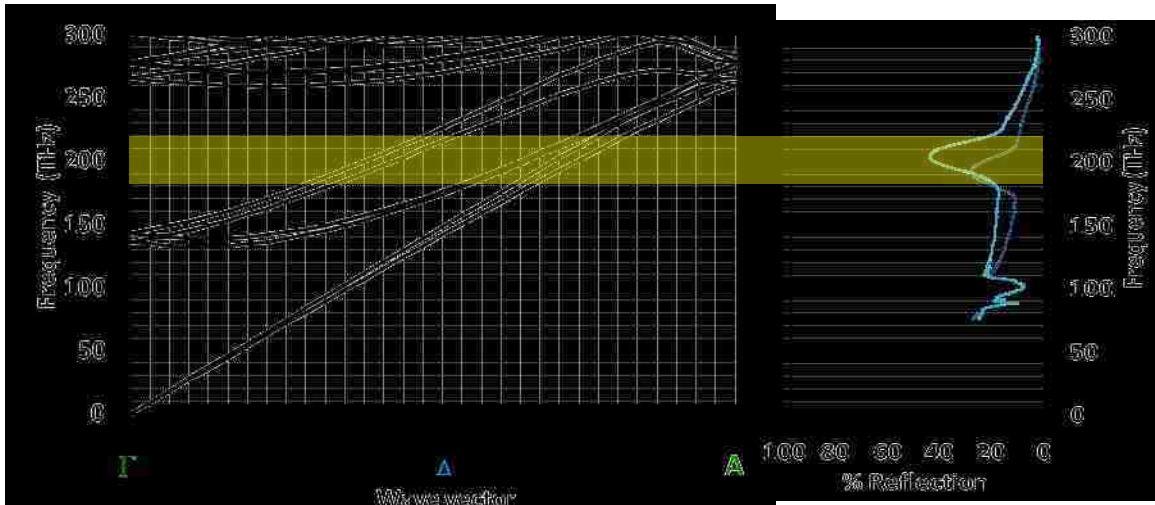
A freely available software package that performs FDTD simulation of photonic crystals is the MIT Electromagnetic Equation Propagation (or "Meep") software package developed at MIT to model electromagnetic systems<sup>35</sup>. Meep however does not allow for inputting of external photonic crystal structures, and relies strictly on crystal structures being defined by combining basic geometric shapes in the control script file. It may be possible to make a reasonable facsimile of the multiple-exposure interferometric lithography photonic crystals by combining geometric spheres and cylinders. In order to calculate the normalized transmission and reflection curves require running the simulation twice, using the output fluxes of the first simulation as the input fluxes for the second simulation that generates the normalized transmission and reflection curves. However due to the software limitations and complexity, in addition to difficult access to a high speed computing cluster or supercomputer, this three-dimensional photonic crystal modeling approach was not pursued.

A simple solution is to compare the photonic crystal transmission and reflection curves in frequency space to the band diagram model along the corresponding  $k$ -vector of

the measurement direction. The frequency gap found along the  $k$ -vector direction of interest should line up with the transmission notch or reflection peak of the photonic crystal. The next two sections will present graphs that contain both the band diagram and FTIR reflection measurement data. This is done for both the three-exposure and four-exposure photonic crystals made by interferometric lithography. Comparison and conclusions will be drawn.

### **Three Exposure Photonic Crystals**

A plot of the simulated band diagram and measured reflectance of the three-dimensional photonic crystals made using three-exposure interferometric lithography is shown in Figure 89. The band diagram was made using a slightly modified version of the “MPB3Exp3DPhC.ctf” script file found in Appendix K that made the band diagram found in Figure 83. The only modifications made were: only wave vectors between the  $\Gamma$  and A  $k$ -points were simulated, and the number of wave vectors computed between the points was increased from 10 to 30. The wave vectors along the  $\Delta$  line (points between  $\Gamma$  and A) correspond to the photonic crystal z-axis in real space, which is the direction the FTIR measurements were made. The reflection frequency plot is the same as the plot in Figure 85 but in frequency units instead of wavelength, for the sake of comparison to the band diagram.



**Figure 89** – Three-exposure Photonic Crystal Band Diagram and Reflection Plot, comparing bandgaps to reflection peaks.

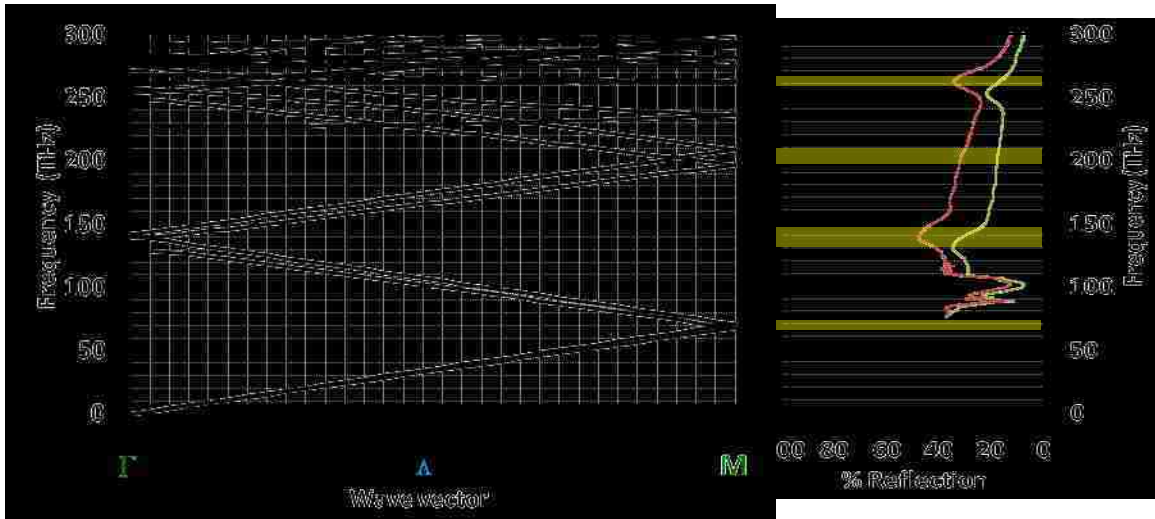
The FTIR reflection peaks are highlighted by the yellow box in Figure 89 and should line up with a bandgap along the  $\Delta$  line. The frequency range that the band diagram covers has no bandgaps. The fact that no bandgaps aligns up with the reflection peak frequency found in the rotated reflection plot in Figure 89, may indicate an error in the band diagram simulation. The simulation error is most likely a programming mistake in the control file, or possible an error in the “3\_exp\_epsilon.m” unit cell input file of the MBP simulation. This issue should be further investigated.

## Four-Exposure Photonic Crystals

A plot of the band diagram and transmission measurements of four-dimensional photonic crystals made using three-exposure interferometric lithography is shown in Figure 90. The band diagram was made using a slightly modified version of the “MPB3Exp3DPhC.ctf” script file found in Appendix K that made the band diagram found in Figure 84. The only modifications made were: only wave vectors between the  $\Gamma$



and M  $k$ -points were simulated, and the number of wave vectors computed between the points was increased from 10 to 30. The wave vectors along the  $\Lambda$  line (points between  $\Gamma$  and M) correspond to the photonic crystal z-axis in real space, which is the direction the FTIR measurements were made. The reflection frequency plot is the same as the plot in Figure 87 but in frequency units instead of wavelength, for the sake of comparison to the band diagram.



**Figure 90** – Four-exposure Photonic Crystal Band Diagram and Reflection Plot, comparing bandgaps to reflection peaks.

The bandgaps along the  $\Lambda$  line are highlighted by the yellow box in the band diagram found in Figure 90. The frequency range that two of the bandgaps covers align up with the reflection peak frequencies found in the rotated reflection plot found in Figure 90. The measured bandgaps along the  $\Lambda$  line are given as follows: between band 2 and 3 centered at 69 THz (4344 nm), between band 4 and 5 centered at 140 THz (2141 nm), between band 6 and 7 centered at 202 THz (1484 nm), and between band 12 and 13 centered at 266 THz (1127 nm). The reflection peaks are at frequency 129 THz (2317 nm) and 253 THz (1184 nm) for the first sample, and at frequency 138 THz (2177 nm)

and 262 THz (1143 nm) for the second sample. The measured reflection peaks are very close to the simulated second and fourth bandgap. This is what is expected, and validates both the simulation and measurements of the four-exposure photonic crystal.

## CHAPTER 6

### SUMMARY and FUTURE WORK

#### ***3D Photonic Crystal Fabrication***

This dissertation presents in detail a novel three-dimensional photonic crystal fabrication process based on multiple-exposure interferometric lithography with off-axis illumination. Interferometric lithography is used to produce photonic crystals over large two-square centimeter areas. Several relatively inexpensive interferometric lithography exposure setups were investigated. By using these interferometric lithography setups one-dimensional, two dimensional, and three-dimensional photonic crystals are made using a variety of methods. All of these methods are explained in great detail in Chapter 2.

Both modeled and real experimental photoresist profiles of three-dimensional photonic crystals are presented. The modeled and experimental photoresist profile results of three-dimensional photonic crystals compared well, as shown in Chapter 4. Many unit-cell thick three-dimensional photonic crystals can be made of high quality over a large two-square centimeter area by interferometric lithography.

#### ***Embedded Waveguide Fabrication***

In addition to large three-dimensional photonic crystals, integrating waveguides in the photonic crystals were demonstrated. This is accomplished by a novel multiple-wavelength lithography technique, where one wavelength is used to create the photonic

crystal using interferometric lithography and a second wavelength is used to create the waveguide using standard lithography.

This novel technique is extended by embedding the waveguides inside the photonic crystal. If the photoresist has the correct properties the waveguide can be exposed in the photoresist, followed by additional layer of photoresist added to the original layers, before the final exposure of the photonic crystal.

### ***Prospects and Limitations***

This dissertation introduced three new novel techniques for making three-dimensional photonic crystal with embedded waveguides. The first technique introduced is multiple-exposure interferometric lithography plus off-axis illumination to manufacture photonic crystals. Second the use of multiple-wavelengths to create waveguides and tailor the waveguide properties independent of the photonic crystal properties. And finally the third technique introduced is embedding the waveguide into the photonic crystal.

The capabilities of making three-dimensional photonic crystal with embedded waveguides, demonstrated by this dissertation, hold tremendous potential. Some of these include; narrow-band filters, waveguide bends, waveguide splitters, waveguide resonators, channel-drop filters, and coupled-cavity waveguides.

One of the limitations of the experimental crystals presented in this paper is that the photonic crystals did not have a full photonic bandgap as a result of the low index contrast. Another limitation is that the photonic crystals did not have full symmetry in the  $x$ ,  $y$ , and  $z$  directions e.g. the  $z$  periodicity was larger than that of  $x$ ,  $y$  direction. To

have the photonic crystals exhibit a full bandgap requires that the index contrast be larger. The next section gives some approaches of how to achieve the higher index contrast. The full crystal symmetry is not achieved because the  $z$ -dimension could not be scaled down sufficiently with the high index ( $n \approx 1.7$ ) of the photoresist used. Lastly the scaling issues of photonic crystals are discussed.

## High Index Contrast

A photonic crystal is a periodic arrangement of dielectric media. Typically the photonic crystal is made from two dielectric materials. The larger the index of refraction delta or contrast ( $\Delta n = n_2 - n_1$ ) between the two dielectric materials that make up the photonic crystal, the larger the gaps in the photonic band structure. For the photonic crystal created using the multiple-exposure interferometric lithography technique used in this dissertation, the first dielectric material is air  $n_1 = 1.0$ , and the second dielectric material is photoresist  $n_2 = n_r \approx 1.7$ . This results in a photonic crystal with an index contrast of  $\Delta n \approx 0.7$ . Normally an index contrast of 2 or higher is required for a photonic crystal to have a complete bandgap (a non-overlapping bandgap for all wave vector directions). The index of refraction of photoresist is 1.2 to 1.9, which is too low to create a photonic crystal with a complete bandgap. A low index of refraction for photoresist is beneficial for creating symmetric three-dimensional phonic crystals, and is discussed further in the section on photonic crystal scaling.

In order to fabricate a photonic crystal with a complete optical bandgap, using multiple-exposure interferometric lithography, further processing is necessary to convert the photonic crystal from low to high-index contrast. There are several ways to achieve

this desired result. The first method considered is a process called “Inverse opal”, and is described in the next subsection. The second method considered is a process utilizing electroforming, and is described in a following subsection. Both of these methods replace the first dielectric medium of air with a much higher index dielectric medium.

## **Inverse Opal**

Inverse opal is a fabrication process that creates a high index contrast photonic crystals from a low contrast photonic crystal with air-filled voids as one of the photonic crystal dielectric media. The low contrast photonic crystal structure is inverted by infiltrating the voids with a high-dielectric material. Examples of such high-dielectric materials are silicon or germanium for the infrared spectrum. This can be accomplished by using chemical vapor deposition.<sup>36</sup> Other examples are the use of sol-gels to infiltrate the photonic crystal with  $\text{TiO}_2$ ,  $\text{SiO}_2$ , or  $\text{GeO}_2$ .<sup>14</sup> Once the voids of the photonic crystal are filled with a high-dielectric material, the lower dielectric constant material is dissolved away. This leaves behind a high contrast photonic crystal with the inverse structure of the original low-contrast photonic crystal. The new high-contrast photonic crystal can now have a complete bandgap.

## **Electroforming**

Electroforming is a metal forming process that forms parts through the electroplating process. In electroforming, as in plating, metal ions are transferred electrochemically through an electrolyte from an anode to a surface where they are deposited as atoms of plated metal onto a base form, known as a mandrel, which is

removed after plating. This process differs from electroplating in that the plating is much thicker and can exist as a self-supporting structure when the mandrel is removed.<sup>37,38,39</sup>

To create a high index contrast photonic crystal via the electroforming process, a low contrast photonic crystal is used as the mandrel. In the case of the photonic crystal fabricated by multiple-exposure interferometric lithography, the photoresist is the mandrel. The air gaps or voids in the photonic crystal are filled with a high index metal via the electroforming process. Typical metals are copper, nickel, iron, silver, and gold. This will produce a photonic crystal that has the mandrel as the low index dielectric material from the original photonic crystal and a high index metal. The index contrast is further increased by chemically removing the mandrel and producing a photonic crystal with air as the low index dielectric material and metal as the high index material.

## **Scaling**

To further scale three-dimensional photonic crystals using the multiple-exposure interferometric lithography to smaller sizes and thus shorter band-gap wavelengths, requires increasing the angles of the beams. The larger the angle between the two beams the smaller the pitch of the crystal in the  $x$  and  $y$  directions. Likewise the larger the angle of the intercept of the two beams from normal of the exposure plane the smaller the pitch in the  $z$  direction. However there comes a point where the angle of the second beam becomes  $90^\circ$  to the exposure plane.

The smallest crystal pitch achievable in air while maintaining equal pitch for  $x$ ,  $y$ , and  $z$  is given as follows.

$$\Lambda_{\min x=y=z} = \frac{\lambda}{1-n_r \sqrt{1-\frac{1}{n_r^2}}} \quad (5.1)$$

$$n_r \leq |\sqrt{2}| \quad (5.2)$$

Where  $\lambda$  is the exposing wavelength and  $n_r$  is the index of the photoresist. This is done by setting the second exposing plane-wave beam angle to  $90^\circ$  and using the boundary condition of  $A_x = A_y = A_x$ . Also in order for  $A_x = A_y = A_x$  the index of the photoresist must be less than  $\sqrt{2}$ , otherwise the angle of the plane-wave in the photoresist is too small to achieve symmetry due to Snell's law. For example the smallest symmetric pitch achievable for an exposure wavelength of 355 nm in a photoresist with an index of  $n_r = 1.2$  is  $\Lambda_{\min x=y=z} = 1.054 \mu\text{m}$ , and for  $n_r = 1.4$  is  $\Lambda_{\min x=y=z} = 17.571 \mu\text{m}$ . Most photoresist have an index of refraction of 1.5 to 1.9 which will not allow for symmetric photonic crystals. This limitation can be overcome by the use of immersion lithography which is described and investigated in the next section.

## Wavelength Scaling

One method to get to smaller sizes, once the second beam becomes  $90^\circ$  to the exposure plane in the air, is to go to shorter wavelengths. This however requires a photoresist that is still sensitive to the shorter wavelength, and retains all the other properties needed to make three-dimensional photonic crystals. This may not always be feasible, especially when going to extreme UV light sources.



## Immersion Lithography

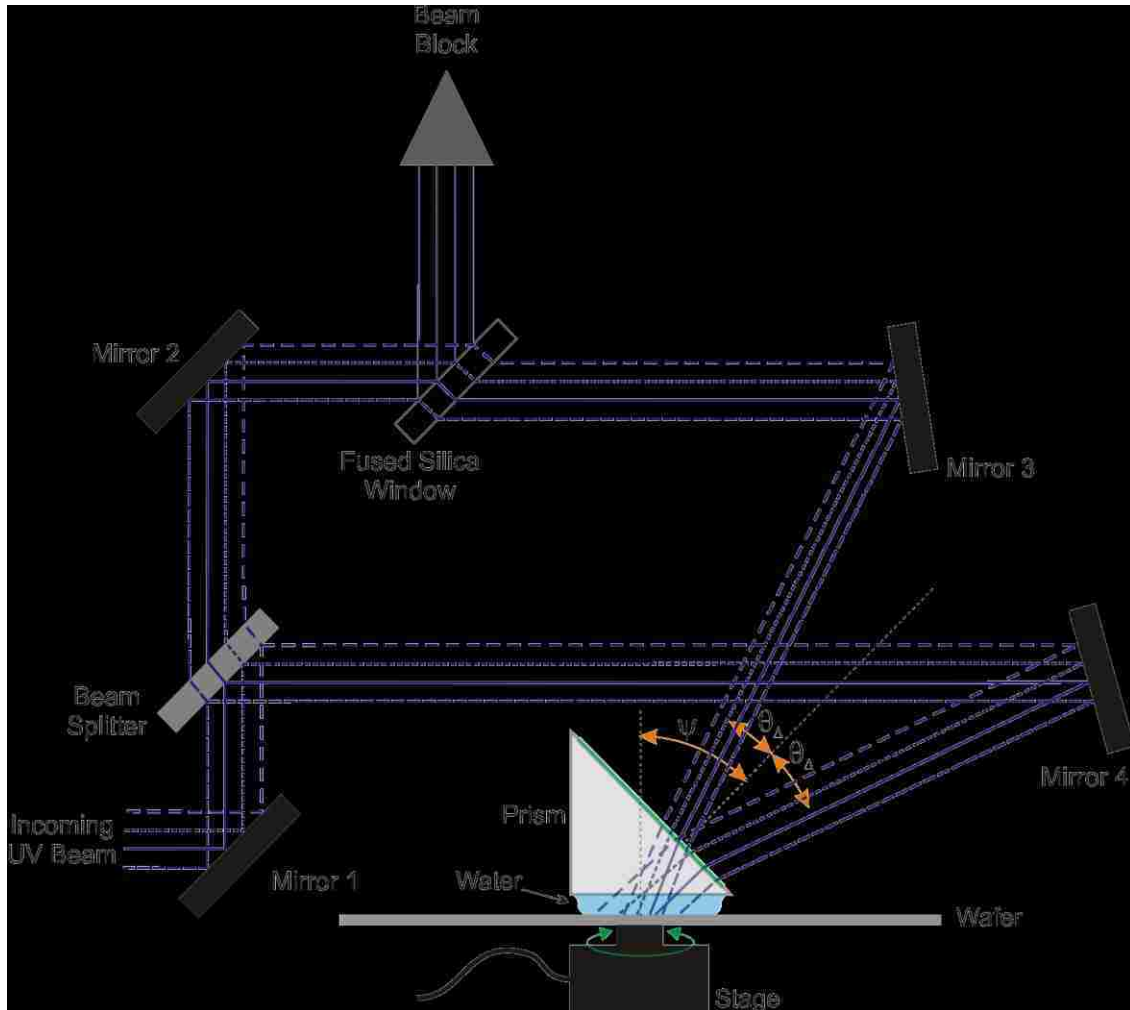
Another method to reach smaller sizes is to carry out the exposure in a medium with an index higher than air. One such medium that is commonly used is pure water. Water that has been de-ionized and degassed provides an index of 1.44 at 193 nm. The resolution is increased by a factor equal to the refractive index of the liquid, and by using water instead of air as an exposure medium the result is a resolution increase up to 44%. Immersion lithography is commonly used in IC manufacturing to get down to very small pitches, and has the same impact on photonic crystal manufacturing.<sup>40,41</sup> More importantly immersion lithography may also be the only way to achieve symmetric pitches in photoresist with higher index of refraction ( $n > 1.414$ ). This is due to decreased bending of the incident plane-wave of light at the photoresist interface. Now the index of the photoresist must meet the following condition to achieve pitch symmetry.

$$\Lambda_{\min x=y=z} = \frac{\lambda}{n_m - n_r \sqrt{1 - \frac{n_m^2}{n_r^2}}} \quad (5.3)$$

$$n_r \leq n_m \cdot |\sqrt{2}| \quad (5.4)$$

Where  $n_m$  is the index of refraction for the exposure medium (e.g. water), and  $n_r$  is the index of refraction for the photoresist. For example the smallest symmetric pitch achievable for an exposure wavelength of 355 nm in a photoresist with an index of 1.6 @ 355 nm exposed in a medium of water with an index of 1.35 @ 355 nm is 723 nm pitch. Similarly the smallest symmetric pitch achievable for exposure wavelengths of 244 nm and 193 nm in a photoresist with an index of 1.7 @ 244 nm & 193 nm exposed in a medium of water with an index of 1.38 @ 244 nm and 1.44 @ 193 nm are 630 nm and 360 nm pitch respectfully.

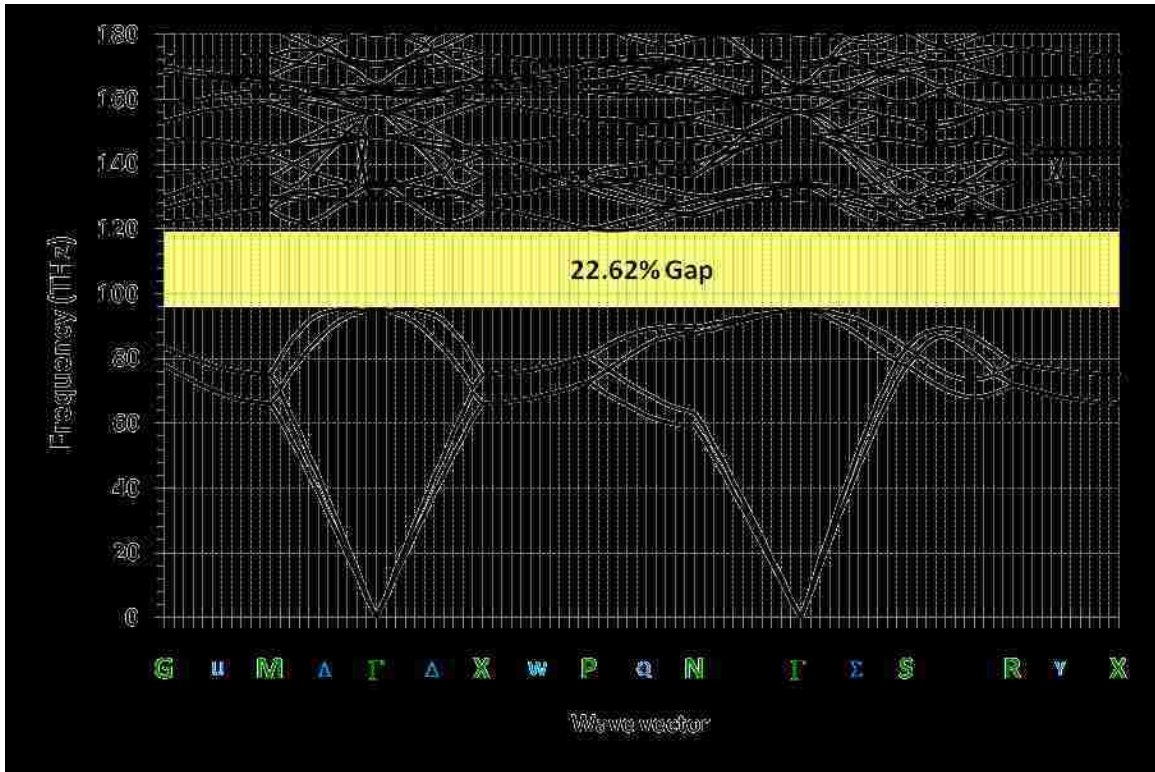
In order to modify the exposure setup used to make the photonic crystals in this dissertation for immersion lithography, a right angle prism would need to be added to the setup. The prism would be placed right over the stage exposure plane, and used to couple the two light beams into the immersion media and further on into the photoresist. The long leg of the prism would face the two incoming beams and preferably have an antireflection coating. The immersion media is injected in small gap between the prism short leg and photoresist coated wafer, before exposing. Normally the light would be totally internally reflected off the short leg of the prism in air, but the higher index or refraction of the immersion media will allow for the light to be coupled out of the prism and into the immersion media by functioning as an antireflection film on the prism short leg surface. The immersion media will also act as an antireflection film for the photoresist. This will change the intensity ratio between the two beams of light in the photoresist, therefore requiring a different beam intensity ratio control for the setup. Figure 91 shows an immersion Michelson interferometric lithography setup use to create three-dimensional photonic crystals.



**Figure 91** – Immersion Michelson interferometric lithography setup with off-axis illumination, beam intensity ratio compensator. Setup needed for making PhCs with symmetrical periodicity.  $\Lambda_x = \Lambda_y = \Lambda_z$

### ***Photonic Crystal with a Complete Bandgap***

By utilizing immersion interferometric lithography to achieve a symmetric pitch symmetry and replacing the photoresist with a high index material like silicon ( $n = 3.159$  @ 1533 nm) it is possible to fabricate a photonic crystal with a complete bandgap. Figure 92 shows the band diagram of a four exposure photonic crystal with a symmetric pitch of  $\Lambda_x = \Lambda_y = \Lambda_z = 1138$  nm, and the photoresist replaced with silicon (not inverse opal - that would be air replaced with silicon).



**Figure 92** – Band diagram of a 4-exposure fully symmetric photonic crystal made of silicon and air. PhC produced by 4-exposure immersion interferometric lithography and dual inverse opal technique.

Figure 92 has a 22.62% complete bandgap from 95 THz (3156 nm) to 119 THz (2519 nm) centered at 107 THz (2802 nm). The bandgap is the percentage of the frequency range to the mid-gap frequency  $\left(\frac{F_{\text{gap.max}} - F_{\text{gap.min}}}{F_{\text{mid-gap}}}\right) \%$ . If the photonic crystal used germanium ( $n = 4.36 @ 1533 \text{ nm}$ ) instead of silicon ( $n = 3.519 @ 1533 \text{ nm}$ ) the complete bandgap would increase to 27.43% and be between the frequencies of 77 THz (3893) to 102 THz (2939 nm) centered at 90 THz (3331 nm). The inverse structure however does not have a complete bandgap, likely due to the larger fill factor ratio of the higher index material. This would be the case if the photonic crystal was filled by inverse opal or electroforming techniques. Such a photonic crystal however could be fabricated by using an immersion Michelson interferometric lithography setup found in

Figure 91, followed by an inverse opal technique using a sol-gel oxide or electroforming technique using a metal creating an inverse photonic crystal structure, and finishing with a final inverse opal technique of silicon or germanium to revert the photonic crystal back to its original structure.

The ability of off-axis multiple-exposure immersion interferometric lithography to produce three-dimensional photonic crystals with definable periodicities along each crystal axis in conjunction with an inverse opal technique, a variety of photonic crystal containing a complete bandgap can be realized. This approach to fabricating photonic crystal containing a complete bandgap lends itself to a straightforward method for mass manufacturing using standard semiconductor lithography equipment

### ***Future Studies***

There are several aspects I would like to study beyond the scope of this dissertation. The fabrication of a six-exposure interferometric lithography helical photonic crystal would be of interest. The fabrication of such photonic crystal slabs could be used as an optical circular polarizer. This chiral polarizer would be similar to current optical linear polarizer, consisting of a metal wire line grating.

One of the main aspects that need to be studied in the future is the light propagation properties of the embedded waveguide in three-dimensional photonic crystal. Light can be injected into the waveguide and the propagation losses can be measured for various waveguide structures of interest. The Meep simulation software can also model the waveguide propagation properties. Measured propagation losses could then be compared to simulation results.

Another aspect of the photonic crystals that can be studied is their optical properties after modifying the developed photoresist structure. Such modification can be the incorporation of nano-particles onto the surface of the photoresist structure, or chemically altering the photoresist compound through the use of chemically reactive gases or liquids. This could also include post processing bakes that modify the photoresist compound, and can possibly be done in conjunction with another modification process.

A similar direction is using the photonic crystal comprised of photoresist as a mandrel for other possible more intriguing optical materials through the use of inverse opal or electroforming processes. Once the new optical materials are incorporated into the photonic crystal structure the photoresist can be optionally removed. This could realize photonic crystals with a large continuous bandgap. Nonlinear optical materials could also be incorporated (i.e. GaAs), creating photonic crystals that could be used for highly efficient frequency doubling. It is possible to phase match the second-harmonic generated wavelength with the fundamental wavelength in the photonic crystal using a 'quasi-phase-matched structure', where the shape of the photonic crystal Bravais lattice is tailored to break dispersion symmetry for the use of artificial birefringence in order to achieve phase matching.<sup>3</sup>

The most significant future evolution of these three-dimensional photonic crystals, with or without embedded waveguides, will be the creation of usable photonic devices. If viable photonic devices are created, capabilities through the techniques developed in this dissertation, the manufacturing can be extended to mass production.

## APPENDICES

## APPENDIX A

### MATHCAD PROGRAM FOR BOTTOM ANTIREFLECTION

#### COATING CALCULATIONS

MathCAD is used to calculate optimal bottom ARC thicknesses for the silicon wafer exposure substrates. The complete film stack is used as the input and the reflection curve off of the ARC is calculated and the ARC thickness is optimized to minimize the reflections. A copy of the “MathCAD 13” program is show below. As can be seen from the program, using Brewer Science iCON series antireflective coating (ARC) on silicon wafers at 355 nm exposure wavelength, the optimal ARC thickness for the three-dimensional photonic crystal exposures is 71 nm.

#### ML Stack Reflectivity Curves.xmcd

##### Instructions:

1. Enter the vacuum wavelength of interest  $\lambda_0$
2. Enter the incident angle of interest  $\theta$ .
3. Enter the polarization state of the incident light %TE, as a percentage of TE light (i.e. 100 - for TE polarized, 50 - for unpolarized, 0- for TM polarized light,
4. Enter the vacuum wavelength refractive index for each layer of the stack as a one-dimensional array  $\mathbf{n}$ .  $\mathbf{n}_0$  is the incident medium,  $\mathbf{n}_1$  is the first layer of the stack,  $\mathbf{n}_{n-1}$  is the last layer of the stack, and  $\mathbf{n}_n$  is the stack substrate. Enter each element in array  $\mathbf{n}$  as  $n+1i*k$ .
5. Enter the thickness of each layer in the stack as a one-dimensional array  $\mathbf{d}$ .  $\mathbf{d}_0$  is the incident medium and is ignored,  $\mathbf{d}_1$  is the thickness of the first layer of the stack,  $\mathbf{d}_n$  is the thickness of the last layer of the stack. Do not put a thickness for the stack substrate (if necessary put air or vacuum as the substrate). Array  $\mathbf{n}$  should have one more element than array  $\mathbf{d}$ .
6. Enter the layer of interest to calculate the reflection from **CalcReflectionFromLayer**. Must be a number from 1 -  $n$ , with  $n$  being the substrate. For example a BARC layer for reflections into photoresist, or the first layer for reflection into incident medium.
7. Enter the layer **LayerToOptimize** which thickness you want to vary to minimize the reflection for the layer of interest. This can be but does not have to be the same layer as the **ReflectionFromLayer**. To optimize the thickness of the BARC layer to minimize reflection into photoresist, the **ReflectionFromLayer** and **LayerToOptimize** would be the same BARC layer. But if you want to optimize the thickness of a layer under the BARC to minimize the reflection into the photoresist, the **ReflectionFromLayer** would be the BARC and **LayerToOptimize**



would be a layer under the BARC layer. The starting seed thickness for the layer being optimized will be taken from the film stack thickness array **d** for the layers being optimized.

8. Enter the minimum and maximum Given **LayerThickness** that the layer to optimize will be optimized over.

The program will calculate the Optimum thickness **OptThick** for the layer being optimized to minimize the reflection of the **CalcReflectionFromLayer** at the incident angle of interest. It will give the reflection from the **CalcReflectionFromLayer** at that optimum thickness as **Refl(OptThick)**.

The program will plot the reflection curve as a function to the layer to optimize thickness. It will make a 3D-plot of reflection as a function of incident angle and optimize layer thickness. It will plot minimum possible reflection as a function of each incident angle for any film thickness of the layer to optimize within the range of thicknesses used in the previous 3D-plot. It will plot reflection as a function of incident angle labeled with corresponding Half-Pitch of an Interferometer Lithography setup using the vacuum wavelength in the incident medium. The target Half-Pitch **HP** is calculated from the incident angle of interest  $\theta$ .

### Parameters

$n_{\text{air.355}} := 1.000276$	$n_{\text{air.193}} := 1.00$	$n_{\text{air.244}} := 1.000302$
$n_{\text{Si.355}} := 5.670984 + i \cdot 3.021476$	$n_{\text{Si.193}} := 0.883134 + i \cdot 2.777792$	$n_{\text{Si.244}} := 1.530 + i \cdot 3.4030$
$n_{\text{SiO2.355}} := 1.56463$	$n_{\text{SiO2.193}} := 1.563117$	$n_{\text{DUV64.244}} := 2.01 + i \cdot 0.49$
$n_{\text{SU8.355}} := 1.61 + i \cdot 0.001614488$	$n_{\text{H2O.193}} := 1.43664$	$n_{\text{Si3N4.193}} := 2.66 + i \cdot 0.28$
$n_{\text{WiDE.355}} := 1.72 + i \cdot .33$	$n_{\text{ARC27.193}} := 1.77 + i \cdot 0.51$	
$n_{\text{SPR500.355}} := 1.7162 + i \cdot 0.02$	$n_{\text{ARC28.193}} := 1.527093 + i \cdot 0.54$	
$n_{\text{iCON.355}} := 1.84 + i \cdot 0.37$	$n_{\text{ARC29A.193}} := 1.826541 + i \cdot 0.34$	
$n_{\text{NR7.355}} := 1.7162 + i \cdot 0.02$	$n_{\text{ARC145.193}} := 1.67 + i \cdot 0.45$	
$n_{\text{Al2O3.355}} := 1.79598$	$n_{\text{PMMA.193}} := 1.697041 + i \cdot 0.003804009$	
$n_{\text{Si3N4.355}} := 2.098553 + i \cdot 0.021$	$n_{\text{PMGI.193}} := 1.572 + i \cdot 0.207$	
$n_{\text{GaN.355}} := 2.66 + i \cdot 0.26$	$n_{\text{ARX2928JN.193}} := 1.709 + i \cdot 0.044$	
	$n_{\text{Al2O3.193}} := 1.928789$	

### Theoretical Calculation

$$\lambda_0 := 355 \text{ nm}$$

$$\theta := 47.05 \text{ deg} \quad \% \text{TE} := 100$$

$$n := \begin{pmatrix} n_{\text{air.355}} \\ n_{\text{NR7.355}} \\ n_{\text{iCON.355}} \\ n_{\text{Si.355}} \end{pmatrix}$$

$$n = \begin{pmatrix} 1 \\ 1.716 + 0.02i \\ 1.84 + 0.37i \\ 5.671 + 3.021i \end{pmatrix}$$

$$d := \begin{pmatrix} 0 \\ 6000 \\ 70 \end{pmatrix} \cdot \text{nm}$$

$$\Lambda := \frac{\lambda_0}{2 \cdot |n_0| \cdot \sin(\theta)}$$

$$\Lambda = 242.436 \text{ nm}$$

$$\text{CalcReflectionFromLayer} := 2$$

$$i := 0, 1 \dots \text{last}(n)$$

$$\cos \theta(i, \theta) := \sqrt{1 - \left( \frac{n_0}{n_i} \cdot \sin(\theta) \right)^2} \quad \cos \theta(i, \theta) = \begin{pmatrix} 0.681 \\ 0.904 + 2.344i \times 10^{-3} \\ 0.928 + 0.032i \\ 0.996 + 5.407i \times 10^{-3} \end{pmatrix}$$

$$H_{\text{TE}}(i, \theta) := \begin{pmatrix} \frac{1}{2} + \frac{n_{i+1} \cdot \cos \theta(i+1, \theta)}{2 \cdot n_i \cdot \cos \theta(i, \theta)} & \frac{1}{2} - \frac{n_{i+1} \cdot \cos \theta(i+1, \theta)}{2 \cdot n_i \cdot \cos \theta(i, \theta)} \\ \frac{1}{2} - \frac{n_{i+1} \cdot \cos \theta(i+1, \theta)}{2 \cdot n_i \cdot \cos \theta(i, \theta)} & \frac{1}{2} + \frac{n_{i+1} \cdot \cos \theta(i+1, \theta)}{2 \cdot n_i \cdot \cos \theta(i, \theta)} \end{pmatrix}$$

$$H_{\text{TM}}(i, \theta) := \begin{pmatrix} \frac{\cos \theta(i+1, \theta)}{2 \cdot \cos \theta(i, \theta)} + \frac{n_{i+1}}{2 \cdot n_i} & \frac{-\cos \theta(i+1, \theta)}{2 \cdot \cos \theta(i, \theta)} + \frac{n_{i+1}}{2 \cdot n_i} \\ \frac{-\cos \theta(i+1, \theta)}{2 \cdot \cos \theta(i, \theta)} + \frac{n_{i+1}}{2 \cdot n_i} & \frac{\cos \theta(i+1, \theta)}{2 \cdot \cos \theta(i, \theta)} + \frac{n_{i+1}}{2 \cdot n_i} \end{pmatrix}$$

$$L(i, d, \theta) := \begin{pmatrix} e^{-i \cdot \frac{2 \cdot \pi}{\lambda_0} \cdot n_i \cdot \cos \theta(i, \theta) \cdot d} & 0 \\ 0 & e^{i \cdot \frac{2 \cdot \pi}{\lambda_0} \cdot n_i \cdot \cos \theta(i, \theta) \cdot d} \end{pmatrix}$$

$$S_{\text{TE.ref}}(\text{Layer}, d, \theta) := H_{\text{TE}}(\text{Layer} - 1, \theta) \cdot \prod_{i=\text{Layer}}^{\text{last}(d)} (L(i, d_i, \theta) \cdot H_{\text{TE}}(i, \theta))$$

$$S_{\text{TM.ref}}(\text{Layer}, d, \theta) := H_{\text{TM}}(\text{Layer} - 1, \theta) \cdot \prod_{i=\text{Layer}}^{\text{last}(d)} (L(i, d_i, \theta) \cdot H_{\text{TM}}(i, \theta))$$

$$R(\text{Layer}, d, \theta) := \left( \left| \frac{S_{\text{TE.ref}}(\text{Layer}, d, \theta)_{1,0}}{S_{\text{TE.ref}}(\text{Layer}, d, \theta)_{0,0}} \right| \right)^2 \cdot \% \text{TE} + \left( \left| \frac{S_{\text{TM.ref}}(\text{Layer}, d, \theta)_{1,0}}{S_{\text{TM.ref}}(\text{Layer}, d, \theta)_{0,0}} \right| \right)^2 \cdot (100 - \% \text{TE})$$

$$S_{\text{TE.trans}}(\text{Layer}, d, \theta) := H_{\text{TE}}(0, \theta) \cdot \prod_{i=1}^{\text{Layer}} (L(i, d_i, \theta) \cdot H_{\text{TE}}(i, \theta))$$

$$S_{\text{TM.trans}}(\text{Layer}, d, \theta) := H_{\text{TM}}(0, \theta) \cdot \prod_{i=1}^{\text{Layer}} (L(i, d_i, \theta) \cdot H_{\text{TM}}(i, \theta))$$

$$T(\text{Layer}, d, \theta) := \left( \left| \frac{1}{S_{\text{TE.trans}}(\text{Layer}, d, \theta)_{0,0}} \right| \right)^2 \cdot \% \text{TE} + \left( \left| \frac{1}{S_{\text{TM.trans}}(\text{Layer}, d, \theta)_{0,0}} \right| \right)^2 \cdot (100 - \% \text{TE})$$

### Optimize Layer Thickness

LayerToOptimize := 2      LayerThickness :=  $\frac{d_{\text{LayerToOptimize}}}{\text{nm}}$       LayerThickness = 70

$$\text{Refl}(\text{LayerThickness}) := \begin{cases} \text{MLstack} \leftarrow d \\ \text{MLstack}_{\text{LayerToOptimize}} \leftarrow \text{LayerThickness} \cdot \text{nm} \\ \text{R}(\text{CalcReflectionFromLayer}, \text{MLstack}, \theta) \end{cases}$$

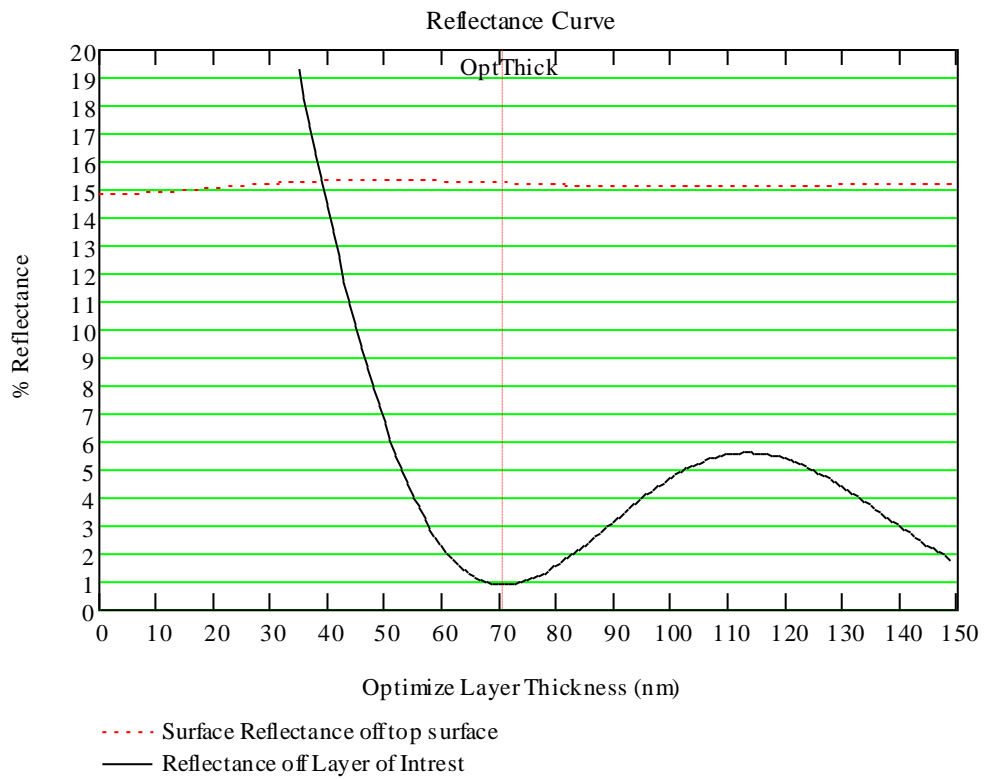
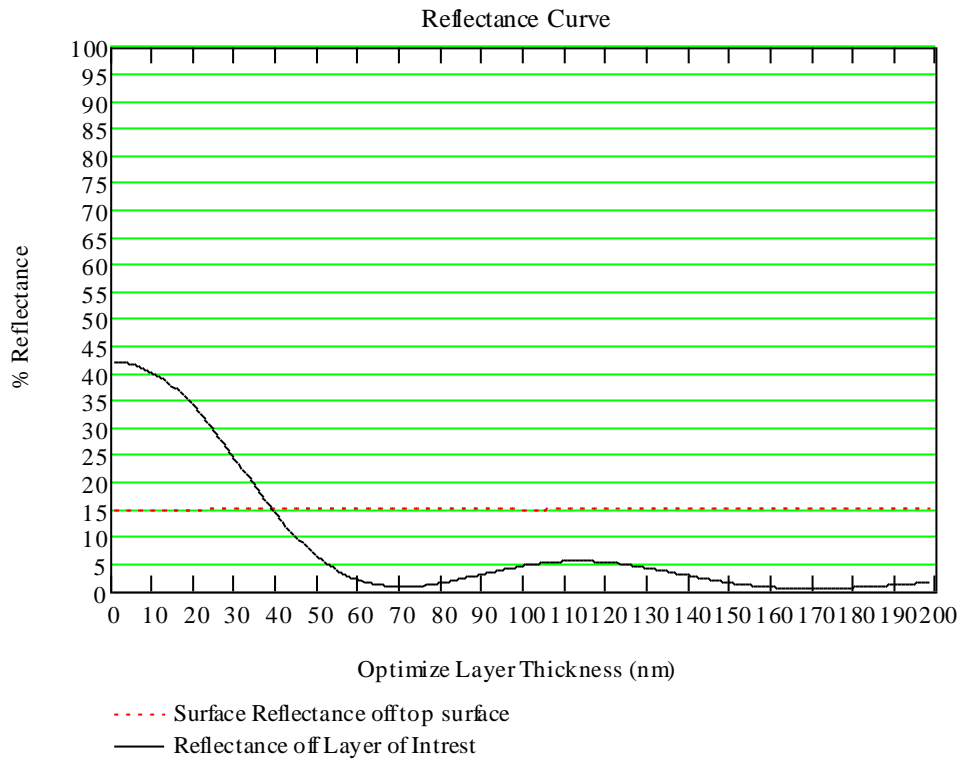
Given      LayerThickness > 0      LayerThickness < 150

OptThick := Minimize(Refl, LayerThickness)      OptThick = 70.867

### Results

LayerThickness := 0nm, 1nm..200nm       $\theta = 47.05\text{deg}$        $\lambda_0 = 355\text{nm}$

OptThick = 70.867       $\text{Refl}(\text{OptThick}) = 0.865$        $\Lambda = 242\text{nm}$

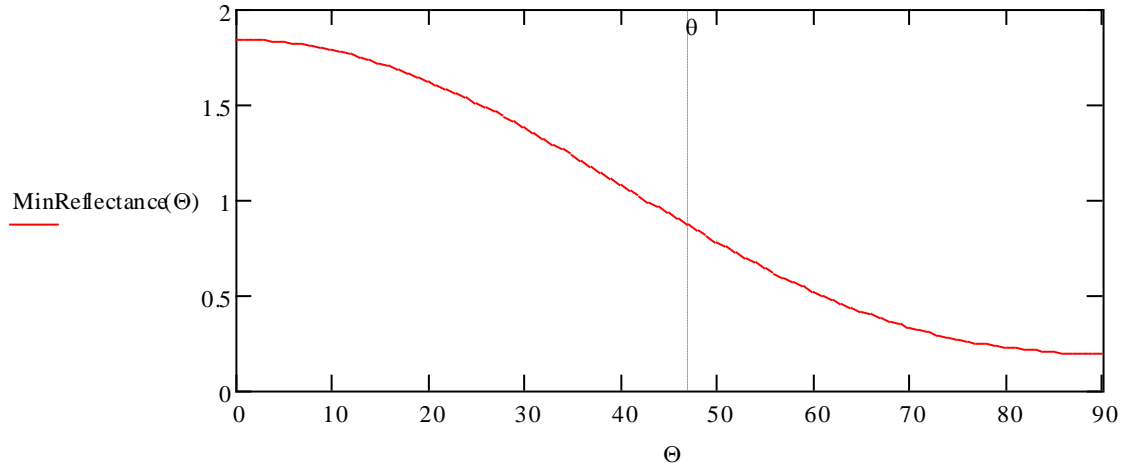




**Minimum reflectance achievable as a function of incident angle**

$$\text{MinReflectance}(\text{Angle}) := \min(\text{Reflection}^{\langle \text{Angle} \rangle})$$

$$\theta := \frac{\theta}{\text{deg}} \quad \theta = 47.05$$



$$\text{MinReflectance}(\text{round}(\theta)) = 0.866$$

$$\text{min}(\text{Reflection}) = 0.192$$

$\theta := 1\text{-deg}, 2\text{-deg} \dots 90\text{-deg}$

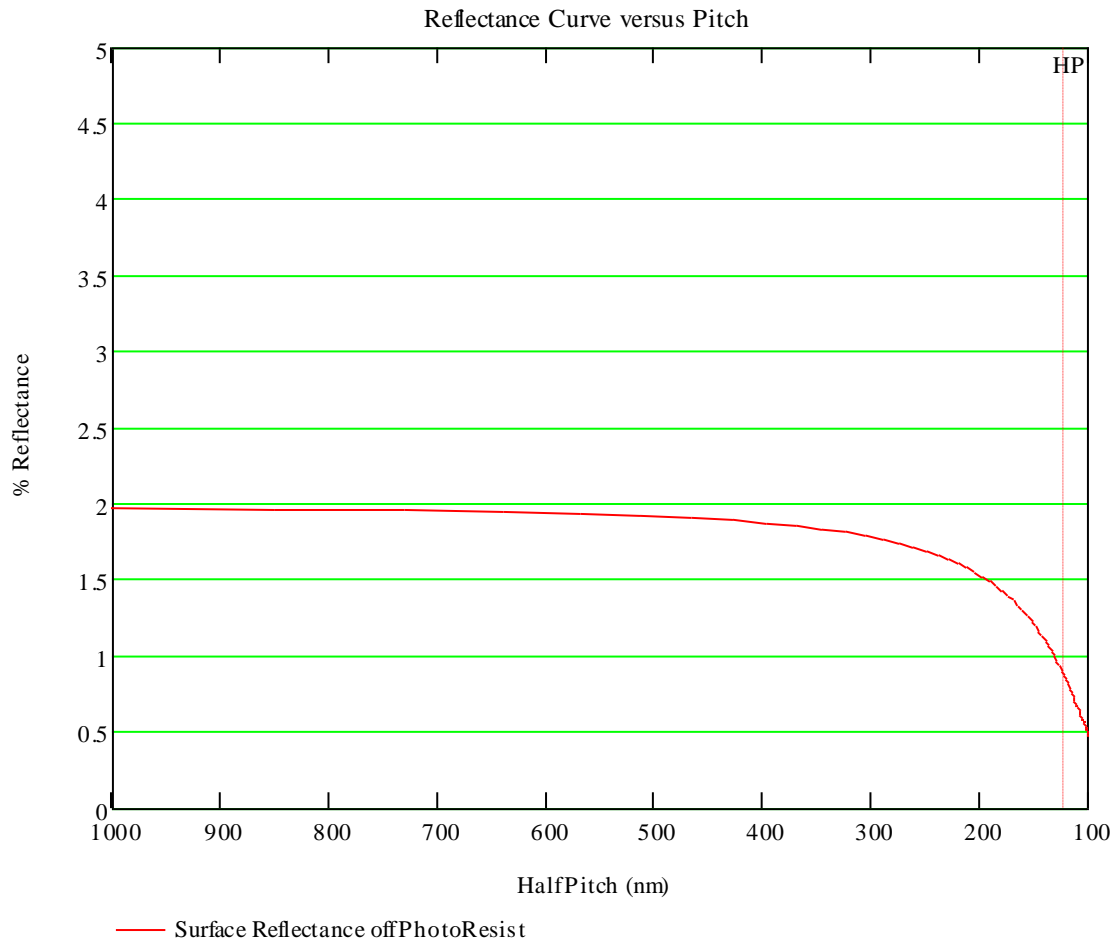
$\lambda_0 = 355\text{nm}$

$\Lambda = 242\text{nm}$

OptThick = 70.867

$HP := \frac{\Lambda}{2 \cdot \text{nm}}$

HP = 121.218



## APPENDIX B

### MatLAB PROGRAM FOR 3D PHOTORESIST PLOTS

MATLAB is used to generate a three-dimensional plot of a photoresist profile generated by mathematically modeling three-dimensional interferometric lithography. The explanation of the math used in the program is found in Chapter 2. The program consists of two files, the main program file called “PhotonicCrystal.m” and a program function call file called “I\_Field.m”. The programs are printed below.

#### PhotonicCrystal.m

```
%%% This file generates a 3D photonic crystal structure %%%
% "PhotonicCrystal.m" Created by Alex Raub
% Also requires "I_Field" file in the same directory

clear;          % Clears items from workspace, freeing up system
memory.
close all;      % Closes all figure window.
deg = pi/180;   % Degree Constant
tic;           % Start timer

% *** Enter Simulation Parameters ***
lambda = 355;   % Vacuum wavelength in nm
n = 1.7;        % Index of resist
theta_pol = 0;  % Polarization angle 0=TE, pi/2=TM
theta_del = 7.458*deg; % The delta angle of the exposing beam
% from the crystal angle in the resist.
psi_c = 26.348*deg; % Crystal angle
phi_del = 120*deg; % The angle rotation between exposures
phase = 0;      % The phase shift between exposures
% (normally 0 % or pi/2)
n_exp = 3;      % The number of separate exposures
% needed to make the crystal
threshold = 0.62; % The resist exposure threshold,
% effects the line-space ratio.
tick_del = 2000; % Set the delta between axes tick marks in nm
array_size_X = 128; % Set the output array size in the X direction
array_size_Y = 128; % Set the output array size in the Y direction
array_size_Z = 128; % Set the output array size in the Z direction
max_x = 10000;    % X model region size in nm
max_y = 10000;    % Y model region size in nm
max_z = 10352;    % Z model region size in nm
% *** End of Parameters ***

k_prop = 2*pi*n/lambda;
del_x = max_x/array_size_X;
del_y = max_y/array_size_Y;
```



```

del_z = max_z/array_size_Z;

% Initializes the output array with zeros
PC_Plot = zeros(array_size_X,array_size_Y,array_size_Z);

% Enters the values into the PC_Plot array
for x = 1:array_size_X;
    for y = 1:array_size_Y;
        for z = 1:array_size_Z;
            % Set the intensity field data minus resist threshold
            PC_Plot(x,y,z)=I_Field((x-1)*del_x,(y-1)*del_y, ...
                (z-1)*del_z,theta_pol,theta_del,psi_c,phi_del, ...
                phase,n_exp,k_prop);
        end
    end
end
array_size_X - x
end
SWR = (max(PC_Plot(:))-min(PC_Plot(:))) ...
    /(max(PC_Plot(:))+min(PC_Plot(:)))
PC_Plot = (PC_Plot/n_exp) - threshold;

% 3D Plot
% Creates a Figure window and plots the 3D surface patch
% and face patches of the crystal
figure; % Creates a new figure window
% Plots the surface of the crystal
p_surf = patch(isosurface(PC_Plot,0));
% Plots the edge surfaces of the crystal at the boundaries
p_face = patch(isocaps(PC_Plot,0));
% Set the Figure window display parameters
% Set the current Figure for 3D Plot view [azimuth ,elevation]
view(23,45);
%Set the display X,Y,Z aspect ratios
daspect([array_size_X/max_x array_size_Y/max_y array_size_Z/max_z]);
axis tight; % Set the axes limits to the data limits
camlight headlight; % Set the Figure window camera light location
% Set the crystal surface color and lighting
set(p_surf,'FaceColor','white','EdgeColor','none');
% Set the crystal edge surface color
set(p_face,'FaceColor',[0.75 0.75 0.75],'EdgeColor','none');
% Set the lighting of the face surface
set(p_surf,'FaceLighting','gouraud');
% Set the transparency and lighting of the edge surface
set(p_face,'FaceAlpha',1,'FaceLighting','flat');
% Set the axes style and line color
set(gca,'Box','on','Color','none','XColor','Black', ...
    'YColor','Black','ZColor','Black');
% Set the X axis scale bar tick marks
set(gca,'XTick',0:(array_size_X/max_x*tick_del):array_size_X);
% Set the Y axis scale bar tick marks
set(gca,'YTick',0:(array_size_Y/max_y*tick_del):array_size_Y);
% Set the Z axis scale bar tick marks
set(gca,'ZTick',0:(array_size_Z/max_z*tick_del):array_size_Z);
% Sets X axis tick values
set(gca,'XTickLabel',0:tick_del:max_x,'FontSize',14, ...
    'FontWeight','bold');
% Sets Y axis tick values
set(gca,'YTickLabel',0:tick_del:max_y,'FontSize',14, ...
    'FontWeight','bold');
% Sets Z axis tick values
set(gca,'ZTickLabel',0:tick_del:max_z,'FontSize',14, ...
    'FontWeight','bold');

```

```

% Set the X axis label name and color
xlabel('X (nm)','Color','Black','FontSize',14,'Fontweight','bold');
% Set the Y axis label name and color
ylabel('Y (nm)','Color','Black','FontSize',14,'Fontweight','bold');
% Set the Z axis label name and color
zlabel('Z (nm)','HorizontalAlignment','right','Rotation',0,...
'Color','Black','FontSize',14,'Fontweight','bold');
% Sets the projection of 3-D objects.
set(gca,'Projection','orthographic');
% Set the current Figure window background and position
set(gcf,'Color','white','Position',[20,20,900,900])

% Set the Plot title name
% title('Photonic Crystal Model','Color','Black');
Filename = sprintf('Pol %2.1f, Theta Delta %2.0f, Crystal Angle %2.0f,
Rotation %3.0f, Phase %1.1f, Threshold %1.2f'...
,theta_pol/pi,theta_del/deg,psi_c/deg,phi_del/deg,phase/pi,threshold);
set(gcf,'Name',Filename);
% end of 3D plot

% Print program execution elapsed time
ElapsedTime=toc;
sprintf('Run time = %.0f minutes %2.1f seconds' ...
,fix(ElapsedTime/60),rem(ElapsedTime,60))

% *** End of Program *** %

```

## I\_Field.m

```

function I = I_Field(x,y,z,theta_pol,theta_del,psi_c,phi,phase,n_exp,k)
theta1 = psi_c-theta_del;
theta2 = psi_c+theta_del;
I = 0;
for r = 0:n_exp-1
    I = I + (.5 * ...
norm(E_Field(x,y,z,theta_pol*r,theta1,phi*r,phase,k) ...
+ E_Field(x,y,z,theta_pol*r,theta2,phi*r,phase*r,k)))^2;
end

function E = E_Field(x,y,z,theta_pol,theta,phi,phase,k)
E = (cos(theta_pol)*[sin(phi); -cos(phi); 0]+sin(theta_pol)* ...
[-cos(theta)*cos(phi); -cos(theta)*sin(phi); sin(theta)])* ...
exp(1i*k*(sin(theta)*cos(phi)*x + sin(theta)*sin(phi)*y ...
+ cos(theta)*z) + 1i*phase);

```

## APPENDIX C

### PROCESS FLOW SHEETS 3D PHOTONIC CRYSTALS.

The process flow and parameters used to create the experimental photonic crystals is provided in the following tables of this appendix. The tables are the process flow sheets or recipes used in the formation of each type of experimental three-dimensional photonic crystal used in this dissertation. They give all the necessary step and parameters needed to recreate the experimental three-dimensional photonic crystals. The first four sections contains the process flow sheets used to create a single photoresist layer photonic-crystal with no waveguides; both three and four exposure three-dimensional photonic crystal done with both 355 nm negative photoresist and 244 nm positive photoresist process flows are specified. Followed by two sections on single photoresist layer photonic-crystal with surface waveguides; one section on the 355 nm negative photoresist with surface waveguides exposed at 244 nm process, and the next section on the 244 nm positive photoresist with surface waveguides exposed at 193 nm process. The last two section present dual photoresist layer photonic-crystal with embedded waveguides; one section on the 355 nm negative photoresist with embedded waveguides exposed at 244 nm process, and the next section on the 244 nm positive photoresist with embedded waveguides exposed at 193 nm process.

#### ***Process Flow for 355 nm One Layer 3-Exposure 3D PhC***

The following table is the process flow sheet or recipe used in the fabrication of the single 355 nm negative photoresist layer three-dimensional photonic crystal done by off-axis three-exposure interferometric lithography. This creates a photonic crystal with

hexagonal symmetry  $\langle 111 \rangle$  on the surface. This twelve step process along with the used materials and parameter is given in the following Table 8.

Step	Description	Value
1	<b>Substrate</b>	silicon wafer
2	<b>Coat Bottom ARC</b>	
	Material	Brewer Science iCON-7
	Spin Speed (RPM)	3000 RPM
	Target Thickness (nm)	72 nm
3	<b>Post Applied Bake (PAB) Bottom ARC</b>	
	PAB Temperature (Celsius)	205°C
	PAB Time (seconds)	60 seconds
4	<b>Coat Adhesion Layer</b>	
	Material	Futurrex NR7-100P
	Spin Speed (RPM)	3000 RPM
	Target Thickness (nm)	100 nm
5	<b>Post Applied Bake (PAB) Adhesion Layer</b>	
	PAB Temperature (Celsius)	130°C
	PAB Time (seconds)	60 seconds
6	<b>Flood Expose Adhesion Layer</b>	
	Exposure Wavelength - $\lambda$ (nm)	355 nm
	Exposure Dose ( $\text{mJ}/\text{cm}^2$ )	$\sim 542 \text{mJ}/\text{cm}^2$ (30 sec.)
7	<b>Post Exposure Bake (PEB) Adhesion Layer</b>	
	PEB Temperature (Celsius)	130°C
	PEB Time (seconds)	60 seconds
8	<b>Coat Thick Photoresist Layer</b>	
	Material	Futurrex NR7-6000P
	Spin Speed (RPM)	2000 RPM
	Target Thickness (nm)	$\sim 7400$ nm
9	<b>Post Applied Bake (PAB) Thick Photoresist Layer</b>	
	PAB Temperature (Celsius)	130°C
	PAB Time (seconds)	120 seconds
10	<b>Expose Thick Photoresist Layer – 3D photonic crystal Exposure</b>	
	Exposure Wavelength - $\lambda$ (nm)	355 nm
	Exposure Dose of each exposure ( $\text{mJ}/\text{cm}^2$ )	$\sim 32.5 \text{mJ}/\text{cm}^2$ (15 sec.)
	Incident Angle - $\theta_i$ (deg)	47.05°
	Delta Angle of the exposing beam from the Incident Angle - $\theta_{\Delta, \text{air}}$ (deg)	15.85°
	Number of Separate Exposures needed to make the crystal - $n$	3
	Rotation Angle between Exposures - $\phi_{\Delta}$ (deg)	120°
Phase Shift between Exposures - $\delta$ (deg)	0°	
11	<b>Post Exposure Bake (PEB) Thick Photoresist Layer</b>	
	PEB Temperature (Celsius)	85°C
	PEB Time (seconds)	120 seconds
12	<b>Develop Thick Photoresist Layer</b>	
	Developer	Futurrex RD-6
	Develop Time (seconds)	180 seconds

	DI H <sub>2</sub> O Rinse Time (seconds)	15 seconds
	DI H <sub>2</sub> O Rinse Spin Speed (RPM)	500 RPM
	N <sub>2</sub> Dry Time (seconds)	15 seconds
	N <sub>2</sub> Dry Spin Speed (RPM)	3000 RPM

**Table 8** – Process flow and parameters for 355 nm single layer 3-exposure 3D PhC.

### ***Process Flow for 355 nm One Layer 4-Exposure 3D PhC***

The following table is the process flow sheet or recipe used in the fabrication of the single 355 nm negative photoresist layer three-dimensional photonic crystal done by off-axis four-exposure interferometric lithography. This creates a photonic crystal with cubic <100> symmetry on the surface. This twelve step process along with the used materials and parameter is given in the following Table 9.

<b>Step</b>	<b>Description</b>	<b>Value</b>
<b>1</b>	<b>Substrate</b>	silicon wafer
<b>2</b>	<b>Coat Bottom ARC</b>	
	Material	Brewer Science iCON-7
	Spin Speed (RPM)	3000 RPM
	Target Thickness (nm)	72 nm
<b>3</b>	<b>Post Applied Bake (PAB) Bottom ARC</b>	
	PAB Temperature (Celsius)	205°C
	PAB Time (seconds)	60 seconds
<b>4</b>	<b>Coat Adhesion Layer</b>	
	Material	Futurrex NR7-100P
	Spin Speed (RPM)	3000 RPM
	Target Thickness (nm)	100 nm
<b>5</b>	<b>Post Applied Bake (PAB) Adhesion Layer</b>	
	PAB Temperature (Celsius)	130°C
	PAB Time (seconds)	60 seconds
<b>6</b>	<b>Flood Expose Adhesion Layer</b>	
	Exposure Wavelength - $\lambda$ (nm)	355 nm
	Exposure Dose (mJ/cm <sup>2</sup> )	~542mJ/cm <sup>2</sup> (30 sec.)
<b>7</b>	<b>Post Exposure Bake (PEB) Adhesion Layer</b>	
	PEB Temperature (Celsius)	130°C
	PEB Time (seconds)	60 seconds
<b>8</b>	<b>Coat Thick Photoresist Layer</b>	
	Material	Futurrex NR7-6000P
	Spin Speed (RPM)	2000 RPM
	Target Thickness (nm)	~7400 nm
<b>9</b>	<b>Post Applied Bake (PAB) Thick Photoresist Layer</b>	
	PAB Temperature (Celsius)	130°C

	PAB Time (seconds)	120 seconds
<b>10</b>	<b>Expose Thick Photoresist Layer – 3D photonic crystal Exposure</b>	
	Exposure Wavelength - $\lambda$ (nm)	355 nm
	Exposure Dose of each exposure ( $\text{mJ}/\text{cm}^2$ )	$\sim 23.8 \text{ mJ}/\text{cm}^2$ (11 sec.)
	Incident Angle - $\theta_i$ (deg)	$47.05^\circ$
	Delta Angle of the exposing beam from the Incident Angle - $\theta_{\Delta, \text{air}}$ (deg)	$15.85^\circ$
	Number of Separate Exposures needed to make the crystal - $n$	4
	Rotation Angle between Exposures - $\phi_{\Delta}$ (deg)	$90^\circ$
	Phase Shift between Exposures - $\delta$ (deg)	$\pi/2^\circ$
<b>11</b>	<b>Post Exposure Bake (PEB) Thick Photoresist Layer</b>	
	PEB Temperature (Celsius)	$85^\circ\text{C}$
	PEB Time (seconds)	120 seconds
<b>12</b>	<b>Develop Thick Photoresist Layer</b>	
	Developer	Futurrex RD-6
	Develop Time (seconds)	180 seconds
	DI H <sub>2</sub> O Rinse Time (seconds)	15 seconds
	DI H <sub>2</sub> O Rinse Spin Speed (RPM)	500 RPM
	N <sub>2</sub> Dry Time (seconds)	15 seconds
	N <sub>2</sub> Dry Spin Speed (RPM)	3000 RPM

**Table 9** – Process flow and parameters for 355 nm single layer 4-exposure 3D PhC.

### **Process Flow for 244 nm One Layer 3-Exposure 3D PhC**

The following table is the process flow sheet or recipe used in the fabrication of the single 244 nm positive photoresist layer three-dimensional photonic crystal done by off-axis three-exposure interferometric lithography. This creates a photonic crystal with hexagonal  $\langle 111 \rangle$  symmetry on the surface. This ten step process along with the used materials and parameter is given in the following Table 10.

<b>Step</b>	<b>Description</b>	<b>Value</b>
<b>1</b>	<b>Substrate</b>	silicon wafer
<b>2</b>	<b>Coat Bottom ARC</b>	
	Material	Brewer Science DUV112
	Spin Speed (RPM)	2000 RPM
	Target Thickness (nm)	65 nm
<b>3</b>	<b>Post Applied Bake (PAB) Bottom ARC</b>	
	PAB Temperature (Celsius)	$205^\circ\text{C}$
	PAB Time (seconds)	60 seconds
<b>4</b>	<b>Coat Thick Photoresist Layer</b>	
	Material	JSR KRF M167J-35cP
	Spin Speed (RPM)	2000 RPM
	Target Thickness (nm)	$\sim 1300 \text{ nm}$

<b>5</b>	<b>Post Applied Bake (PAB) Thick Photoresist Layer</b>	
	PAB Temperature (Celsius)	130°C
	PAB Time (seconds)	90 seconds
<b>6</b>	<b>Coat Thick Photoresist Layer</b>	
	Material	JSR KRF M167J-35cP
	Spin Speed (RPM)	2000 RPM
	Target Thickness (nm)	~1300 nm
<b>7</b>	<b>Post Applied Bake (PAB) Thick Photoresist Layer</b>	
	PAB Temperature (Celsius)	130°C
	PAB Time (seconds)	90 seconds
<b>8</b>	<b>Expose Thick Photoresist Layer – 3D photonic crystal Exposure</b>	
	Exposure Wavelength - $\lambda$ (nm)	244 nm
	Exposure Dose of each exposure ( $\text{mJ}/\text{cm}^2$ )	~1.2 - 2.0 $\text{mJ}/\text{cm}^2$ (15 - 25 sec.)
	Incident Angle - $\theta_i$ (deg)	47.05°
	Delta Angle of the exposing beam from the Incident Angle - $\theta_{\Delta, \text{air}}$ (deg)	15.85°
	Number of Separate Exposures needed to make the crystal - $n$	3
	Rotation Angle between Exposures - $\phi_{\Delta}$ (deg)	120°
	Phase Shift between Exposures - $\delta$ (deg)	0°
<b>9</b>	<b>Post Exposure Bake (PEB) Thick Photoresist Layer</b>	
	PEB Temperature (Celsius)	95°C
	PEB Time (seconds)	90 seconds
<b>10</b>	<b>Develop Thick Photoresist Layer</b>	
	Developer	Futurrex RD-6
	Develop Time (seconds)	180 seconds
	DI H <sub>2</sub> O Rinse Time (seconds)	15 seconds
	DI H <sub>2</sub> O Rinse Spin Speed (RPM)	500 RPM
	N <sub>2</sub> Dry Time (seconds)	15 seconds
	N <sub>2</sub> Dry Spin Speed (RPM)	3000 RPM

**Table 10** – Process flow and parameters for 244 nm single layer 3-exposure 3D PhC.

### ***Process Flow for 244 nm One Layer 4-Exposure 3D PhC***

The following table is the process flow sheet or recipe used in the fabrication of the single 244 nm positive photoresist layer three-dimensional photonic crystal done by off-axis four-exposure interferometric lithography. This creates a photonic crystal with cubic <100> symmetry on the surface. This ten step process along with the used materials and parameter is given in the following Table 11.

<b>Step</b>	<b>Description</b>	<b>Value</b>
<b>1</b>	<b>Substrate</b>	silicon wafer
<b>2</b>	<b>Coat Bottom ARC</b>	

	Material	Brewer Science DUV112
	Spin Speed (RPM)	2000 RPM
	Target Thickness (nm)	65 nm
<b>3</b>	<b>Post Applied Bake (PAB) Bottom ARC</b>	
	PAB Temperature (Celsius)	205°C
	PAB Time (seconds)	60 seconds
<b>4</b>	<b>Coat Thick Photoresist Layer</b>	
	Material	JSR KRF M167J-35cP
	Spin Speed (RPM)	2000 RPM
	Target Thickness (nm)	~1300 nm
<b>5</b>	<b>Post Applied Bake (PAB) Thick Photoresist Layer</b>	
	PAB Temperature (Celsius)	130°C
	PAB Time (seconds)	90 seconds
<b>6</b>	<b>Coat Thick Photoresist Layer</b>	
	Material	JSR KRF M167J-35cP
	Spin Speed (RPM)	2000 RPM
	Target Thickness (nm)	~1300 nm
<b>7</b>	<b>Post Applied Bake (PAB) Thick Photoresist Layer</b>	
	PAB Temperature (Celsius)	130°C
	PAB Time (seconds)	90 seconds
<b>8</b>	<b>Expose Thick Photoresist Layer – 3D photonic crystal Exposure</b>	
	Exposure Wavelength - $\lambda$ (nm)	244 nm
	Exposure Dose of each exposure ( $\text{mJ}/\text{cm}^2$ )	~1.2 $\text{mJ}/\text{cm}^2$ (15 sec.)
	Incident Angle - $\theta_i$ (deg)	47.05°
	Delta Angle of the exposing beam from the Incident Angle - $\theta_{\Delta, \text{air}}$ (deg)	15.85°
	Number of Separate Exposures needed to make the crystal - $n$	4
	Rotation Angle between Exposures - $\phi_{\Delta}$ (deg)	90°
	Phase Shift between Exposures - $\delta$ (deg)	$\pi/2^\circ$
<b>9</b>	<b>Post Exposure Bake (PEB) Thick Photoresist Layer</b>	
	PEB Temperature (Celsius)	95°C
	PEB Time (seconds)	90 seconds
<b>10</b>	<b>Develop Thick Photoresist Layer</b>	
	Developer	Futurrex RD-6
	Develop Time (seconds)	180 seconds
	DI H <sub>2</sub> O Rinse Time (seconds)	15 seconds
	DI H <sub>2</sub> O Rinse Spin Speed (RPM)	500 RPM
	N <sub>2</sub> Dry Time (seconds)	15 seconds
	N <sub>2</sub> Dry Spin Speed (RPM)	3000 RPM

**Table 11** – Process flow and parameters for 244 nm single layer 4-exposure 3D PhC.

### ***Process Flow for 355 nm PhC with 244 nm Surface Waveguides***

The following table is the process flow sheet or recipe used in the fabrication of the single 355 nm negative photoresist layer three-dimensional photonic crystal done by off-axis three-exposure interferometric lithography with a surface waveguide. The



surface waveguide was created using a chrome-on-glass contact mask exposed at 244 nm. This creates a photonic crystal with hexagonal <111> symmetry on the surface and a solid photoresist waveguide on the surface of the photonic crystal. This thirteen-step process along with the used materials and parameter is given in the following Table 12.

Step	Description	Value
1	<b>Substrate</b>	silicon wafer
2	<b>Coat Bottom ARC</b>	
	Material	Brewer Science iCON-7
	Spin Speed (RPM)	3000 RPM
	Target Thickness (nm)	72 nm
3	<b>Post Applied Bake (PAB) Bottom ARC</b>	
	PAB Temperature (Celsius)	205°C
	PAB Time (seconds)	60 seconds
4	<b>Coat Adhesion Layer</b>	
	Material	Futurrex NR7-100P
	Spin Speed (RPM)	3000 RPM
	Target Thickness (nm)	100 nm
5	<b>Post Applied Bake (PAB) Adhesion Layer</b>	
	PAB Temperature (Celsius)	130°C
	PAB Time (seconds)	60 seconds
6	<b>Flood Expose Adhesion Layer</b>	
	Exposure Wavelength - $\lambda$ (nm)	355 nm
	Exposure Dose ( $\text{mJ}/\text{cm}^2$ )	$\sim 542 \text{mJ}/\text{cm}^2$ (30 sec.)
7	<b>Post Exposure Bake (PEB) Adhesion Layer</b>	
	PEB Temperature (Celsius)	130°C
	PEB Time (seconds)	60 seconds
8	<b>Coat Thick Photoresist Layer</b>	
	Material	Futurrex NR7-6000P
	Spin Speed (RPM)	2000 RPM
	Target Thickness (nm)	$\sim 7400$ nm
9	<b>Post Applied Bake (PAB) Thick Photoresist Layer</b>	
	PAB Temperature (Celsius)	130°C
	PAB Time (seconds)	120 seconds
10	<b>Expose Thick Photoresist Layer – 3D photonic crystal Exposure</b>	
	Exposure Wavelength - $\lambda$ (nm)	355 nm
	Exposure Dose of each exposure ( $\text{mJ}/\text{cm}^2$ )	$\sim 32.5 \text{mJ}/\text{cm}^2$ (15 sec.)
	Incident Angle - $\theta_i$ (deg)	47.05°
	Delta Angle of the exposing beam from the Incident Angle - $\theta_{\Delta, \text{air}}$ (deg)	15.85°
	Number of Separate Exposures needed to make the crystal - $n$	3
	Rotation Angle between Exposures - $\phi_{\Delta}$ (deg)	120°
Phase Shift between Exposures - $\delta$ (deg)	0°	
11	<b>Expose Thick Photoresist Layer – Waveguides Exposure</b>	
	Exposure Wavelength - $\lambda$ (nm)	244 nm

	Exposure Dose of each exposure (mJ/cm <sup>2</sup> )	~20.9 mJ/cm <sup>2</sup> (11 sec.)
<b>12</b>	<b>Post Exposure Bake (PEB) Thick Photoresist Layer</b>	
	PEB Temperature (Celsius)	85°C
	PEB Time (seconds)	120 seconds
<b>13</b>	<b>Develop Thick Photoresist Stack</b>	
	Developer	Futurrex RD-6
	Develop Time (seconds)	180 seconds
	DI H <sub>2</sub> O Rinse Time (seconds)	15 seconds
	DI H <sub>2</sub> O Rinse Spin Speed (RPM)	500 RPM
	N <sub>2</sub> Dry Time (seconds)	15 seconds
	N <sub>2</sub> Dry Spin Speed (RPM)	3000 RPM

**Table 12** – Process flow for 355 nm PhC with 244 nm surface waveguides in negative photoresist.

### ***Process Flow for 244 nm PhC with 193 nm Surface Waveguides***

The following table is the process flow sheet or recipe used in the fabrication of the single 244 nm positive photoresist layer three-dimensional photonic crystal done by off-axis three-exposure interferometric lithography with a surface waveguide. The surface waveguide was created using a chrome-on-glass contact mask exposed at 193 nm. This creates a photonic crystal with hexagonal <111> symmetry on the surface and an air void waveguide on the surface of the photonic crystal. This eleven step process along with the used materials and parameter is given in the following Table 13.

<b>Step</b>	<b>Description</b>	<b>Value</b>
<b>1</b>	<b>Substrate</b>	silicon wafer
<b>2</b>	<b>Coat Bottom ARC</b>	
	Material	Brewer Science DUV112
	Spin Speed (RPM)	2000 RPM
	Target Thickness (nm)	65 nm
<b>3</b>	<b>Post Applied Bake (PAB) Bottom ARC</b>	
	PAB Temperature (Celsius)	205°C
	PAB Time (seconds)	60 seconds
<b>4</b>	<b>Coat Thick Photoresist 1<sup>st</sup> Lower Layer</b>	
	Material	JSR KRF M167J-35cP
	Spin Speed (RPM)	2000 RPM
	Target Thickness (nm)	~1300 nm
<b>5</b>	<b>Post Applied Bake (PAB) Thick Photoresist 1<sup>st</sup> Layer</b>	
	PAB Temperature (Celsius)	130°C
	PAB Time (seconds)	90 seconds
<b>6</b>	<b>Coat Thick Photoresist 2<sup>nd</sup> Layer</b>	

	Material	JSR KRF M167J-35cP
	Spin Speed (RPM)	2000 RPM
	Target Thickness (nm)	~1300 nm
<b>7</b>	<b>Post Applied Bake (PAB) Thick Photoresist 2<sup>nd</sup> Layer</b>	
	PAB Temperature (Celsius)	130°C
	PAB Time (seconds)	90 seconds
<b>8</b>	<b>Expose Thick Photoresist Stack – 3D photonic crystal Exposure</b>	
	Exposure Wavelength - $\lambda$ (nm)	244 nm
	Exposure Dose of each exposure ( $\text{mJ}/\text{cm}^2$ )	~1.6 $\text{mJ}/\text{cm}^2$ (20 sec.)
	Incident Angle - $\theta_i$ (deg)	47.05°
	Delta Angle of the exposing beam from the Incident Angle - $\theta_{\Delta, \text{air}}$ (deg)	15.85°
	Number of Separate Exposures needed to make the crystal - $n$	3
	Rotation Angle between Exposures - $\phi_{\Delta}$ (deg)	120°
	Phase Shift between Exposures - $\delta$ (deg)	0°
<b>9</b>	<b>Expose Thick Photoresist Stack – Waveguides Exposure</b>	
	Exposure Wavelength - $\lambda$ (nm)	193 nm
	Exposure Dose of each exposure ( $\text{mJ}/\text{cm}^2$ )	~681 $\text{mJ}/\text{cm}^2$ (60,000 Pulses)
<b>10</b>	<b>Post Exposure Bake (PEB) Thick Photoresist Stack</b>	
	PEB Temperature (Celsius)	95°C
	PEB Time (seconds)	90 seconds
<b>11</b>	<b>Develop Thick Photoresist Stack</b>	
	Developer	Futurrex RD-6
	Develop Time (seconds)	180 seconds
	DI H <sub>2</sub> O Rinse Time (seconds)	15 seconds
	DI H <sub>2</sub> O Rinse Spin Speed (RPM)	500 RPM
	N <sub>2</sub> Dry Time (seconds)	15 seconds
	N <sub>2</sub> Dry Spin Speed (RPM)	3000 RPM

**Table 13** – Process flow for 244 nm PhC with 193 nm surface waveguides in positive photoresist.

## ***Process Flow for 355 nm PhC with 244 nm Embedded Waveguides***

The following table is the process flow sheet or recipe used in the fabrication of the dual 355 nm negative photoresist layer three-dimensional photonic crystal done by off-axis three-exposure interferometric lithography with an embedded waveguide. The embedded waveguide was created using a chrome-on-glass contact mask exposed at 244 nm between photoresist coats. This creates a photonic crystal with hexagonal <111> symmetry on the surface and a solid photoresist waveguide in the middle of the photonic

crystal. This sixteen step process along with the used materials and parameter is given in the following Table 14.

Step	Description	Value
1	<b>Substrate</b>	silicon wafer
2	<b>Coat Bottom ARC</b>	
	Material	Brewer Science iCON-7
	Spin Speed (RPM)	3000 RPM
	Target Thickness (nm)	72 nm
3	<b>Post Applied Bake (PAB) Bottom ARC</b>	
	PAB Temperature (Celsius)	205°C
	PAB Time (seconds)	60 seconds
4	<b>Coat Adhesion Layer</b>	
	Material	Futurrex NR7-100P
	Spin Speed (RPM)	3000 RPM
	Target Thickness (nm)	100 nm
5	<b>Post Applied Bake (PAB) Adhesion Layer</b>	
	PAB Temperature (Celsius)	130°C
	PAB Time (seconds)	60 seconds
6	<b>Flood Expose Adhesion Layer</b>	
	Exposure Wavelength - $\lambda$ (nm)	355 nm
	Exposure Dose ( $\text{mJ}/\text{cm}^2$ )	$\sim 542 \text{mJ}/\text{cm}^2$ (30 sec.)
7	<b>Post Exposure Bake (PEB) Adhesion Layer</b>	
	PEB Temperature (Celsius)	130°C
	PEB Time (seconds)	60 seconds
8	<b>Coat Thick Photoresist 1<sup>st</sup> Layer</b>	
	Material	Futurrex NR7-6000P
	Spin Speed (RPM)	2000 RPM
	Target Thickness (nm)	$\sim 7400$ nm
9	<b>Post Applied Bake (PAB) Thick Photoresist 1<sup>st</sup> Layer</b>	
	PAB Temperature (Celsius)	130°C
	PAB Time (seconds)	120 seconds
10	<b>Expose Thick Photoresist 1<sup>st</sup> Layer – Waveguides Exposure</b>	
	Exposure Wavelength - $\lambda$ (nm)	244 nm
	Exposure Dose of each exposure ( $\text{mJ}/\text{cm}^2$ )	$\sim 47.4 \text{mJ}/\text{cm}^2$ (25 sec.)
11	<b>Post Exposure Bake (PEB) Thick Photoresist 1<sup>st</sup> Layer</b>	
	PEB Temperature (Celsius)	85°C
	PEB Time (seconds)	120 seconds
12	<b>Coat Thick Photoresist 2<sup>nd</sup> Layer</b>	
	Material	Futurrex NR7-6000P
	Spin Speed (RPM)	2000 RPM
	Target Thickness (nm)	$\sim 7400$ nm
13	<b>Post Applied Bake (PAB) Thick Photoresist 2<sup>nd</sup> Layer</b>	
	PAB Temperature (Celsius)	130°C
	PAB Time (seconds)	540 seconds
14	<b>Expose Thick Photoresist Layer – 3D photonic crystal Exposure</b>	

	Exposure Wavelength - $\lambda$ (nm)	355 nm
	Exposure Dose of each exposure ( $\text{mJ}/\text{cm}^2$ )	$\sim 86.5 \text{mJ}/\text{cm}^2$ (40 sec.)
	Incident Angle - $\theta_i$ (deg)	$47.05^\circ$
	Delta Angle of the exposing beam from the Incident Angle - $\theta_{\Delta, \text{air}}$ (deg)	$15.85^\circ$
	Number of Separate Exposures needed to make the crystal - $n$	3
	Rotation Angle between Exposures - $\phi_{\Delta}$ (deg)	$120^\circ$
	Phase Shift between Exposures - $\delta$ (deg)	$0^\circ$
<b>15</b>	<b>Post Exposure Bake (PEB) Thick Photoresist Stack</b>	
	PEB Temperature (Celsius)	$85^\circ\text{C}$
	PEB Time (seconds)	120 seconds
<b>16</b>	<b>Develop Thick Photoresist Stack</b>	
	Developer	Futurrex RD-6
	Develop Time (seconds)	180 seconds
	DI H <sub>2</sub> O Rinse Time (seconds)	15 seconds
	DI H <sub>2</sub> O Rinse Spin Speed (RPM)	500 RPM
	N <sub>2</sub> Dry Time (seconds)	15 seconds
	N <sub>2</sub> Dry Spin Speed (RPM)	3000 RPM

**Table 14** – Process flow for 355 nm PhC with 244 nm embedded waveguides in negative photoresist.

## APPENDIX D

### BARC COAT PROGRAM

The bottom anti-reflecting coating (BARC) is applied to the silicon wafer using a Brewer Science model 100 spinner. The 3 ml of BARC material is hand dispensed on the wafer using a 5 ml syringe with a 0.1  $\mu\text{m}$  Millipore filter during step 0 of the spin program. The coat program used in the spinner is given in Table 15 below. Step zero is used to evenly dispense the BARC, step one is used to quickly spread the BARC across the wafer, and step two is used to thin the BARC to desired thickness. This produces a uniform film across the bare silicon wafer.

<b>Auto Dispense</b> (1=on, 0=off)	<b>Step</b> (0-9)	<b>Spin Speed</b> (0-6000 RPM, Clear=END)	<b>Ramp Rate</b> (0-30000 RPM/sec)	<b>Time</b> (0-999 sec)
0	0	30	5000	10
	1	500	10000	2
	2	3000	500	30
	3	END		

**Table 15** – BARC coat spin program.

## APPENDIX E

### PHOTORESIST COAT PROGRAM

The photoresist is applied to the silicon wafer using a Brewer Science model 100 spinner. The 3 ml of photoresist material is hand dispensed on the wafer using a 5 ml syringe with a 0.1  $\mu\text{m}$  Millipore filter during step 0 of the spin program. This spin coat program is optimized for very viscous photoresist used for the thick photoresist films needed to fabricate three-dimensional photonic crystals. The coat program used in the spinner is given in Table 16 below. Step zero is used to evenly dispense the photoresist, step one is used to quickly spread the photoresist across the wafer, and step two is used to thin the photoresist to desired thickness. The spin speed needed in step two depended on the viscosity photoresist used, and is normally between 1500 RPM to 4000 RPM. For Futerrex NR7-6000P photoresist the spin speed used was 2000 RPMs. This produce a uniform photoresist film of 6- $\mu\text{m}$  thick over the BARC film on the bare silicon wafer.

<b>Auto Dispense</b> (1=on, 0=off)	<b>Step</b> (0-9)	<b>Spin Speed</b> (0-6000 RPM, Clear=END)	<b>Ramp Rate</b> (0-30000 RPM/sec)	<b>Time</b> (0-999 sec)
0	0	50	5000	10
	1	1500	10000	3
	2	2000 (1500-4000)*	500	45
	3	END		
* Final spin speed determined by photoresist used.				

**Table 16** – Photoresist coat spin program.

## APPENDIX F

### PHOTORESIST DEVELOP PROGRAM

The photoresist is developed in a Brewer Science model 100 spinner. The develop program used in the spinner is given in Table 17 below. The Futurrex RD6 developer is automatically dispensed on the wafer during step two of the spin program. This developer program is optimized for very thick photoresist development used for the thick photoresist films needed to fabricate three-dimensional photonic crystals. Step zero is used to get the wafer at initial spin speed, step one ramps down the spin speed to ensure an even dispersal of developer during the next step. Step two is used to quickly dispense and spread the developer across the wafer as the wafer slows down to the final spin speed of this step. Step three is used to puddle develop the photoresist for three minutes, step four start ramping the spin speed up before step five, which quickly rinses the wafer by dispensing DI water for 15 seconds, and step six dries the wafer by blowing nitrogen gas across the wafer as it spins at a high speeds. This produces a uniform and consistent photoresist development.

<b>Auto Dispense</b> (1=on, 0=off)	<b>Step</b> (0-9)	<b>Spin Speed</b> (0-6000 RPM, Clear=END)	<b>Ramp Rate</b> (0-30000 RPM/sec)	<b>Nozzle*</b> (0-4, 0=off)	<b>Time</b> (0-999 sec)
1	0	500	10000	0	1
	1	500	175	0	1
	2	30	175	2	3
	3	10	5000	0	180
	4	150	500	0	1
	5	500	1000	3	15
	6	3000	5000	4	15
	7	END			
* Nozzle: 2=Developer, 3=DI H2O, 4=Dry N <sub>2</sub> Gas					

**Table 17** – Photoresist develop program.



## APPENDIX G

### NEWPORT ROTATION STAGE CONTROLLER LABVIEW

#### PROGRAM

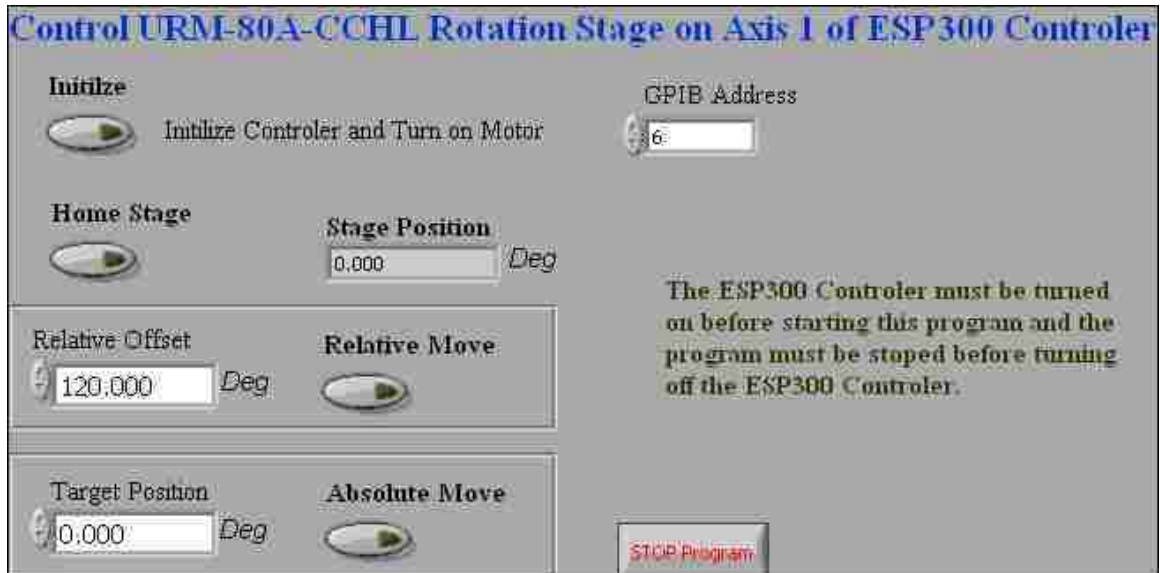
The rotation stage for the Michelson interferometric lithography setup used a Newport URM-80A-CCHL rotation stage hooked up to a Newport ESP300 Universal Motion Controller/Driver. The stage controller is controlled by a LabVIEW program through a GBIP interface. The front panel and block diagram for the program are seen below. The program has four functions: initialize controller and rotation stage (normally performed after starting the program), home the rotation stage (normally performed after initializing the controller), move the rotation stage to a relative position, and move the rotation stage to an absolute position. The program also always reports the current stage position.

#### Control URM 80A CCHL Rotation Stage on Axis 1 of ESP300 Controller.vi

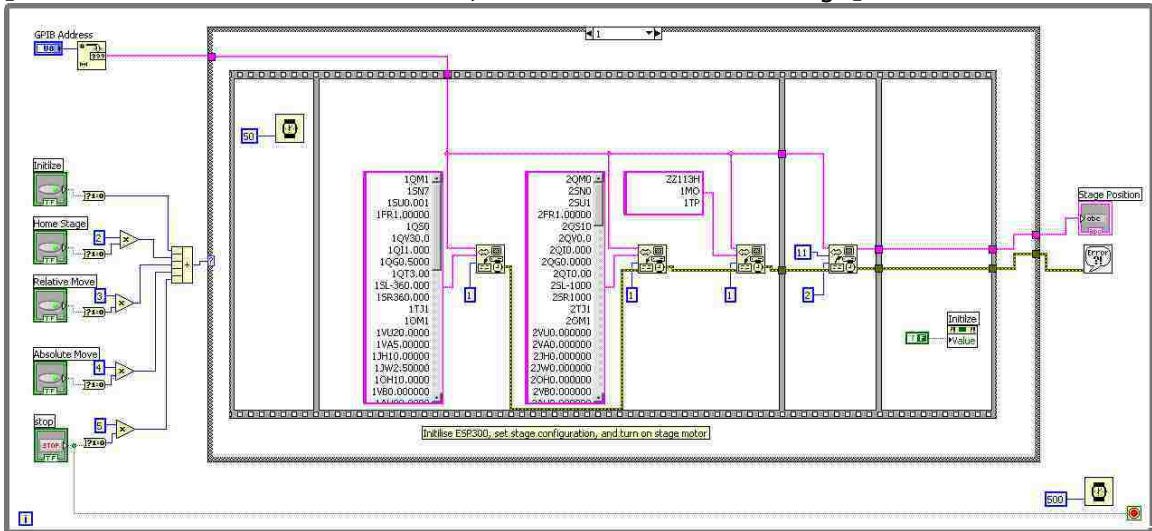
vi Icon



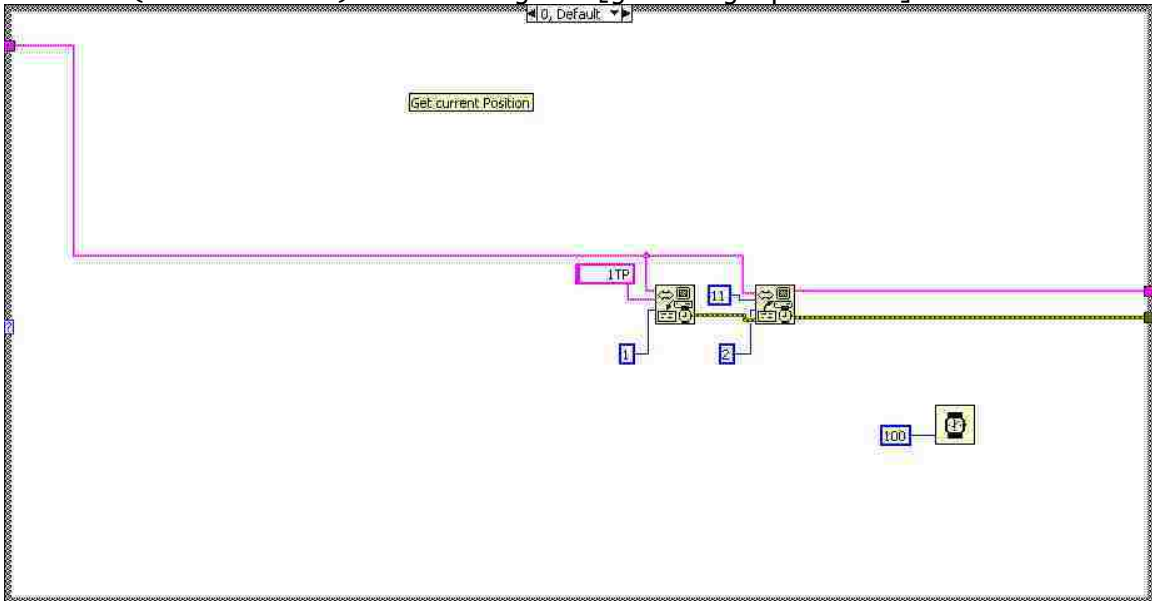
Front Panel



Main Block Diagram, with case #1 block diagram  
 [initialize ESP300 controller, and URM 80A CCHL Stage]



case #0 (default case) block diagram [get stage position]







## APPENDIX H

# COHERENT INFINITY LASER EXPOSURE CONTROL LABVIEW PROGRAM

The Coherent Infinity 40-100 NdYAG laser output is controlled by a LabVIEW program. The LabVIEW program controls the gate of the laser mode lock source, which controls the lasing of the laser. The program also counts the triggered pulses of the laser firing and the pulse rep rate. The program works by entering an exposure time and calculating the number of pulses to fire. The user can then have the program execute that number of pulses from the laser. The front panel and block diagram for the program is seen below.

### Infinity Laser Exposure Timer.vi

vi Icon

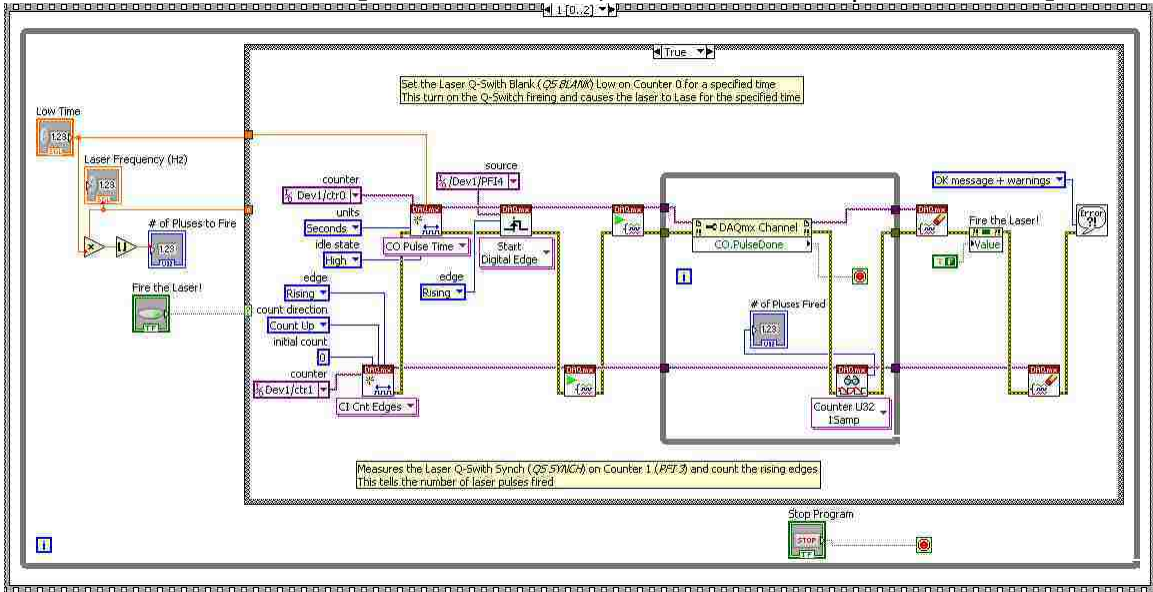


Front Panel

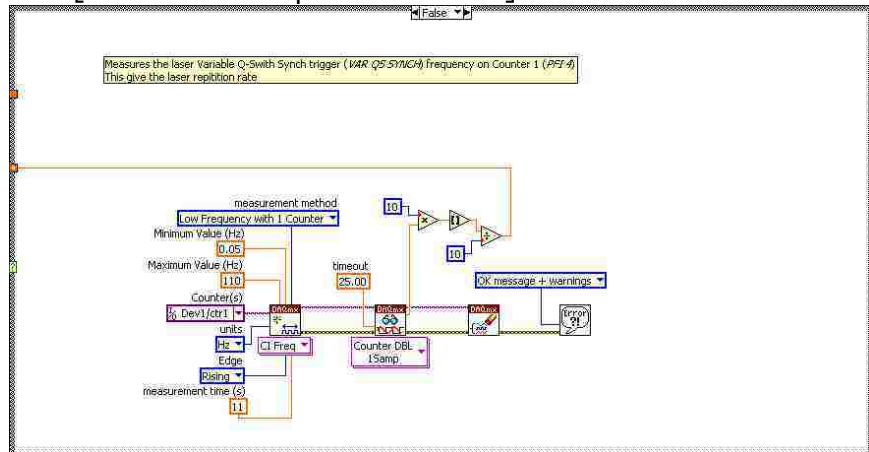




Main Block Diagram, with block sequence #1 [main program loop], and if statement true [fire the laser, and count the pulses fired]



If statement false [read laser repetition rate]



## APPENDIX I

### JEOL SEM IMAGE CAPTURE LABVIEW PROGRAM

A JEOL 6400F field emission scanning electron microscope is used to capture all the images of the fabricated photonic crystals. A LabVIEW program was written to capture high resolution 16-bit depth images off of the JOEL SEM, using a PCIe-6251 multifunction data acquisition card. It uses the SEM's EDX interface, for controlling the scan coils on the gun. It captures the conditioned PMT voltage signal in synchronization with the scan signals to recreate the scanned image. The front panel and block diagram for the program is seen on the next page. The program reads default configuration and calibration data from a text file named "SEM\_Capture\_Config.txt" which is given below.

#### SEM Capture Config.txt

```
Configuration File for Labview "SEM Capture.vi"
*****
Default Image Size:      512
Default SEM Mag: 50000
Default # of Iterations: 25
Default Sampling Rate: 500000
X Pixel size in um:      0.036697
Y Pixel size in um:      0.036529
Mag at which pixel size was measured: 5000
Resolution at which pixel size was measured: 512
X Scan Ampitude in Volts (X Pixel Mag) {0-10}: 10
Y Scan Ampitude in Volts (Y Pixel Mag) {0-10}: 7.37
```

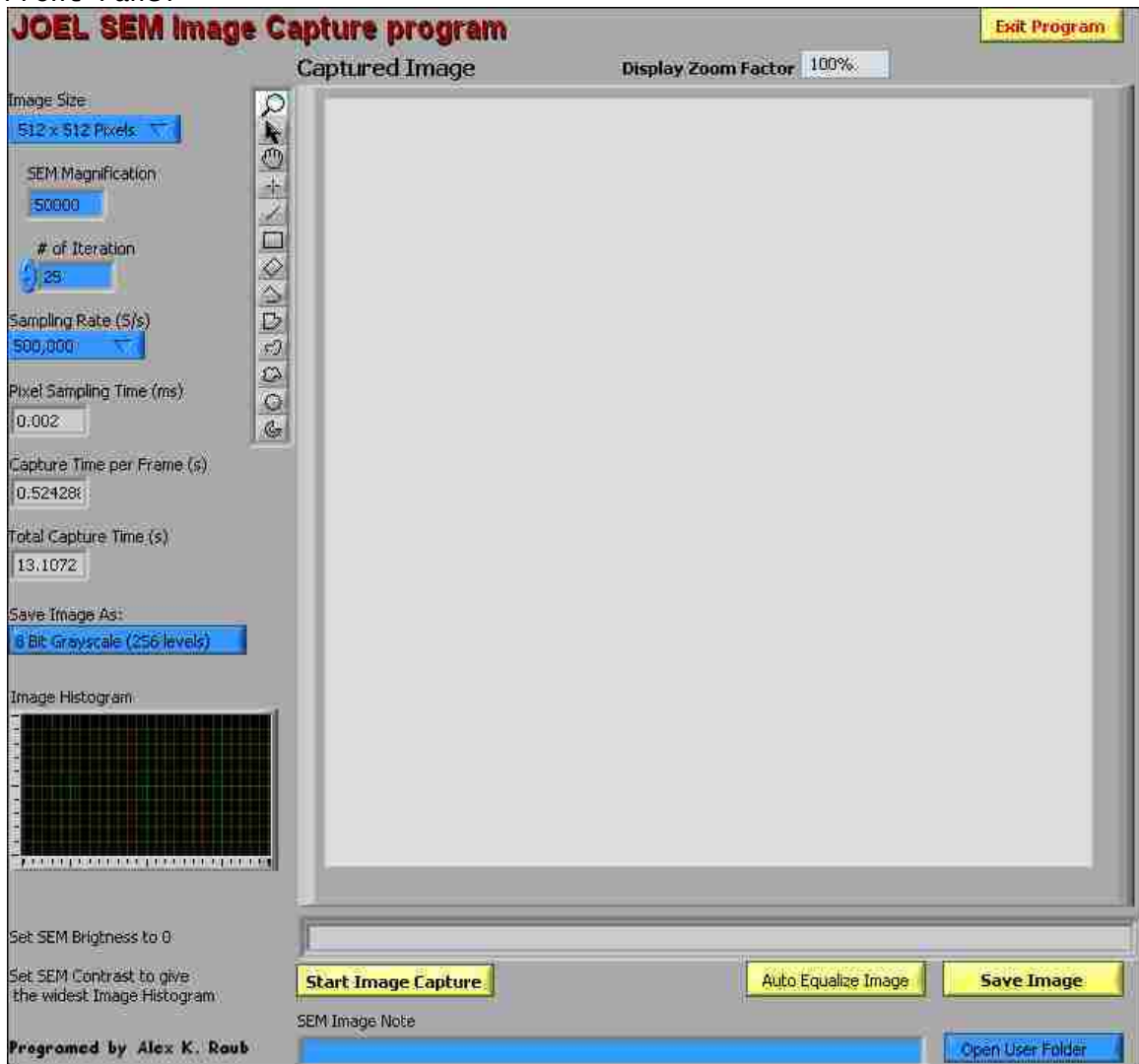


# SEM Capture.vi

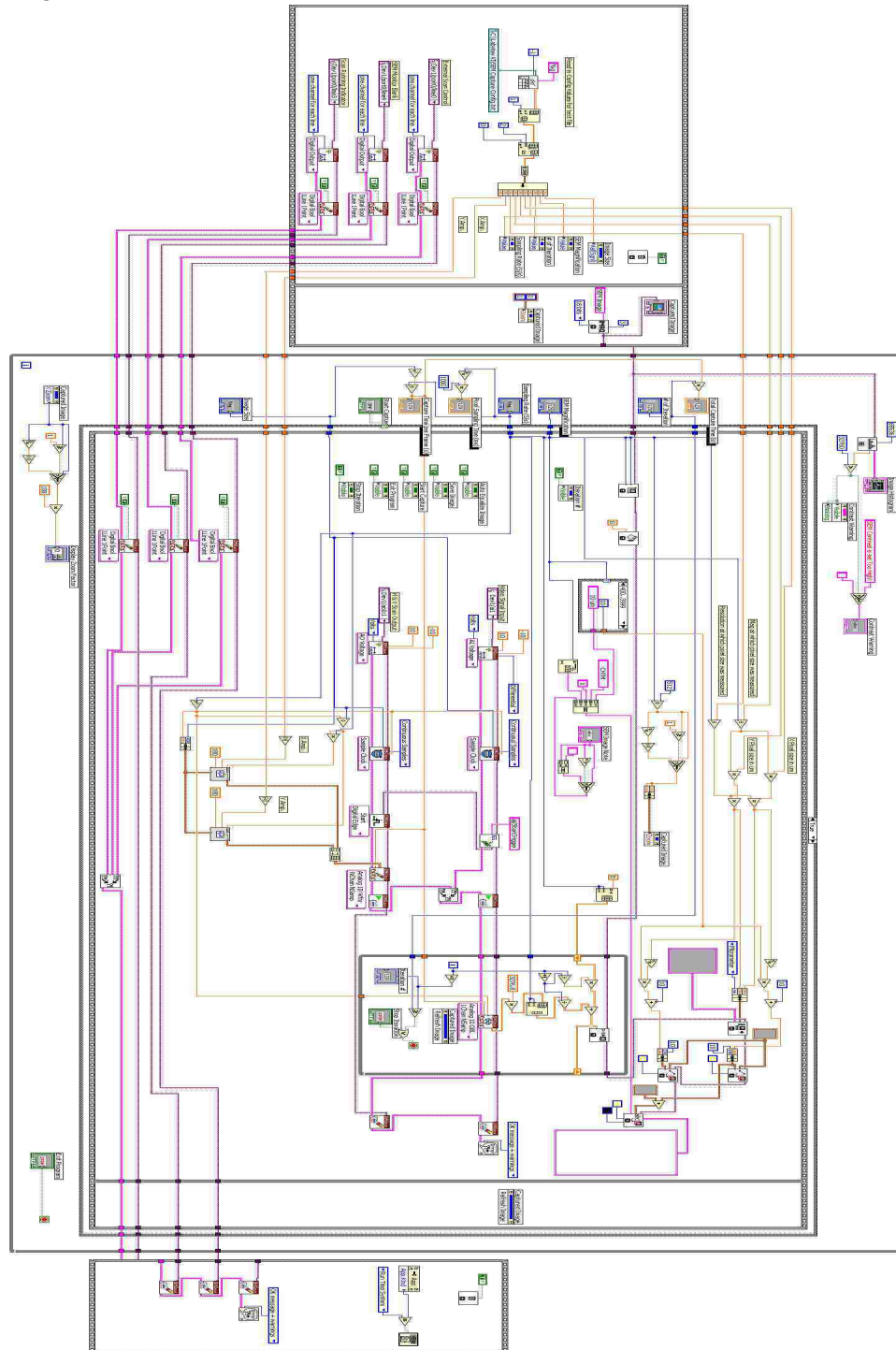
vi Icon



Front Panel



Main Block Diagram [Block Rotated 90° to fit better on the page],  
with image capture block if statement set to True.



Each SEM Magnification block cases

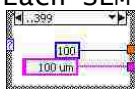


Image capture block if statement set to False,  
 with auto equalize image block set to True,  
 save image block set to True,  
 use last directory block set to True,  
 and save image as block set to False (8-bit grayscale).

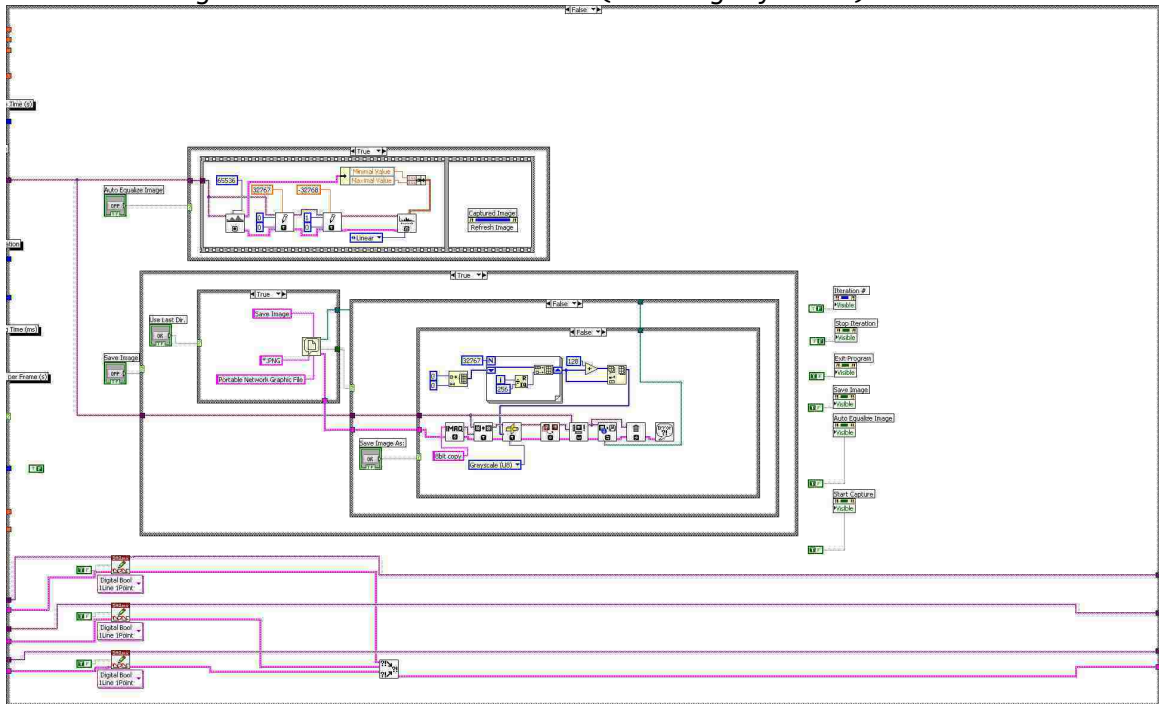


Image capture block if statement set to False,  
 with auto equalize image block set to False,  
 and save image block set to False.



Image capture block if statement set to False,  
with auto equalize image block set to True,  
save image block set to True,  
use last directory block set to False (User Folders directory),  
and save image as block set to True (16-bit grayscale).

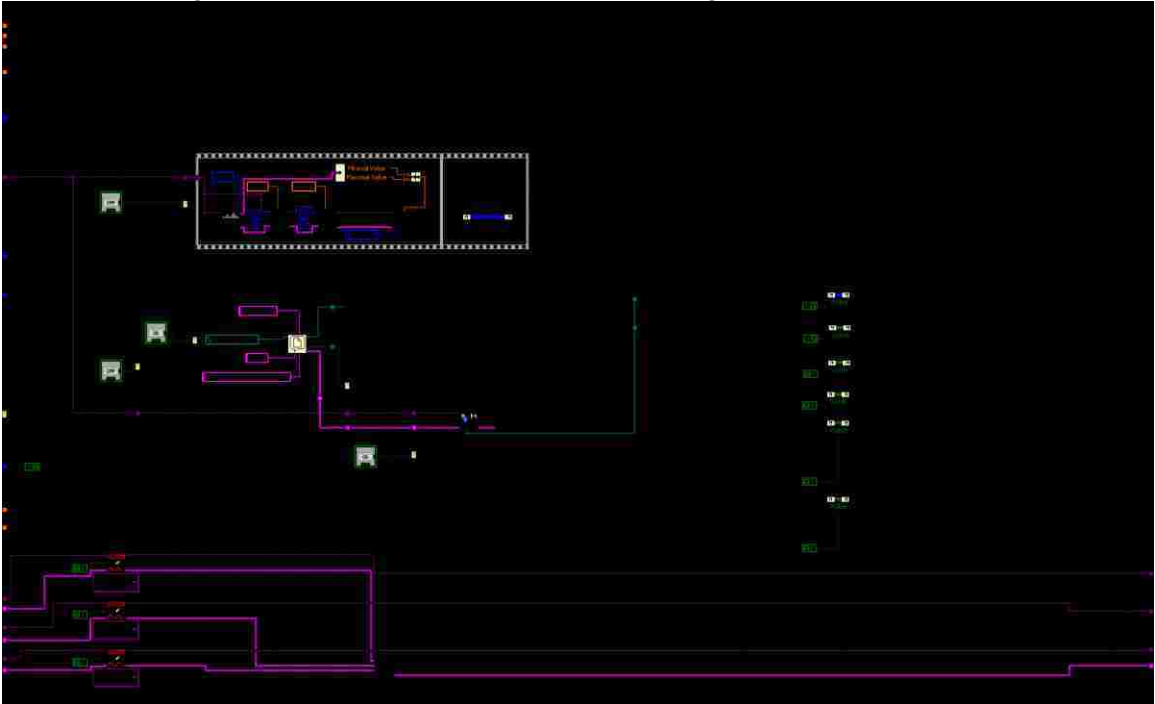


Image capture block if statement set to False,  
with save image block set to True,  
use last directory block set to True,  
and invalid file name block set to True.



## APPENDIX J

### MatLAB PROGRAM FOR PHOTONIC CRYSTAL UNIT CELL

MATLAB is used to generate a four-dimensional matrix describing a three-dimensional photonic crystal unit cell. This program is used to generate the HDF5 epsilon input file used by the MPB simulation software. The explanation of the math used in the program is found in Chapter 2. This program is very similar to “PhotonicCrystal.m” the one used to generate three-dimensional plot of photoresist profiles model of three-dimensional interferometric lithography found in Appendix B. The program consists of two files, the main program file called “PhC\_UnitCell.m” and a program function call file called “I\_Field.m”, the same function call used for “PhotonicCrystal.m” found in Appendix B. The programs “PhC\_UnitCell.m”, “I\_Field.m” are printed below.

#### PhC\_UnitCell.m

```
%% This file generates a 3D photonic crystal unit cell structure %%%
% "PhC_UnitCell.m" Created by Alex Raub
% Also requires "I_Field.m" file in the same directory

%%
clear;          % Clears items from workspace, freeing up system
memory.
close all;     % Closes all figure window.
deg = pi/180;  % Degree Constant
tic;          % Start timer

%% *** Enter Simulation Parameters ***
lambda = 355;  % Vacuum wavelength in nm
n = 1.7;      % Index of resist
theta_pol = 0; % Polarization angle 0=TE, pi/2=TM
theta_del = 7.458*deg; % The delta angle of the exposing beam
% from the crystal angle in the resist.
psi_c = 26.348*deg; % Crystal angle
phi_del = 120*deg; % The angle rotation between exposures
% 3 Exposures = 120*deg, 4 Exposures = 90*deg
phase = 0;    % The phase shift between exposures
% 3 Exposures = 0, 4 Exposures = pi/2
```

```

n_exp = 3; % The number of separate exposures (3, 4, or 6)
% needed to make the crystal
threshold = 0.62; % The resist exposure threshold,
% effects the line-space ratio.
array_size = 64; % Set the output array size
tick_del = 200; % Set the delta between axes tick marks in nm

% Set the Unit Cell Angles
gamma = 60*deg; % = 60deg for 3 Exposures, = 90deg for 4 Exposures

%% Set the lattice size of the Unit Cell %%
% Unit cell length in the X direction
a_x = lambda/(n*(sin(psi_c+theta_del)-sin(psi_c-theta_del)));
% Unit cell length in the Y direction
a_y = a_x/sin(phi_del);
% Unit cell length in the Z direction
a_z = a_x/tan(psi_c);

%% Set the offset to Unit Cell Origin %%
offset_x = 0; % = 0 for 3 Exposures, = a_x/4 for 4 Exposures
offset_y = 0; % = 0 for 3 Exposures, = a_y/4 for 4 Exposures
offset_z = 0; % = 0 for 3 Exposures, = a_z/8 for 4 Exposures

% *** End of Parameters ***
%% Set constants %%
k_prop = 2*pi*n/lambda;
del_x = a_x/array_size;
del_y = a_y/array_size;
del_z = a_z/array_size;

%% Initializes the output array with ones
PC_Plot = ones(array_size,array_size,array_size);

%% Enters the values into the PC_Plot array %
for x = 1:array_size;
    for y = 1:array_size;
        for z = 1:array_size;
            % Set the Unit cell index data to 1
            % or the resist epsilon n^2 based on the resist threshold
            if (1/n_exp*I_Field((x-1)*del_x+offset_x, ...
                (y-1)*del_y+offset_y+(x-
1)*del_x+offset_x)*cot(gamma), ...
                (z-1)*del_z+offset_z,theta_pol, ...
                theta_del,psi_c,phi_del,phase,n_exp,k_prop) ...
                - threshold) > 0
                PC_Plot(x,y,z) = n^2; % The output array PC_Plot
            end
        end
    end
end

%% 3D Plot %%
% Creates a Figure window and plots the 3D surface patch
% and face patches of the crystal unit cell
figure; % Creates a new figure window
% Plots the surface of the crystal
p_surf = patch(isosurface(PC_Plot,1));
% Plots the edge surfaces of the crystal at the boundaries
p_face = patch(isocaps(PC_Plot,1));
% Set the Figure window display parameters
% Set the current Figure for 3D Plot view [azimuth ,elevation]
view(45,45);

```

```

% Set the display X,Y,Z aspect ratios
daspect([1/a_x 1/a_y 1/a_z]);
axis tight; % Set the axes limits to the data limits
camlight headlight; % Set the Figure window camera light location
% Set the crystal surface color and lighting
set(p_surf,'FaceColor','white','EdgeColor','none');
% Set the crystal edge surface color
set(p_face,'FaceColor',[.75 .75 .75],'EdgeColor','none');
% Set the lighting of the face surface
set(p_surf,'FaceLighting','gouraud');
% Set the transparency and lighting of the edge surface
set(p_face,'FaceAlpha',1,'FaceLighting','flat');
% Set the axes style and line color
set(gca,'Box','on','Color','none',...
'XColor','Black','YColor','Black','ZColor','Black');
% Set the X axis scale bar tick marks
set(gca,'XTick',0:(array_size/a_x*tick_del):array_size);
% Set the Y axis scale bar tick marks
set(gca,'YTick',0:(array_size/a_y*tick_del):array_size);
% Set the Z axis scale bar tick marks
set(gca,'ZTick',0:(array_size/a_z*tick_del):array_size);
% Sets X axis tick values
set(gca,'XTickLabel',0:tick_del:a_x,'FontSize',14, ...
'FontWeight','bold');
% Sets Y axis tick values
set(gca,'YTickLabel',0:tick_del:a_y,'FontSize',14, ...
'FontWeight','bold');
% Sets Z axis tick values
set(gca,'ZTickLabel',0:tick_del:a_z,'FontSize',14, ...
'FontWeight','bold');
% Set the X axis label name and color
xlabel('X (nm)','Color','Black','FontSize',14,'FontWeight','bold');
% Set the Y axis label name and color
ylabel('Y (nm)','Color','Black','FontSize',14,'FontWeight','bold');
% Set the Z axis label name and color
zlabel('Z (nm)','HorizontalAlignment','right','Rotation',0,...
'Color','Black','FontSize',14,'FontWeight','bold');
% Sets the projection of 3-D objects.
set(gca,'Projection','orthographic','linewidth',3);
% Set the current Figure window background and position
set(gcf,'Color','white','Position',[20,20,900,900])

%% Set the Plot title name
title('Photonic Crystal Unit Cell','Color','Black','FontSize',14, ...
'FontWeight','bold');
% end of 3D plot

%% Write PC_Plot to HDF5 file "epsilon.h5"
hdf5write('epsilon.h5','/dataset1', PC_Plot);

%% Print program execution elapsed time
ElapsedTime=toc;
sprintf('Run time = %.0f minutes %2.1f seconds' ...
,fix(ElapsedTime/60),rem(ElapsedTime,60))

% *** End of Program *** %

```

## I\_Field.m

```
function I = I_Field(x,y,z,theta_pol,theta_del,psi_c,phi,phase,n_exp,k)
theta1 = psi_c-theta_del;
theta2 = psi_c+theta_del;
I = 0;
    for r = 0:n_exp-1
        I = I + (.5 * ...
            norm(E_Field(x,y,z,theta_pol*r,theta1,phi*r,phase,k) ...
                + E_Field(x,y,z,theta_pol*r,theta2,phi*r,phase*r,k)))^2;
    end

function E = E_Field(x,y,z,theta_pol,theta,phi,phase,k)
E = (cos(theta_pol)*[sin(phi); -cos(phi); 0]+sin(theta_pol)* ...
    [-cos(theta)*cos(phi); -cos(theta)*sin(phi); sin(theta)])* ...
    exp(1i*k*(sin(theta)*cos(phi)*x + sin(theta)*sin(phi)*y ...
    + cos(theta)*z) + 1i*phase);
```



## APPENDIX K

### MPB CONTROL SCRIPT FILES

The following two files are the control script input files for the MPB simulation software. The first file “MPB3Exp3DPhC.ctf” is for the three-exposure three-dimensional photonic crystal, and the second file “MPB4Exp3DPhC.ctf” is for the four-exposure three-dimensional photonic crystal.

#### MPB3Exp3DPhC.ctf

```
; Three Exposure Band Structure MPB Control File
; "MPB3Exp3DPhC.ctf" Created by Alex Raub

; define a couple of parameters
; (which we can set from the command-line)

(define-param a 898) ; a unit vector in real space
(define-param b a) ; b unit vector in real space
(define-param c 1813) ; c unit vector in real space

(set! geometry-lattice (make lattice
                        (basis-size a b c)
                        (basis1 1 0 0)
                        (basis2 (/ (sqrt 3) 2) 0.5 0)
                        (basis3 0 0 1)))

; Corners of the irreducible Brillouin zone
; for the Hexagonal primitive lattice.
(define Gamma (vector3 0 0 0))
(define A (vector3 0 0.5 0.5))
(define H (vector3 0 0.625 0.375))
(define K (vector3 (/ 3) (/ 3) 0.0))
(define L (vector3 0 0.5 0.5))
(define M (vector3 0.0 0.5 0))

(set! k-points (interpolate 10 (list Gamma A H K Gamma M L H K M)))

(set! epsilon-input-file "3_exp_epsilon.h5")

(set-param! resolution 32) ; use a 32x32x32 grid
(set-param! mesh-size 10)
(set-param! num-bands 30)

; run calculation
(run)
```

## MPB4Exp3DPC.ctf

```
; Four Exposure Band Structure MPB Control File
; "MPB4Exp3DPC.ctf" Created by Alex Raub

; define a couple of parameters
; (which we can set from the command-line)

(define-param a 898) ; a unit vector in real space
(define-param b a) ; b unit vector in real space
(define-param c 1813) ; c unit vector in real space

(set! geometry-lattice (make lattice
                        (basis-size a b c)
                        (basis1 1 0 0)
                        (basis2 0 1 0)
                        (basis3 0 0 1)))

; Corners of the irreducible Brillouin zone
; for the Tetragonal Centred lattice.
(define Gamma (vector3 0 0 0))
(define M (vector3 0 0 0.5))
(define X (vector3 0 0.5 0))
(define N (vector3 0.25 0.25 0.25))
(define P (vector3 0 0.5 0.25))
(define R (vector3 0.25 0.5 0))
(define G (vector3 0.25 0.25 0.5))
(define S (vector3 0.25 0.25 0.5))
(define T (vector3 0 0 0.25))

(set! k-points (interpolate 10 (list G M Gamma X P N Gamma S R X)))

(set! epsilon-input-file "4_exp_epsilon.h5")

(set-param! resolution 32) ; use a 32x32x32 grid
(set-param! mesh-size 10)
(set-param! num-bands 30)

; run calculation
(run)
```

## REFERENCES

- <sup>1</sup> William A. Goddard III, Donald W. Brenner, Sergey E. Lyshevski, Gerald H. Iafrate, Handbook of NANOSCIENCE, ENGINEERING, and TECHNOLOGY, *CRC Press*, 2nd ed (2007)
- <sup>2</sup> Steven G. Johnson, John D. Joannopoulos, PHOTONIC CRYSTALS The Road from Theory to Practice, *Kluwer Academic* (2002)
- <sup>3</sup> Jean-Michel Lourtioz, Vicent Berger, Daniel Maystre, Photonic Crystals: towards nanoscale photonic devices, *Springer*, 2<sup>nd</sup> ed. (2008)
- <sup>4</sup> E. Yablonovitch, Photonic Crystals: Semiconductors of Light, *Scientific American*, p47 (December 2001)
- <sup>5</sup> E. Yablonovitch, T. J. Gmitter, Photonic band structure: The face-centered-cubic case employing nonspherical atoms, *Phys. Rev. Lett.* 67, p2295–2298 (1991)
- <sup>6</sup> S. Y. Lin, J. G. Fleming, D. L. Hetherington, B. K. Smith, R. Biswas, K. M. Ho, M. M. Sigalas, W. Zubrzycki, S. R. Kurtz, J. Bur, A three-dimensional photonic crystal operating at infrared wavelengths, *Nature* **394**, p251 (1998)
- <sup>7</sup> M. Campbell, D. N. Sharp, M. T. Harrison, R. G. Denning, A. J. Turberfield Fabrication of photonic crystals for the visible spectrum by holographic lithography, *Nature* **404**, p53-56 (2000)
- <sup>8</sup> Y. Lin, D. Rivera, K. P. Chen, Woodpile-type photonic crystals with orthorhombic or tetragonal symmetry formed through phase mask techniques, *OSA* **14-2**, p887-892 (2006)
- <sup>9</sup> T. Sondergaard, K.H. Dridi, Energy flow in photonic crystal waveguides, *Phys. Rev. B* **61**, p15688-15696 (2000)
- <sup>10</sup> M. Bayindir, B. Temelkuran, E. Ozbay, Tight-Binding Description of the Coupled Defect Modes in Three-Dimensional Photonic Crystals, *Phys. Rev. Lett.* **84**, p2140-2143 (2000)
- <sup>11</sup> E. Yablonovitch, K. M. Leung, Hope for photonic bandgaps, *Nature* **351**, p278-278 (1991)

- <sup>12</sup> C. Cuisin, A. Chelnokov, D. Decanini, D. Peyrade, Y. Chen, J. M. Lourtioz, Sub-micrometre dielectric and metallic yablonovite structures fabricated from resist templates, *Optical and Quantum Electronics* **34**, p13–26 (2002).
- <sup>13</sup> D. Xia, J. Zhang, X. He, S. R. J. Brueck, Fabrication of three-dimensional photonic crystal structures byinterferometric lithography and nanoparticle self-assembly, *Applied Phys. Letters* **93**, p071105 (2008)
- <sup>14</sup> Geoffrey I.N. Waterhouse, and Mark R. Waterland, Opal and inverse opal photonic crystals: Fabrication and characterization, *Polyhedron*, **26**, p356-368 (2007)
- <sup>15</sup> S. H. Zaidi, S. R. J. Brueck, Multiple-exposure interferometric lithography *J. Vac. Sci. Technol. B*, **11** No. 3, p658-666, May/June 1993
- <sup>16</sup> S. Cristoloveanu, M. Shur, Frontiers in Electronics, *World Scientific Publishing Co. Pte. Ltd.* **50**, p132, (2009)
- <sup>17</sup> M. V. Klein, T. E. Furtak, Optics, J. Wiley & Sons, 2<sup>nd</sup> ed. (1986)
- <sup>18</sup> Chris A. Mack, Lithographic Simulation: A Review, *Lithographic and Micromachining Techniques for Optical Component Fabrication*, SPIE **4440**, p 59-72 (2001)
- <sup>19</sup> S.G.Johnson, C.Manolatou, S.H.Fan, P.R.Villeneuve, J.D.Joannopoulos, H.A.Haus, TE Elimination of cross talk in waveguide intersections, *Optics Letters* **23**, No. 23, p1855-1857 (1998)
- <sup>20</sup> J. D. Joannopoulos, S. G. Jhonson, J. N Winn, R. D. Meade, Photonic crystals: molding the flow of light, *Princeton University Press* (2008)
- <sup>21</sup> Jordi Martorell, R. Vilaseca, R. Corbalán, Second harmonic generation in a photonic crystal, *Appl. Phys. Lett.* **70**, No.6, p702-704 (1997)
- <sup>22</sup> P. V. Braun, A. Rinne, F. García-Santamarí, Introducing Defects in 3D Photonic Crystals: State of the Art, *Adv. Mater*, **18**, p2665–2678 (2006)
- <sup>23</sup> Alex K. Raub, S. R. J. Brueck, Large area three-dimensional photonic crystals with embedded waveguides, *J. Vac. Sci. Technol. B* **28**, No.6 (2010)
- <sup>24</sup> K. Ronse, M. Op de Beeck, L. Van den hove, J Engelens, Fundamental principles of phase shifting masks by Fourier optics: Theory and experimental verification, *J. Vac. Sci. Technol. B*, **12**, No. 2, p589-600, Mar/Apr 1994.

- <sup>25</sup> M. D. Levenson, Wavefront Engineering For Photolithography, Physics Today, July 1993, p28-36
- <sup>26</sup> K. K. Sharma, Optics: principles and applications, Academic Press, (2006)
- <sup>27</sup> Justyna K. Gansel, Martin Wegener, Sven Burger, and Stefan Linden, Gold helix photonic metamaterials: A numerical parameter study, *Optics Express* **18** (2), p1059-1069 (2010)
- <sup>28</sup> Justyna K. Gansel, Michael Thiel, Michael S. Rill, Manuel Decker, Klaus Bade, Volker Saile, Georg von Freymann, Stefan Linden, Martin Wegener, Gold Helix Photonic Metamaterial as Broadband Circular Polarizer, *Science* **325**, p1513-1515 (2009)
- <sup>29</sup> M. Thiel, H. Fischer, G. von Freymann, and M. Wegener, Three-dimensional chiral photonic superlattices, *Optics Letters* **35** (2), p166-168 (2010)
- <sup>30</sup> Yong Jun Park, K. M. A. Sobahan, and Chang Kwon Hwangbo, Wideband circular polarization reflector fabricated by glancing angle deposition, *Optics Express* **16** (8), p5186-5192 (2008)
- <sup>31</sup> Marc De Graef, Micheal E. McHenry, Structure of materials : an introduction to crystallography, diffraction and symmetry, *Cambridge University Press* (2007)
- <sup>32</sup> Wikipedia Crystal system *Wikimedia Foundation*, 25 September 2010. Web. [http://en.wikipedia.org/wiki/Crystal\\_systems](http://en.wikipedia.org/wiki/Crystal_systems). 8 October 2010.
- <sup>33</sup> Bilbao Crystallographic Server, The k-vector types and Brillouin zones of the space groups, *University of the Basque Country*, Web. [http://www.cryst.ehu.es/cryst/get\\_kvec.html](http://www.cryst.ehu.es/cryst/get_kvec.html), 8 October 2010.
- <sup>34</sup> Steven G. Johnson and J. D. Joannopoulos, Block-iterative frequency-domain methods for Maxwell's equations in a planewave basis, *Optics Express* **8** (3), p173-190 (2001)
- <sup>35</sup> Ardavan Farjadpour, David Roundy, Alejandro Rodriguez, Mihai Ibanescu, Peter Bermel, J. D. Joannopoulos, Steven G. Johnson, and Geoffrey Burr, Improving accuracy by subpixel smoothing in FDTD, *Optics Letters* **31** (20), p2972–2974 (2006)
- <sup>36</sup> Alvaro Blanco, Emmanuel Chomski, Serguei Grabtchak, Marta Ibisate, Sajeev John, Stephen W. Leonard, Cefe Lopez, Francisco Meseguer, Hernan Miguez, Jessica P. Mondia, Geoffrey A. Ozin, Ovidiu Toader, and Henry M. van Driel, Large-scale synthesis of a silicon photonic crystal with a complete three-dimensional bandgap near 1.5micrometres, *NATURE*, **40**, p437-440 (MAY 2000)

- <sup>37</sup> William Blum and George H. Hogaboom, Principles of electroplating and electroforming (electrotyping), *McGraw-Hill* (1949)
- <sup>38</sup> Graham, A. Kenneth, Electroplating engineering handbook; prepared by a staff of specialists *Reinhold Pub. Corp.* 2<sup>nd</sup> ed (1962)
- <sup>39</sup> Wikipedia Electroforming *Wikimedia Foundation*, 26 May 2010. Web. <http://en.wikipedia.org/wiki/Electroforming>. 5 July 2010.
- <sup>40</sup> A. K. Raub, Deep UV immersion interferometric lithography, Thesis UNM, (2002)
- <sup>41</sup> A. K. Raub, A. Frauenglass, S. R. J. Brueck, W. Conley, R. R. Dammel, A. Romano, M. Sato, W. Hinsberg, Deep-UV immersion interferometric lithography, *Proc. SPIE* **5377**, p306 (2004)